

# **CHARACTERISING THE STRUCTURE AND PROPERTIES OF BIMETALLIC NANOPARTICLES**

by

Ruth L. Chantry

A thesis submitted to The University of Birmingham for the degree of  
DOCTOR OF PHILOSOPHY

Nanoscale Physics Research Laboratory

School of Physics and Astronomy

The University of Birmingham

June 2013

## **Abstract**

The work presented in this thesis explores the use of aberration corrected scanning transmission electron microscopy (ac-STEM) in characterising the structure and properties of bimetallic nanoparticles. STEM imaging and energy dispersive X-ray spectroscopy (EDX) are used to show the influence that reaction kinetics have over the formation of structure in AuRh and AuPd nanorods. Correlated imaging and electron energy loss spectroscopy (EELS) are used to characterise the localised surface plasmon resonance (LSPR) response of single AuPd and AuRh nanorods, showing how ac-STEM can be used to identify the origins of this response. Finally the full range of ac-STEM techniques (imaging, EDX and EELS) are applied to identify the formation of ordered AuAg oxide structures in AuAg nanoparticles that have been aged in air and to show the impact their structural evolution has on LSPR properties. Through this work we show that the unrivalled spatial resolution and range of elementally sensitive techniques available in ac-STEM is essential to the characterisation of bimetallic nanoparticles. The capabilities of these instruments give the possibility to gain a fundamental understanding of the metal-metal interactions taking place in these systems, and thus form connections to the properties that result from them, which is necessary to their effective use in both catalytic and plasmonic applications.

## **Acknowledgments**

I have received help and support from many people whilst conducting this work, in particular I would like to thank the following individuals.

Dr Ziyou Li, my supervisor, for her help and advice throughout this study, but also for her enthusiasm for this project, which has helped make it such an enjoyable experience.

Prof. Richard Palmer for the opportunity to work in the Nanoscale Physics Research Laboratory.

All of my colleagues, past and present, but in particular Miriam Dowle, Charlotte O'Neale, Dongsheng He, and Tianluo Pan whose consistent friendship and support has been invaluable.

Dr Zhiwei Wang, Paul Hambridge and Dr Adam Papworth for their expertise and assistance with aberration corrected scanning transmission microscopy and electron energy loss spectroscopy.

Dr Sarah Horswell, Prof. Roy Johnston and Prof. Simon Brown for their helpful advice and suggestions in relation to many aspects of this project.

Wilai Siriwatcharapiboon, Domagoj Belic and Bishnu Khanal for making the samples.

Nima Zardoshti and Dr Andrew Logsdail for their assistance with DDSCAT and many other matters, both related and unrelated.

## **Author's Contribution**

All of the work presented in this thesis was conducted by the author under the supervision of Dr Ziyou Li. This study involved the assistance of a number of collaborators; these contributions are described in full at the start of each chapter.

## Author's Publications

“An Atomistic View of the Interfacial Structures of Au-Core Rh and Pd-Shell Nanorods” Chantry, R.L.; Siriwatcharapiboon, W.; Horswell, S.L.; Khanal, B.P.; Zubarev, E.R.; Atanasov, I.; Johnston, R.L.; Li, Z.Y., *Nanoscale*, **2013**, *5*, 7452-7457

“HRTEM and STEM-HAADF Characterisation of Au-TiO<sub>2</sub> and Au-Al<sub>2</sub>O<sub>3</sub> Catalysts for a Better Understanding of the Parameters Influencing Their Properties in CO Oxidation” Delannoy, L.; Chantry, R.L.; Casale, S.; Li, Z.Y.; Borenzstein, Y.; Louis, C., *Chem. Phys. Phys. Chem.*, **2013**, *15*, 3473-3479

“Overgrowth of Rhodium on Gold Nanorods” Chantry, R.L.; Siriwatcharapiboon, W.; Horswell, S.L.; Logsdail, A.J.; Johnston, R.L.; Li, Z.Y., *J. Phys. Chem. C* **2012**, *116*, 10312-10317

“Au-Ag Nanoparticles: Structure and Phase Segregation” Belic, D.; Chantry, R.L.; Li, Z.Y.; Brown, S.A., *Appl. Phys. Lett.*, **2011**, *99*, 1179

# Table of Contents

<b>List of Figures .....</b>	<b>viii</b>
<b>List of Tables.....</b>	<b>xiii</b>
<b>Abbreviations.....</b>	<b>xiv</b>
<b>Chapter 1 Introduction .....</b>	<b>1</b>
List of References .....	8
<b>Chapter 2 Literature Review.....</b>	<b>10</b>
2.1 Structure in Segregated Bimetallic Nanoparticles .....	10
2.1.1 <i>AuRh</i> .....	14
2.1.2 <i>AuPd</i> .....	20
2.1.3 <i>AuAg</i> .....	24
2.2 Localised Surface Plasmon Resonance in Bimetallic Nanoparticles .....	28
2.2.1 <i>Theoretical background</i> .....	29
2.2.2 <i>Surface plasmons of Au, Ag, Rh and Pd</i> .....	32
2.2.3 <i>LSPR characterisation</i> .....	36
List of References .....	43
<b>Chapter 3 Experimental Methods: Characterisation of Structure.....</b>	<b>51</b>
3.1. Overview of STEM .....	52
3.2. Resolution.....	56
3.3. Imaging.....	65
3.4. Energy Dispersive X-ray Spectroscopy .....	78
3.5. Conclusions .....	81
List of References .....	82

<b>Chapter 4</b>	<b>Experimental Methods: Characterisation of Electronic Properties</b>	<b>84</b>
4.1.	Electron Energy Loss Spectroscopy	85
4.1.1	<i>Overview</i>	86
4.1.2	<i>Plasmon mapping using STEM-EELS spectrum imaging</i>	96
4.2.	Supporting Techniques	102
4.2.1	<i>UV-visible spectroscopy</i>	102
4.2.2	<i>Discrete Dipole Approximation simulation</i>	104
4.3	Conclusions	110
	List of References	112
<b>Chapter 5</b>	<b>Structure of Segregated Bimetallic Nanorods</b>	<b>114</b>
5.1.	Rh Over-Growth on Au-Seed Nanorods	115
5.1.1	<i>Au seed nanorods</i>	116
5.1.2	<i>AuRh nanorods</i>	119
5.1.3	<i>Impact on optical response</i>	124
5.1.4	<i>Rh growth mode</i>	128
5.2.	Atomic Structure of Metal-Metal Interfaces in Bimetallic Nanorods	130
5.2.1	<i>STEM-EDX results</i>	131
5.2.2	<i>STEM imaging results</i>	133
5.2.3	<i>Discussion</i>	139
5.3.	Conclusions	143
	List of References	145
<b>Chapter 6</b>	<b>Localised Surface Plasmon Response of Bimetallic Nanorods</b>	<b>147</b>
6.1	LSPR Response of AuPd Nanorods	149
6.1.1	<i>STEM-EELS spectrum image mapping</i>	149
6.1.2	<i>Comparison to DDA simulation</i>	159

6.1.3	<i>Asymmetric shell growth</i> .....	163
6.1.4	<i>Summary</i> .....	165
6.2	LSPR Response of AuRh Nanorods.....	165
6.3	Investigating the Impact of Uneven Shell Growth Using Optical Response Simulation .....	172
6.4	Conclusions .....	179
	List of References .....	181
<b>Chapter 7</b>	<b>AuAg Nanoparticle Oxidation</b> .....	<b>183</b>
7.1	Initial Studies.....	185
7.2	Oxidation of Ag-only Nanoparticles .....	193
7.2.1	<i>Atomic structure of aged Ag nanoparticles</i> .....	195
7.2.2	<i>More complex structures</i> .....	197
7.3	Oxidation of AuAg Nanoparticles.....	199
7.3.1	<i>Comparison of aged AuAg and Ag-only nanoparticles</i> .....	199
7.3.2	<i>Au atoms in AuAg oxide surface structures</i> .....	207
7.3.3	<i>Au atoms in AuAg oxide underlying structures</i> .....	212
7.4	Impact on Localised Surface Plasmon Response.....	215
7.5	Conclusions .....	221
	List of References .....	222
<b>Chapter 8</b>	<b>Conclusions &amp; Future Work</b> .....	<b>224</b>
8.1	Conclusion.....	224
8.1.1	<i>Structural characterisation</i> .....	224
8.1.2	<i>LSPR response</i> .....	225
8.1.3	<i>Long term stability</i> .....	226
8.1.4	<i>Summary</i> .....	227



8.2	Future Work .....	227
<b>Appendix I</b>	<b>Summary of AuRh and AuPd nanorod synthesis methodology .....</b>	<b>230</b>
<b>Appendix II</b>	<b>Summary of the molecular dynamics simulation methodology.....</b>	<b>233</b>

## **List of Figures**

1.1	Periodic table of elements	4
1.2	The role of ac-STEM	5
2.1	Schematic examples of possible multimetallic nanosystem structures	11
2.2	Simple Scheme for the categorisation of growth modes	13
2.3	Bulk phase diagram for Au-Rh	15
2.4	STM images of Rh deposited on Au(111)	16
2.5	STM images stages of Rh deposition on Au(111)	18
2.6	Bulk phase diagram for Au-Pd	22
2.7	HRTEM images of segregated Au-Pd nanoparticles	23
2.8	STEM-HAADF images of Au-Pd nanoparticles	23
2.9	Bulk phase diagram for Au-Ag	25
2.10	Simulated structures for AuAg nanoparticles	26
2.11	Frequency dependent optical constants	35
2.12	An Example of UV-vis characterisation of LSPR for AuAg nanorods	37
2.13	An example of optical dark field spectroscopic characterisation of AuAg nanoparticles	38
2.14	STEM-EELS plasmon maps of AuAg nanoparticles	40
2.15	STEM-EELS plasmon maps of AuAg dumbbell nanorods	42
3.1	JEOL 2100f STEM	53
3.2	Schematic representation of spherical aberration	58
3.3	CEOS double hexapole spherical aberration corrector	59
3.4	CEOS alignment software and resulting ronchigram	61
3.5	Principle aberrations present in an ac-STEM with double hexapole corrector	63

3.6	Demonstration of 0.11 nm spatial resolution	64
3.7	STEM imaging detectors	66
3.8	Example of atomically resolved imaging	67
3.9	Example of Z-contrast	71
3.10	Schematic representation and an example of electron diffraction	72
3.11	Example of image noise reduction using fft mask	74
3.12	Example of image filtering using fft masks	75
3.13	An example of beam damage to an Au cluster	76
3.14	Schematic representations of stimulated X-ray emission and the EDX detector	78
3.15	An example of STEM-EDX characterisation of bimetallic nanoparticles	80
4.1	Schematic representation of the principle components of the EELS spectrometer	85
4.2	Typical EELS spectrum from 0 eV to 500 eV energy loss	87
4.3	The impact on energy resolution of lowering emission current	90
4.4	The impact of background subtraction and zero loss extraction	92
4.5	Illustration of the delocalisation of inelastic scattering	93
4.6	Illustration of the impact of different methods of noise reduction on STEM-EELS spectra	95
4.7	Schematic illustration of STEM-EELS spectrum image mapping	98
4.8	A comparison of different methods of setting spectrum image map contrast	100
4.9	STEM-EELS carbon spectrum from 1.5 eV to 9.5 eV	101
4.10	Schematic representation of the principle components of a UV-vis spectrophotometer	102
4.11	Illustration of DDA simulation in the DDSCAT program and the impact of dipole density	105
4.12	An example of systematic simulation of optical response	106

4.13	An example illustrating the use of field simulation to identify spectral features	108
4.14	An example illustrating the use of DDfield to interpret STEM-EELS plasmon maps	109
5.1	Typical STEM-HAADF and SEM images of Au nanorods	116
5.2	Au nanorod size analysis	118
5.3	STEM-HAADF images of the ends of Au nanorods	118
5.4	Typical SEM and STEM-HAADF images of AuRh nanorods	120
5.5	A comparison of typical Au-only and AuRh nanorods	121
5.6	STEM-EDX elemental maps of an AuRh nanorod	123
5.7	UV-vis and optical simulation results for Au-only and AuRh nanorods	125
5.8	Investigating the impact of Rh end growth on optical response using UV-vis and DDA simulation	126
5.9	STEM-HAADF and BF images of low coverage AuRh nanorod	128
5.10	EDX elemental maps from AuRh and AuPd nanorods	132
5.11	Atomically resolved STEM-HAADF and BF images of the AuPd metal-metal interface	134
5.12	Lattice spacing measurements around the AuPd metal-metal interface	135
5.13	Atomically resolved STEM-HAADF and BF images of the AuRh metal-metal interface	136
5.14	Lattice spacing measurements around the AuRh metal-metal interface	138
5.15	STEM-HAADF images of AuRh and AuPd nanorods taken more than one year a part	140
5.16	Molecular dynamics simulation results for AuRh and AuPd	141
6.1	STEM-EELS plasmon maps from the ends of Au-only and AuPd nanorods	150
6.2	Typical examples of Au-only and AuPd STEM-EELS spectra over the energy loss range from 1.5 eV to 9.5 eV	152

6.3	STEM-EELS spectrum image maps and point spectra taken around an AuPd nanorod	154
6.4	STEM-EELS spectrum image maps from whole Au and AuPd nanorods from 1.5 eV to 4.0 eV energy loss	157
6.5	Simulated spectra for Au-only, Pd-only and AuPd nanorods	160
6.6	DDfield simulations for AuPd, Au-only and Pd-only nanorods	162
6.7	STEM-EELS spectrum image maps from an Au nanorod with asymmetric shell coverage	164
6.8	Spectrum image maps from the ends of AuPd and AuRh nanorods	166
6.9	Simulated spectra for Au-only, Rh-only and AuRh nanorods	167
6.10	Point spectra taken from around AuRh, Au-only and AuPd nanorods	169
6.11	Simulated spectra for AuRh nanorods with full shells	173
6.12	Simulated spectra for AuRh nanorods with end and side shells only	174
6.13	DDfield simulations for AuRh nanorods with shell only at one end	176
6.14	Simulated spectra for end-capped AuRh, Au-only and Rh-only nanorods of equal volume	177
7.1	HRTEM images of AuAg nanoparticles	186
7.2	HRTEM and STEM-HAADF images of aged AuAg nanoparticles	187
7.3	Image intensity analysis from an aged AuAg nanoparticle	188
7.4	STEM-EELS core loss mapping from an aged AuAg nanoparticle	189
7.5	STEM-HAADF image of aged AuAg particles in profile	190
7.6	STEM-HAADF images of AuAg particles taken more than 12 months apart	191
7.7	STEM-HAADF images of aged Ag-only particles	194

7.8	Comparison between experimental and theoretical Ag oxide structures in {111} orientation	195
7.9	STEM-HAADF image and fft of Ag <sub>2</sub> O in {111} orientation	197
7.10	Ag <sub>2</sub> O with more complex structure in {100} orientation	198
7.11	Atomically resolved STEM-HAADF images of aged AuAg nanoparticles	200
7.12	STEM-EDX elemental maps of aged AuAg nanoparticles	202
7.13	AuAg and Ag-only nanoparticles before and after interaction with the electron beam	203
7.14	Monitoring the evolution of an aged AuAg nanoparticle under the electron beam	205
7.15	Atomic structure of an oxidised AuAg nanoparticle after interaction with the electron beam	206
7.16	Schematic comparison of the structural evolution of AuAg and Ag-only nanoparticles	208
7.17	An aged AuAg nanoparticle exhibiting complex lattice structure in {111} orientation	209
7.18	An aged AuAg nanoparticle exhibiting complex lattice structure in {100} orientation	210
7.19	Comparison of aged AuAg and Ag-only atomic structure in {111} orientation	213
7.20	STEM-EELS map of an aged AuAg nanoparticle	216
7.21	Evolution of STEM-EELS mapping of an aged AuAg nanoparticle through interaction with the electron beam	217
7.22	The evolution of two aged AuAg nanoparticles under the electron beam	219
7.23	Example of core formation between adjacent AuAg nanoparticles	220

## List of Tables

2.1	Key parameters of Au and Rh	15
2.2	Key parameters of Au and Pd	21
2.3	Key parameters of Au and Ag	24
2.4	Surface plasmon resonances	33

## Abbreviations

ac-STEM	aberration corrected Scanning Transmission Electron Microscope/Microscopy
BF	Bright Field
$C_c$	Chromatic Aberration
$C_s$	Spherical Aberration
CTAB	Cetyl Trimethylammonium Bromide
DDA	Discrete Dipole Approximation
EDX	Energy Dispersive X-ray Spectroscopy
EELS	Electron Energy Loss Spectroscopy
fcc	face centred cubic
FEG	Field Emission Gun
fft	fast fourier transform
FWHM	Full-Width-Half-Maximum
HAADF	High Angle Annular Dark Field
LEED	Low Energy Electron Diffraction
LEIS	Low Energy Ion Spectroscopy
LSPR	Localised Surface Plasmon Resonance
SEM	Scanning Electron Microscope/Microscopy
STEM	Scanning Transmission Electron Microscope/Microscopy
STM	Scanning Tunnelling Microscope/Microscopy
TEM	Transmission Electron Microscope/Microscopy
XPS	X-ray Photoelectron Spectroscopy



---

# Chapter 1

## Introduction

Interest in bimetallic nanoparticles has increased significantly in recent years with the identification of many potential applications for which they may be suited, and in particular for their use as industrial catalysts. They allow the possibility to combine the novel nanoscale properties of more than one element within one nanoparticle, and to gain enhancement to properties through synergistic interactions between those elements.<sup>1-4</sup> This gives bimetallic nanoparticles significant advantages over their monometallic counterparts. Their greatest advantage lies in the tunability of their properties, as they offer possibilities for levels of control that are not available in monometallic nanoparticles. For example, their properties can potentially be controlled through altering composition and chemical ordering, as well as through controlling size and shape. In the case of sequentially synthesised systems size and shape can be influenced through both the template particle and the deposition of the second metal. This tunability means bimetallic nanoparticles form the most likely candidates for the realisation of the goal of rationally designed catalysts,<sup>5</sup> and are now the system of choice for the development of new industrial catalysts.

One area of current research activity in this field is the investigation of potential enhancements to catalytic reactivity, and the monitoring of reactivity, through exploiting the localised surface plasmon resonances (LSPR) of nanoparticles. The ability to control LSPR of monometallic nanoparticles through altering particle size and shape is well established.<sup>6</sup> The LSPR of bimetallic nanoparticles, whilst being more complex than that of monometallic nanoparticles,<sup>7</sup> is potentially equally tuneable and offers the possibility to combine a catalytically active metal with another of desirable plasmonic capabilities to realise plasmonic enhancement benefits.<sup>8-11</sup> This makes bimetallic nanoparticles of great interest as model systems for the investigation of LSPR catalytic interactions, as well as also being of interest in other fields where tuneable LSPR is desirable such as in bio-sensing and nanoplasmonics. However, the full realisation of the potential of bimetallic nanoparticles, both for their catalytic and LSPR properties, is dependent on gaining a fundamental understanding of the source of their novel and tuneable properties, and it is this that forms the focus of the research presented in this thesis.

Nanoparticles are broadly defined by size, with the range 1-100 nm often taken as an informal definition. In this size regime, lying between the classical behaviour of bulk matter and the quantum behaviour of individual atoms, surface effects and other factors, such as interaction with a substrate, become more influential, and can result in novel nanoscale properties that potentially deviate significantly from those of bulk matter. One example of nanoscale systems yielding unusual properties not present in bulk matter is that of monometallic Au nanoparticles. Au is not catalytically active in bulk form but Au nanoparticles, both in the form of very small clusters<sup>12</sup> and much larger nanorods,<sup>13</sup> have been found to be catalytically active to reactions such as carbon monoxide reduction. However, despite a significant amount of ongoing research activity in this area, the exact

cause of this reactivity is still not known. Initially, when Au reactivity was identified in very small nanoclusters, it was linked directly to cluster size. More recent work, whilst not disproving a link between size and reactivity, have emphasised a potential role from the nature of the substrate used, indicating a contribution to reactivity from cluster-substrate interaction effects.<sup>14</sup> However, reactivity has also been found in larger Au nanosystems, where substrate interactions are not a factor and where no link between size and reactivity is apparent. The recent development of single particle reactivity measurements on large Au nanorods identified a pattern of reactivity with a gradient from the centre to the ends of the nanorods; this was speculated to be linked to a comparable gradient in the density of atomic scale surface defects on the nanorods.<sup>13</sup> This example of monometallic Au nanoparticle reactivity shows that whilst significant progress has been made in both the synthesis and measurement of the properties of these systems, and also in the development of computer simulation techniques to explore them theoretically, fundamental understanding of the origin of properties gained through controlled experiments is in most cases still lacking. It also illustrates the necessity for atomic scale investigation in identifying the origin of novel nanoscale properties, as for both very small Au clusters and much larger Au nanorods the speculated causes of particle reactivity are linked to structural factors at the atomic scale, and thus can only be proved through forming a link between reactivity and atomically resolved structural characterisation.

The lack of fundamental understanding of the origin of nanoscale properties is an even greater issue for bimetallic nanosystems, which is a more recent field of research, with a wide variety of systems, all of which have differing characteristics, and because the properties of bimetallic systems do not just depend on the nanoscale behaviour of one element, but of two, and on the interactions between them. The metal-metal interactions

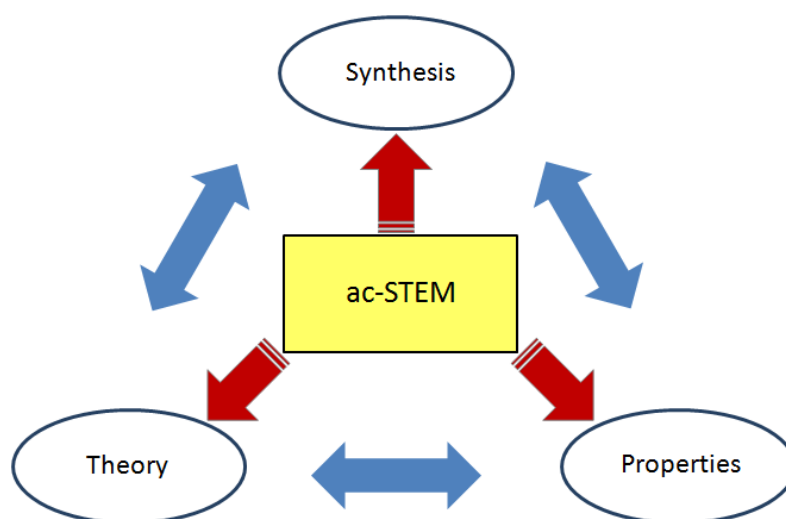
that are the source of the desirable and tuneable properties of bimetallic nanoparticles are complex and may occur beneath the surface of the particle, even when they affect surface properties. Thus gaining fundamental understanding of the driving forces behind the properties of bimetallic nanoparticles is a challenging task.

To address this challenge in this thesis we apply ac-STEM characterisation techniques to three similar bimetallic systems. These systems comprise metals with comparable relative atomic numbers. They all contain Au in combination with respectively adjacent period 5 metals Rh, Pd and Ag (shown in the periodic table of elements given in Figure 1.1).

Group →	1	2	3	4	5	6	7	8	9	10	11	12	13	14	15	16	17	18							
↓ Period																									
1	1 H																	2 He							
2	3 Li	4 Be											5 B	6 C	7 N	8 O	9 F	10 Ne							
3	11 Na	12 Mg											13 Al	14 Si	15 P	16 S	17 Cl	18 Ar							
4	19 K	20 Ca	21 Sc	22 Ti	23 V	24 Cr	25 Mn	26 Fe	27 Co	28 Ni	29 Cu	30 Zn	31 Ga	32 Ge	33 As	34 Se	35 Br	36 Kr							
5	37 Rb	38 Sr	39 Y	40 Zr	41 Nb	42 Mo	43 Tc	44 Ru	45 Rh	46 Pd	47 Ag	48 Cd	49 In	50 Sn	51 Sb	52 Te	53 I	54 Xe							
6	55 Cs	56 Ba		72 Hf	73 Ta	74 W	75 Re	76 Os	77 Ir	78 Pt	79 Au	80 Hg	81 Tl	82 Pb	83 Bi	84 Po	85 At	86 Rn							
7	87 Fr	88 Ra		104 Rf	105 Db	106 Sg	107 Bh	108 Hs	109 Mt	110 Ds	111 Rg	112 Cn	113 Uut	114 Uuq	115 Uup	116 Uuh	117 Uus	118 Uuo							
				Lanthanides							57 La	58 Ce	59 Pr	60 Nd	61 Pm	62 Sm	63 Eu	64 Gd	65 Tb	66 Dy	67 Ho	68 Er	69 Tm	70 Yb	71 Lu
				Actinides							89 Ac	90 Th	91 Pa	92 U	93 Np	94 Pu	95 Am	96 Cm	97 Bk	98 Cf	99 Es	100 Fm	101 Md	102 No	103 Lr

**Figure 1.1 Periodic table of elements.** Periodic table of elements, with the metals used in systems that are the subject of this study, Rh, Pd, Ag and Au, highlighted.

The latest generation of aberration corrected scanning transmission electron microscopes (ac-STEM) makes available an unrivalled range of imaging and spectroscopic techniques within one instrument with the potential to provide elemental and structural information, including from sub-surface locations, to atomic resolution, as well as allowing characterisation of electronic properties through electron energy loss spectroscopy (EELS). In this thesis we seek to explore the possibilities offered by one ac-STEM instrument in addressing the challenge of atomic scale characterisation of bimetallic nanoparticles.



**Figure 1.2: The role of ac-STEM.** Schematic representation of the role of ac-STEM in the characterisation of bimetallic nanoparticles

To gain a fundamental understanding of the factors driving the structure and properties of bimetallic nanoparticles, and thus achieve the ultimate goal of rational design in bimetallic nanocatalysts, a link must be formed between synthesis, measurement of properties, and fundamental theoretical understanding (Figure 1.2), we believe ac-STEM has the potential to provide this link. It is only in the last few years that ac-STEM instruments have become more widely available, so their use in the structural

characterisation of bimetallic nanoparticles has to date been limited. In Chapter 2 we summarise the key literature in this field, with a focus on core-shell systems that are the subject of this current work: AuRh, AuPd and AuAg. A wide range of parameters affect the metal-metal interactions in these systems, including the elemental and structural characteristics of the individual component metals, and the relative differences between them, so in Chapter 2 we also set out the key parameters for each of the relevant systems.

In Chapters 3 and 4 we describe the imaging and spectroscopic capabilities of the ac-STEM instrument used for this work, including considering the limitations and advantages of the techniques it offers. Despite the wide range of data potentially available through these instruments, it is still necessary to use supporting techniques in the interpretation of ac-STEM results, so in these chapters we also describe other supporting techniques that were used in this study.

In Chapter 5 we present results using the imaging and energy dispersive X-ray spectroscopy (EDX) capabilities of ac-STEM in the characterisation of Rh over-growth on Au-seed nanorods at the single particle level, and consider how this impacts on the optical response of this system. We then extend this work to include a comparative study of the atomic structure of the buried metal-metal interfaces of Au<sub>core</sub>Rh<sub>shell</sub> and Au<sub>core</sub>Pd<sub>shell</sub> nanorods, including consideration of the driving forces for the formation of their interfacial structures.

In Chapter 6 we use STEM-EELS to investigate the LSPR response of bimetallic nanoparticles. We present single particle measurements for AuRh and AuPd nanorods. Through correlation to STEM images and by making comparison to similar measurements taken from monometallic Au nanorods, we show how STEM-EELS spectrum image

mapping can be used to identify the origins and influencing factors on bimetallic LSPR response.

A factor that is of considerable interest in nanoparticle systems with a view to their practical use is their long term stability. In Chapter 7 we present results that employ elementally sensitive ac-STEM imaging and spectroscopy to characterise the impact of sample evolution on the structure of AuAg nanoparticles that have been stored in air, both at the single particle and atomic scale. We also examine the influence that structural evolution has on the LSPR response of this system, which is of key importance to the use of AuAg nanoparticles in plasmonic applications.

The work presented in this study was conducted in conjunction with a number of collaborators. The respective contributions made by the author and collaborators to each part of this study are identified at the start of each chapter. References made to the literature in this field are listed separately at the end of each chapter.

## List of References

1. Cortie, M.B.; McDonagh, A.M., Synthesis and Optical Properties of Hybrid and Alloy Plasmonic Nanoparticles, *Chem. Rev.*, **2011**, *111*, 3713-3735
2. Ferrando, R.; Jellinek, J.; Johnston, R.L., Nanoalloys: From Theory to Applications of Alloy Clusters and Nanoparticles, *Chem. Rev.*, **2008**, *108*, 845-910
3. Goesmann, H.; Feldmann, C., Nanoparticulate Functional Materials, *Angew. Chem., Int. Ed.*, **2010**, *49*, 1362-1395
4. Wang, D.; Li, Y., Bimetallic Nanocrystals: Liquid-Phase Synthesis and Catalytic Applications, *Adv. Mater.*, **2011**, *23*, 1044-1060
5. Greeley, J.; Mavrikakis, M., Alloy Catalysts Designed From First Principles, *Nat. Mater.*, **2004**, *3*, 810-815
6. Kreibig, U.; Vollmer, M., *Optical properties of metal clusters*, Springer-Verlag: Berlin, 1995
7. Moskovits, M.; Smova-Sloufova, I.; Vickova, B., Bimetallic Ag-Au Nanoparticles: Extracting Meaningful Optical Constants From the Surface-Plasmon Extinction Spectrum, *J. Chem. Phys.* **2002**, *116*, 10435-10446
8. Christopher, P.; Xin, H.; Linic, S., Visible-Light-Enhanced Catalytic Oxidation Reactions on Plasmonic Silver Nanostructures. *Nature Chem.*, **2011**, *3*, 467-472
9. Huang, J.; Zhu, Y.; Lin, M.; Wang, Q.; Zhao, L.; Yang, Y.; Yao, K.X.; Han, Y, Site-Specific Growth of Au-Pd Alloy Horns on Au Nanorods: A Platform for Highly Sensitive Monitoring of Catalytic Reactions by Surface Enhanced Raman Spectroscopy, *J. Am. Chem. Soc.*, **2013**, *135*, 8552-8561
10. Shan, X.; Díez-Pérez, I.; Wang, L.; Wiktor, P.; Gu, Y.; Zhang, L.; Wang, W.; Lu, J.; Wang, S.; Gong, Q.; Li, J.; Tao, N., Imaging the electrocatalytic activity of single nanoparticles, *Nature Nanotech.*, **2012**, *7*, 668-672
11. Wang, F.; Li, C.; Chen, H.; Jian, R.; Sun, L.D.; Li, Q.; Wang, J.; Yu, J.C.; Yan, C.H., Plasmonic Harvesting of Light Energy for Suzuki Coupling Reactions, *J. Am. Chem. Soc.*, **2013**, *135*, 5588-5601
12. Herzing, A.A.; Kiely, C.J.; Carley, A.F.; Landon, P.; Hutchings, G.J., Identification of Active Gold Nanoclusters on Iron Oxide Supports for CO Oxidation, *Science* **2008**, *321*, 1331-1335
13. Zhou, X.; Andoy, N.M.; Liu, G.; Choudhary, E.; Han, K.-S.; Shen, H.; Chen, P., Quantitative super-resolution imaging uncovers reactivity patterns on single nanocatalysts, *Nature Nanotech.* **2012**, *7*, 237-241



14. Delannoy, L.; Chantry, R.L.; Casale, S.; Li, Z.Y.; Borensztein, Y.; Louis, C., HRTEM and STEM-HAADF Characterisation of Au/TiO<sub>2</sub> and Au/Al<sub>2</sub>O<sub>3</sub> Catalysts for a Better Understanding of the Parameters Influencing Their Properties in CO Oxidation, *Phys. Chem. Chem. Phys.*, **2013**, doi:10.1039/C2CP44157H

---

## **Chapter 2**

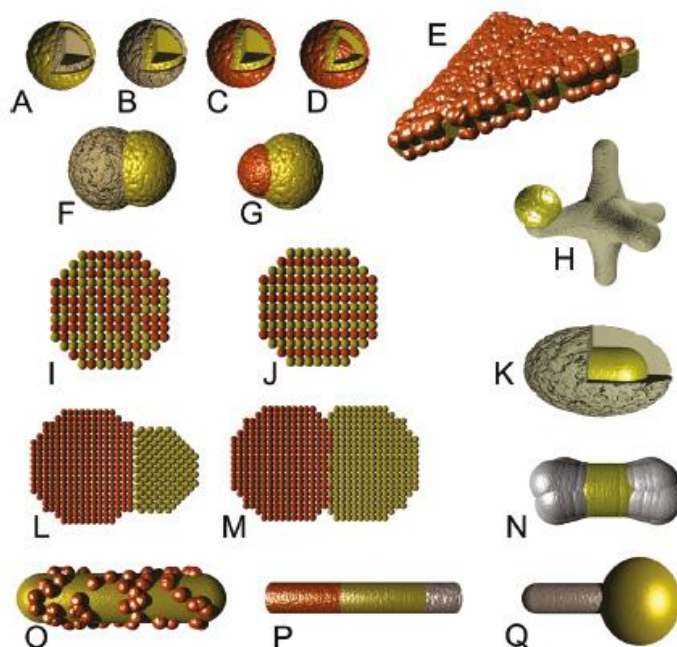
### **Literature Review**

This thesis is focused on exploring the potential offered by aberration corrected scanning transmission electron microscopy (ac-STEM) in the characterisation of the atomic structure and localised surface plasmon resonance (LSPR) properties of bimetallic nanoparticles. In this chapter we summarise the relevant background literature for this work, covering the structural characterisation of bimetallic nanoparticles in Section 2.1, and in particular the three systems, AuRh, AuPd and AuAg, and LSPR characterisation in Section 2.2.

#### **2.1 Structure in Segregated Bimetallic Nanoparticles**

The advantages bimetallic nanoparticles offer over monometallic equivalents derive from the addition of the second metal, and specifically from atomic scale interactions between their component metals. Thus, gaining a fundamental understanding of the origin of their novel and tuneable properties requires conducting a complete structural characterisation, to atomic resolution. However, the location and nature of the metal-metal

interactions is dependent upon particle structure, which can take a wide variety of forms, as illustrated by the extract from reference 1 given in Figure 2.1.



**Figure 2.1. Schematic examples of possible multi-element nanosystem structures.** A – D segregated core-shell spheres, E layered segregation, F – G heterodimer segregation, H branched structure with attached nanosphere, I – J cross sections through disorder and ordered alloying, K segregated core-shell nanorod, L –M cross sections through differing interfacial structures, N end-capped nanorods, O nanorod with sparse island overgrowth, P segmented nanowires, and Q nanowire with attached nanoparticle. From reference 1

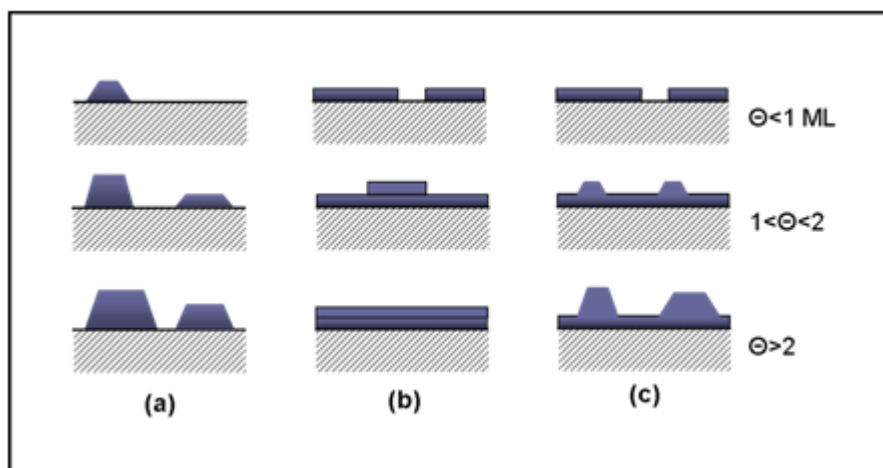
In core-shell nanoparticles, which are the subject of the majority of the work presented in this thesis, the metal-metal interactions occur predominantly in sub-surface sites, at their buried interfaces. The interfacial structures of core-shell systems determine their surface structure, and thus also their surface properties.<sup>2</sup> The connection between core-shell structure and resulting properties has been demonstrated by recent work

conducted on AgPd<sup>3</sup> and PtNi<sup>4</sup> nanoparticles, where enhanced catalytic reactivity was attributed to the influence of lattice strain at the core-shell interface. Core-shell structure has also been found to provide additional stability to nanoparticles, allowing them to deliver greater durability compared with monometallic equivalents, which is an important factor in many industrial applications.<sup>5</sup>

The wide variety of structures that are possible in bimetallic nanoparticles is a consequence of the range of parameters that influence their formation. The complexity of structure formation between two metals becomes apparent in even quite simplified models. Figure 2.2 shows a simple schematic model for the growth modes that may be followed by one metal deposited on the flat surface of another.<sup>6</sup> Considering only the key parameters of the relative lattice constants and bond strengths, Vollmer-Weber island growth is expected in systems with a high lattice mismatch and low tendency to form inter-metallic bonds, and layer-by-layer Frank van der Merwe growth in systems with low lattice mismatch and a high preference for inter-metallic bonds. However, for systems between these extremes growth modes can become more complex, such as Stranski-Krastanov layer-plus-island growth, where a tendency to form inter-metallic bonds initially favours layer growth, but accumulated strain caused by lattice mismatch then induces a second phase of 3D island growth.<sup>7</sup> The point at which the growth changes from layer to island depends upon the balance between bond strength and lattice strain, so even in a simple model, constrained to just two determining parameters, the exact growth mode followed may not be easy to predict.

In real systems the range of influencing factors is greater and more complicated structures are possible. For example, layered overgrowth in the simple model only occurs where there is small lattice mismatch, however, in real systems it can occur even when

there is significant mismatch, for example, through overgrowth that proceeds in a different orientation to the substrate, or with a different crystal structure to the substrate,<sup>8</sup> or through the formation of systematic defects to relieve lattice strain.<sup>9</sup>



**Figure 2.2. Simple Scheme for the categorisation of growth modes.** (a) Vollmer-Weber island growth, (b) Frank van der Merwe layer-by-layer growth, (c) Stranski-Krastanov layer-plus-island. From reference 6.

Other parameters that may also be important to the formation of structure in bimetallic nanoparticles systems, where the greater surface to volume ratio increases the influence of surface effects, include the relative surface energies of the constituent metals, their respective rates of surface diffusion, the conditions prevailing during or after deposition, and the existence of non-flat surfaces. These additional factors make complete structural characterisation a challenging task in these systems; however, it also gives more potential routes to controlling structure, and so also properties. For example, Au and Pd are miscible in bulk form<sup>10</sup> but AuPd nanoparticles have been synthesised with both segregated<sup>11-14</sup> and alloyed<sup>12,15</sup> structures, by varying synthesis conditions.

Transformations between these structures have been linked to variations in catalytic reactivity and has been induced by heating the samples.<sup>16,17</sup>

The fundamental structural and energetic parameters of the constituent metals, and relative differences between them, vary considerably between bimetallic systems. For example, lattice mismatch can range from almost no mismatch between Au and Ag, to a mismatch as great as 12% between Cu and Ag. In addition, whilst lattice mismatch might be the principal driving factor in one size or structure of particle, in one bimetallic system, other parameters, such as surface or cohesive energy may override the influence of lattice mismatch and become more dominant in others. Thus, whilst useful observations can be made through comparing the behaviour of similar systems, the detailed behaviour of each system must be considered individually. The relevant background for the structural characterisation of the systems covered by this study are summarised in the following three sections.

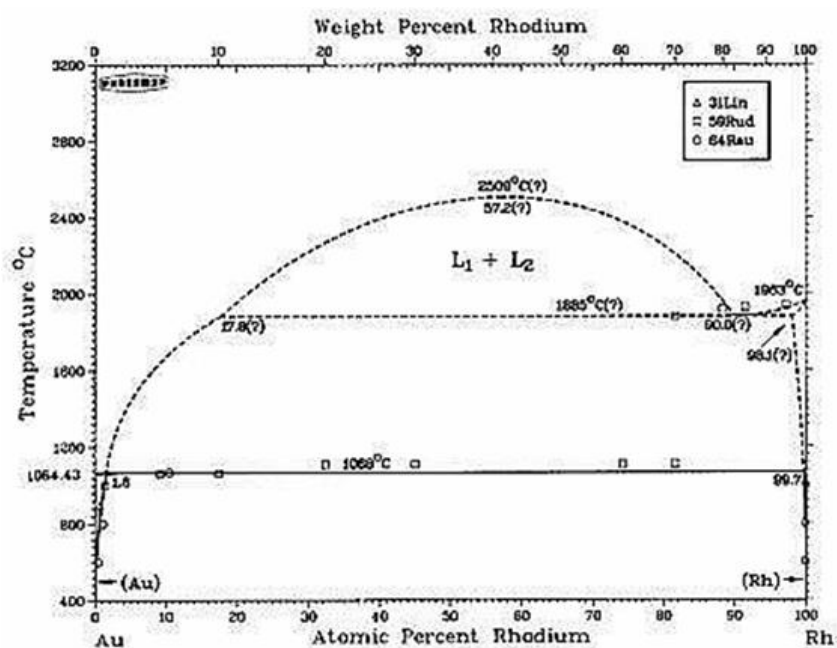
### **2.1.1 AuRh**

The electronic configuration, relative surface and bulk energies, lattice constants, and bond strengths are key parameters in any bimetallic system; Table 2.1 summarises and compares these key parameters for Au and Rh. The theoretical diatomic binding energies given in Table 2.1 do not necessarily correspond to either bulk binding energies or binding energies present in nanosystems, but provide a relevant context when considering the behaviours of this system.

**Table 2.1. Key parameters of Au and Rh**

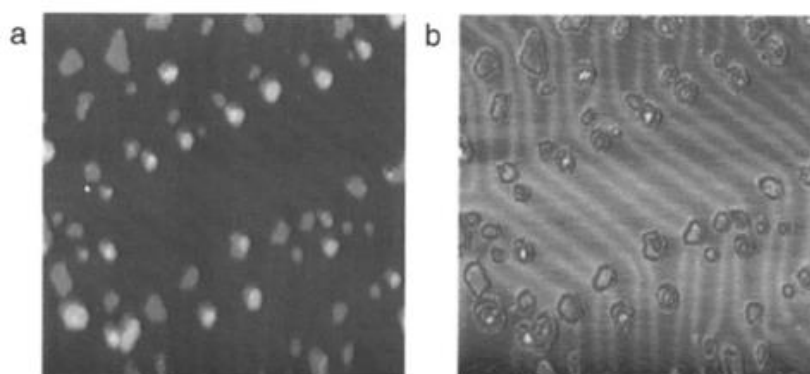
	<b>Au</b>	<b>Rh</b>
Atomic number <sup>18</sup>	79	45
Outer electrons <sup>18</sup>	6s 5d <sup>10</sup>	5s 4d <sup>8</sup>
Lattice constant <sup>18</sup>	0.408 nm	0.380 nm
Average surface energy <sup>19</sup>	1.6 J/m <sup>2</sup>	2.8 J/m <sup>2</sup>
Bulk cohesive energy <sup>18</sup>	3.8 eV/atom	5.8 eV/atom
Theoretical diatomic binding energy <sup>20</sup>		
- Au-Au / Rh-Rh	2.29 eV	2.92 eV
- Au-Rh	2.37 eV	

Interactions between these key structural and energetic parameters result in the complete immiscibility of Au and Rh in bulk form; illustrated by their bulk phase diagram reproduced in Figure 2.3.<sup>21</sup> Despite this there have been reports of the successful chemical synthesis of both alloyed<sup>22</sup> and segregated<sup>23,24</sup> AuRh particles.

**Figure 2.3. Bulk phase diagram for Au-Rh.** Reproduced from reference 21.

Studies by Essinger *et al.*<sup>22</sup> and Sneed *et al.*,<sup>24</sup> reporting the synthesis of respectively alloyed and segregated nanoparticles, did not use ac-STEM for characterisation and did not include atomically resolved imaging of their systems. To date we have found no atomic scale characterisation of the AuRh system, motivating the work presented in Chapter 5 of this thesis. There have been a limited number of surface science studies conducted on the growth mode of Rh on Au;<sup>19,25-28</sup> the key findings of these are summarised in the following paragraphs.

Altman and Colton deposited Rh onto Au(111) at room temperature using thermal evaporation.<sup>25</sup> They used scanning tunnelling microscopy (STM) and Auger electron spectroscopy (AES) to characterise the deposition, and interpreted their results as Rh following a Vollmer-Weber island growth mode. They identified a preference for Rh nucleation at elbow and dislocation sites on the Au(111) surface, as shown in the STM images from their work reproduced in Figure 2.4.



**Figure 2.4.** *STM images of Rh deposited on Au(111).* a) normal contrast, and b) enhanced by subtraction of step heights. From reference 25.



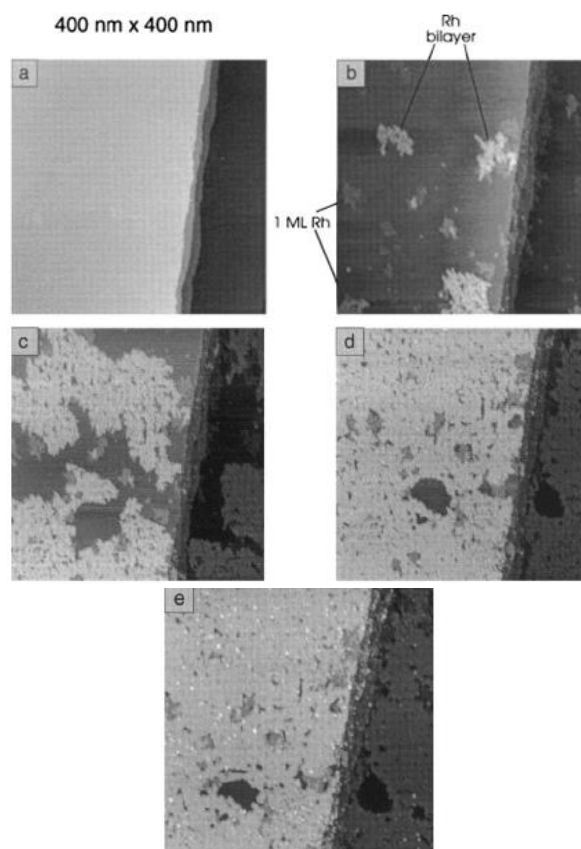
Altman and Colton extended their work to include annealing the system to 400°C.<sup>25</sup> This induced the appearance of Au islands on the surface, which was interpreted as thermally assisted covering of the post-deposited Rh by atoms from the Au substrate. This was considered to be in accordance with the relatively lower surface energy of Au (see Table 2.1). These results demonstrate the key role of kinetics in forming structure in the AuRh system.

Kibler *et al.* also deposited Rh onto Au(111), however, they did so using the method of electrochemical deposition.<sup>27</sup> Their STM investigation produced results that differ from those of Altman and Colton, showing Rh growth progressing with an initial bilayer, on top of which 3D clusters formed. They considered this to be characteristic of Stranski-Krastanov growth. STM images from this work are reproduced in Figure 2.5 for comparison with those of Altman and Colton in Figure 2.4. The difference between the results of Kibler *et al.* and those of Altman and Colton may be due to observations made at differing stages of Rh deposition. Also close inspection of the images of Kibler *et al.* given in Figure 2.5 show that the initial Rh growth may not have formed a complete bilayer prior to the 3D cluster overgrowth. However, these differences may also demonstrate the sensitivity of Rh growth on Au to the deposition methods used in sample preparation.

Liu and Bader deposited Rh on to Au(100) using evaporative techniques.<sup>28</sup> They used low energy electron diffraction (LEED) and AES to characterise the system, interpreting their results as showing the initial stages of Rh growth occurring in what were described as epitaxial layers, matching facet orientation to that of the Au substrate. Consistent with the findings of other groups, Liu and Bader also observed a shift to island

growth after the deposition of two initial monolayers of Rh. They attributed this growth mode to the relatively high surface energy of Rh compared to Au (see Table 2.1).

Ovari *et al.* and Kiss *et al.* working as part of the same group both studied a system of Au and Rh clusters deposited onto TiO<sub>2</sub> substrate, using physical vapour deposition at room temperature.<sup>19,29</sup> They used a range of techniques, including STM, low energy ion spectroscopy (LEIS) and X-ray photoelectron spectroscopy (XPS), to characterise this system. Both studies found that where the post-deposited Rh clusters impinged onto pre-deposited Au clusters they became covered by Au. This behaviour was attributed to the relative surface energies of Au and Rh causing non-thermal place exchange between Rh and Au atoms.



**Figure 2.5.** STM images stages of Rh deposition on Au(111). a) bare Au, b) – d) Rh bilayer growth, and e) Rh clusters on bilayer. From reference 27.

In a continuation of the same work Ovari *et al.* increased the Rh deposition concentration, finding that for higher Rh concentrations Au coverage did not occur.<sup>19</sup> These results were interpreted as being due to the limited number of Au atoms in sub-surface positions favourable to overcoming the place exchange energy barrier given the bond exchange energy available. They supported this interpretation by annealing the system to 500°C, finding that this caused more Au/Rh place exchange, consistent with the altered kinetics of the system.

Chado *et al.* used a system of Rh deposited onto Au(111) substrate using thermal evaporation at room temperature, which they characterised primarily through STM and AES.<sup>26</sup> Consistent with the study of Altman and Colton,<sup>25</sup> they found preferential Rh deposition at elbow sites and dislocations. They identified an initial formation of an incomplete bi-layer of Rh followed by 3D Rh cluster overgrowth, similar to the findings of Kibler *et al.*,<sup>27</sup> and categorised this as between Vollmer-Weber and Stranski-Krastanov. Interestingly they also interpreted their results as indicating the formation of an interfacial alloy layer, formed by place exchange between Au and Rh atoms, caused by the relatively high surface energy of Rh. They extended their work to include samples prepared at 30K, and samples annealed to 300K, finding the same behaviour in all of the samples; based on these results they concluded that the observed behaviour was not thermally dependent. These results are contrary to those of Ovari *et al.*<sup>19</sup> who found more place exchange in annealed samples. It is possible that the difference between these and the Ovari *et al.* results may be attributed to the influence of their differing substrates of Au(111) and TiO<sub>2</sub> respectively.

The work summarised in this section demonstrates the complex deposition and growth behaviour of Rh on well-defined Au surfaces, and highlights the role played by

kinetics in this process. Rh-only nanoparticles have been demonstrated to give enhanced and structure dependent catalytic activity,<sup>30</sup> however, controlling the shape of Rh in nanoparticle form has proved challenging, motivating the use of Au-seeds to provide template for Rh growth and thus improve their effectiveness as nanocatalysts.<sup>24</sup> The considerable interest in Rh for its use in catalytic applications, and its high intrinsic cost, makes the development of structural control over this metal at the atomic scale of vital importance to its efficient exploitation, providing motivation for the structural characterisation work presented in Chapter 5 of this thesis.

### **2.1.2 AuPd**

Work conducted to date on AuPd nanoparticles shows the potential to manipulate the structure of bimetallic nanoparticles through controlled synthesis. Enhanced activity in a range of industrially relevant reactions have been demonstrated by combining Au and Pd in a range of different nanoparticle forms,<sup>31-36</sup> and increased surface enhanced Raman effects have been found with the addition of Pd shells of varying thickness to Au seed nanoparticles.<sup>14</sup> In addition, the enhanced properties of AuPd nanoparticles have been demonstrated to be tuneable through manipulating particle structure.<sup>17</sup>

The demonstrated structural versatility and enhanced properties of AuPd nanoparticles means they have been extensively studied in both segregated and alloyed forms.<sup>11-17,37</sup> However, despite this the complexity of the metal-metal interactions that drive the formation of structure in this system are still not well understood. This motivates the structural characterisation work presented in Chapter 5 of this thesis.

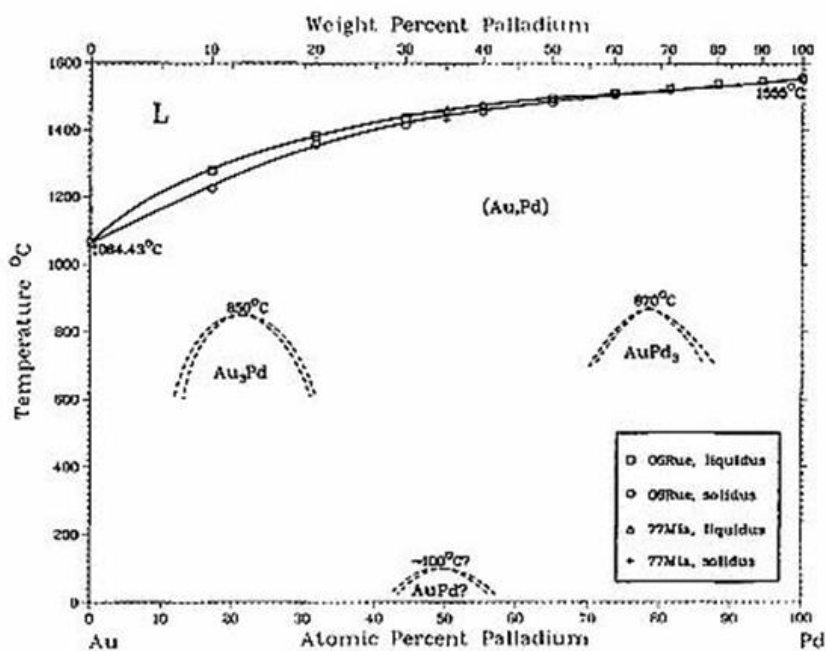
The key parameters of Au and Pd are given in Table 2.2.

	<b>Au</b>	<b>Pd</b>
Atomic number <sup>18</sup>	79	46
Outer electrons <sup>18</sup>	6s 5d <sup>10</sup>	4d <sup>10</sup>
Lattice constant <sup>18</sup>	0.408 nm	0.389 nm
Surface energy <sup>38</sup>	1.6 J/m <sup>2</sup>	2.0 J/m <sup>2</sup>
Bulk cohesive energy <sup>18</sup>	3.8 eV/atom	3.9 eV/atom
Theoretical diatomic binding energy <sup>20</sup>		
- Au-Au / Pd-Pd	2.29 eV	1.69 eV
- Au-Pd	1.44 eV	

Pd and Rh have adjacent atomic numbers, are both of high interest for their catalytic properties. In addition, as can be seen from comparing Table 2.2 with Table 2.1 above, when compared to Au, Pd and Rh both have a smaller lattice constant and higher surface and cohesive energies. A significant difference between the AuPd and AuRh systems is their miscibility; as shown by the bulk phase diagram of Figure 2.6, Au and Pd are miscible in bulk form, whereas Au and Rh are completely immiscible (Figure 2.3).

Some atomically resolved structural characterisation has already been conducted on the AuPd system. Ding *et al.* used HRTEM imaging to find differences in structure with variations in the thickness of the Pd shell.<sup>9</sup> Systematic stacking defects were found in thin Pd shells, whereas an ordered alloy structure was identified in thick shells. The particles used in this study were made through Au-seeded sequential chemical synthesis. They considered that Au diffusion into thick Pd shells was consistent with both relative surface energy and lattice mismatch between Au and Pd. However, they did not explain why

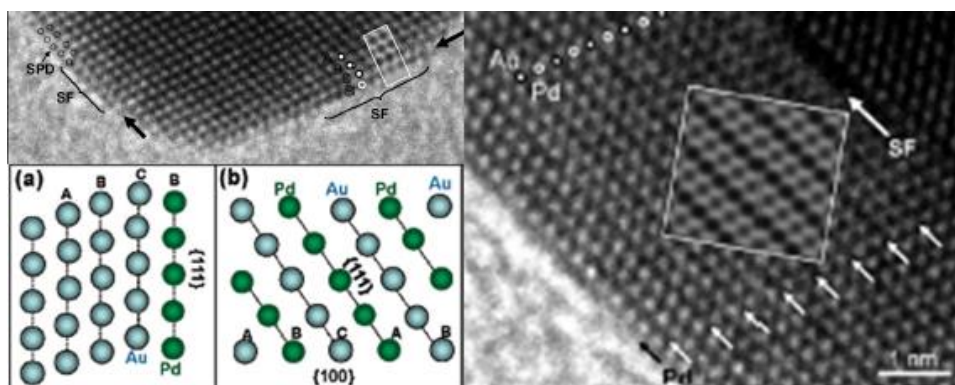
comparable diffusion did not occur in thin Pd-shells, or why instead thin shells favoured the formation of stacking defects to relieve lattice mismatch strain. As they used only HRTEM, they also presented no atomically resolved elemental characterisation of these structures. Figure 2.7 shows extracts from this work illustrating the two differing structures they identified.<sup>9</sup>



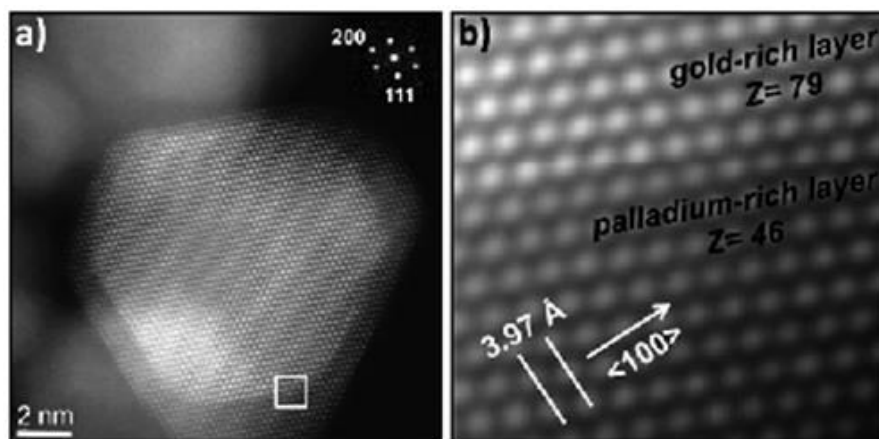
**Figure 2.6.** Bulk phase diagram for Au-Pd. Reproduced from reference 10.

Ferrer *et al.* also conducted an atomic scale characterisation of segregated AuPd nanoparticles, using both HRTEM and STEM-HAADF imaging, an extract from which is given in Figure 2.8.<sup>13,39</sup> They found a three layer segregated structure, and identified some degree of alloying between the metals in the different layers.<sup>13</sup> Their atomically resolved STEM-HAADF imaging was interpreted as showing coherent interfaces between the layers, although the 3.97 Å {100} lattice spacing identified in the layer described as

palladium rich did not correspond to that of pure Pd in bulk form (3.89 Å from Table 2.2).<sup>39</sup> The particles were chemically synthesised using polymer protection.



**Figure 2.7. HRTEM images of segregated Au-Pd nanoparticles.** Showing different structures found in thin and thick Pd shells, with schematic representations of the identified stacking fault defect in thin over-growth and alloy structure for thick over-growth. From reference 9.



**Figure 2.8. STEM-HAADF images of Au-Pd nanoparticles.** Showing three layer segregated structure to atomic resolution. From reference 39.

These studies of the atomic structure of AuPd nanoparticles show the potential available for structural characterisation of bimetallic nanoparticles using atomically

resolved electron microscopy, and form a useful basis for comparison to the work we present in Chapter 5 of this thesis. However, they also demonstrate the difficulties of conducting full atomic scale characterisation, showing the techniques capable of providing unambiguous elemental information to atomic resolution are required to achieve this goal. In addition, the variety of structures found in these studies also demonstrate that, even when atomic structure can be unambiguously identified, the driving forces that are responsible for its formation may still not be clear. We consider this further when presenting our results in Chapter 5 of this thesis.

### 2.1.3 AuAg

AuAg is probably the most widely studied of all bimetallic nanoparticle systems due to its desirable catalytic and plasmonic properties.<sup>40</sup> It has been synthesised in both segregated and alloyed forms, in many different morphologies, and using a range of different techniques, including chemical and inert gas aggregation methods.<sup>41-48</sup>

Table 2.3 gives the key parameters of Au and Ag for comparison.

	<b>Au</b>	<b>Ag</b>
Atomic number <sup>18</sup>	79	47
Outer electrons <sup>18</sup>	6s 5d <sup>10</sup>	5s 4d <sup>10</sup>
Lattice constant <sup>18</sup>	0.408 nm	0.409 nm
Surface energy <sup>49</sup>	1.6 J/m <sup>2</sup>	1.3 J/m <sup>2</sup>
Bulk cohesive energy <sup>18</sup>	3.8 eV/atom	2.9 eV/atom
Theoretical diatomic binding energy <sup>20</sup>		
- Au-Au / Ag-Ag	2.29 eV	1.65 eV
- Au-Ag	2.06 eV	



Comparison of Table 2.3 with Tables 2.1 and 2.2 above shows that, despite similarity in the relative atomic numbers of these three systems, Au and Ag have very different relative key parameters when compared to either Au and Rh or Au and Pd. Where both AuRh and AuPd systems have large lattice mismatches (respectively 7% and 5%), Au and Ag have almost identical lattice parameters. In addition, these systems differ in the relative surface and cohesive energies of their constituent metals, as Ag has lower surface and lower cohesive energy compared to Au.

Au and Ag are miscible in bulk form, as illustrated by their bulk phase diagram reproduced in Figure 2.9.<sup>50</sup> However, as with the similarly bulk miscible AuPd system, through altering synthesis methods and conditions, AuAg nanoparticles have been successfully synthesised in both alloyed and segregated forms, including both Au<sub>core</sub>Ag<sub>shell</sub> and Ag<sub>core</sub>Au<sub>shell</sub>.<sup>45</sup>

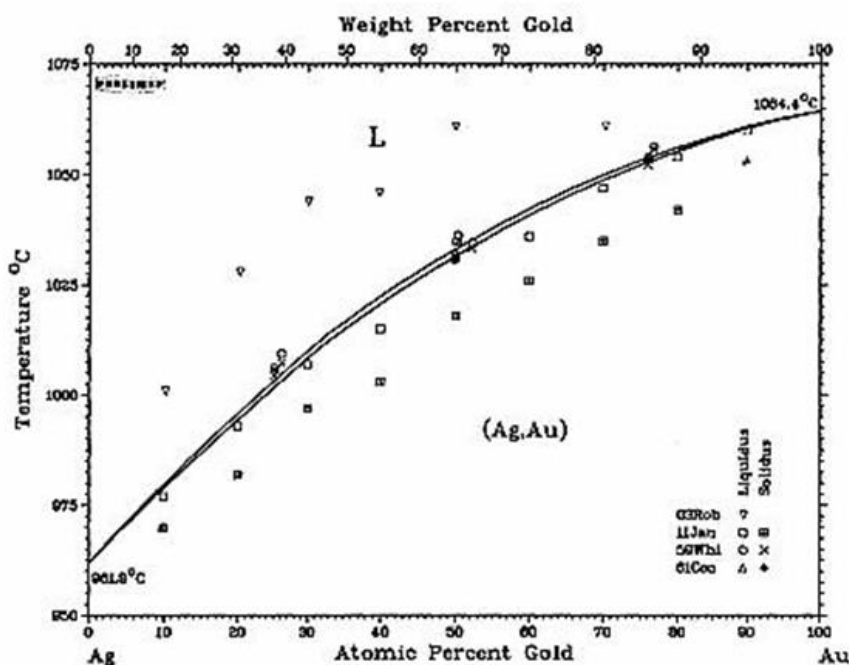
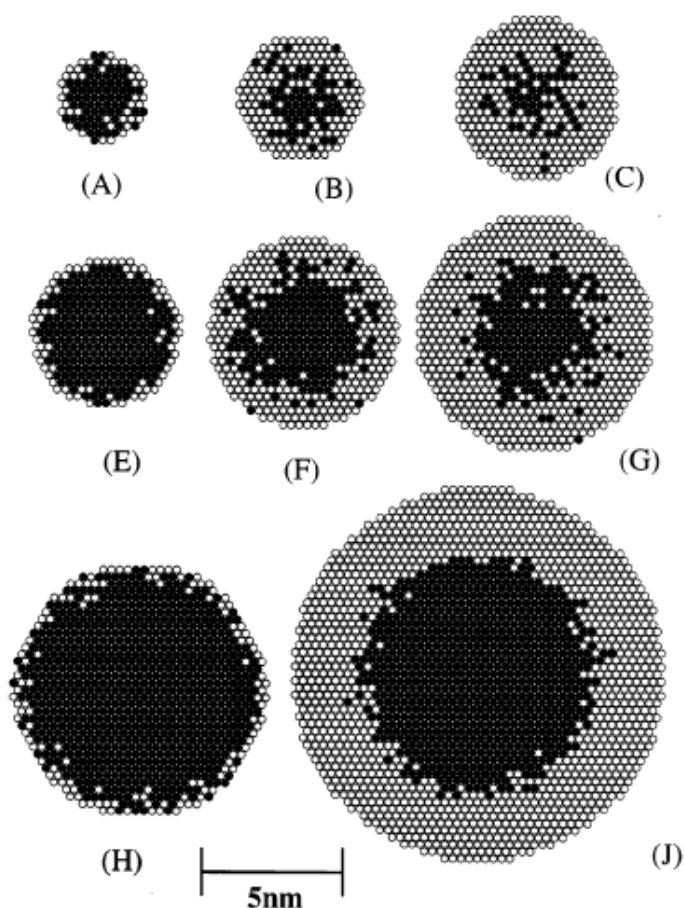


Figure 2.9. Bulk phase diagram for Au-Ag. Reproduced from reference 50.

Theoretical and experimental studies conducted investigating the process of alloying in AuAg nanoparticles have found a size dependence;<sup>47,51,52</sup> an example extract from one of these studies is given in Figure 2.10.<sup>47</sup>



**Figure 2.10. Simulated structures for AuAg nanoparticles.** Showing size dependent alloying in AuAg nanoparticles. From reference 47.

Based on comparison between their experimental and simulated results Shibata *et al.* speculated that the driving force behind this phenomenon was not size-dependent changes in melting point, but most likely the presence of vacancy defects between the two metals.<sup>47</sup> This study again highlights the complex range of factors that potentially influence metal-metal interactions in bimetallic nanoparticles.

Despite the ease with which Ag oxidises, prior to our recent study conducted with our collaborators, Belic *et al.*,<sup>41</sup> we have found no work examining the effects of long term aging of AuAg nanoparticles. The study conducted by Belic *et al.* found that significant structural change occurred in AuAg nanoparticles aged in air, with a transformation from alloyed to asymmetric segregated structures.<sup>41</sup> We consider the continued evolution of this system when presenting our results in Chapter 7 of this thesis.

Work that has been conducted using surface science techniques has indicated that Ag oxidation may have a profound impact on structure beyond just the first few atomic layers. Petterson and Snyder recorded the progressive oxidation of Ag thin films, showing that although it begins at the Ag surface exposure to oxygen, it proceeds through the Ag to sub-surface regions, not in direct contact with the applied oxygen, until the films were fully oxidised.<sup>53</sup> They found that oxidation progressed through a rough interface between the Ag substrate and the Ag oxide, which increased in thickness until the film was fully oxidised, at which point the films were found to be twice as thick as the originally prepared Ag films, having increased from 10.8 nm and 40.3 nm thick to 21.5 nm and 81.6 nm thick respectively. They also observed that the films altered appearance during the process.

There are a number of different forms of Ag oxide, some of which can potentially exist in more than one crystal structure.<sup>54</sup> Identified structures include relatively simple cubic forms, as well as more complex monoclinic, tetragonal, rhombic and hexagonal structures. In addition, using STM characterisation techniques, Ag oxides have also been found to form surface layers with structures that differ from those of the underlying Ag or Ag oxide substrate.<sup>55-62</sup> As a consequence the structures formed through Ag oxidation have been the subject of some considerable debate in the surface science field, however, they have not been addressed using STEM that we have identified to date. Whilst surface

science techniques, such as STM, have advantages in terms of revealing surface topology and electronic structure to atomic resolution, ac-STEM can potentially provide comparable atomically resolved structural and elemental information, through the thickness of the sample. It seems likely that the complexity of Ag oxide atomic structures identified in the surface science studies will extend to nanoparticle form and, given the findings of Belic *et al.*, must be considered relevant to the long term evolution of AuAg nanoparticles.<sup>41</sup> Extending this work by employing the full capabilities of ac-STEM to gain a greater understanding of the impact of long term sample evolution is the focus of the results presented in Chapter 7 of this thesis.

## **2.2 Localised Surface Plasmon Resonance in Bimetallic Nanoparticles**

The results presented in Chapters 6 and 7 of this thesis use ac-STEM Electron Energy Loss Spectroscopy (STEM-EELS) to characterise the LSPR of bimetallic nanoparticles. Interest in the LSPR response has largely been due to the ability to tune the resonant frequency of response in monometallic nanoparticles, through altering size, shape and morphology.<sup>1</sup> This offers the potential for their use in frequency sensitive applications such as in the manufacture of nanoplasmonic devices and biosensors.<sup>63</sup> However, more recent research has highlighted a further, potentially very interesting, use for LSPR response in the field of catalysis, with plasmonic enhancements to,<sup>64-66</sup> and monitoring of,<sup>67</sup> catalytic reactivity having recently been reported. Bimetallic nanoparticles are of particular interest in this emerging field of research as they allow the possibility to combine the tuneable LSPR response of one metal with the enhanced the catalytic reactivity of another.

Although the LSPR response of bimetallic nanoparticles has been investigated through the ensemble results of UV-visible spectroscopy (UV-vis), there has been little work to date characterising their LSPR response on a single particle basis. Single particle characterisation is necessary to establish unambiguously the link between particle structure and LSPR response. We have identified only three studies that have examined the LSPR response of bimetallic nanoparticles on a single particle basis, all concerned with AuAg systems.<sup>42,68,69</sup>

### 2.2.1 Theoretical background

Plasmon excitation entails the collective oscillation of electrons in response to an external influence, such as an incident electric field. The external field may be the electromagnetic radiation of optical excitation,<sup>70</sup> or the fields generated by fast electrons, such as in an electron microscope.<sup>71</sup>

In bulk material plasmon excitation takes the form of a longitudinal wave. The resonant frequency of the bulk plasmon response in a free electron metal, known as the plasma frequency,  $\omega_p$ , is determined primarily by electron density, and is given by equation 2.1<sup>70</sup>

$$\omega_p = \sqrt{\frac{ne^2}{\epsilon_0 m_e}} \quad 2.1$$

where  $n$  is the number of electrons per unit volume,  $e$  is the charge of an electron,  $\epsilon_0$  is the permittivity of free space, and  $m_e$  is the mass of an electron.

Collective plasmon excitations can also occur at an interface, as a consequence of the boundary conditions that apply between media; at an interface between a metal and a

dielectric medium, such as at a metal surface exposed to vacuum, this excitation is known as a surface plasmon. Surface plasmons are travelling transverse waves. As they derive from excitation of the same free electron population as bulk plasmons, can be related to the bulk plasma frequency as follows<sup>70</sup>

$$\omega = \frac{\omega_P}{\sqrt{2}} \quad 2.2$$

Localised surface plasmons arise from the manifestation of surface plasmons in nanoparticles, where the high surface-to-volume ratio means all the free electrons in the particle participate in surface plasmon excitation to form the LSPR response. As it derives from surface plasmon resonance, LSPR also takes the form of a transverse wave, but because it encompasses all of the free electrons in the particle it has the form of a standing wave. As it derives from the surface plasmon response LSPR is directly related to the density of the free electron population. This was demonstrated by Mulvaney *et al.* who detected an alteration in LSPR frequency after injecting additional electrons into Au nanorods.<sup>72</sup>

In the simplest model of dielectric response, the Drude-Sommerfield-Lorentz model, the plasma frequency is arrived at by taking the response of a single electron under the influence of an external force and multiplying it by the total number of free electrons in the material.<sup>70</sup> Where the target is small relative to the wavelength of incident radiation, less than 10% of the wavelength of incident radiation,<sup>70</sup> a further assumption can be made that the free electrons respond without phase retardation. When this condition is met the LSPR response is said to fall within the quasi-static regime, allowing it to be treated as an electrostatic system. Within the quasi-static regime, LSPR oscillations can be regarded as equivalent to a damped and driven harmonic oscillator, with the time varying

electromagnetic field of the incident radiation acting as the driving force, opposed by the damping effect of the restoring force from the positive ionic background of the atomic nuclei. In its simplest form it occurs as a dipole resonance, however, if the dimensions of the particle allow, higher order, or multipole, modes of oscillation can also be excited.<sup>70</sup>

For the simplest case of the dipole resonance of a single metal sphere, within the quasi-static limit, LSPR is related to bulk plasma frequency as follows<sup>70</sup>

$$\omega = \frac{\omega_P}{\sqrt{3}} \quad 2.3$$

The electrostatic collective response of free electrons under the influence of external electric fields, and thus LSPR response, is directly related to the polarizability of the particle. Polarizability is an atomic property deriving from the local electric field of an atom,<sup>18</sup> and for a particle from the combined local fields of all of the constituent atoms, making it shape dependent. Equation 2.4 gives the polarizability,  $\alpha$ , of a simple sphere of radius  $R$ ,<sup>70</sup>

$$\alpha = 4\pi\epsilon_0 R^3 \frac{\epsilon - \epsilon_m}{\epsilon + 2\epsilon_m} \quad 2.4$$

where  $\epsilon_0$  is the permittivity of free space,  $\epsilon$  is the dielectric function of the sphere, and  $\epsilon_m$  is the dielectric function of the embedding medium. The dependence of polarizability on the shape and size of the particle, the dielectric response of the constituent material, and the dielectric response of the surrounding medium, gives considerable potential for its manipulation, and thus also the manipulation of nanoparticle LSPR. This phenomenon has been investigated extensively through both theoretical simulation and experimental studies.<sup>1,63,73,74</sup>

The addition of a second metal in bimetallic nanoparticles impacts LSPR through altering structure, for example by adding a second interface in segregated particles, and

through altering dielectric response, as a consequence of interactions between the constituent metals.<sup>70</sup> This has been demonstrated experimentally and theoretically for AuAg nanoparticles, revealing variations in response between segregated and alloyed structures, and with variations in compositions.<sup>75-79</sup> These studies also demonstrated that for alloyed particles the dielectric function for the mix of two metals cannot be arrived at by a simple linear combination of the responses of the constituent metals.

In practice few metals are true free electron metals and contributions to the dielectric response from phenomena such as interband transitions cannot be ignored.<sup>70</sup> Interband transitions have a larger interaction cross section than the LSPR response, and thus tend to broaden and shift the LSPR response if they occur at comparable energy levels.<sup>71</sup> As a consequence the ideal plasmonic metals are often regarded as those whose surface plasmon resonance is far from any interband transitions, the best example of which is Ag. However, few other metals exhibit this property, and it is often not possible to make a clear distinction between surface plasmon excitations and interband transitions.<sup>63</sup> This can potentially have a significant impact on the dielectric response of bimetallic nanoparticles, where there is the possibility for the interband transitions of one metal to overlap with the plasmon resonance of the other. We consider this further in the context of the metals that are the focus of this study in the following section and when presenting results in Chapter 6.

### ***2.2.2 Surface plasmons of Au, Ag, Rh and Pd***

Experimentally determined responses attributed to surface plasmon resonances of monometallic Au, Ag, Pd and Rh are given in Table 2.4. For Au, Ag and Pd these were acquired from thin film systems and for Rh from bulk samples.



**Table 2.4. Surface plasmon resonances**

	nm	eV
Au <sup>80-82</sup>	520	2.2 – 2.7
Ag <sup>80-82</sup>	330	3.7 – 4.0
Pd <sup>82-84</sup>	150 - 160	7 - 9
Rh <sup>82,85,86</sup>	130 - 140	8 - 10

From Table 2.4 it can be seen that the responses of Au and Ag both lie in the optical part of the electromagnetic spectrum, which is why they are considered desirable for use in a range of plasmonic applications, whereas those of both Pd and Rh are found at UV wavelengths. It is also noticeable that, whilst the resonances of Au and Ag occur over relatively narrow energy ranges, those of Pd and Rh are much broader. Experimental studies of the optical responses of Pd and Rh indicate a significant overlap between their interband transitions and their surface plasmon response.<sup>83-86</sup> This makes the LSPR response of Rh and Pd nanoparticles of less interest for use in practical applications requiring a well-defined optical response at visible wavelengths, however, this contrast in response, when compared to a metal such as Au, makes them of interest in studying the LSPR bimetallic nanoparticles, where a combination of metals with contrasting response may allow more ready distinction between the contributions of the constituent metals, and thus reveal interesting results. In addition, Rh and Pd are both active catalysts; bimetallic AuRh and AuPd nanoparticle systems have been shown to have enhanced catalytic reactivity, and AuPd nanorods have already been used in the investigation of plasmonic enhancements to catalytic reactivity,<sup>65,66</sup> so a more complete characterisation of the LSPR response of these systems is of interest in this context.

The frequency and width of surface plasmon resonance is determined by the real part of the frequency dependent dielectric response of the respective metals.<sup>70</sup> In terms of the frequency dependent refractive index, or optical constants as they are also known, resonances occur where there is a change  $\text{Re}(n)$  with frequency; the greater the rate of change, the more well defined is the resulting resonance. Figure 2.11 illustrates experimentally determined real and imaginary parts of the optical constants of Au, Ag, Pd and Rh. For Au, Ag and Pd this data was obtained from thin film measurements,<sup>87,88</sup> whereas from Rh it was obtained from bulk measurements.<sup>89</sup> Although thin film measurements have been made on Rh, this data has not been made available in the form of real and imaginary parts of the dielectric function, other than over a relatively narrow energy range, so for the purposes of this study the bulk dielectric function of Rh has been used.

The green boxes given in Figure 2.11 highlight the resonant energy ranges corresponding to the experimentally measured surface plasmon resonances set out in Table 2.4. For Ag and Au these energy ranges are coincident with steep increases in  $\text{Re}(n)$ , consistent with the well-defined nature of their surface plasmon resonances.<sup>63</sup> For Pd and Rh the increase in  $\text{Re}(n)$  around the energy range associated with their experimentally measured surface plasmon resonance is less strong and happens over a much wider energy range. This is consistent with these metals having much broader surface plasmon resonances due to overlaps with interband transitions.

The strength of surface plasmon response is determined by the imaginary part,  $\text{Im}(k)$ , of the frequency dependent optical constants.<sup>70</sup> Large values of  $\text{Im}(k)$  will tend to damp out any resonance, even when there is a steep change in  $\text{Re}(n)$ . For example, both Pd and Rh have changes in  $\text{Re}(n)$  at lower energies that might be expected to cause surface

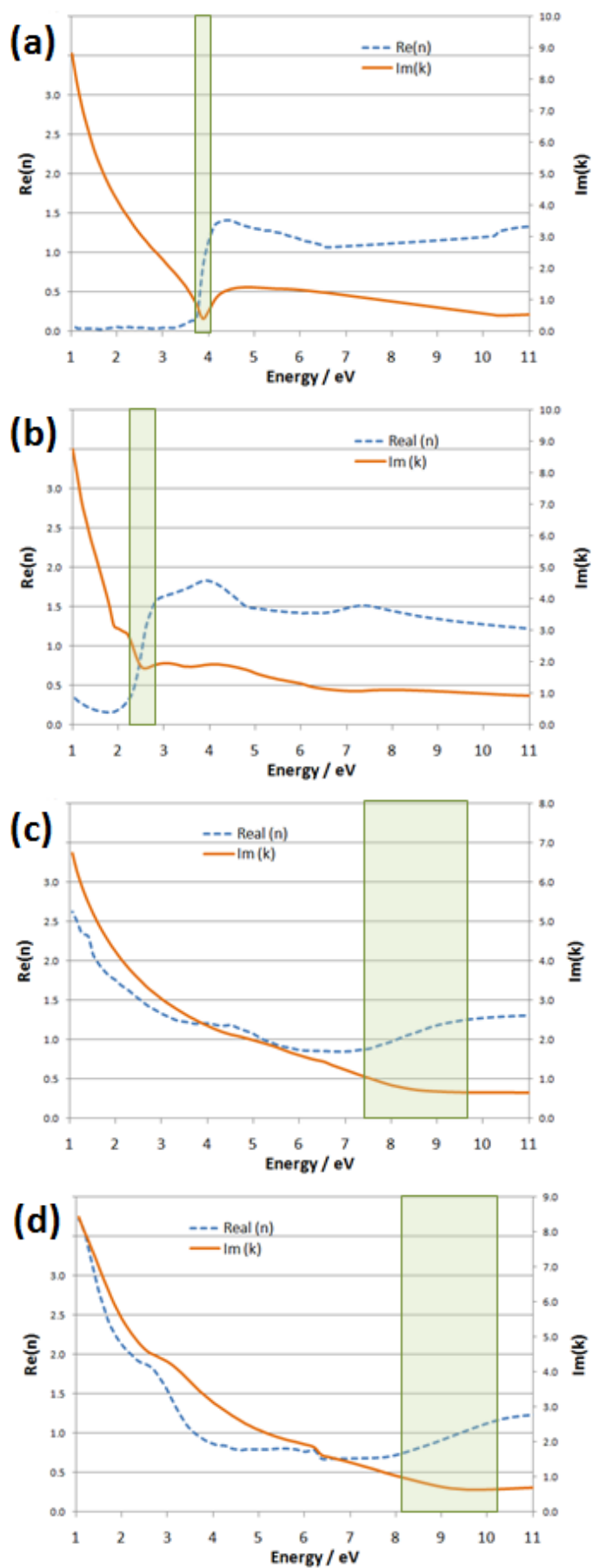


Figure 2.11. Frequency dependent optical constants. (a) Ag, (b) Au, (c) Pd, and (d) Rh. Data obtained from references 87-89.

plasmon resonances, however, both also have material values for  $\text{Im}(k)$  over this energy range, which damps out any possible surface plasmon response from these metals in the energy range below approximately 6.0 eV.

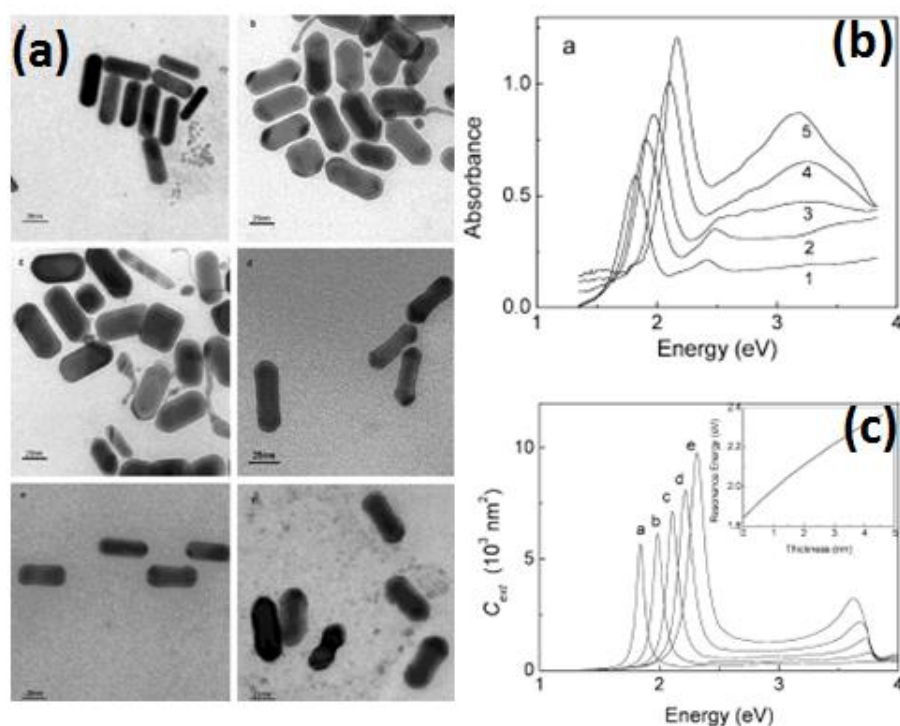
The progressive oxidation of a metal such as Ag might also be expected to alter the dielectric response of any system of which it is part. Work conducted measuring the evolution in optical response with progressive oxidation of Ag thin films revealed a shift from metallic to dielectric behaviour.<sup>53,90</sup> This shift was found to happen progressively as more of the free electrons of Ag metal become incorporated into the oxide structure. Our previous work on aged AuAg nanoparticles also indicates that significant structural changes can occur through oxidation, causing fully alloyed particles to shift to a segregated, off-centred core-shell structure.<sup>41</sup> Although there has been a recent theoretical study carried out on the impact of asymmetric segregation on optical response<sup>91</sup> we have found no experimental studies on this phenomenon. We consider this further when presenting results in Chapter 7 of this thesis.

### **2.2.3 LSPR characterisation**

Experimental work to date investigating the influence of size, structure, composition and medium on LSPR of bimetallic nanoparticles has been conducted largely with the optical technique of UV-vis, with only one study identified using optical dark field spectroscopy,<sup>42</sup> and two using STEM-EELS mapping.<sup>68,69</sup>

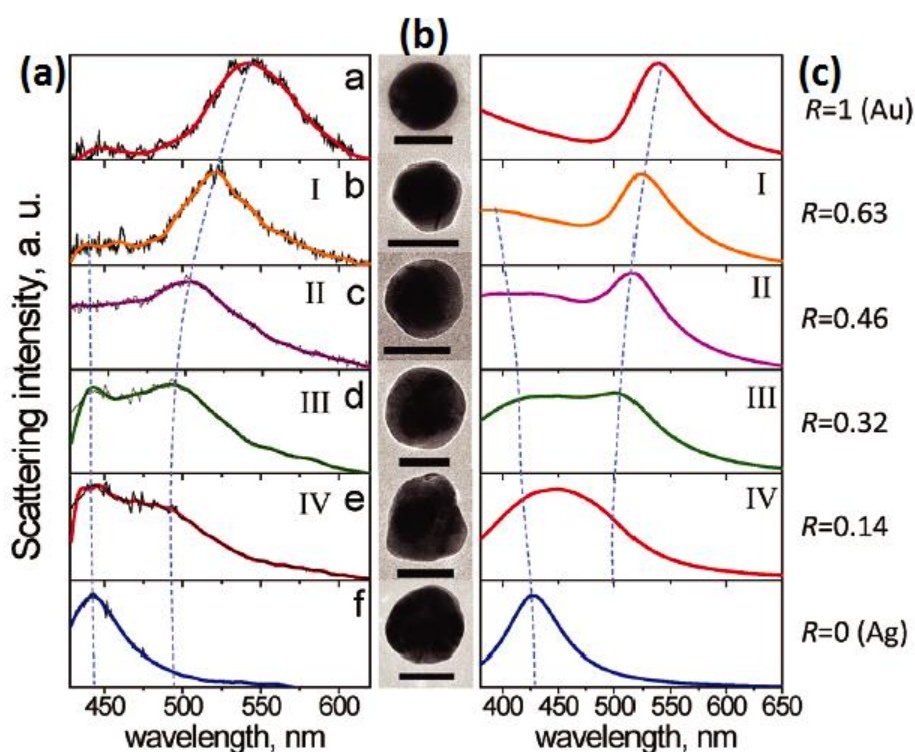
In combination with appropriate theoretical simulation, variations in UV-vis experimental spectra have often been used to confirm the successful synthesis of bimetallic nanoparticles. This technique has been applied to the characterisation of a range of different systems, including AuPd,<sup>11,12,14,92</sup> and AuAg.<sup>76-79</sup> Example extracts from the

work of Liu and Guyot-Sionnest, using UV-vis and optical response simulation to characterise the variation in optical response on the addition of Ag shells of increasing thickness to Au seed nanorods, are shown in Figure 2.12.<sup>77</sup> This work demonstrates the close match that can be achieved between UV-vis and optical response simulation for samples that are relatively monodisperse in size and morphology. However, as an ensemble technique UV-vis is less effective in characterising samples where there is variation in morphology or composition, and cannot be used to characterise the response on a single particle basis.



**Figure 2.12.** An example of UV-vis characterisation of LSPR for AuAg nanorods. (a) TEM images of AuAg core-shell nanorod samples, with (b) their experimental UV-vis spectra, and (c) optical response simulation for an Au-core nanorod with increasing thicknesses of Ag-shell. Adapted from reference 77

Dark field optical microscopy has a demonstrated capability to acquire single particle data that can be correlated to the morphology of individual particles, and has been used, in combination with electron microscopy imaging and theoretical simulation, to correlate LSPR response with structure.<sup>73,93,94</sup> We have identified one study of bimetallic segregated AuAg nanoparticles using dark field microscopy, where it was used in combination with TEM tomography to produce three dimensional structural characterisation of a single particle; an extract from this work is shown in Figure 2.13.<sup>42</sup>

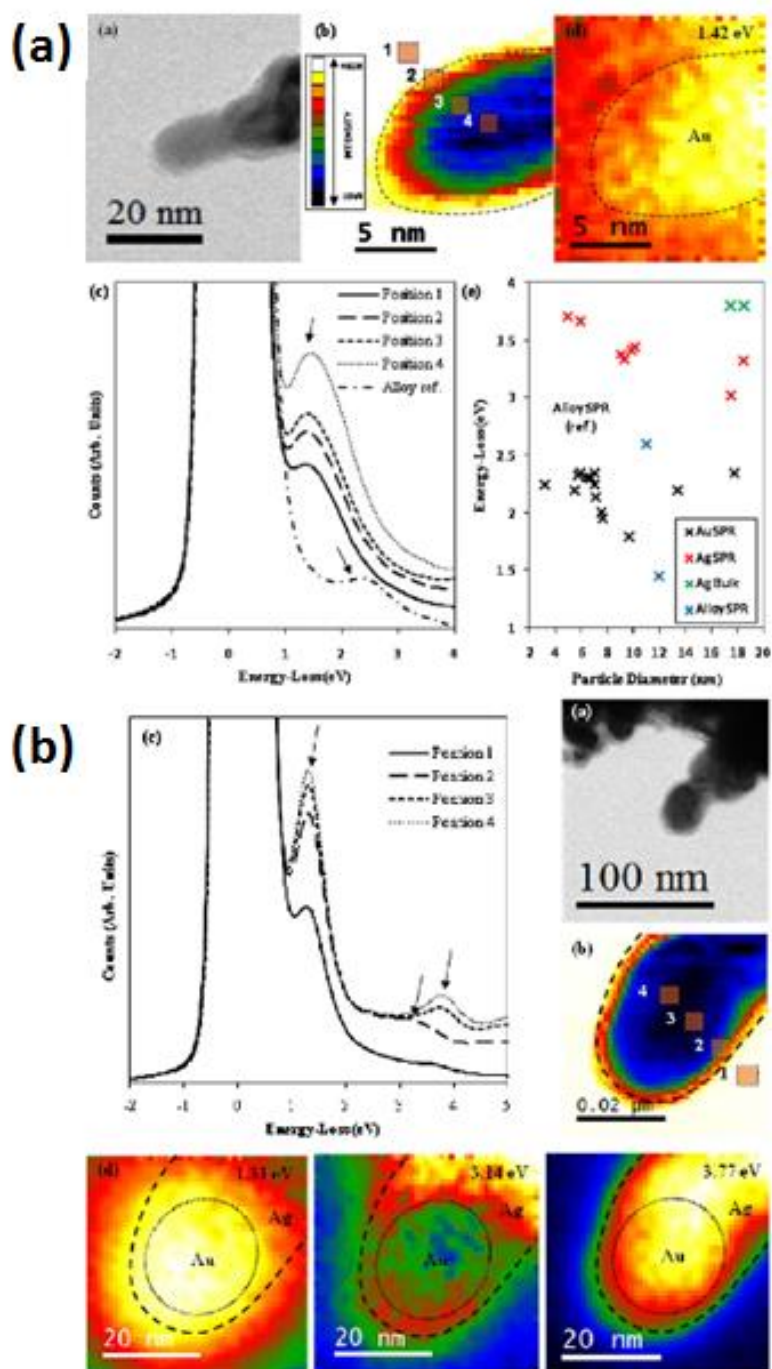


**Figure 2.13.** An example of optical dark field spectroscopic characterisation of AuAg nanoparticles. (a) Optical dark field spectra obtained from the same single particle shown in (b) (scale bar 50 nm), over a range of different tilt angles, a-f, with (c) corresponding simulated spectra. Reproduced from reference 42

The work of Chuntonov *et al.* highlights how effective this technique can be; however, as it gives a spectrum for the whole particle, it cannot be used to characterise the localisation of LSPR response at the sub-particle level.<sup>42</sup> Also, as it is an optical technique, it is limited to use on relatively large particles, of the order of several tens of nanometres in size, and can only be used on particles that can be identified for imaging using other techniques.

The only techniques capable of characterising LSPR response with direct spatial correlation to simultaneously acquired images of individual nanoparticles, and of revealing the localisation of LSPR response to sub-particle resolution, are those used in a transmission electron microscope (TEM); either energy filtered transmission electron microscopy (EFTEM)<sup>95,96</sup> or electron energy loss spectroscopy (EELS).<sup>97</sup> To date these techniques have been successfully applied characterising the LSPR response of Ag nanoprisms<sup>97</sup> and nanorods,<sup>95,98,99</sup> as well as Au nanopillars<sup>100</sup> and nanorods.<sup>96,98,101</sup> This has included demonstrating field enhancements that occur due to the coupling of response between adjacent nanoparticles,<sup>102-104</sup> and the existence of higher order multipole resonance modes in high aspect ratio nanorods.<sup>99,102</sup>

Despite the advantages that STEM-EELS provides in being the only technique capable of directly linking size, morphology and structure with LSPR response on a single particle basis, to our knowledge there have to date been only three studies employing this technique in the characterisation of bimetallic nanoparticles. One of these studies used STEM-EELS plasmon mapping as a means of determining the degree of alloying or segregation present in AuAg nanoparticles; extracts from this work are reproduced in Figure 2.14.<sup>68</sup>



**Figure 2.14.** STEM-EELS plasmon maps of AuAg nanoparticles. (a) showing a particle that the authors considered showed dominant Au resonances, and (b) a particle the authors considered demonstrated LSPR consistent with a segregated structure. From reference 68.

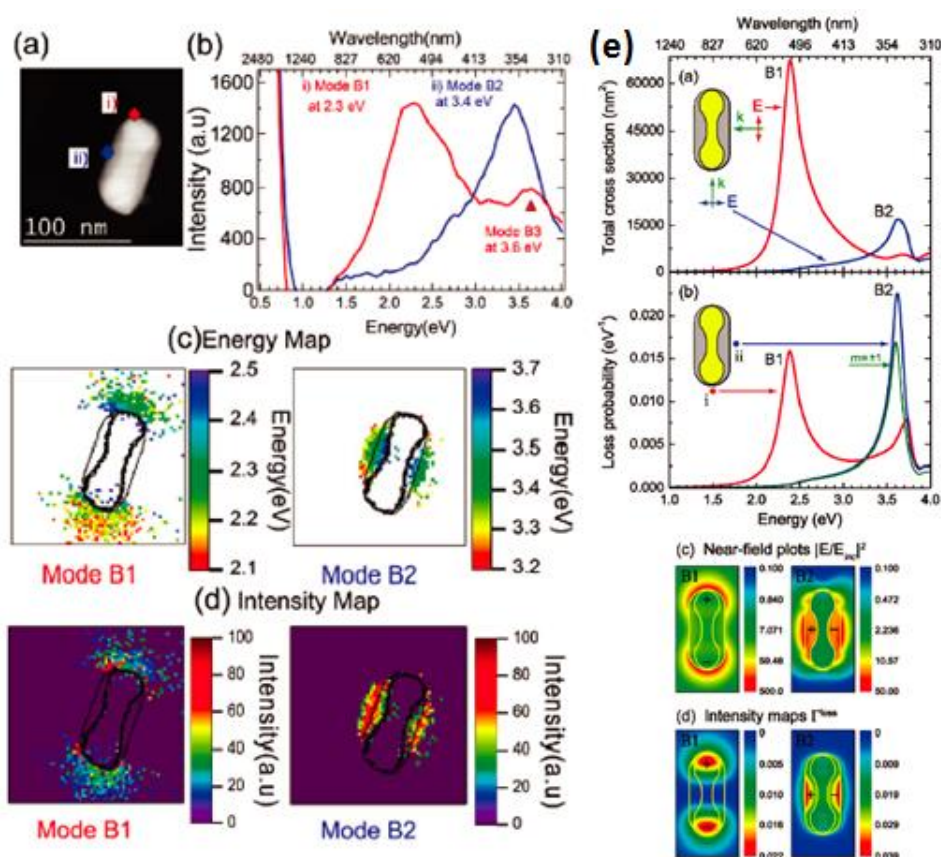
This work demonstrated the capability of STEM-EELS in mapping LSPR response to sub-nanometre resolution, however, as can be seen from the TEM images given in



Figure 2.14(a), these measurements were not taken from single isolated particles, but from agglomerations of particles. In addition, simultaneous STEM-HAADF images of these particles, which might have revealed any segregation present through elemental image contrast, were not acquired. Nonetheless this work successfully demonstrated variations in the response between particles with differing composition, indicating the potential that might be available in applying this technique to the characterisation of bimetallic nanoparticles.

Another study by Rodriguez-Gonzalez *et al.*, also addressing AuAg nanoparticles, used STEM-EELS to identify distinct resonance modes associated with the addition of an uneven Ag shell on dumbbell shaped Au nanorods; extracts from this work are reproduced in Figure 2.15.<sup>69</sup> The energy maps of Figure 2.15(c) show the localisation of Ag response at the centre of the particle, demonstrating the sub-particle spatial characterisation capability of this technique. This study also identified a quadrupolar mode, arising from the irregular dumbbell shape of the particles, highlighting the more complex response that is a consequence of more varied particle morphology. We consider this issue further when presenting results in Chapters 6 and 7 of this thesis.

With the exception of the two studies described above we have identified no other work to date using STEM-EELS mapping to characterise the LSPR response of bimetallic nanoparticles, and no studies at all addressing any system other than AuAg. We describe the capabilities for STEM-EELS in the characterisation of the LSPR response of bimetallic nanoparticles in Chapter 4 of this thesis, and present results characterising the LSPR response of catalytically relevant AuRh and AuPd nanorods in Chapter 6, and the impact of sample evolution on the LSPR response of AuAg nanoparticles in Chapter 7 of this thesis.



**Figure 2.15.** STEM-EELS plasmon maps of AuAg dumbbell nanorods. (a) STEM-HAADF image with (b) STEM-EELS point spectra acquired from the end and side as indicated, (c) STEM-EELS energy and (d) intensity maps, and (e) optical response and energy loss simulation. Reproduced from reference 69.

The only study to date using STEM-EELS to measure the LSPR response of a bimetallic system other than AuAg was a very recent study by Huang *et al.*, where it was used to support surface enhanced Raman spectroscopy as part of the work conducted identifying catalytic enhancements to reactivity in Pd-capped Au nanorods with low Pd coverage.<sup>65</sup> As such, that study was focused on identifying the influence of the longitudinal Au LSPR and did not examine the impact that the Pd caps had on the response. The work we present in Chapter 6 of this thesis provides a more detailed characterisation of the LSPR response of AuPd nanorods with a complete Pd shell.

## List of References

1. Cortie, M.B.; McDonagh, A.M., Synthesis and Optical Properties of Hybrid and Alloy Plasmonic Nanoparticles, *Chem. Rev.* **2011**, *111*, 3713-3735
2. Campbell, C.T., Bimetallic Surface Chemistry, *Annu. Rev. Phys. Chem.* **1990**, *41*, 775-837
3. Yang, J.; Yang, J.; Ying, J.Y., Morphology and Lateral Strain Control of Pt Nanoparticles via Core-Shell Construction Using Alloy AgPd Core Toward Oxygen Reduction Reaction, *ACS Nano* **2012**, *6*, 9373-9382
4. Gan, L.; Heggen, M.; Rudi, S.; Strasser, P., Core-Shell Compositional Fine Structures of Dealloyed Pt<sub>x</sub>Ni<sub>1-x</sub> Nanoparticles and Their Impact on Oxygen Reduction Catalysis, *Nano Lett.*, **2012**, *12*, 5423-5430
5. Wang, C.; van der Vliet, D.; More, K.L.; Zaluzec, N.J.; Peng, S.; Sun, S.; Daimon, H.; Wang, G.; Greeley, J.; Pearson, J.; Paulikas, A.P.; Karapetrov, G.; Strmcnik, D.; Markovic, N.M.; Stamenkovic, V.R., Multimetallic Au/FePt<sub>3</sub> Nanoparticles as Highly Durable Electrocatalyst, *Nano Lett.* **2011**, *11*, 919-926
6. [http://en.wikipedia.org/wiki/stranski-krastanov\\_growth](http://en.wikipedia.org/wiki/stranski-krastanov_growth)
7. Seifert, W.; Carlsson, N.; Miller, M.; Pistol, M.E.; Samuelson, L.; Wallenberg, L.R., In-Situ Growth of Quantum Dot Structures by the Stranski-Krastanow Growth Mode, *Prog. Cryst. Growth. Ch.*, **1996**, *33*, 423-471
8. Gong, J., Structure and Surface Chemistry of Gold Based Metal Catalysts, *Chem. Rev.* **2012**, *112*, 2987-3054
9. Ding, Y.; Fan, F.; Tian, Z.; Wang, Z.L., Atomic Structure of Au-Pd Bimetallic Alloyed Nanoparticles, *J. Am. Chem. Soc.* **2010**, *132*, 12480-12486
10. Okamoto, H.; Massalski, T.B., The Au-Pd (Gold-Palladium) System, *J. Phase Equilib.*, **1985**, *6*, 229-235
11. Akita, T.; Hiroki, T.; Tanaka, S.; Kojima, T.; Kohyama, M.; Iwase, A.; Hori, F., Analytical TEM Observation of Au-Pd Nanoparticles Prepared by Sonochemical Method, *Catal. Today* **2008**, *131*, 90-97
12. Dash, P.; Bond, T.; Fowler, C.; Hou, W.; Coombs, N.; Scott, R.W.J., Rational Design of Supported PdAu Nanoparticle Catalysts from Structured Nanoparticle Precursors, *J. Phys. Chem. C* **2009**, *113*, 12719-12730
13. Ferrer, D.; Torres-Castro, A.; Gao, X.; Sepulveda-Guzman, S.; Ortiz-Mendes, U.; Jose-Yacaman, M., Three-Layer Core/Shell Structure in Au-Pd Bimetallic Nanoparticles, *Nano Lett.*, **2007**, *7*, 1701-1705

14. Hu, J.W.; Li, J.F.; Ren, B.; Wu, D.Y.; Sun, S.G.; Tian, Z.Q., Palladium-Coated Gold Nanoparticles with a Controlled Shell Thickness Used as Surface-Enhanced Raman Scattering Substrate, *J. Phys. Chem. C* **2007**, *111*, 1105-1112
15. Lee, Y.W.; Kim, N.H.; Lee, K.Y.; Kwon, K.; Kim, M.; Han, S.W., Synthesis and Characterization of Flower-Shaped Porous Au-Pd Alloy Nanoparticles, *J. Phys. Chem. C*, **2008**, *112*, 6717-6722
16. Jana, D.; Dandapat, A.; De, G., Au@Pd Core-Shell Nanoparticles Incorporated Alumina Sols and Coatings: Transformation of Au@Pd to Au-Pd Alloy Nanoparticles, *J. Phys. Chem. C*, **2009**, *113*, 9101-9107
17. Lee, A.F.; Baddeley, C.J.; Hardacre, C.; Ormerod, R.M.; Lambert, R.M., Structural and Catalytic Properties of Novel Au/Pd Bimetallic Colloid Particles: EXAFS, XRD, and Acetylene Coupling, *J. Phys. Chem.*, **1995**, *99*, 6096-6102
18. Kittel, C., *Introduction to Solid State Physics*, John Wiley & Sons: Hoboken New Jersey, 2008.
19. Ovari, L.; Bugyi, L.; Majzik, Z.; Berko, A.; Kiss, J., Surface Structure and Composition of Au-Rh Bimetallic Nanoclusters on TiO<sub>2</sub>(110): a LEIS and STM Study, *J. Phys. Chem. C* **2008**, *112*, 18011-18016
20. Morse, M.D., Clusters of Transition-Metal Atoms, *Chem. Rev.* **1986**, *86*, 1049-1109
21. Okamoto, H.; Massalski, T.B., The Au-Rh (Gold-Rhodium) System, *J. Phase Equilib.*, **1984**, *5*, 384-387
22. Essinger-Hileman, E.R.; DeCicco, D.; Bondi, J.F.; Schaak, R.E., Aqueous Room Temperature Synthesis of Au-Rh, Au-Pt, Pt-Rh, and Pd-Rh Alloy Nanoparticles: Fully Tunable Composition Within the Miscibility Gaps, *J. Mater. Chem.* **2011**, *21*, 11599-11604
23. Chantry, R.L.; Siritwatcharapiboon, W.; Horswell, S.L.; Logsdail, A.J.; Johnston, R.L.; Li, Z.Y., Overgrowth of Rhodium on Gold Nanorods, *J. Phys. Chem. C* **2012**, *116*, 10312-10317
24. Sneed, B.T.; Kuo, C.H.; Brodsky, C.N.; Tsung, C.K., Iodide-Mediated Control of Rhodium Epitaxial Growth on Well-Defined Noble Metal Nanocrystals: Synthesis, Characterization, and Structure-Dependent Catalytic Properties, *J. Am. Chem. Soc.*, **2012**, *134*, 18417-18426
25. Altman, E.I.; Colton, R.J., Growth of Rh on Au(111): Surface Intermixing of Immiscible Metals, *Surf. Sci. Lett.* **1994**, *304*, L400-L406
26. Chado, I.; Scheurer, F.; Bucher, J.P., Absence of Ferromagnetic Order in Ultrathin Rh Deposits Grown Under Various Conditions on Gold, *Phys. Rev. B* **2001**, *64*, 094410
27. Kibler, L.A.; Kleinert, M.; Kolb, D.M., The Initial Stages of Rhodium Deposition on Au(111), *J. Electroanal. Chem.*, **1999**, *467*, 249-257

28. Liu, C.; Bader, S.D., Absence of Ferromagnetism in Epitaxial Films of Ultrathin Pd, Rh, and Rh on Pd grown on Au(100), *Phys. Rev. B*, **1991**, *440*, 12062-12065
29. Kiss, J.; Ovari, L.; Bugyi, L.; Berko, A., Characterisation of Au-Rh and Au-Mo Bimetallic Nanoclusters on TiO<sub>2</sub>(110), *React. Kinet. Catal. Lett.* **2009**, *96*, 391-396
30. Kundu, S.; Wang, K.; Liang, H., Photochemical Generation of Catalytically Active Shape Selective Rhodium Nanocubes, *J. Phys. Chem. C*. **2009**, *113*, 18570-18577
31. Enache, D.I.; Edwards, J.K.; Landon, P.; Solsona-Espriu, B.; Carley, A.F.; Herzing, A.A.; Watanabe, M.; Kiely, C.J.; Knight, D.W.; Hutchings, G.J., Solvent-Free Oxidation of Primary Alcohols to Aldehydes Using Au-Pd/TiO<sub>2</sub>, *Science*, **2006**, *311*, 362-365
32. Nutt, M.O.; Hughes, J.B.; Wong, M.S., Designing Pd-on-Au Bimetallic Nanoparticle Catalysts for Trichloroethene Hydrodechlorination, *Environ. Sci. Technol.* **2005**, *39*, 1346-1353
33. Sankar, M.; He, Q.; Morad, M.; Pritchard, J.; Freakley, S.J.; Edwards, J.K.; Taylor, S.H.; Morgan, D.J.; Carley, A.F.; Knight, D.W.; Kiely, C.J.; Hutchings, G.J., Synthesis of Stable Ligand-Free Gold-Palladium Nanoparticles Using a Simple Excess Anion Method, *ACS Nano*, **2012**, *6*, 6600-6613
34. Serpell, C.J.; Cookson, J.; Ozkaya, D.; Beer, P.D., Core@Shell Bimetallic Nanoparticle Synthesis via Anion Coordination, *Nat. Chem.*, **2011**, *3*, 478-483
35. Su, R.; Tiruvalam, R.; He, Q.; Dimitratos, N.; Kesavan, L.; Hammond, C.; Lopez-Sanchez, J.A.; Bechstein, R.; Kiely, C.J.; Hutchings, G.J.; Besenbacher, F., Promotion of Phenol Photodecomposition Over TiO<sub>2</sub> Using Au, Pd, and Au-Pd Nanoparticles, *ACS Nano*, **2012**, *6*, 6284-6292
36. Xu, J.; Wilson, A.R.; Rathmell, A.R.; Howe, J.; Chi, M.; Wiley, B.J., Synthesis and Catalytic Properties of Au-Pd Nanoflowers, *ACS Nano*, **2011**, *5*, 6119-6127
37. Cui, C.H.; Yu, J.W.; Li, H.H.; Gao, M.R.; Liang, H.W.; Yu, S.H., Remarkable Enhancement of Electrocatalytic Activity by Tuning the Interface of Pd-Au Bimetallic Nanoparticle Tubes, *ACS Nano* **2011**, *5*, 4211-4218
38. Yi, C.W.; Luo, K.; Wei, T.; Goodman, D.W., The Composition and Structure of Pd-Au Surfaces, *J. Phys. Chem. B* **2005**, *109*, 18535-18540
39. Ferrer, D.; Blom, D.A.; Allard, L.F.; Mejia, S.; Perez-Tijerina, E.; Jose-Yacamán, M., Atomic Structure of Three-Layer Au/Pd Nanoparticles Revealed by Aberration Corrected Scanning Transmission Microscopy, *J. Mater. Chem.* **2008**, *18*, 2442-2446
40. Ferrando, R.; Jellinek, J.; Johnston, R.L., Nanoalloys: From Theory to Applications of Alloy Clusters and Nanoparticles, *Chem. Rev.* **2008**, *108*, 845-910
41. Belic, D.; Chantry, R.L.; Li, Z.Y.; Brown, S.A., Ag-Au nanoclusters: structure and phase segregation, *Appl. Phys. Lett.*, **2011**, *99*, 171914

42. Chuntunov, L.; Bar-Sadan, M.; Houben, L.; Haran, G., Correlating Electron Tomography and Plasmon Spectroscopy of Single Noble Metal Core-Shell Nanoparticles, *Nano Lett.* **2011**, *12*, 145-150
43. Herzing, A.A.; Watanabe, M.; Edwards, J.K.; Conte, M.; Tang, Z.R.; Hutchings, G.J.; Kiely, C.J., Energy Dispersive X-Ray Spectroscopy of Bimetallic Nanoparticles in an Aberration Corrected Scanning Transmission Electron Microscopy, *Faraday Discuss.* **2008**, *138*, 337-351
44. Kim, S.; Kim, S.K.; Park, S., Bimetallic Gold-Silver Nanorods Produce Multiple Surface Plasmon Bands, *J. Am. Chem. Soc.*, **2009**, *131*, 8380-8381
45. Li, Z.Y.; Yuan, J.; Chen, Y.; Palmer, R.E.; Wilcoxon, J.P., Direct Imaging of Core-Shell Structure in Silver-Gold Bimetallic Nanoparticles, *Appl. Phys. Lett.* **2005**, *87*, 243103
46. Mayoral, A.; Vazquez-Duran, A.; Ferrer, D.; Montejano-Carrizales, J.M.; Jose-Yacamán, M., On the Structure of Stellated Single Crystal Au/Ag Nanoparticles, *Cryst. Eng. Comm.*, **2009**, *12*, 1090-1095
47. Shibata, T.; Bunker, B.A.; Zhang, Z.; Meisel, D.; Vardeman, C.F.; Gezelter, J.D., Size Dependent Spontaneous Alloying of Au-Ag Nanoparticles, *J. Am. Chem. Soc.*, **2002**, *124*, 11989-11996
48. Xiang, Y.; Wu, X.; Liu, D.; Li, Z.; Chu, W.; Feng, L.; Zhang, K.; Zhou, W.; Xie, S., Gold Nanorod-Seeded Growth of Silver Nanostructures: From Homogeneous coating to Anisotropic Coating, *Langmuir*, **2008**, *24*, 3465-3470
49. Curley, B.C.; Rossi, B.; Ferrando, R.; Johnston, R.L., Theoretical Study of Structure and Segregation in 38-Atom, Ag-Au Nanoalloys, *Eur. Phys. J. D*, **2007**, *43*, 53-56
50. Okamoto, H.; Massalski, T.B., The Ag-Au (Silver-Gold) System, *J. Phase Equilib.*, **1983**, *4*, 30-38
51. Ouyang, G.; Tan, X.; Wang, C.X.; Yang, G.W., Physical and Chemical Origin of Size-Dependent Spontaneous Interfacial Alloying of Core-Shell Nanostructures, *Chem. Phys. Lett.* **2006**, *420*, 65-70
52. Park, J.; Lee, J., The Phase Diagram Reassessment of Ag-Au System Including Size Effect, *Calphad*, **2008**, *32*, 135-141
53. Pettersson, L.A.A.; Snyder, P.G., Preparation and Characterization of Oxidized Silver Thin Films, *Calphad*, **2008**, *32*, 135-141
54. Allen, J.P.; Scanlon, D.O.; Watson, G.W., Electronic Structures of Silver Oxides, *Phys. Rev. B* **2011**, *84*, 115141
55. Carlisle, C.I.; Fujimoto, T.; Sim, W.S.; King, D.A., Atomic Imaging of the Transition Between Oxygen Chemisorptions and Oxide Film Growth on Ag{111}, *Surf. Sci.* **2000**, *470*, 15-31

56. Carlisle, C.I.; King, D.A., Imaging the Surface and Interface Atoms of an Oxide Film on Ag{111} by Scanning Tunneling Microscope: Experiment and Theory, *Phys. Rev. Lett.* **2000**, *84*, 3899-3902
57. Costina, I.; Schmid, M.; Schiechl, H.; Gajdos, M.; Stierle, A.; Kumaragurubaran, S.; Hafner, J.; Dosch, H.; Varga, P., Combined STM, LEED, DFT Study of Ag(100) Exposed to Oxygen Near Atmospheric Pressures, *Surf. Sci.* **2006**, *600*, 617-624
58. Michaelides, A.; Bocquet, M.L.; Sautet, P.; Alavi, A.; King, D.A., Structures and Thermodynamic Phase Transitions for Oxygen and Silver Oxide Phases on Ag{111}, *Chem. Phys. Lett.* **2003**, *367*, 344-350
59. Rovida, G.; Pratesi, F.; Maglietta, M.; Ferroni, E., Chemisorption of Oxygen on the Silver (111) Surface, *Surf. Sci.* **1974**, *43*, 230-256
60. Schmid, M.; Reicho, A.; Stierle, A.; Costina, I.; Klikovits, J.; Kostelnik, P.; Dubay, O.; Kresse, G.; Gustafson, J.; Lundgren, E.; Andersen, J.N.; Dosch, H.; Varga, P., Structure of Ag(111)-p(4 x 4)-O: No Silver Oxide, *Phys. Rev. Lett.* **2006**, *96*, 146102
61. Schnadt, J.; Michaelides, A.; Knudsen, J.; Vang, R.T.; Reuter, K.; Laegsgaard, E.; Scheffler, M.; Besenbacher, F., Revisiting the Structure of the p(4 x 4) Surface Oxide on Ag(111), *Phys. Rev. Lett.*, **2006**, *96*, 146101
62. Schnadt, J.; Knudsen, J.; Hu, X.L.; Michaelides, A.; Vang, R.T.; Reuter, K.; Li, Z.; Laegsgaard, E.; Scheffler, M.; Besenbacher, F., Experimental and Theoretical Study of Oxygen Adsorption Structures on Ag(111), *Phys. Rev. B*, **2009**, *80*, 075424
63. Blaber, M.G.; Arnold, M.D.; Ford, M.J., A Review of the Optical Properties of Alloys and Intermetallics for Plasmonics, *J. Phys.: Condens. Matter.*, **2010**, *22*, 143201
64. Christopher, P.; Xin, H.; Linic, S., Visible-Light-Enhanced Catalytic Oxidation Reactions on Plasmonic Silver Nanostructures. *Nature Chem.*, **2011**, *3*, 467-472.
65. Huang, J.; Zhu, Y.; Lin, M.; Wang, Q.; Zhao, L.; Yang, Y.; Yao, K.X.; Han, Y, Site-Specific Growth of Au-Pd Alloy Horns on Au Nanorods: A Platform for Highly Sensitive Monitoring of Catalytic Reactions by Surface Enhanced Raman Spectroscopy, *J. Am. Chem. Soc.*, **2013**, *135*, 8552-8561
66. Wang, F.; Li, C.; Chen, H.; Jian, R.; Sun, L.D.; Li, Q.; Wang, J.; Yu, J.C.; Yan, C.H., Plasmonic Harvesting of Light Energy for Suzuki Coupling Reactions, *J. Am. Chem. Soc.*, **2013**, *135*, 5588-5601
67. Shan, X.; Díez-Pérez, I.; Wang, L.; Wiktor, P.; Gu, Y.; Zhang, L.; Wang, W.; Lu, J.; Wang, S.; Gong, Q.; Li, J.; Tao, N., Imaging the electrocatalytic activity of single nanoparticles, *Nature Nanotech.*, **2012**, *7*, 668-672.
68. Eccles, J.W.L.; Bangert, U.; Bromfield, M.; Christian, P.; Harvey, A.J., Do Nanomaterials Form Truly Homogeneous Alloys?, *J. Appl. Phys.*, **2010**, *107*, 104325

69. Rodriguez-Gonzalez, B.; Attouchi, F.; Cardinal, M.F.; Myroshnychenko, V.; Stephan, O.; Garcia de Abajo, F.J.; Liz-Marzan, L.M.; Kociak, M., Surface Plasmon Mapping of Dumbbell-Shaped Gold Nanorods: The Effect of Silver Coating, *Langmuir*, **2012**, *28*, 9063-9070
70. Kreibig, U.; Vollmer, M., *Optical properties of metal clusters*, Springer-Verlag: Berlin, 1995
71. Egerton, R.F., *Electron Energy-Loss Spectroscopy in the Electron Microscope*, Springer: New York, 2011
72. Mulvaney, P.; Perez-Juste, J.; Giersig, M.; Liz-Marzan, L.M.; Pecharroman, C., Drastic Surface Plasmon Mode Shifts in Gold Nanorods Due to Electron Charging, *Plasmonics*, **2006**, *1*, 61-66
73. Henry, A.I.; Bingham J.M.; Ringe, E.; Marks, L.D.; Schatz, G.C.; Van Duyne, R.P., Correlated Structure and Optical Property Studies of Plasmonic Nanoparticles, *J. Phys. Chem. C*, **2011**, *115*, 9291-9305
74. Kelly, K.L.; Coronado, E.; Zhao, L.L.; Schatz, G.C., The Optical Properties of Metal Nanoparticles: the Influence of Size, Shape and Dielectric Environment, *J. Phys. Chem. B* **2003**, *107*, 668-677
75. Cottancin, E.; Lerme, J.; Gaudry, M.; Pellarin, M.; Vialle, J.L.; Broyer, M.; Prevel, B.; Treilleux, M.; Melinon, P., Size Effects in the Optical Properties of Au<sub>n</sub>Ag<sub>n</sub> Embedded Clusters, *Phys. Rev. B* **2000**, *62*, 5179-5185
76. Link, S.; Wang, Z.L.; El-Sayed, M.A., Alloy Formation of Gold-Silver Nanoparticles and the Dependence of the Plasmon Absorption on Their Composition, *J. Phys. Chem. B*, **1999**, *103*, 3529-3533
77. Liu, M.; Guyot-Sionnest, P., Synthesis and Optical Characterisation of Au/Ag Core/Shell Nanorods, *J. Phys. Chem. B*, **2004**, *108*, 5882-5888
78. Moskovits, M.; Smova-Sloufova, I.; Vickova, B., Bimetallic Ag-Au Nanoparticles: Extracting Meaningful Optical Constants From the Surface-Plasmon Extinction Spectrum, *J. Chem. Phys.* **2002**, *116*, 10435-10446
79. Wilcoxon, J, Optical Absorption Properties of Dispersed Gold and Silver Alloy Nanoparticles, *J. Phys. Chem. B.*, **2009**, *113*, 2647-2656
80. Ingram, J.C.; Nebesny, K.W.; Pemberton, J.E., Optical Constants of the Noble Metals Determined by Reflection Electron Energy Loss Spectroscopy, *Appl. Surf. Sci.*, **1990**, *44*, 293-300
81. Leiro, J.; Minni, E.; Suoninen, E., Study of Plasmon Structure in XPS Spectra of Silver and Gold, *J. Phys. F: Met. Phys.*, **1983**, *13*, 215-221
82. Lynch, M.J.; Swan, J.B., The Characteristic Loss Spectra of the Second and Third Series Transition Metals, *Aust. J. Phys.*, **1968**, *21*, 811-816



83. Vankar, V.D.; Vook, R.W., EELS and AES Study of Epitaxially Grown Pd(111) Thin Films, *Surf. Sci.*, **1983**, *131*, 463-474
84. Vehse, R.C.; Arakawa, E.T., Optical and Photoemissive Properties of Palladium in the Vacuum Ultraviolet Spectral Region, *Phys. Rev. B*, **1970**, *1*, 517-522
85. Pierce, D.T.; Spicer, W.E., Optical Properties of Rhodium, *Phys. Stat. Sol. (b)*, **1973**, *60*, 689-694
86. Thiam, M.M.; Nehasil, V.; Matolin, V.; Gruzza, B., The AES and EELS Study of Small Rhodium Clusters Deposited onto Alumina Substrates, *Surf. Sci.* **2001**, *487*, 231-242
87. Johnson, P.B.; Christy, R.W., Optical Constants of the Noble Metals, *Phys. Rev. B*, **1972**, *6*, 4370-4379
88. Johnson, P.B.; Christy, R.W., Optical Constants of Transition Metals: Ti, V, Cr, Mn, Fe, Co, Ni, and Pd, *Phys. Rev. B*, **1974**, *9*, 5056-5070
89. *Handbook of Optical Constants of Solids*, ed. Palik, E.D., Academic Press, London, 1998
90. Qiu, J.H.; Zhou, P.; Gao, X.Y.; Yu, J.N.; Wang, S.Y.; Li, J.; Zheng, Y.X.; Yang, Y.M.; Song, Q.H.; Chen, L.Y., Ellipsometric Study of the Optical Properties of Silver Oxide Prepared by Reactive Magnetron Sputtering, *J. Korean Phys. Soc.*, **2005**, *46*, S269-S275
91. Logsdail, A.J.; Johnston, R.L., Predicting the Optical Properties of Core-Shell and Janus Segregated Au-M Nanoparticles (M = Au, Pd), *J. Phys. Chem. C*, **2012**, *116*, 23616-23628
92. Logsdail, A.J.; Cookson, N.J.; Horswell, S.L.; Wang, Z.W.; Li, Z.Y.; Johnston, R.L., Theoretical and Experimental Studies of the Optical Properties of Conjoined Gold-Palladium Nanospheres, *J. Phys. Chem. C*, **2010**, *114*, 21247-21251
93. Grillet, N.; Manchon, D.; Bertorelle, F.; Bonnet, C.; Broyer, M.; Cottancin, E.; Lerme, J.; Hillenkamp, M.; Pellarin, M., Plasmon coupling in silver nanocube dimers: Resonance splitting induced by edge rounding, *ACS Nano*, **2012**, *5*, 9450-9462.
94. Mock, J.J.; Barbic, M.; Smith, D.R.; Schultz, D.A.; Schultz S.; Shape Effects in Plasmon Resonance of Individual Colloidal Silver Nanoparticles, *J. Phys. Chem.*, **2002**, *116*, 6755-6759
95. N'Gom, M.; Ringnalda, J.; Mansfield, J.F.; Agarwal, A.; Kotov, N.; Zaluzec, N.J.; Norris, T.B., Single Particle Plasmon Spectroscopy of Silver Nanowires and Gold Nanorods, *Nano Lett.*, **2008**, *8*, 3200-3204
96. Schaffer, B.; Hohenester, U.; Trugler, A.; Hofer, F., High-Resolution Surface Plasmon Imaging of Gold Nanoparticles by Energy-Filtered Transmission Electron Microscopy, *Phys. Rev. B*, **2009**, *79*, 041401

97. Nelayah, J.; Kociak, M.; Stephan, O.; Garcia de Abajo, F.J.; Tence, M.; Henrard, L.; Taverna, D.; Pstoriza-Santos, I.; Liz-Marzan, L.M.; Colliex, C., Mapping Surface Plasmons on a Single Metallic Nanoparticle, *Nature Phys.*, **2007**, *3*, 348-353
98. Bosman, M.; Keast, V.J.; Watanabe, M.; Maarof, A.I.; Cortie, M.B., Mapping Surface Plasmons at the Nanometer Scale with an Electron Beam, *Nanotechnology*, **2007**, *18*, 165505
99. Roussow, D.; Couillard, M.; Vickery, J.; Kumacheva,.; Botton, G.A., Multipolar Plasmonic Resonances in Silver Nanowire Antennas Imaged with a Subnanometer Electron Probe, *Nano Lett.*, **2011**, *11*, 1499-1504
100. Koh, A.L.; Fernandez-Dominguez, A.I.; McComb, D.W.; Maier, S.A.; Yang, J.K.W., High-Resolution Mapping of Electron-Beam-Excited Plasmon Modes in Lithographically Defined Gold Nanostructures, *Nano Lett.*, **2011**, *11*, 1323-1330
101. N’Gom, M.; Li, S.; Schatz, G.; Erni, R.; Agarwal, A.; Kotov, N.; Norris, T.B., Electron-Beam Mapping of Plasmon Resonances in Electromagnetically Interacting Gold Nanorods, *Phys. Rev. B*, **2009**, *80*, 113411
102. Alber, I.; Sigle, W.; Demmin-Janssen, F.; Neumann, R.; Trautmann, C.; van Aken, P.A.; Toimil-Molares, M.E., Multipole Surface Plasmon Resonances in Conductively Coupled Metal Nanowire Dimers, *ACS Nano*, **2012**, *6*, 9711-9717
103. Grzelczak, M.; Mezzasalma, S.A.; Ni, W.; Herasimenka, Y.; Feruglio, L.; Montini, T.; Perez-Juste, J.; Fornasiero, P.; Prato, M.; Liz-Marzan, L.M., Antibonding Plasmon Modes in Colloidal Gold Nanorod Clusters, *Langmuir*, **2011**, *28*, 8826-8833
104. Song, F.; Wang, T.; Wang, X.; Xu, C.; He, L.; Wan, J.; Van Haesendonck, C.; Ringer, S.P.; Han, M.; Liu, Z.; Wang, G., Visualizing Plasmon Coupling in Closely Spaced Chains of Ag Nanoparticles by Electron Energy-Loss Spectroscopy, *Small*, **2010**, *6*, 446-451

---

## Chapter 3

# Experimental Methods: Characterisation of Structure

Establishing an unambiguous link between properties and structure in bimetallic nanoparticles requires characterisation conducted to the best possible resolution, because enhancements to properties measured on addition of a second metal derive from atomic scale interactions. Thus the challenge in this work is to collect atomically resolved structural and elemental information, including from sub-surface locations, and link that data to measured properties. Aberration corrected scanning transmission electron microscopy (ac-STEM) is one of the few techniques with the potential to carry out this work. It has the capability to obtain the most complete range of characterisation data of any single instrument; through employing a combination of imaging and spectroscopy techniques it can be used to collect both elemental and structural data to atomic resolution.

In this chapter we outline the potential of ac-STEM in the structural characterisation of bimetallic nanoparticles; in Chapter 4 we describe the techniques it offers for the characterisation of electronic properties. Section 3.1 of this chapter gives an overview of the basic principles of ac-STEM in this context, whilst Section 3.2 discusses in more detail the atomically resolved spatial resolution that is essential to this work. The

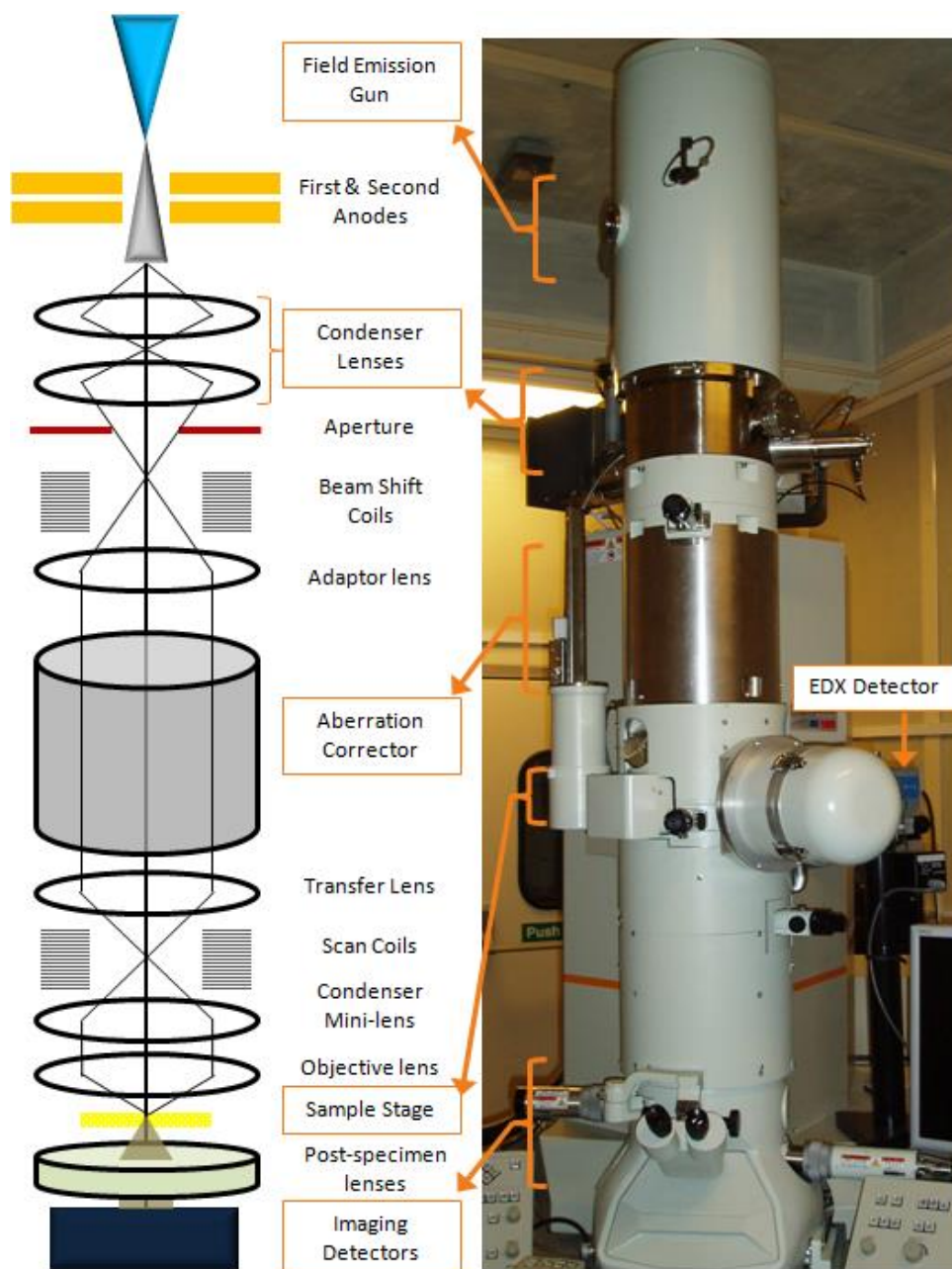
data used for the structural characterisation of bimetallic nanoparticles presented in Chapters 5 and 7 of this thesis were primarily obtained through STEM imaging and energy dispersive X-ray spectroscopy (EDX); these techniques are described in detail in Section 3.3 and 3.4 of this chapter respectively.

### 3.1 Overview of STEM

Transmission electron microscopy (TEM) is a well-established method in the structural characterisation of materials, with fast electrons transmitted through a sample first being used for this purpose more than 70 years ago.<sup>1</sup> STEM employs a focussed probe of electrons scanned across an area of a sample. Its development followed the discovery of field emission electron sources, and this technique has been in use for more than 40 years.<sup>2,3</sup> Although the capability of STEM imaging to reveal contrast variation between single heavy metal atoms and a thin carbon support was established by Crewe *et al.* in 1970,<sup>2</sup> single atoms could not be fully spatially resolved whilst the probe size was limited by spherical aberration ( $C_s$ ) in the lens systems. Devices to counter the impact of spherical aberration, allowing the potential for sub-angstrom probe sizes and atomically resolved imaging, were not developed until 1998, and did not become readily available in commercially produced instruments until the last 5 years.<sup>4</sup> This means that exploration of the full capabilities of ac-STEM in the characterisation of bimetallic nanoparticles has yet to be realised.

The ac-STEM structural characterisation results presented in Chapters 5 and 7 of this thesis were collected by the author using an aberration corrected Jeol 2100F STEM, located in the Nanoscale Physics Research Laboratory, School of Physics and Astronomy, University of Birmingham (shown in Figure 3.1). In STEM mode the instrument employs

a CEOS spherical aberration corrector.<sup>5</sup> The principle detectors available for structural and elemental characterisation work are high angle annular dark field (HAADF) and bright field (BF) imaging detectors, and a Bruker XFlash 4030 EDX detector. Digital Micrograph software was used to collect and process STEM images.<sup>6</sup>



**Figure 3.1: JEOL 2100f STEM.** Summary schematic diagram of the principle components of an aberration corrected STEM and photograph of the instrument used in this study, with key components indicated.

Figure 3.1 shows a summary schematic representation of the principle components of an aberration corrected STEM, which are described further in the following paragraphs. The electron source in instrument is a Schottky field emission gun (FEG). The beam electrons are generated from a thin covering of Zirconium Oxide on the surface of the FEG tip. The tip is sharp to nanometre proportions, so a voltage bias applied between it and the first anode creates an extremely strong electric field that is sufficient to extract electrons from the tip through quantum tunnelling, in a phenomenon known as field emission. In a Schottky FEG the tip is heated to improve the efficiency of field emission, however, this also increases the energy spread of emitted electrons, a factor that is discussed further in the context of EELS energy resolution in Chapter 4.

The second anode applies the accelerating voltage to propel the extracted electrons down the column. The accelerating voltage for the instrument used in this study is 200 kV, which accelerates the beam electrons to approximately 70% of the speed of light in a vacuum.

The condenser lens system collimates and focuses the beam electrons using strong electromagnetic fields generated by the lens coils. Other coils are used to tilt and shift the beam to align it with the sample. After the condenser lenses, the beam passes through an aperture, which removes the more widely scattered electrons. The size of the aperture can be selected to allow balance between the requirements of beam intensity and beam quality. All the images in this study were taken using an intermediate aperture; the third out of the four available on the instrument used, with a diameter of 40  $\mu\text{m}$ .

After passing through the condenser lenses the beam enters the aberration corrector. The aberration corrector removes most of the spherical aberration caused by the condenser lenses from the beam; its operation is described in more detail in Section 3.2 below. After

passing through the aberration corrector the beam is formed into a probe by the pre-specimen objective lens. Scan coils are used to scan the probe across a selected region of the sample in a raster pattern. The imaging and EELS detectors are positioned below the sample, after a series of post-specimen lenses that alter the geometry of the beam, allowing control over the portion of the scattered electron beam entering the detectors. In contrast, the EDX detector (partially obscured by the sample arm cover in Figure 3.1) is positioned above the sample. The imaging and EDX detectors used in this study are described in detail in Sections 3.3 and 3.4.

The microscope column is maintained in vacuum conditions, using a series of pumps. The quality of the vacuum is vital to both the operation of the FEG and the quality of the beam. Any atoms present in the column can potentially scatter the beam electrons, reducing beam coherence, and can also interact with the sample causing contamination. A series of pumps create varying levels of vacuum in different parts of the column, with the highest vacuum being in the gun chamber, where it is necessary to avoid degradation of the tip. The vacuum in the gun chamber is of the order of  $10^{-9}$  Pa.

In order to transmit sufficient electrons to form an image the sample must be thin, typically less than 100 nm thick, a condition that is readily met by the nanoscale samples that are the subject of this study.<sup>1</sup> For all of the experimental work presented in this study samples were mounted on amorphous carbon coated copper grids. Where the samples are kept in solution for long term storage, they were prepared for imaging one day prior to being loaded into the microscope by drop casting a small amount of sample solution onto TEM grids. Excess solution was removed and the samples left to dry in ambient conditions for approximately one hour before being transferred to a pumped desiccator to complete the drying process. It is essential that the samples are fully dry before being

loaded into the microscope to reduce the effects of contamination. For non-liquid samples, such as samples prepared directly on TEM supports by inert gas aggregation, the grids were kept in appropriately labelled proprietary grid storage boxes in a desiccator between all imaging sessions.

## 3.2. Resolution

The effectiveness of ac-STEM in the characterisation of nanoparticles is primarily due to its atomic scale spatial resolution. Applying the small angle approximation, the Rayleigh criterion can be used to relate the smallest distance that can be resolved by an instrument,  $\delta$ , to the wavelength of the radiation incident on the sample,  $\lambda$ , as follows.<sup>1</sup>

$$\delta \approx 0.61\lambda \quad 3.1$$

In STEM the incident radiation takes the form of electrons, so the relevant wavelength is the de Broglie wavelength of an electron. For the relativistic conditions of the STEM beam the de Broglie wavelength  $\lambda_{dB}$ , of an object of mass  $m$ , and velocity  $v$ , is given by the following,<sup>1</sup> where  $h$  is Planck's constant.

$$\lambda_{dB} = \frac{h}{\sqrt{2meV\left(1 + \frac{eV}{2mc^2}\right)}} \quad 3.2$$

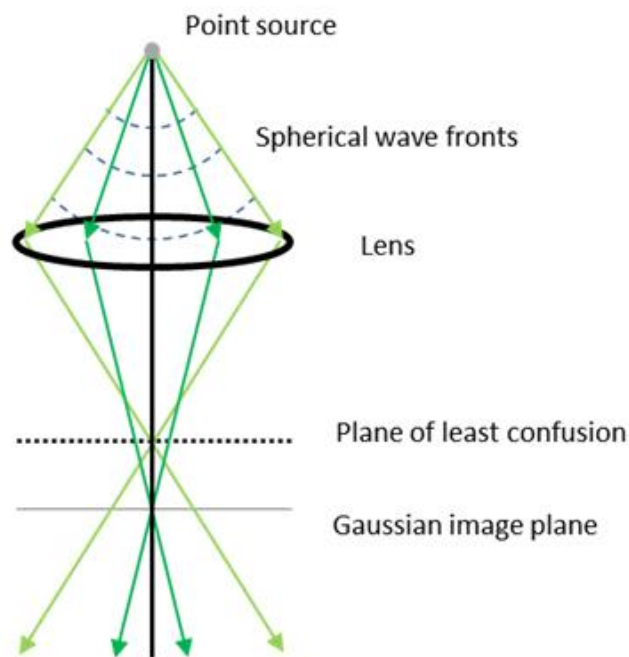
Using  $V = 200$  kV, consistent with the imaging conditions of the instrument used in this study, equation 3.2 gives a de Broglie wavelength of  $2.5 \times 10^{-3}$  nm and thus, from equation 3.1, an approximate theoretical minimum resolvable distance of  $\delta \sim 1.5 \times 10^{-3}$  nm. This is much less than the length scales of atoms, where atomic radii are typically of the order of 0.1 nm, however, the limitations imposed by imaging systems mean the theoretical limits of image resolution are never reached in real experimental conditions.



The true limits to image resolution are determined by aberrations within the imaging system, together with other sources of noise and instability within the microscope, such as electronic instabilities in the lenses. The minimisation of noise and instability is dependent on the effective microscope design and the environment in which the instrument is located. It is essential that it is insulated from stray external electric and magnetic fields, so the STEM laboratory incorporates electrical shielding and a magnetic field cancellation system. The instrument is also run from a single power supply to reduce the introduction of additional noise from different power supply phases. The impact of sample drift on imaging stability can also be improved by leaving the sample in the column for as long as possible before switching the beam on, for example by loading the sample the night before an imaging session. This practice allows any residual physical vibrations to subside and lets the sample reach full thermal equilibrium with the column.

The maximisation of image resolution requires the minimisation of aberrations in the imaging system. There is no formal definition of aberration, however, aberrations can be regarded as anything within the geometry of the imaging system such that the spherical wave front from a point source is prevented by the imaging system from forming a point image.<sup>7</sup> Using this definition the primary aberrations with any instrument are defocus and two-fold astigmatism, however, these can be removed easily through correctly focussing and aligning the microscope and so do not generally limit imaging resolution. Assuming the elimination of defocus and two-fold astigmatism, the next most significant resolution limiting aberration in STEM instruments is spherical aberration, primarily originating from the strong condenser lenses.

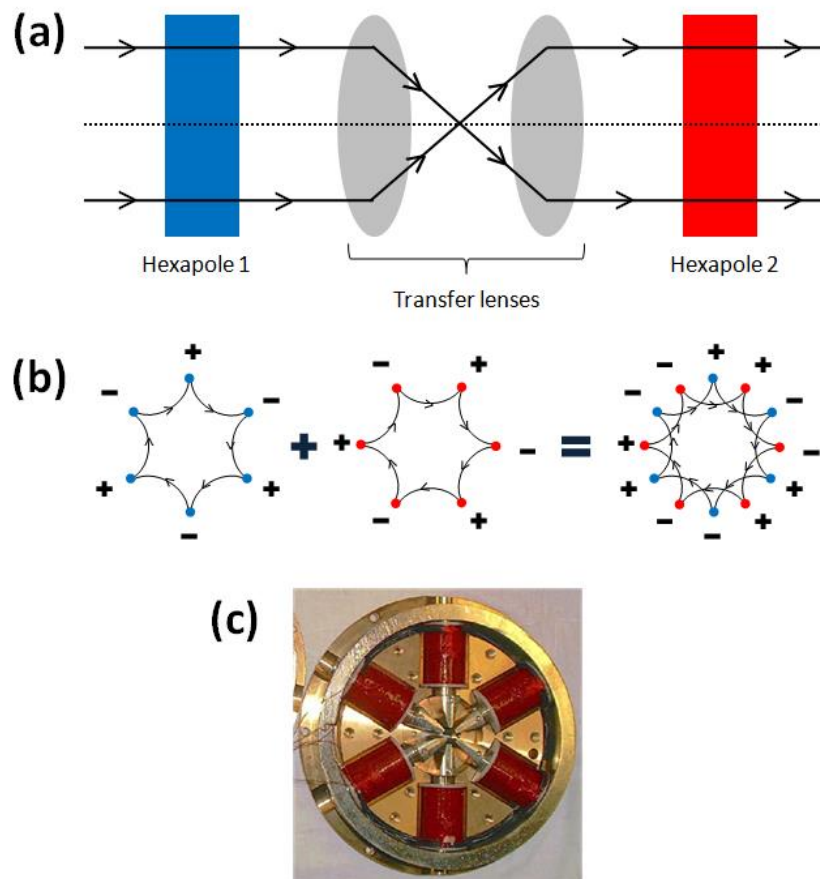
Spherical aberration occurs because in circular lenses the degree to which the incident rays are bent by the lens is dependent on distance from the centre of the lens; shown schematically in Figure 3.2. As a consequence, spherical aberration causes a point source to appear as a disc in the plane of least confusion, where the image is taken. Hence, to achieve the best possible resolution spherical aberration must be removed through the use of a spherical aberration corrector.



**Figure 3.2: Schematic representation of spherical aberration**

The spherical aberration correctors used in STEM introduce the equivalent of negative spherical aberration, which cancels out the positive spherical aberration caused by the lens system.<sup>8</sup> Scherzer proved that circular lenses must always have positive spherical aberration,<sup>9</sup> meaning it is not possible to have an imaging system employing only circular lenses that is free of spherical aberration. However, Zach *et al.* discovered that it is possible to generate negative spherical aberration using a pole piece lens system in a

scanning electron microscope.<sup>10</sup> The aberration corrector fitted in the microscope used in this study employs a double hexapole lens system.<sup>11</sup> This comprises two sets of six pole pieces, together with their related transfer lenses, aligned axially within the column. Figure 3.3 shows a ray diagram of the corrector and a schematic representation of the poles present in double hexapole system.



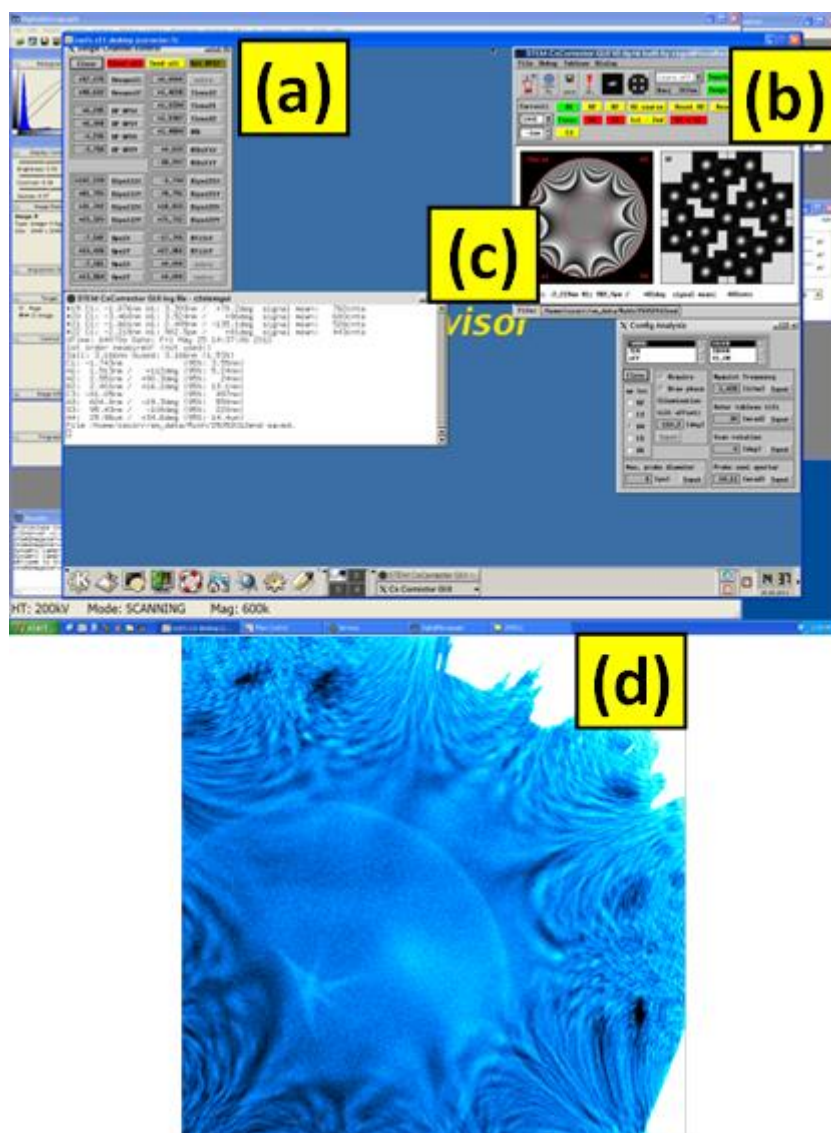
**Figure 3.3: CEOS double hexapole spherical aberration corrector.** (a) Schematic representations of the corrector lenses, and (b) the fields generated by the hexapoles, with (c) an image of one hexapole element taken from reference 12.

The two hexapole elements are rotationally offset, making it possible, taking into account both sets of fields, to produce an approximation to a circularly symmetric field

without using a circular lens. The field gradients between sets of pole pieces in the hexapole elements are adjusted to generate fields along the axis of the corrector that introduce the equivalent of negative spherical aberration to the beam, with the objective of cancelling as far as possible the positive spherical aberration generated by the lens system. Figure 3.3(c) shows a picture of one hexapole element, similar to those fitted in the instrument used in this study, taken from reference 12.

The pole piece lenses of the aberration corrector have the potential to introduce further aberrations into the imaging system; these are termed parasitic aberrations, because they do not derive from the main microscope lenses, but from lenses introduced to correct aberrations in the main microscope lenses. As a consequence, alignment of the aberration corrector entails not just generating negative spherical aberration to cancel the positive spherical aberration of the condenser lenses, but also balancing the fields generated by the corrector pole pieces, so as to minimise the impact of their parasitic aberrations. Software is employed to recognise and correct these aberrations.<sup>5</sup> The software shifts the probe between over-focus and under-focus and through a succession of tilt angles to produce a Zemlin tableau.

Figure 3.4 shows a screen shot from the CEOS software used to align the aberration corrector on the microscope used in this study. Figure 3.4(a) shows the parameters that can be varied during alignment and Figure 3.4(b) shows the Zemlin tableau. From analysis of the Zemlin tableau the program calculates the probe shape, an approximation to which is shown in Figure 3.4(c). Figure 3.4(d) gives an image of the ronchigram that corresponds to the alignment shown in Figure 3.4(c).

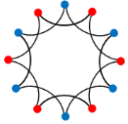


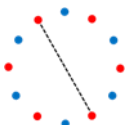



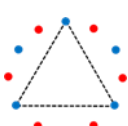


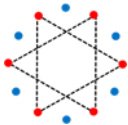

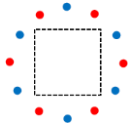



**Figure 3.4: CEOS alignment software and resulting ronchigram.** Screen shot of CEOS aberration corrector alignment software<sup>5</sup> showing (a) the configuration panel, (b) the Zernin tableau, and (c) the calculated ronchigram, together with (d) an image of the ronchigram taken from the microscope.

The ronchigram is a projection of the probe formed below the sample stage. The uniform and symmetrical shape of the centre of the ronchigram shown in Figure 3.4(d), and the appearance of projections of all twelve of the corrector pole pieces, are indicative of good alignment. It is also important to good alignment that the shape of the ronchigram remains constant through from under-focus to over-focus.

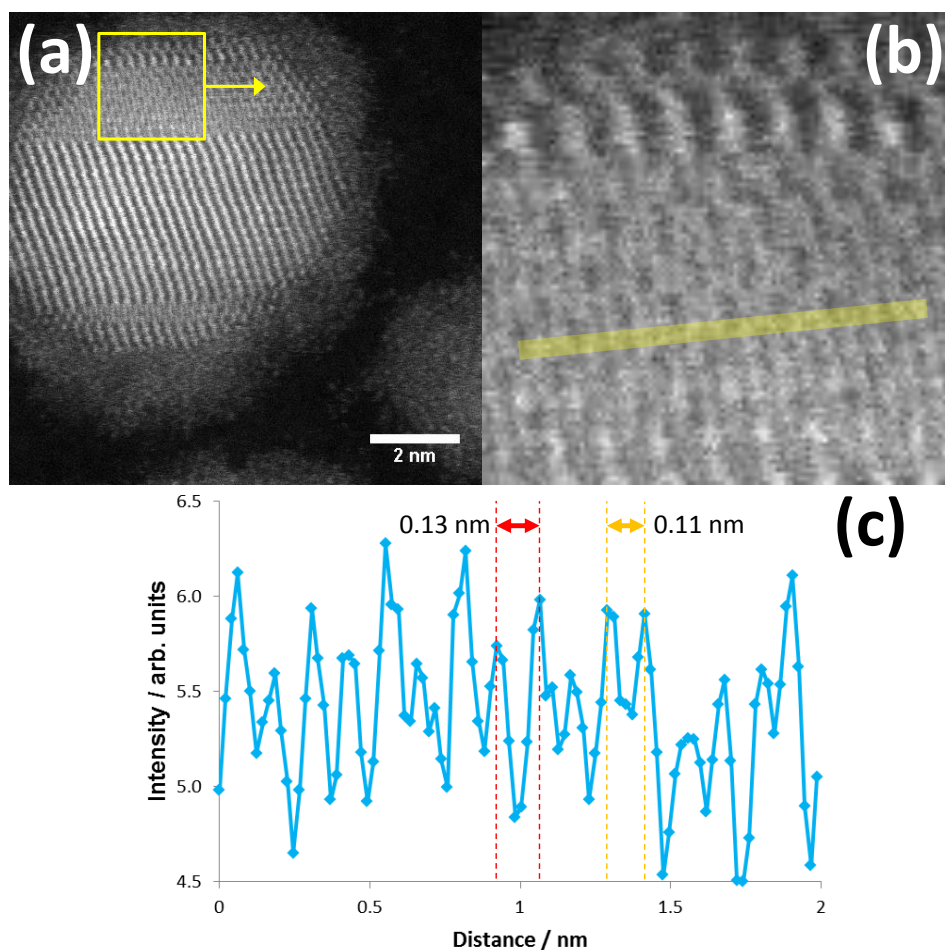
The principle aberrations that can be corrected using the CEOS software in the JEOL2100F microscope used in this study are listed in Figure 3.5. By analysing how the probe shape varies through the tableau, and in particular by analysing the variation and symmetry of the probe misshape between over and under-focus, the software works out the dominant aberration affecting the probe to a stated degree of confidence, and suggests the correction that should be made. The user is free to accept this suggestion, or to ignore it and make their own decision as to which aberration to correct, or to re-run the tableau. Each adjustment to the alignment of the corrector can potentially impact on other aberrations, so alignment is an iterative process. If the suggestions of the software are followed, it gradually converges to a good alignment through successive runs of the tableau.

Careful alignment of the corrector can produce a probe that is virtually free of both spherical aberration and the aberrations of the corrector itself. The symmetric shape and largely featureless region apparent in the centre of the ronchigram of Figure 3.4(d) is indicative of effective eradication of spherical and parasitic aberrations from the probe. The central featureless area of this ronchigram was calculated by the software as 29 mrad in size, which is close to the best that can be achieved in this instrument using this software. Atomically resolved imaging is possible with a ronchigram of lesser quality than this, however, the better the ronchigram is the more detail that can be resolved in a sample; resolving higher order crystal orientations, or complex crystal structure, is only possible with good alignment of the corrector.

	Symmetry	Cause	Schematic example of corrector balance	Simulation of probe shape at over, in and under-focus from reference 10
Aberration free	0	n/a		
De-focus	0	Condenser lenses	n/a	
A1 : 2-fold astigmatism	2	Condenser lenses or corrector		
B2 : axial coma	0	Corrector or column alignment		
A2 : 3-fold astigmatism	3	Corrector		
Cs : spherical	0	Condenser lenses	Condenser lenses	
S3 : star	2	Corrector		
A3 : 4 fold astigmatism	4	Corrector		

**Figure 3.5: Principle aberrations present in an ac-STEM with double hexapole corrector.** Summary of the principle aberrations that can be corrected using the CEOS software in the JEOL2100F microscope with schematic representations of their cause and simulations of the impact they have on the probe shape (from reference 10).

Figure 3.6(a) shows a STEM-HAADF image taken on the instrument used in this study, after alignment of the aberration corrector to a standard comparable to that shown in Figure 3.4(d), and Figure 3.6(b) shows an enlarged extract from this image.



**Figure 3.6: Demonstration of 0.11 nm spatial resolution.** (a) STEM-HAADF image of the end of an Ag nanoparticle, (b) extract taken as indicated from (a) showing the location of the line intensity profile shown in (c).

Figure 3.6(c) shows a line intensity profile taken as indicated in Figure 3.6(b) over a width of 6 pixels. The line intensity profile shows an alternating pattern of two different atomic lattice spacings; over this line profile the mean wider spacing is  $0.13 \pm 0.01$  nm and

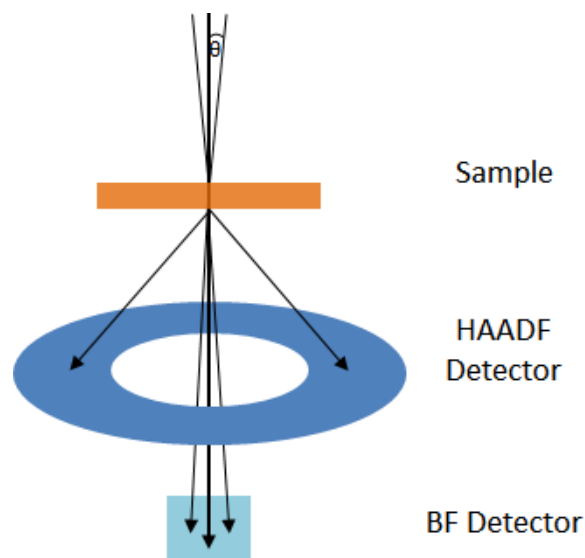


the mean narrower spacing is  $0.11 \pm 0.01$  nm. This latter spacing compares well with the calibrated resolution of this instrument at the time of installation of 0.1045 nm, which was measured using a bulk silicon sample in [115] orientation.<sup>13</sup>

In addition to aberrations arising through geometric factors in the imaging system the STEM probe is also affected by chromatic aberration ( $C_c$ ).<sup>14</sup>  $C_c$  is not a geometric aberration but rather impacts through loss of information on transfer through the lenses, and thus affects image contrast rather than spatial resolution. It originates from the energy dependence of focussing in electromagnetic lenses, causing variation in focus where there is a spread of energy in the electrons passing through the lens. In STEM the relevant lenses are the condenser lenses and the spread of energy of electrons derives from the electron source. As the spread of electrons from a Schottky FEG is relatively narrow, at around 1 eV, STEM imaging is largely unaffected by  $C_c$  and is not corrected for in the instrument used in this study.

### **3.3. Imaging**

As the electrons pass through the sample they interact with it and are scattered through a range of forward angles. They are then collected post-specimen by the STEM imaging detectors. The information that can be gathered about the sample is dependent on the detector used, and in particular a distinction is made between the more widely scattered electrons that are detected in DF images, and the electrons scattered to smaller forward angles that are detected for BF images. Figure 3.7 gives a schematic diagram illustrating the location of the two principal imaging detectors used in this study; the dimensions are exaggerated for the purposes of the diagram.

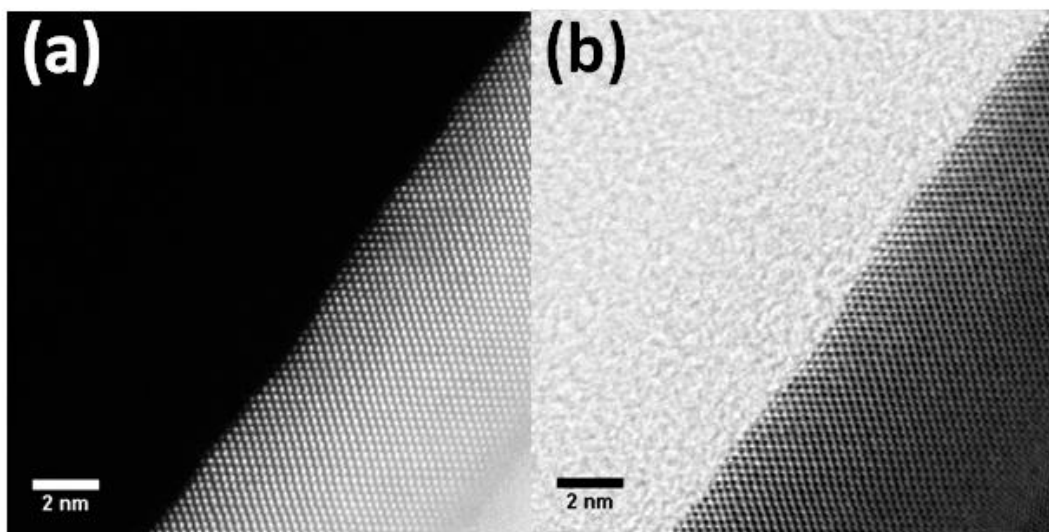


**Figure 3.7: STEM imaging detectors.** Schematic diagram illustrating the location of the imaging detectors and the beam convergence semi-angle,  $\theta$  (not to proportion).

The principle of wave-particle duality and the small size of the electron source in electron microscopes allow the assumption that pre-sample beam electrons can be described by one wave equation, and are thus coherent.<sup>1</sup> The electrons scattered to very small angles, and collected by the BF detector, are assumed to retain their coherence. Thus, even though image contrast in BF images is formed from the spatial distribution of scattered electrons, the assumption that the electrons remain coherent means BF image contrast can be related to phase changes caused by interactions between the beam electrons and the sample. BF images are sensitive to extremely fine structural detail, such as the presence of lattice strain, and are also more affected by lighter elements such as the amorphous carbon substrate of TEM grids than DF images.

Figure 3.8 shows simultaneously acquired STEM-HAADF and STEM-BF ‘as taken’ images from the edge of an Au nanorod illustrating the difference in resolution between DF amplitude contrast images compared to BF phase contrast images. Atomic

resolution is apparent in both images, however, the greater sensitivity of BF imaging to lighter atoms means the grain of the underlying amorphous carbon support is apparent in the BF image but not in the HAADF image, which detrimentally affects the resolution in the BF image.



**Figure 3.8: Example of atomically resolved imaging.** (a) STEM-HAADF and (b) simultaneously acquired STEM-BF images taken of the edge of an Au nanorod.

As shown schematically in Figure 3.7, the HAADF detector collects electrons that have been scattered to wider angles. If the collection angle of the detector is sufficiently large then electrons collected by the HAADF detector can be regarded as incoherent. An inner collection angle of three times the beam convergence semi-angle has been proposed as a condition for ensuring incoherent imaging,<sup>15</sup> or alternatively an inner collection angle of greater than 50 mrad has also been stated as sufficient.<sup>1</sup> These conditions for incoherent imaging are considered further in the context of the imaging parameters employed within instrument used in this study below.

The incoherent nature of HAADF image contrast makes interpretation more straightforward, as it is no longer affected by complex phase changes caused by wave-like interactions with the sample. The incoherence of HAADF images is key to their use in quantitative STEM work and to the generation of elemental image contrast, as it allows the assumption that image contrast derives solely from the numbers of electrons detected; we discuss this further below.

The numbers of electrons scattered to larger angles by the specimen is determined by sample thickness and elemental variation, because the principle cause is Rutherford scattering. The Rutherford scattering differential cross section for an atomic nucleus, neglecting the screening effect of the electron cloud, is given by the following expression,<sup>1</sup>

$$\sigma_R(\theta) = \frac{e^4 Z^2}{16(4\pi\epsilon_0 E_0)} \frac{d\Omega}{\sin^4 \frac{\theta}{2}} \quad 3.3$$

where  $\Omega$  is the solid angle of scattering,  $e$  is the charge of an electron,  $\epsilon_0$  is the permittivity of free space,  $E_0$  is beam energy,  $\theta$  is angle of incidence (as shown in Figure 3.7) and  $Z$  is the atomic number of the sample.

An alternative approach, treating the incident beam as a wave rather than as a particle, gives scattering intensity proportional to the square of the scattering factor,  $|f(\theta)|^2$ . The scattering factor,  $f(\theta)$ , neglecting electron-electron scattering, is given by the following equation,<sup>1</sup>

$$f(\theta) = \frac{\left(1 + \frac{E_0}{m_0 c^2}\right)}{8\pi^2 a_0} \left(\frac{\lambda}{\sin \frac{\theta}{2}}\right)^2 Z \quad 3.4$$

where  $m_0$  is the mass of an electron,  $c$  is the speed of light in a vacuum,  $a_0$  is the Bohr radius, and the other terms are as described above.

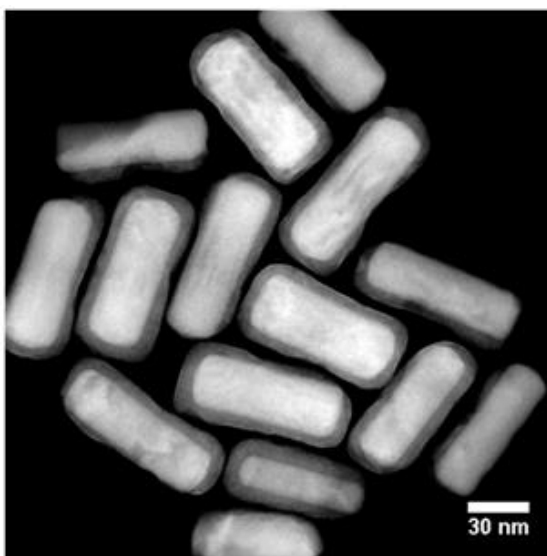
Equation 3.3 and  $|f(\theta)|^2$  from equation 3.4 derive from different approaches, but give comparable expressions where, if screening effects are ignored, scattering intensity is proportional to the square of the atomic number,  $Z$ . However, in real experimental conditions the effect of electron screening cannot be ignored. In addition, in an electron microscope the imaging conditions, and in particular the collection angle of the HAADF detector, will also impact on the numbers of scattered electrons that are detected. Thus, HAADF image intensity is taken as proportional to  $Z^\alpha$ , where the maximum value  $\alpha$  can take is 2, consistent with the detection of all unscreened Rutherford scattered electrons.

The HAADF detector collection angle can be altered by selecting different pre-set camera lengths. In an imaging system camera length is the effective distance between the object and the image plane.<sup>1</sup> In STEM the physical distance between the specimen and the HAADF detector always remains constant, so camera length is an effective distance that is determined by post-specimen beam geometry. Changing STEM camera length alters the magnification of the post-specimen lenses to direct different portions of the more widely scattered parts of the electron beam into the HAADF detector. Selecting a camera length requires balancing image intensity against the desirability of collecting more widely scattered electrons. A smaller inner collection angle will allow the detection of more electrons, thus giving greater image intensity, however, if it is too small it will also allow coherently scattered electrons to contribute to the HAADF image, giving the potential for factors other than atomic number or sample thickness to affect image contrast. For example, channelling is a diffraction effect that occurs when collection angles are narrow enough to include electrons that have interacted as Bloch waves with the crystal lattice. It occurs when the sample is oriented such that beam electrons are preferentially scattered down atomic columns at the Bragg angle, resulting in enhanced image intensity

corresponding to constructive interference caused by the periodicity of the crystal lattice.<sup>1</sup> The impact of channelling can be avoided by tilting the sample out of orientation or by using a HAADF inner collection angle that is large enough to exclude coherently scattered electrons. In this study the majority of images were taken using the pre-set camera length of 10 cm; this camera length gives an inner HAADF collection angle of 62 mrad and an outer collection angle of 164 mrad. When compared to the suggested criteria of three times beam convergence semi-angle,<sup>15</sup> with a convergence semi-angle of 14 mrad, this gives a limit of 42 mrad on the instrument used in this study, or a minimum inner collection angle of 50 mrad,<sup>1</sup> these parameters are considered sufficient to ensure incoherent imaging. Where relevant the HAADF3 camera length was also used to verify Z-contrast, which has a larger collection angle, with an inner collection angle of 92 mrad and an outer collection angle of 228 mrad.

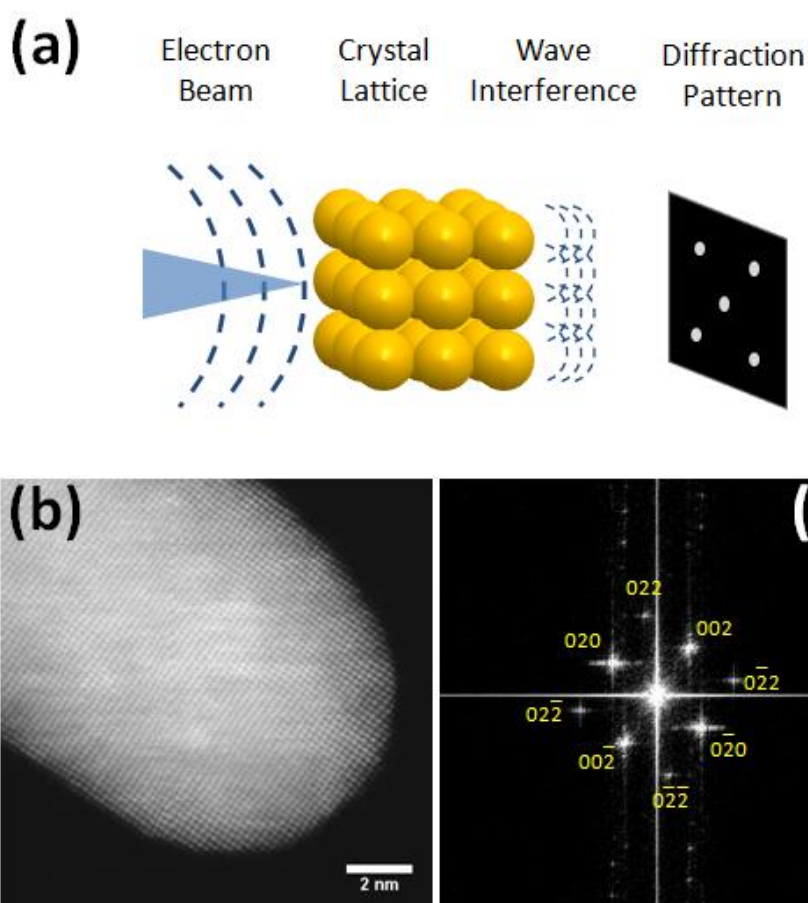
The proportionality of image intensity to  $Z^\alpha$  means, for sufficiently larger collection angles, and where the sample is of uniform thickness, image contrast variation is directly related to sample elemental variation. An experiment conducted on the instrument used in this study, using the 10 cm camera length to image size selected Au and Pd clusters, gave a power exponent factor of 1.5. This was based on a measured Au:Pd image intensity ratio for clusters of the same size of 2.3.<sup>16,17</sup> The ability to give elemental image contrast to atomic resolution is particularly useful in the characterisation of bimetallic nanoparticles comprised of elements of sufficiently different atomic numbers. Figure 3.9 shows a typical HAADF image of segregated AuPd nanorods,<sup>18</sup> demonstrating a clear difference in image intensity between the Au-core ( $Z = 79$ ) and the Pd-shell ( $Z = 46$ ) consistent with this principle.

The contrasting nature of STEM-HAADF and BF imaging can be used to maximise the imaging information gained from a sample by using the two detectors simultaneously. This allows the simplicity of HAADF interpretation, with its dependence primarily on thickness and Z number, to aid interpretation of more complex BF images, whilst the finer structural detail available in BF images can complement the superior atomic resolution of HAADF images. Simultaneous STEM-HAADF and BF imaging is a technique that has been used extensively in this thesis.



**Figure 3.9: Example of Z-contrast.** STEM-HAADF image showing Z-contrast between the segregated Au-core and Pd-shells, taken using 10 cm camera length, giving an inner collection angle of 62 mrad and an outer collection angle of 164 mrad. From reference 18.

Further information about the crystal structure of a sample can be obtained from STEM images by taking a fast fourier transform (fft) of the image. Taking an fft converts the image from real space into frequency space to give the approximate equivalent of an electron diffraction pattern. These patterns are formed by constructive interference caused by the periodicity of an appropriately oriented crystal lattice acting as a three dimensional diffraction grating for the spherical wave front of the electron beam. Figure 3.10 shows a schematic representation of electron diffraction, together with a STEM-HAADF image of an Au nanorod and its indexed whole image fft.



**Figure 3.10: Schematic representation and an example of electron diffraction.** (a) Schematic representation of electron diffraction. (b) STEM-HAADF image and (c) associated fft from an Au nanorod in  $\{100\}$  orientation.

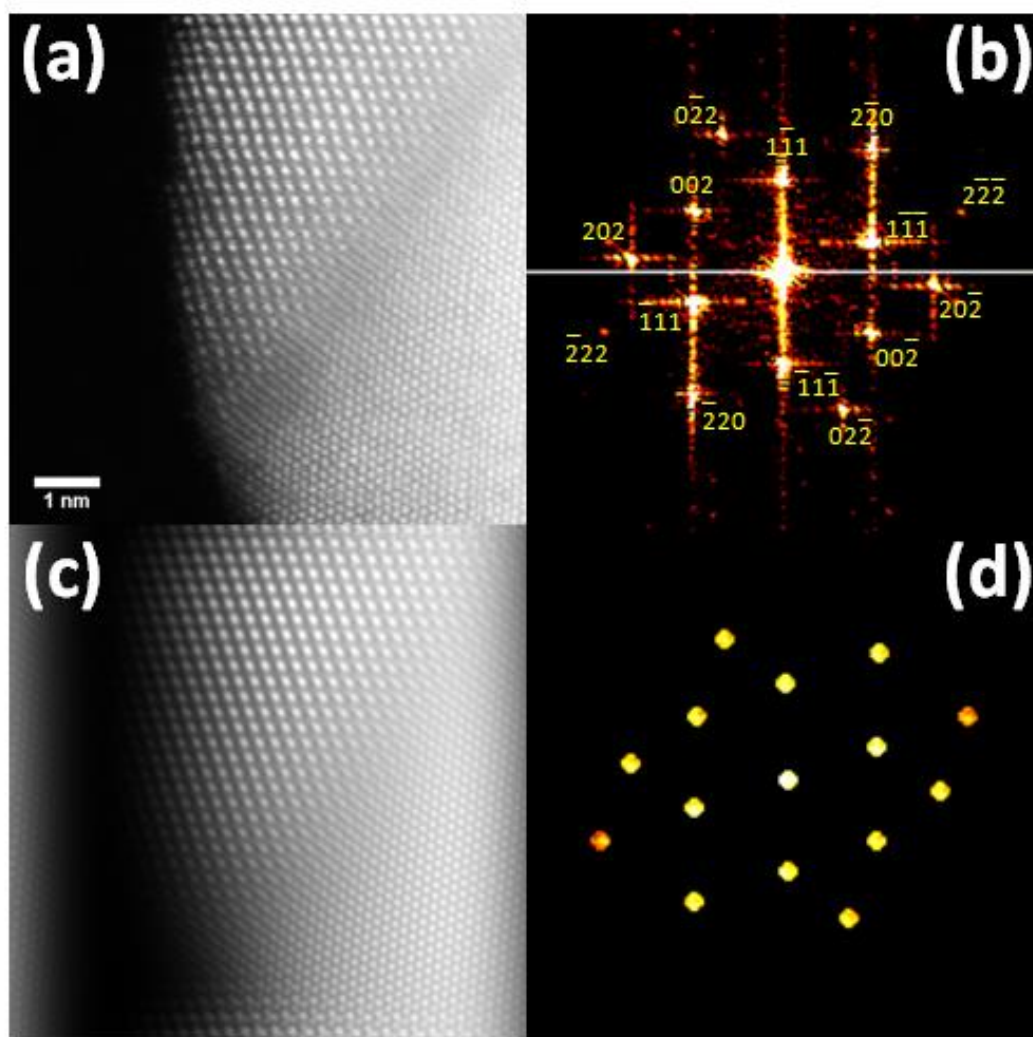


The pattern of an fft is determined by crystal structure and its orientation relative to the electron beam, whilst the distance of the diffraction spots from the centre of the fft is inversely related to the lattice dimensions. The presence of a clear pattern in the fft of an image is an indication of an ordered crystal structure, and its analysis can be a powerful tool in structural characterisation, and forms part of the results presented in Chapter 7 of this thesis.

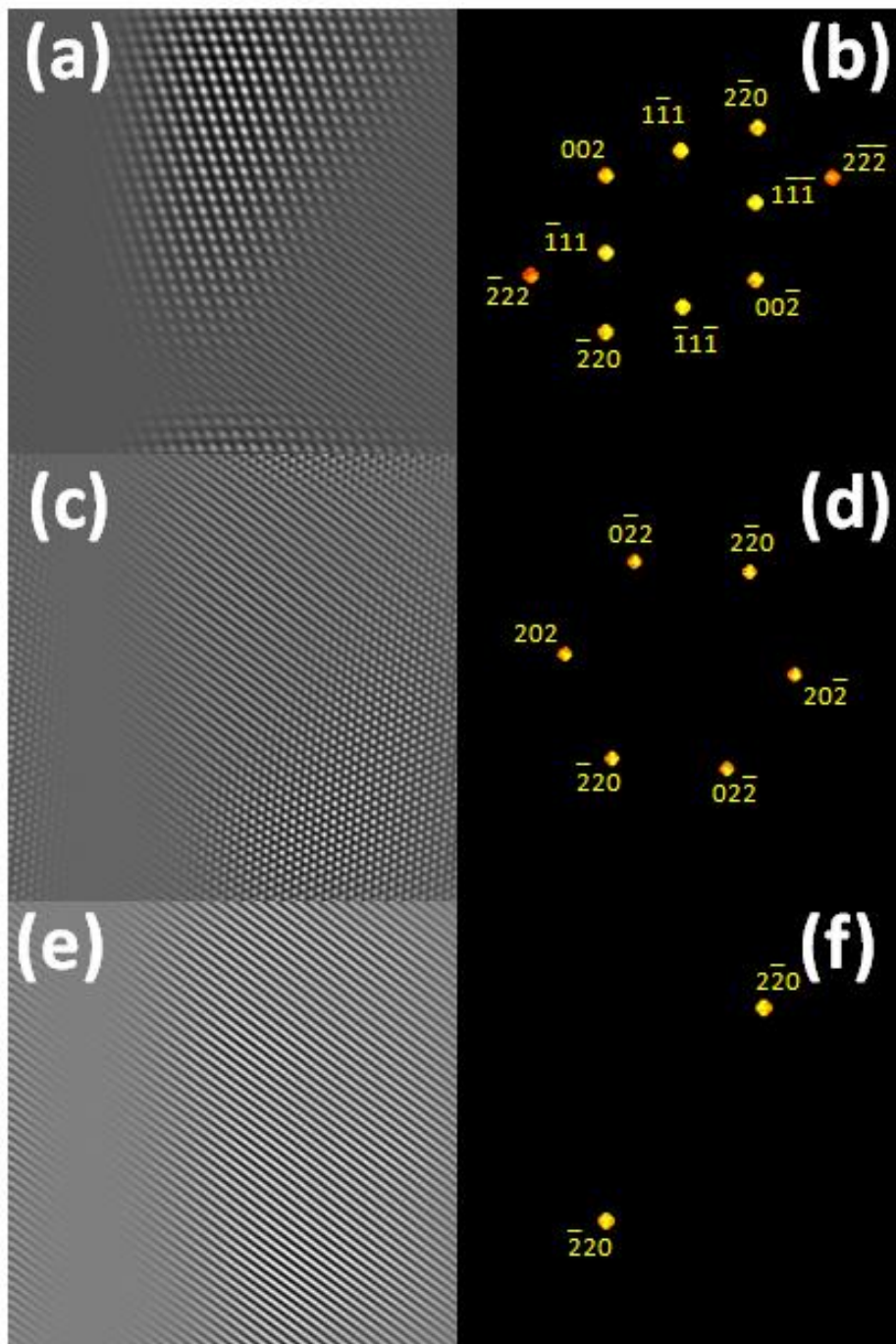
Masks can be used to extract selected parts of the fft. Taking an inverse of the masked fft converts the selected diffraction spots back from frequency space to real space, reproducing the parts of the original image that contributed to their formation. By using a mask that selects all the spots in the fft this technique can be used to filter background noise from an image; an example of this shown in Figure 3.11. Figure 3.11(a) shows a STEM-HAADF image of the end of an Au nanorod and Figure 3.11(b) shows the fft of the image. Although resolution of the original image is good, electronic noise is apparent in its fft in the blurring of spots and the presence of speckling between spots. Figure 3.11(c) shows a filtered image produced using a mask selecting all of the principle diffraction spots from the fft (shown in Figure 3.11(d)). Comparison of Figure 3.11(a) with Figure 3.11(c) shows how the mask removes background noise from the image. This process does not increase the level of detail present in the image but can make it easier to identify structure and measure crystal lattice spacing.

In comparison to Figure 3.11(c), which was filtered using a mask that selected all the spots in the fft, Figure 3.12 shows a series of filtered images that have been formed from the same image shown in Figure 3.11(a), but using masks selecting only parts of the whole image fft. The filtered image of Figure 3.12(a), formed using the mask given in Figure 3.12(b), indicate that the top part of the nanorod is in  $\{110\}$  orientation, whilst the

filtered image and associated mask of Figure 3.12(c) and (d) indicate the bottom part of the nanorod is in  $\{111\}$  orientation. This analysis shows that the nanorod has a structure formed from multiple crystals of Au, arranged in differing orientations to the electron beam.

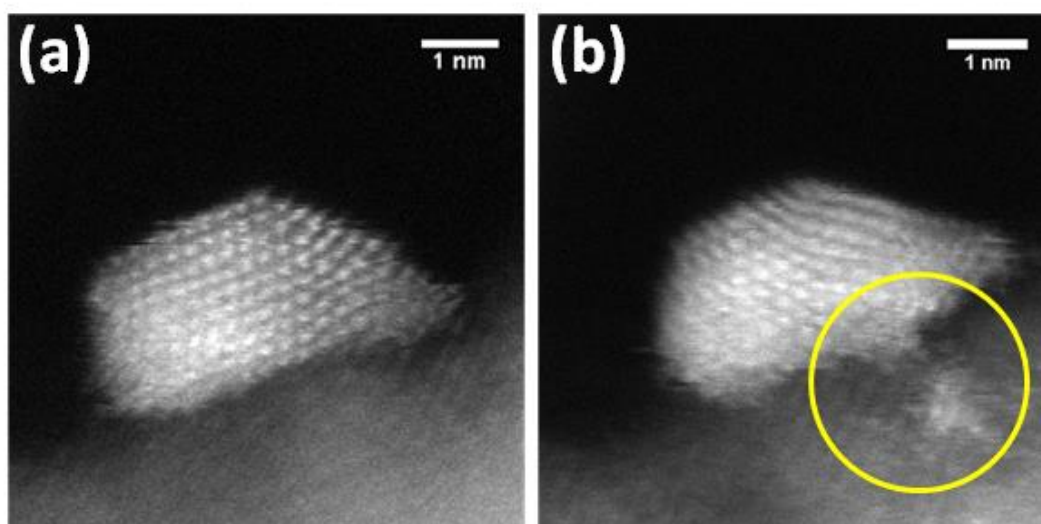


**Figure 3.11: Example of image noise reduction using fft mask.** (a) STEM-HAADF image of the end of an Au nanorod with (b) the fft of the image. (c) fft filtered version of (a) produced using the mask shown in (d).



**Figure 3.12:** Example of image filtering using fft masks. Filtered images and associated fft masks taken from the Au nanorod end shown in Figure 3.10, respectively (a) and (b) from the top section of the nanorod, (c) and (d) from the bottom section of the nanorods, and (e) and (f) showing the fft spots that are common to both parts of the nanorod.

As the beam comprises fast electrons its interaction with nanoscale samples can be extremely disruptive, causing samples to evolve under the beam. An example of this is shown in Figure 3.13 where interaction with the beam causes the detachment of atoms from the cluster between two successive images. The intense nature of the ac-STEM probe is a particular issue when imaging small clusters, such as the one shown in Figure 3.13, where beam-sample interactions can potentially cause significant localised heating and momentum transfer.



**Figure 3.13:** An example of beam damage to an Au cluster. STEM-HAADF image showing an Au cluster on TiO<sub>2</sub> support (a) before and (b) after the knock off of a small cluster by beam interaction (circled), reproduced from reference 19.

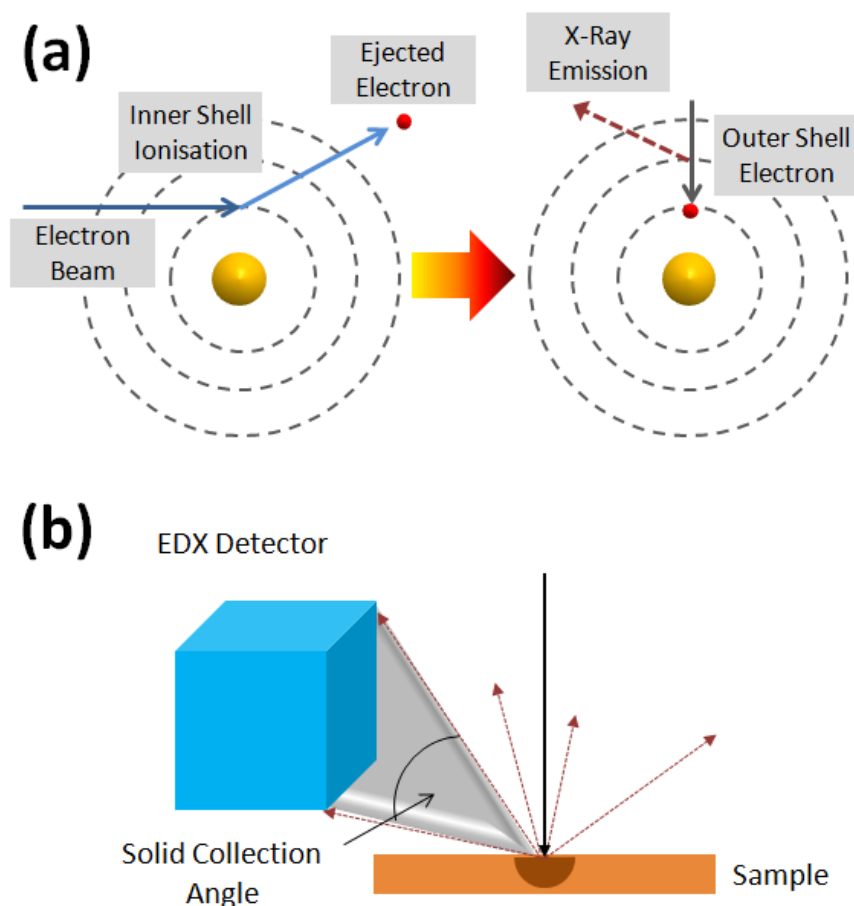
The exact nature of interaction between the beam and the sample cannot be fully determined, as it derives from a complex range of factors ranging from single electron events to collective excitations caused by the influence of the electric field generated by the beam. Although the impact is likely to be largest for small clusters, the influence of the

beam must always be considered when imaging any sample in ac-STEM. We consider this further, in the context of the evolution of AuAg nanoparticles, when presenting results in Chapter 7 of this thesis.

A further significant issue that affects imaging in ac-STEM is contamination. Hydrocarbon contamination is present on most samples, as it can only be completely avoided by maintaining samples in good vacuum at all times between preparation and imaging, which is not practical in most circumstances. It presents a problem in any electron microscope as the negative charge of the electron beam acts to attract the positively charged ends of any hydrocarbon molecules present, resulting in degradation of imaged resolution. However, it is a particular problem in ac-STEM due to the intense nature of the electron probe. It is also a particular problem for chemically synthesised nanoparticle samples, because there are often residues from the synthesis process present in the sample solution that cannot easily be removed without altering the sample. In these circumstances the technique of beam shower can be used, which entails flooding the desired region of the sample with a broad, weak beam for a period of time. This effectively pins the hydrocarbon molecules to the substrate for the selected region, allowing imaging free of mobile hydrocarbon contamination for a limited period until the hydrocarbon molecules become active again. However, as described in the preceding paragraph, beam electrons will interact with the sample even when the beam is relatively weak, so care must always be taken to monitor the potential impact of a beam shower, where possible by acquiring pre- and post-beam shower images for comparison. It was necessary to beam shower a number of the samples used in this study and all necessary precautions were taken to ensure this did not cause material alteration to the samples.

### 3.4. Energy Dispersive X-ray Spectroscopy

STEM-EDX is a form of spectroscopy that utilises the detection of X-ray emissions that occur when beam electrons interact with the sample ejecting an inner shell electron (shown schematically in Figure 3.14(a)). As the ejected electron is replaced by an electron from an outer shell and a characteristic X-ray emission may occur as a means to allow the outer shell electron to lose excess energy. These X-ray emissions are entirely elementally specific, so EDX is an effective technique for the elemental characterisation of a sample.



**Figure 3.14:** Schematic representations of stimulated X-ray emission and the EDX detector. Simple schematic representations of (a) electron beam stimulated X-ray emission, and (b) the EDX detector, where the darker hemisphere in the sample represents the interaction volume. Not drawn to scale.

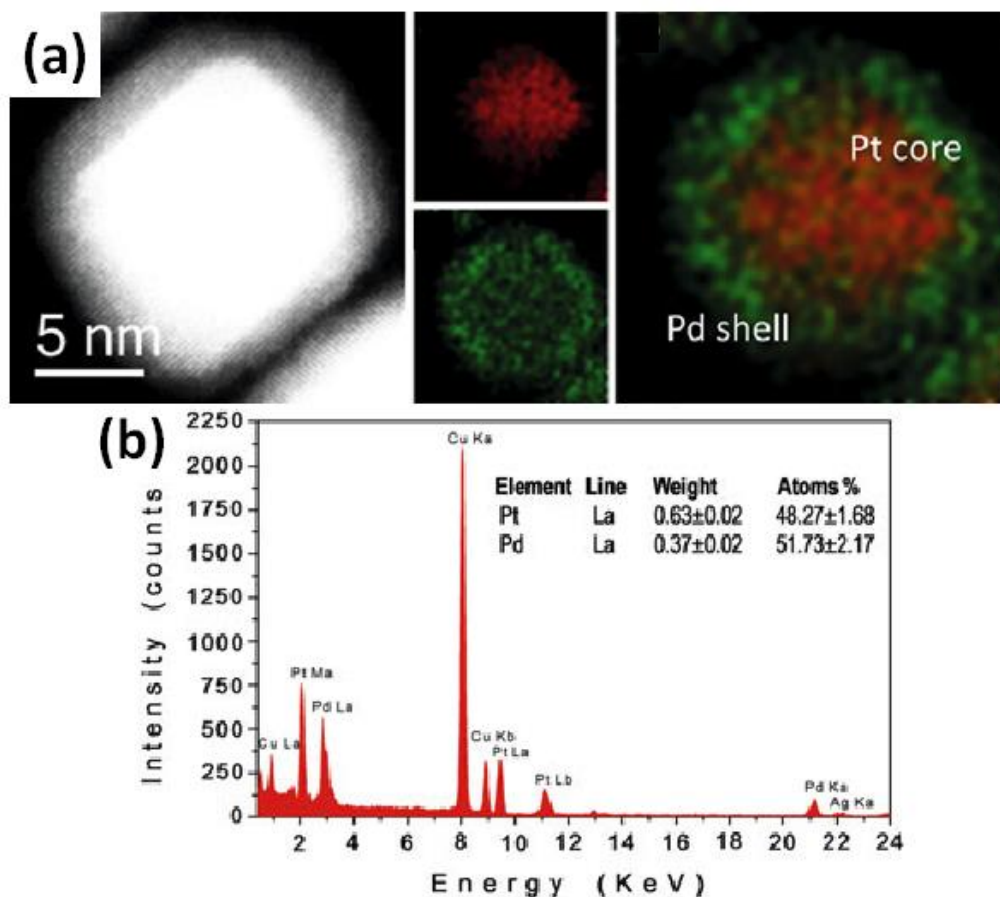
The EDX detector is usually positioned in the microscope column above the sample, as indicated in Figure 3.1 and illustrated schematically in Figure 3.14(b). The instrument used in this study is fitted with a Bruker XFlash 4030 detector. The detector is mechanically inserted only when spectra are to be taken. It has a 30 mm<sup>2</sup> detector area and a solid collection angle of 0.16 srad.

In silicon drift X-ray detectors, such as the one used in this study, X-ray emission is recorded by measuring the interband response of silicon caused by X-ray interactions. A voltage is applied across the detector to collect electrons that are generated by this interaction. The pulses of electrons generated by each X-ray interaction form the counts recorded by the detector.<sup>1</sup>

X-rays are generated isotropically by the sample. As illustrated in Figure 3.14(b), the EDX detector collects a proportion of the X-ray emissions corresponding to its solid collection angle. The solid angle of collection is determined by the active area of the detector and the specimen-detector geometry, and can be increased by tilting the sample towards the detector. The signal recorded is related to the position of the probe as it scans the sample. EDX mapping to atomic resolution has been demonstrated,<sup>20</sup> however, to date this has only been reported for bulk samples, and has required associated simulation to support interpretation. The latest generation of microscopes now use multiple X-ray detectors to improve count rates;<sup>21</sup> however, this is yet to become routinely available, and the instrument used in this study employs only one detector.

Given a sufficient number of X-ray counts, statistical methods can be used to accurately calculate the relative quantities of elements present in the sample from EDX spectra.<sup>22</sup> An example of EDX mapping in ac-STEM is shown in Figure 3.15, where it has

been used by Esparza *et al.* to identify the location of Pt and Pd in an PtPd bimetallic nanoparticle sample.<sup>23</sup>



**Figure 3.15: An example of STEM-EDX characterisation of bimetallic nanoparticles.** (a) Example of EDX mapping in ac-STEM of a PdPt nanoparticle showing STEM-HAADF image, the Pt signal (red) the Pd signal (green), and an overlay of both Pt and Pd, with (b) and example EDX spectrum and associated quantitative analysis. Reproduced from reference 23.

The technique of elemental mapping is particularly useful for analysing bimetallic samples, and has been used extensively in this study to ascertain the spatial distribution of elements in our samples. However, the small size of single nanoparticles, and the nature of the EDX detector used in this study, means the count rates achieved were low, preventing



the generation of a statistically significant number of counts. This means that, although EDX measurements presented in Chapters 5 and 7 of this thesis were sufficient to confirm the presence of elements qualitatively, and to determine their spatial location, they were not sufficient for accurate quantitative analysis.

### **3.5 Conclusions**

The above sections describe the capability of ac-STEM imaging and EDX spectroscopy in characterising the structure of bimetallic nanoparticles. STEM-HAADF imaging has the demonstrated potential to provide both elemental and structural information to atomic resolution. In addition, simultaneously acquired STEM-BF images can give additional structural detail, such as revealing the presence of lattice strain. Within the same instrument STEM-EDX can also give qualitative elemental characterisation to sub-nanometre spatial resolution. Thus these techniques, when used in combination, provide a powerful means to examine the structure of bimetallic nanoparticles at the atomic scale, and underpin the characterisation work presented in this thesis.

## List of References

105. Williams, D.B.; Carter, C.B., *Transmission Electron Microscopy*, Springer: New York, 2009.
106. Crewe, A.V.; Wall, J.; Langmore, J., Visibility of Single Atoms, *Science*, **1970**, *168*, 1338-1340
107. Spence, J.C.H., *High Resolution Electron Microscopy*, Oxford University Press: New York, 2003.
108. Tanaka, N., Present Status and Future Prospects of Spherical Aberration Corrected TEM/STEM for Study of Nanomaterials, *Sci. Technol. Adv. Mater.* **2008**, *9*, 014111
109. CESCOR, Corrected Electron Optical Systems GmbH, Germany
110. Digital Micrograph, Version 1.83.842, Gatan Inc. USA
111. Lentzen, M., Progress in Aberration-Corrected High-Resolution Transmission Electron Microscopy Using Hardware Aberration Correction, *Microsc. Microanal.*, **2006**, *12*, 191-205
112. Uno, S.; Honda, K.; Nakamura, N.; Matsuya, M.; Zach, J., Aberration Correction and Its Automatic Control in Scanning Electron Microscopes, *Optik*, **2005**, *116*, 438-448
113. Scherzer, O., Uber einige Fehler von Elektronenlinsen, *Z. Phys.*, **1936**, *101*, 593-603
114. Zach, J.; Haider, M., Aberration Correction in a Low Voltage SEM by a Multipole Corrector, *Nucl. Instrum. Methods Phys. Res. A*, **1995**, *363*, 316-325
115. JEOL 2100F Instruction Manual, JEOL: Tokyo, Japan, 2007.
116. Muller, H.; Uhlemann, S.; Hartel, P.; Haider, M., Advancing the Hexapole Cs-Corrector for the Scanning Transmission Microscope, *Microsc. Microanal.*, **2006**, *12*, 442-455
117. JEOL Standard Acceptance Test Report for the JEM-2100F at the University of Birmingham, dated 3 June 2009
118. Haider, M.; Uhlemann, S.; Zach, J., Upper Limits for the Residual Aberrations of a High-Resolution Aberration-Corrected STEM, *Ultramicroscopy*, **2000**, *81*, 163-175
119. Hartel, P.; Rose, H.; Dinges, C., Conditions and Reasons for Incoherent Imaging in STEM, *Ultramicroscopy*, **1996**, *63*, 93-114
120. Wang, Z.W.; Li, Z.Y.; Park, S.J.; Abdela, A.; Tang, D.; Palmer, R.E., Quantitative Z-Contrast Imaging in the Scanning Transmission Electron Microscope with Size-Selected Clusters, *Phys. Rev. B* **2011**, *84*, 073408

121. Wang, Z.W.; Palmer, R.E., Intensity Callibration and Atomic Imaging of Size-Selected Au and Pd Clusters in Aberration-Corrected HAADF-STEM, *J. Phys. Conf. Ser.* **2012**, *371*, 012010
122. Chantry, R.L.; Siritwacharapiboon, W.; Horswell, S.L.; Khanal, B.P.; Zubarev, E.R.; Atanasov, I.; Johnston, R.L.; Li, Z.Y., An Atomistic View of the Interfacial Structures of Au-Core Rh and Pd-Shell Nanorods, *Nanoscale*, **2013**, *5*, 7452-7457
123. Delannoy, L.; Chantry, R.L.; Casale, S.; Li, Z.Y.; Borenzstein, Y.; Louis, C., HRTEM and STEM-HAADF Characterisation of Au-TiO<sub>2</sub> and Au-Al<sub>2</sub>O<sub>3</sub> Catalysts for a Better Understanding of the Parameters Influencing Their Properties in CO Oxidation, *Chem. Phys. Phys. Chem.*, **2013**, *15*, 3473-3479
124. D'Alfonso, A.J.; Freitag, B.; Klenov, D.; Allen, L.J., Atomic-Resolution Chemical Mapping Using Energy-Dispersive X-Ray Spectroscopy, *Phys. Rev. B*, **2010**, *81*, 100101
125. von Harrach, H.S.; Dona, P.; Freitag, B.; Soltau, H.; Niculae, A.; Rohde, M., An Integrated Multiple Silicon Drift Detector System for Transmission Electron Microscopes, [www.fei.com/uploadedfiles/documents/content/multiple\\_silicon\\_drift\\_detector\\_system-2009.pdf](http://www.fei.com/uploadedfiles/documents/content/multiple_silicon_drift_detector_system-2009.pdf)
126. Herzing, A.A.; Watanabe, M.; Edwards, J.K.; Conte, M.; Tang, Z.R.; Hutchings, G.J.; Kiely, C.J., Energy Dispersive X-Ray Spectroscopy of Bimetallic Nanoparticles in an Aberration Corrected Scanning Transmission Electron Microscopy, *Faraday Discuss.* **2008**, *138*, 337-351
127. Esparza, R.; Garcia-Ruiz, A.F.; Velazquez Salazar J.J.; Perez, R.; Jose-Yacamán, M., Structural Characterization of Pt-Pd Core-Shell Nanoparticles by C<sub>s</sub>-Corrected STEM, *J. Nanopart. Res.*, **2013**, *15*, 1342

---

## **Chapter 4**

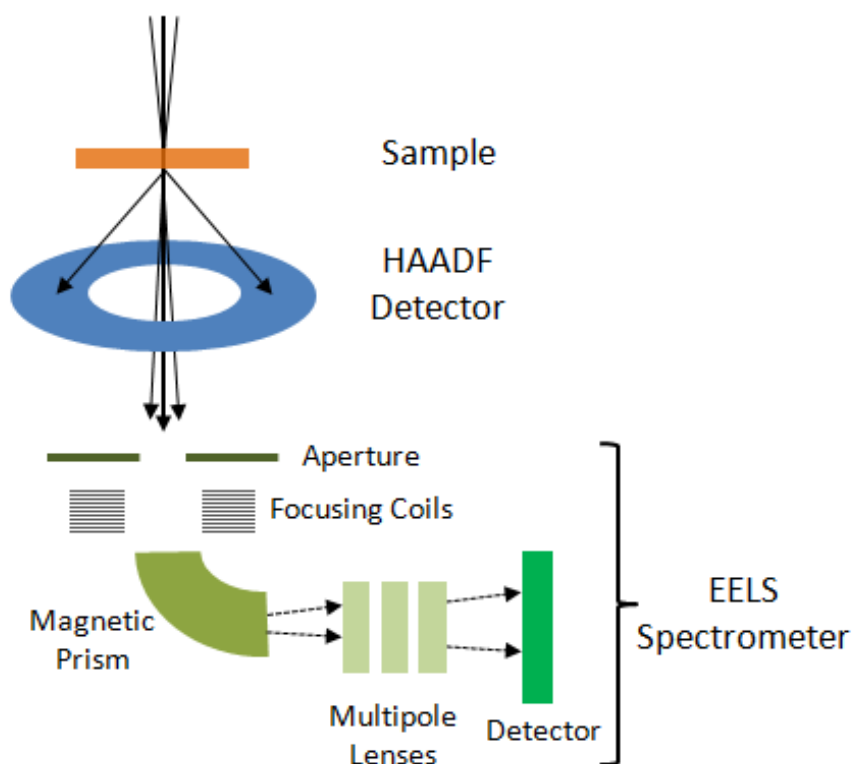
# **Experimental Methods: Characterisation of Electronic Properties**

The previous chapter described the techniques available in an aberration corrected scanning transmission electron microscope (ac-STEM) for the structural characterisation of bimetallic nanoparticles; in this chapter we described its capability in characterising the electronic properties of bimetallic nanoparticles, with particular focus on their localised surface plasmon resonance (LSPR).

Electron energy loss spectroscopy within ac-STEM (STEM-EELS) has the potential to provide the most complete possible information about the electronic structure and dielectric response of bimetallic nanoparticles of any currently available technique, and to the best possible spatial resolution.<sup>1,2</sup> In Section 4.1 of this chapter we describe the capabilities of STEM-EELS, and in Section 4.2 we describe supporting techniques that were used to aid interpretation of the STEM-EELS results presented in this thesis.

## 4.1. Electron Energy Loss Spectroscopy

STEM-EELS uses a detector positioned at the base of the microscope column (shown schematically in Figure 4.1) to measure the energy lost by electrons as they are transmitted through the sample.



*Figure 4.1: Schematic representation of the principle components of the EELS spectrometer.* Schematic diagram showing the location and principle components of the EELS spectrometer. Not drawn to scale.

Interactions causing energy loss include individual electron-electron interactions and collective beam-electron interactions, and are dependent on the electronic structure and properties of the sample; analysis of EELS spectra can in principle give a complete characterisation of the electronic response of a sample.<sup>3,4</sup> STEM-EELS can be used for

elemental characterisation, because different elements have different electronic responses, however, it is also capable of providing a wide range of other data, including details of atomic bonding, dielectric response, and sample thickness. This capability makes EELS an extremely powerful technique when used in combination with atomically resolved STEM imaging.

The STEM-EELS results presented in this thesis were collected using a JEOL2100F STEM fitted with a CEOS spherical aberration corrector and a Gatan Enfina EELS spectrometer.

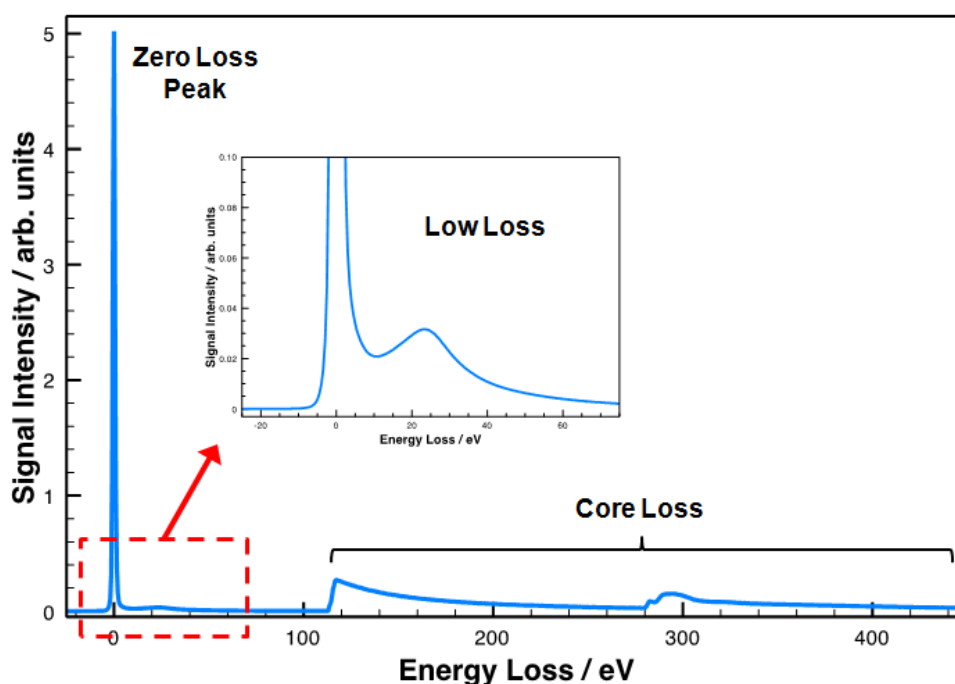
#### ***4.1.1 Overview***

Figure 4.1 gives a schematic representation of the principle components of the EELS spectrometer. The spectrometer comprises a magnetic prism that exploits the effect of chromatic aberration ( $C_c$ ) to spread the beam based on the energy of the electrons. Multipole lenses are used to magnify the dispersion of the beam, and a detector records the energy loss of each electron based on the spatial location of its detection. The size of the entrance aperture and the degree of dispersion can both be altered by the user to achieve a balance between signal-to-noise ratio and spatial resolution.

The magnetic prism is extremely sensitive to external magnetic fields. The use of an external magnetic field cancellation system helps compensate for this, however, the presence of rapidly changing external fields can be seriously detrimental to the quality of EELS results.

Figure 4.2 shows a typical EELS spectrum taken through a thin film of carbon. The zero loss peak comprises electrons that have lost little or no energy to the sample. The width of the zero loss peak, taken as its full width at half maximum (fwhm), is used to

define the energy resolution of the instrument. The primary contributor to the width of the zero loss peak is the thermal spread of the electrons as they leave the tip, which has a Gaussian distribution. However, all field emission gun (FEG) electron sources have a zero loss peak that is asymmetric in shape, caused by the quantum tunnelling probability associated with field emission.<sup>5</sup>



**Figure 4.2:** Typical EELS spectrum from 0 eV to 500 eV energy loss. A typical EELS spectrum for Carbon from -25 eV to 440 eV energy loss, showing the zero loss, low loss and core loss regions of the spectrum.

The narrower thermal spread of electrons emitted from cold FEG results in better energy resolution than the thermally assisted field emission of a Schottky FEG, because the thermal assistance of electron emission of a Schottky FEG increases the energy spread of beam electrons. Energy resolution can also be improved through the use of a monochromator, which filters the beam to exclude electrons that do not fit within a defined

energy range; this has the consequent effect of also reducing beam intensity. The instrument used in this study was not fitted with a monochromator. Energy resolution is a key factor influencing EELS plasmon mapping, where the signals can occur at extremely low energy losses, and is discussed further in this context below.

The zero loss peak is used to align the electron beam through the spectrometer and to focus it spatially and energetically. Focusing is accomplished by adjusting pre-spectrometer focusing coils, with the aim of producing a peak as narrow and intense as possible. Energy shift adjustments are also made to ensure the zero loss peak is located at zero energy loss. Spectra can also be calibrated post-acquisition using an appropriate, well defined feature in the spectrum, to accommodate small drift in energy that might have occur during data acquisition.

The core loss region of the EELS spectrum comprise energy losses caused by interaction between the beam electrons and the inner shell, or core, electrons in the sample, causing ionisation events. These interactions result in spectral features that are known as edges, such as the features apparent at above 100 eV energy loss in spectrum shown in Figure 4.2. The shape and intensity of these edges are determined by the elements present in the sample, and also by the electronic bond structure of the sample.

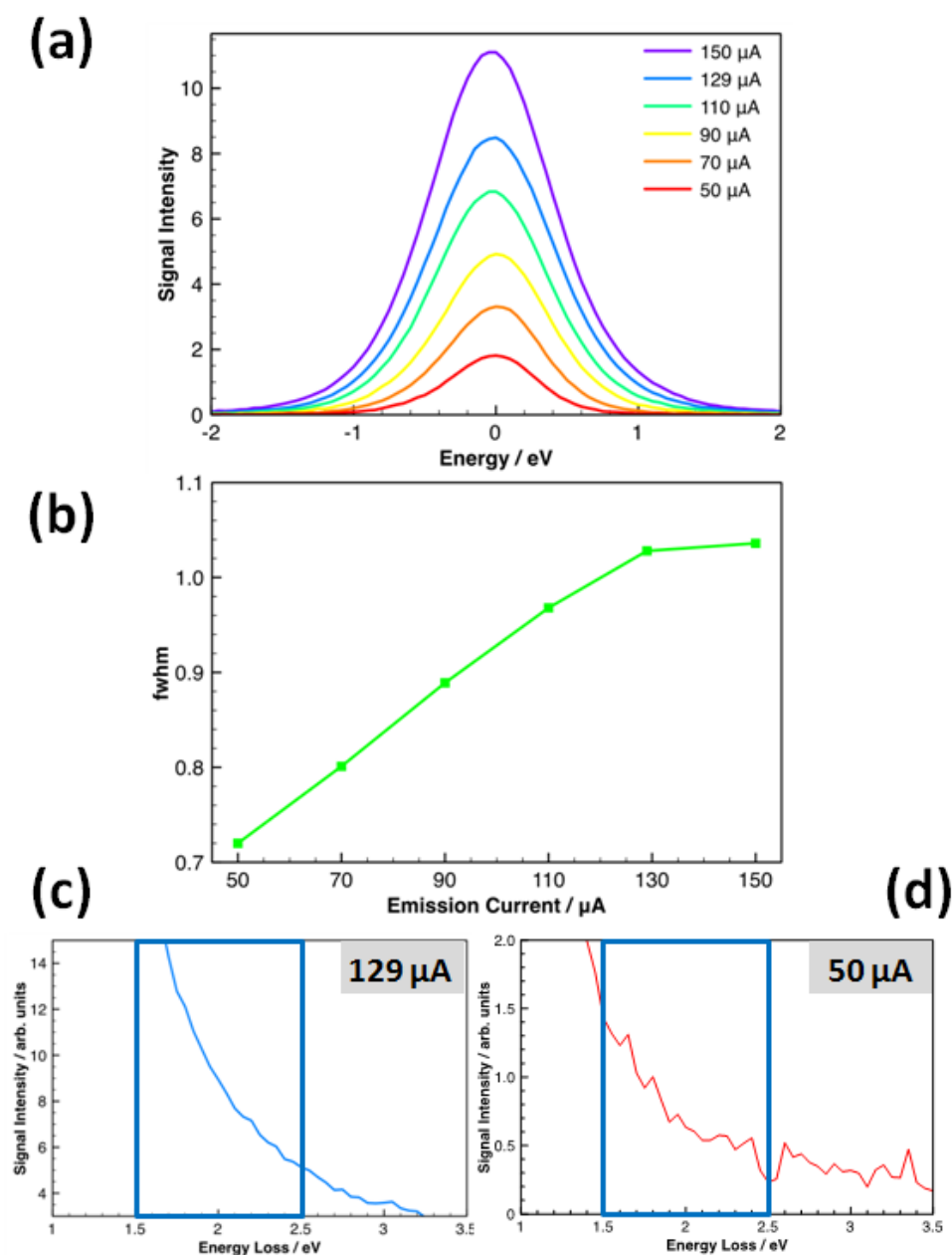
The elements for which core loss EELS can be used are limited by the dynamic range of the spectrometer; the spectrometer fitted to the instrument used in this study is most effective energy losses below 1000 eV; above this energy level the signal-to-noise ratio deteriorates making identification of core loss edges challenging. This limits its use for identifying the inner shell losses for heavier elements, and in particular meant that core loss EELS could not be used for elemental mapping of Au in this study; for Au elemental analysis we relied on energy dispersive X-ray spectroscopy (EDX).



The low loss region (shown in Figure 4.2 at energy loss below approximately 60 eV) comprises energy losses caused by interaction between the beam electrons and the more weakly bound valence, or outer shell, electrons. These interactions include collective beam-electron responses, such as bulk and surface plasmons, as well as electron-electron interactions, such as interband transitions. The response shown in the low loss region can be related to the frequency dependent dielectric function of the sample.<sup>3,6</sup> Low loss spectra are sensitive to a range of factors, including sample thickness, valence band structure, sample shape, the presence of dopant atoms, and may also include interactions between different forms of excitation, such as between interband transitions and plasmon responses, so can be more complex to interpret than core loss spectra.

The LSPR responses that are the focus of the results presented in Chapter 6 of this thesis occur in the extremely low loss region, from 0 eV to approximately 10 eV energy loss. Acquiring signals in this region of the spectrum is challenging because they occur in the tail of the zero loss peak, and therefore require the best possible energy resolution to minimise the impact of the zero loss tail on the results. The latest generation of ac-STEM instruments, fitted with cold field emission guns and monochromators, can achieve energy resolution of less than 0.1 eV.<sup>1</sup> In comparison, the energy resolution of the instrument used in this study, when operated at full current, is typically around 1 eV. For the purposes of making LSPR measurements energy resolution was improved by reducing the extraction voltage, thus reducing energy spread of the emitted electrons.

Figure 4.3(a) illustrates how the zero loss peak narrows as the emission current is reduced. Figure 4.3(b) shows a plot of fwhm against emission current for each of the zero loss peaks of Figure 4.3(a), demonstrating the improvement in energy resolution gained by lowering the emission current.



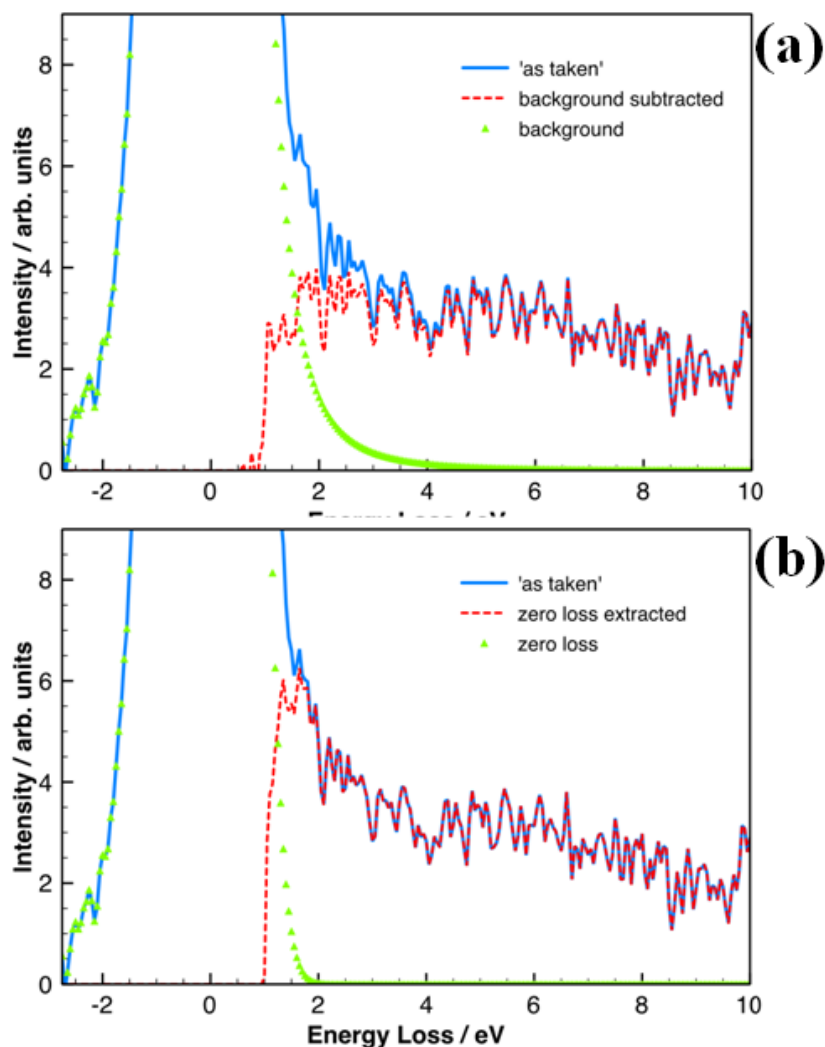
**Figure 4.3: The impact on energy resolution of lowering emission current.**

(a) Zero loss peaks taken at emission currents from 50  $\mu\text{A}$  to 150  $\mu\text{A}$ , with (b) their fwhm. (c) and (d) spectra taken at emission currents of 129  $\mu\text{A}$  and 50  $\mu\text{A}$  respectively showing the improved information available at energy loss between 1.5 eV and 2.5 eV with lower emission current (highlighted).

Lowering the extraction voltage until the emission current reached 40  $\mu\text{A}$ , the minimum emission current at which it was still possible to see the ronchigram sufficient to

be able to align the microscope, improved energy resolution to between 0.6 eV and 0.7 eV. Comparison of Figures 4.3(c) and (d), which were taken from the same sample with emission current of 129  $\mu\text{A}$  and 50  $\mu\text{A}$  respectively, show how features become apparent below 2.0 eV with lower emission current; however, they also show an associated deterioration in the signal-to-noise ratio. Energy resolution of between 0.6 eV and 0.7 eV was considered adequate to conduct the work of this study, as the principle features of interest in the work presented in Chapters 6 and 7 of this thesis occur between 1.5 eV and 9.5 eV energy loss.

The tail of the zero loss peak causes a falling background over the region of the spectrum shown in Figures 4.3(c) and (d). The impact of the zero loss tail can be reduced through data processing, for example, by extracting the zero loss peak itself, or by subtracting an appropriate background model fitted to the tail of the zero loss peak; Figure 4.4 shows the impact of these two possibilities on an experimental spectrum. There are a number of models that can be used for the zero loss peak or background subtraction, in Figure 4.4(a) a power law background model has been used, fitted over a window from 0.6 to 1.0 eV, and in Figure 4.4(b) the extracted zero loss is based on a double Gaussian model. Examination of Figure 4.4 shows that in both cases the spectra at energy losses above approximately 4 eV are unaffected by processing. In comparison, at the lowest energy losses, below 2 eV, the two models shown in Figure 4.4 impact significantly, and in differing ways, on the appearance of the presented spectrum. We chose background subtraction using power law fitting to present the results in this thesis, both point spectra and spectrum image maps, because this is the simplest model available, and thus gives results that are as close as possible to the raw experimental data, minimising the possibility of distorting the data.

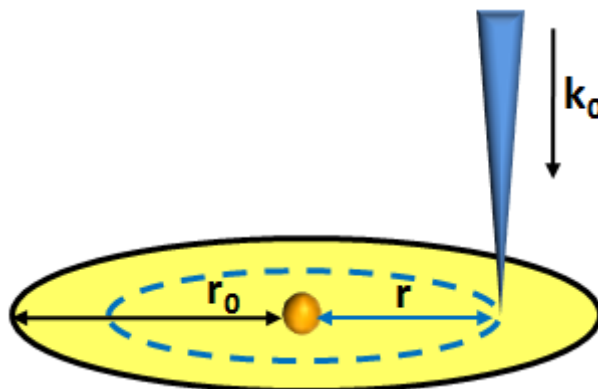


**Figure 4.4: The impact of background subtraction and zero loss extraction.** STEM-EELS experimental spectra from an AuPd nanorod showing the effect of (a) background subtraction using a power law model, and (b) zero loss extraction using double Gaussian fit.

The spatial resolution of STEM-EELS depends on the nature of the interaction being measured and the size of the probe. Inelastic scattering amplitude of a single, spherical scattering object, such as an atom, can be described by a point spread function (PSF) with an  $r^2$  dependency, as follows,<sup>3</sup>

$$PSF(r) \propto \left(1 + \frac{r^2}{r_0^2}\right)^{-1} \exp(-2k_0\theta_E r) \quad 4.1$$

where, as illustrated schematically in Figure 4.5,  $r$  is the radial distance from the scattering object,  $r_0$  is the interaction cut off radius,  $k_0$  is the wave number, and  $\theta_E$  is the characteristic scattering angle.



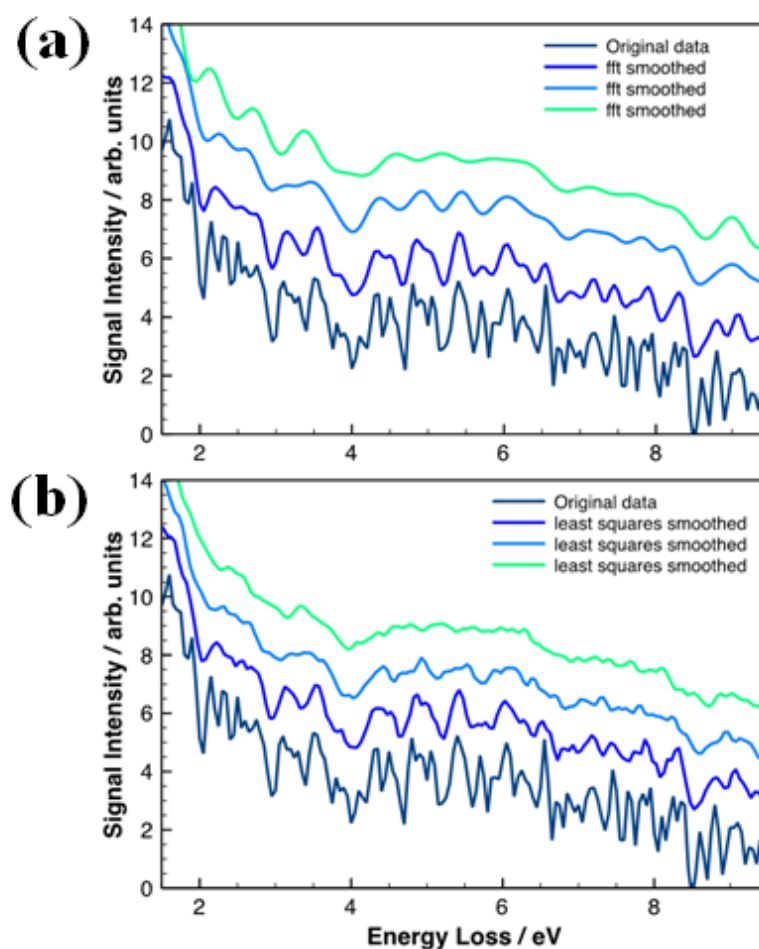
**Figure 4.5: Illustration of the delocalisation of inelastic scattering.**

Schematic diagram of inelastic scattering delocalisation in EELS, where  $k_0$  is the wave vector of the electron beam,  $r$  is the distance from the scattering object and  $r_0$  is the interaction cut off radius beyond which no scattering occurs. Not drawn to scale.

Equation 4.1 shows that inelastic scattering is delocalised beyond the edge of the scattering object, with inelastic scattering amplitude having an  $r^{-2}$  dependency, with exponential attenuation dependent on the characteristic scattering angle of the interaction. For low energy loss interactions, such as surface plasmons presented in Chapters 6 and 7 of this thesis, the characteristic scattering angle is small, giving a larger PSF, whereas higher energy core loss signals have a larger characteristic scattering angle and small PSF. For core loss EELS in aberration corrected STEM, probe size typically limits spatial resolution of the signal, allowing the potential for atomically resolved EELS signals.<sup>2,3</sup> Signal detection is more delocalised, and spatial resolution of the EELS signal consequently lower, for low loss signals.

The EELS signal potentially includes all electrons scattered to forward angles, so the resulting spectra can contain significant levels of background noise, particularly when collected using low emission currents. For low loss signals it is possible to improve the signal-to-noise ratio by selecting the appropriate camera length for the desired signal.<sup>7</sup> As described in Section 3.3 above, changing camera length alters the geometry of the post-specimen lenses, this in turn alters the collection angle of the spectrometer. For lower energy loss signals selecting a longer camera length, and thus a smaller collection angle into the spectrometer, can exclude noise from more widely scattered electrons. For high energy core loss signals, however, the larger acceptance angle of shorter camera lengths is desirable to maximise the number of electrons detected from these weaker signals. The LSPR work presented in Chapters 6 and 7 of this thesis were collected using a 12 cm camera length. The collection angle that this gives in the instrument used in this study is not known, however, of the standard camera length settings on the instrument this was found to give the best signal-to-noise ratio for LSPR signals in the 1.0 eV to 9.5 eV energy loss range.

Even with experimental conditions optimised the low beam intensity at low emission current results in a poor signal to noise ratio. The clarity of spectral features can be improved by processing the spectra to reduce background noise; however, this must be done with care to minimise the impact on the features present in the spectrum. Figure 4.6 shows how processing can improve the clarity of spectral features but also shows the consequence of applying successive degrees of smoothing on an experimental spectrum, using two different methods of processing, fast fourier transform (fft) and least squares fitting. In each plot the bottom (dark blue) line shows the raw experimental data.



**Figure 4.6:** *Illustration of the impact of different methods of noise reduction on STEM-EELS spectra.* STEM-EELS spectra showing the impact of (a) fft smoothing, and (b) least square smoothing on the data. In all cases the raw data is given as the dark blue line, with successive degrees of noise reduction shown in lighter colours.

In Figure 4.6(a) increasing degrees of fft smoothing removes the narrow features in the spectrum, making broader features more obvious, but also rounds the shape of the retained features, and if over used, causes small shifts in the position of features. The least squares method of Figure 6.4(b) reduces the magnitude of spectral features and merges some features, resulting in the removal of features from the spectrum if over used. So,

although processing can help clarify features in a spectrum, it must be used with care. When we processed STEM-EELS spectra presented in Chapter 6 of this thesis, the original unprocessed experimental data is shown for comparison. In addition, for the plasmon mapping that is the focus of the work presented in Chapter 6, the signal used to produce the maps is unprocessed other than for background subtraction.

#### ***4.1.2 Plasmon mapping using STEM-EELS spectrum imaging***

As described in Chapter 2 LSPR response derives from the collective excitation of free electrons in the sample under the influence of a time varying external electric field. In STEM-EELS the electron beam both excites and measures the LSPR response through field-electron interactions. The STEM electron beam can be approximated to a current carrying wire, which generates a radial electric field that excites the LSPR response.<sup>6</sup> The free electron oscillations occur in a plane normal to the surface, so to maximise LSPR excitation the plane of the incident time varying field should be normal to the sample surface; in EELS this occurs when the beam is immediately adjacent to the sample, in an aloof position.<sup>3</sup>

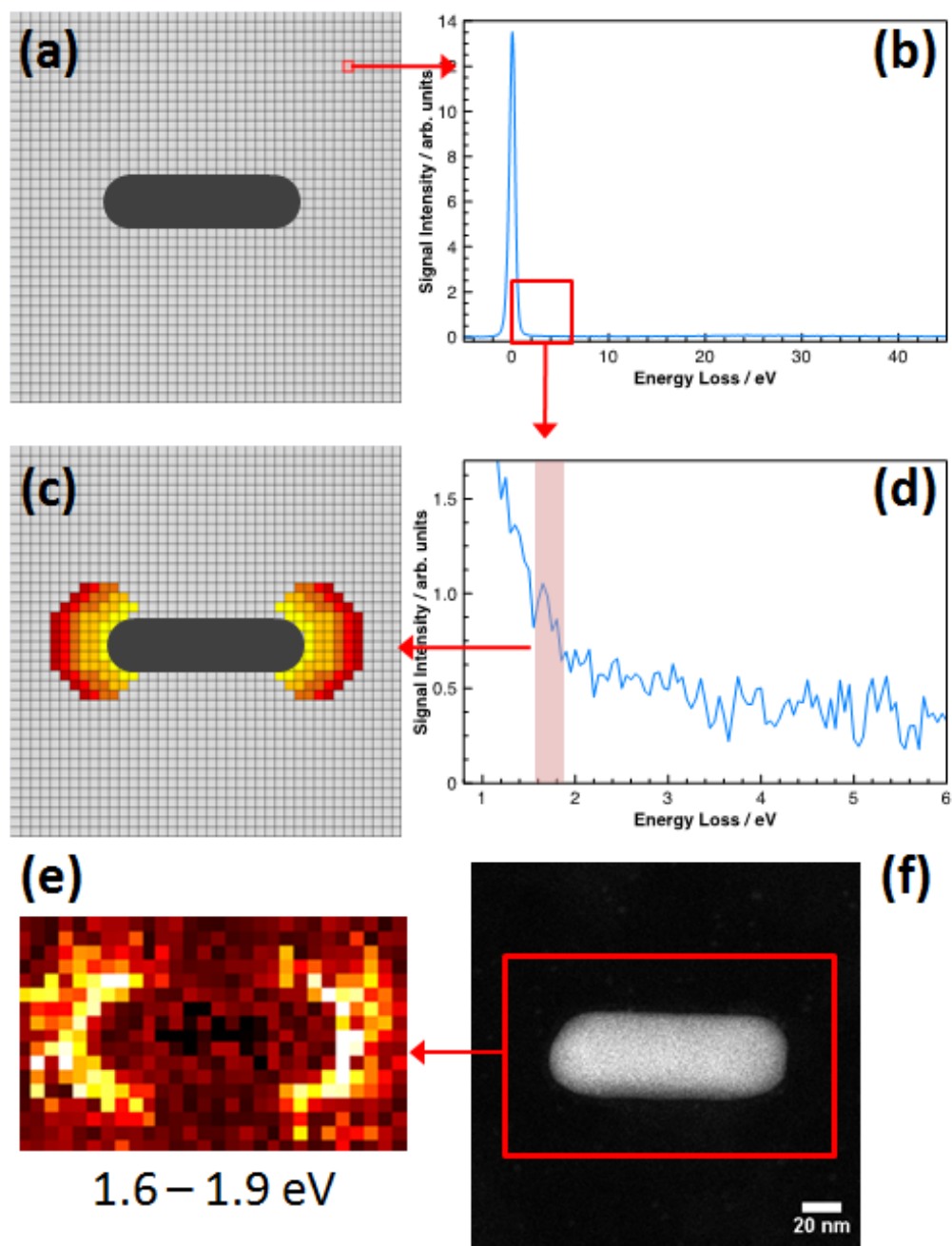
The acceleration of the free electrons as they oscillate generates induced electric fields that are spatially characteristic to the nature of the excitation. Individual beam electrons lose energy doing work as they pass through the induced field, and this energy loss is detected by the EELS spectrometer. In this way the spatial distribution of the induced electric fields can be mapped by taking a series of EELS spectra, across a region around a selected target, and recording spatial variations in signal intensity.<sup>8</sup> The Digital Micrograph software has a routine to facilitate this process, known as spectrum image mapping.<sup>9</sup>



In spectrum image mapping a region of the sample is selected and divided into pixels, and a separate spectrum is acquired for each pixel;<sup>10</sup> this process is illustrated schematically in Figure 4.7(a) and (b). The potential spatial resolution of a spectrum image in principle is the same as that for any EELS spectrum, however, in practice is limited by maximum time over which a map can be acquired, which in turn is determined by the cumulative effects of spatial drift and sample contamination as the map is collected. Each pixel has a minimum required dwell time to capture the desired signal, thus the pixel size for a map is determined by balancing the required dwell time against the size of the region to be mapped and the maximum available mapping time.

During the experimental work conducted in this study, by allowing the sample to stabilise as much as possible and using the automatic drift correction routine in Digital Micrograph,<sup>9</sup> the maximum time over which a spectrum image could be accurately acquired was approximately 30 to 40 minutes. Typically pixel sizes were of the order of a few nanometers square, much larger than the probe size, so sub-pixel mapping was used to acquire an average signal for the area covered by each pixel. The highly delocalised nature of the electric fields induced means that the relatively large pixel sizes used did not limit spatial resolution sufficiently to prevent mapping of the LSPR response.

Once the spectrum image map has been acquired, all of the spectra within the map must be aligned and calibrate and background subtracted; this was accomplished consistently for all spectra in a map using facilities available the Digital Micrograph software.<sup>9</sup> For LSPR mapping the zero loss peak forms part of the acquired spectra, providing an ideal reference for the alignment and calibration of the spectrum image maps.



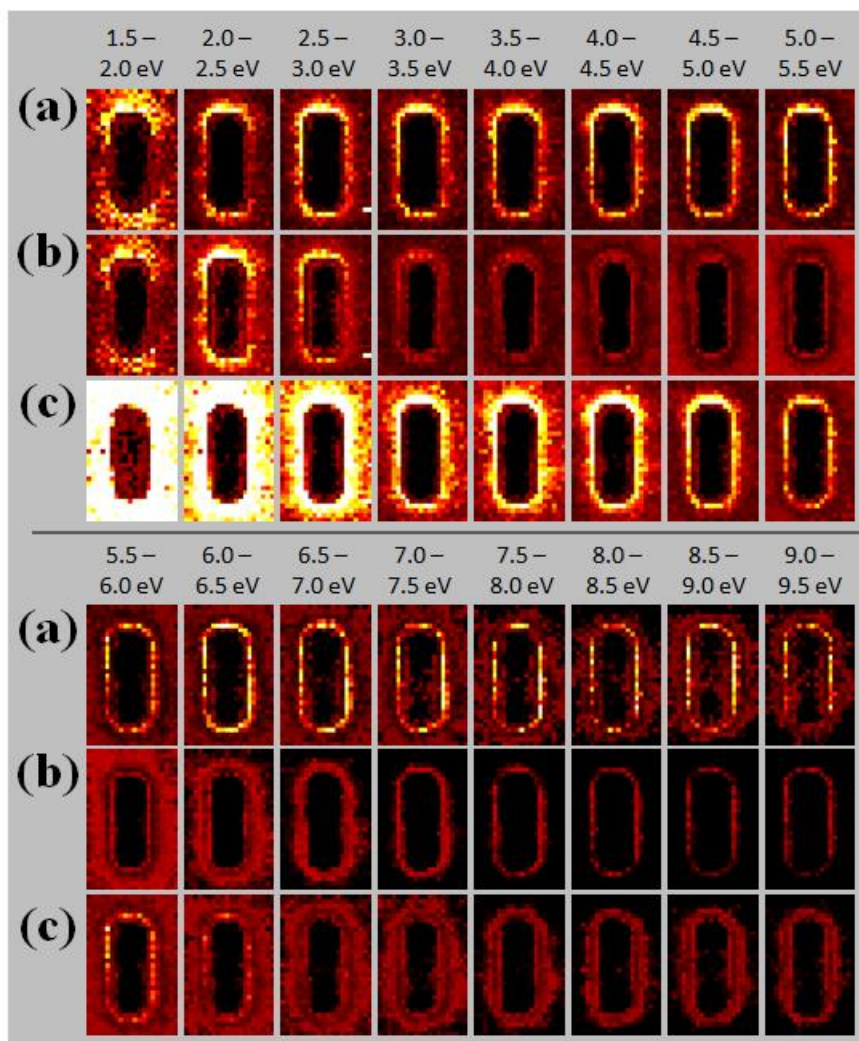
**Figure 4.7: Schematic illustration of STEM-EELS spectrum image mapping.** Schematic illustration of plasmon field mapping using EELS spectrum imaging. A selected area of the sample is divided into pixels (a), and spectra acquired for each pixel, (b). (c) Energy loss maps can then be formed showing the integrated signal intensity for a selected range of energy loss, (d) STEM-EELS spectrum image map of an Ag nanorod over the energy loss range 1.6 eV to 1.9 eV, and (e) corresponding STEM-HAADF image.

Once all the spectra in a spectrum image map have been aligned and background subtracted, an energy loss window of interest can be selected and the intensity of the integrated energy loss signal for each pixel mapped using Digital Micrograph.<sup>9</sup> This process is illustrated schematically in Figure 4.7(c) and (d). Figure 4.7(e) shows a STEM-EELS spectrum image map of the integrated signal intensity over the energy loss range from 1.6 eV to 1.9 eV acquired from around the Ag nanorod shown in the STEM-HAADF image of Figure 4.7(f).

In the spectrum image map shown in Figure 4.7 contrast has been allocated automatically within Digital Micrograph based on a linear contrast model applied between the maximum and minimum contrast in each map, after discarding the lowest and highest 0.1% of pixels sampled.<sup>9</sup> This method of setting contrast means that map contrast may not represent the same variation in the absolute value of integrated signal intensity between maps. Figure 4.8(a) shows a series of maps taken over arbitrary 0.5 eV energy loss ranges from 1.5 eV to 9.5 eV using automatically determined map contrast; these maps show measured signal throughout the selected energy loss range, including from the weaker signals at higher energy losses. In comparison, Figure 4.8(b) shows the impact of using fixed contrast ranges for all maps based on the maximum and minimum contrast values across the series and show no appreciable signal above around 3.0 eV, because the contrast range is too great. In contrast, Figure 4.8(c) uses a narrower fixed contrast range, based on the mean for the series, which is allowed to vary with the level of the background signal; this series reveals signals in the middle part of the energy range but saturates the maps at lower energy loss and still does not reveal signals at higher energy loss.

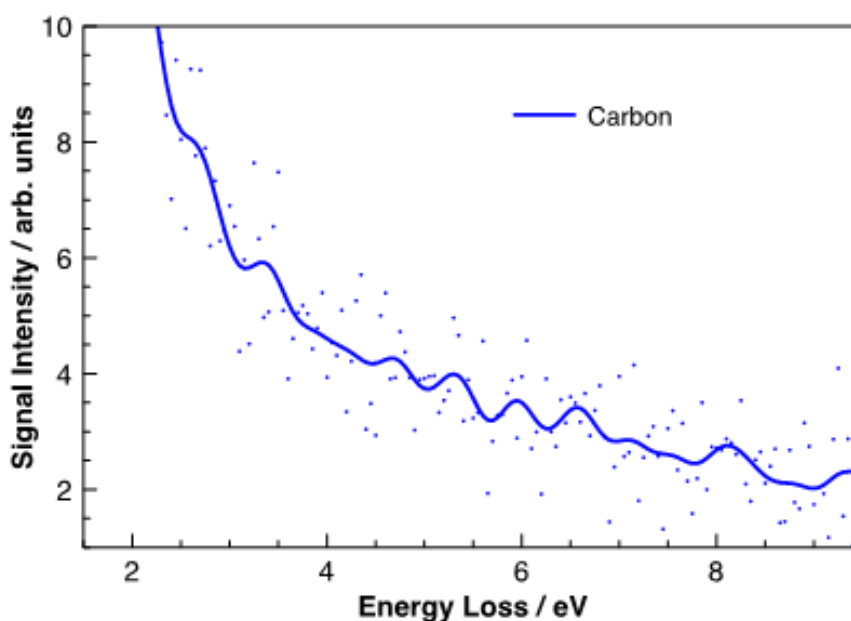
The results in Figure 4.8 illustrate the difficulty of allocating contrast over an extended energy loss range. As the work presented in this thesis is concerned with

measuring LSPR response over an extended energy range, unless otherwise stated, all maps presented in this thesis use Digital Micrograph automatically determined contrast limits.



**Figure 4.8:** A comparison of different methods of setting spectrum image map contrast. Series of STEM-EELS spectrum image maps of an Au nanorod taken over arbitrary 0.5 eV energy loss ranges using different contrast limits, (a) constant, fixed range for all maps using the maximum and minimum intensity across the energy range shown, (b) fixed contrast range that moves with the background signal, and (c) set on a map by map basis by Digital Micrograph.<sup>9</sup>

For all the results presented in this thesis the particles were mounted on amorphous carbon supports, so the signal measured in STEM-EELS includes contribution from both the particle and the amorphous carbon substrate. Figure 4.9 shows a typical spectrum acquired from the amorphous carbon substrate; the features apparent in this spectrum indicate that the contribution of carbon cannot be ignored when analysing the detail of individual spectra. However, as all samples used in this study were mounted on comparable substrates, the contribution from carbon is the same in all cases and so does not affect comparisons made between spectra acquired from different samples.



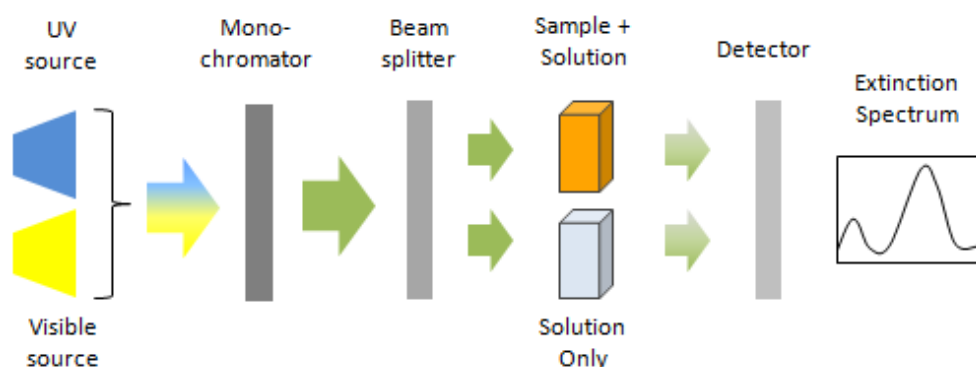
**Figure 4.9:** *STEM-EELS carbon spectrum from 1.5 eV to 9.5 eV.* Typical spectrum taken from the carbon substrate, with raw data as dots.

## 4.2. Supporting Techniques

The amount of detail potentially available in STEM-EELS spectra makes their unambiguous interpretation challenging. Thus it is necessary to use other techniques to support interpretation, for example, by making comparison to data acquired using alternative acquisition methods or to theoretical simulation models. In this study comparisons have been made to data collected using UV-visible spectroscopy (UV-vis) and to optical response simulation using the discrete dipole approximation (DDA); these techniques are described in the following sections.

### 4.2.1. UV-visible spectroscopy

UV-vis measures the collective response of nanoparticle samples to a broad spectrum of electromagnetic radiation, from UV through to visible wavelengths. The resulting extinction spectrum includes the combined effect of both scattering and absorption of electromagnetic radiation by all of the particles in the sample. Figure 4.10 shows a schematic illustration of a typical UV-vis experimental set up.



**Figure 4.10: Schematic representation of the principle components of a UV-vis spectrophotometer.** A schematic illustration showing the principle components of UV-vis experimental set up.

The wavelength range covered requires the use of two sources, one for the shorter wavelength UV radiation and another for visible radiation. A monochromator is used to select narrow sections of the available wavelength range, adjusted to suit the level of detail required; it scans through the wavelength range in incremental steps, measuring the response for each, to form the complete spectrum. Spectra are acquired for both the sample in solution and the solution with no sample for each wavelength step; an extinction spectrum is produced for the sample alone by subtracting these spectra.

Acquiring data using UV-vis is relatively quick and straightforward, so it is ideally suited for gaining a first impression of the optical response of samples prepared in solution. As it is an ensemble technique, giving collective results for all the particles in the sample, it has a much better signal-to-noise ratio than STEM-EELS. However, this means that the clarity of spectral features in UV-vis can be detrimentally impacted by variations in size, shape and composition of the particles in the sample, and forming a link between particle size, shape and composition and spectral features requires using additional techniques.

For relatively monodisperse samples the clarity of features in the UV-vis spectrum can be of use in identifying the likely location of plasmon response in STEM-EELS data, where the signal-to-noise ratio is much lower. However, the comparison of UV-vis spectra with those of EELS must be done with care as, although the resulting collective oscillation of free electrons that characterises the LSPR response may be comparable for modes common to both forms of excitation, some modes cannot be excited optically, and also strength of the excitation can vary depending on the method used.<sup>6,11,12</sup> The UV-vis results presented in this study were taken using a Camspec M550 double-beam spectrophotometer. The spectra were measured with the samples in solution, held in quartz cuvettes in the spectrophotometer.

### **4.2.2. Discrete Dipole Approximation simulation**

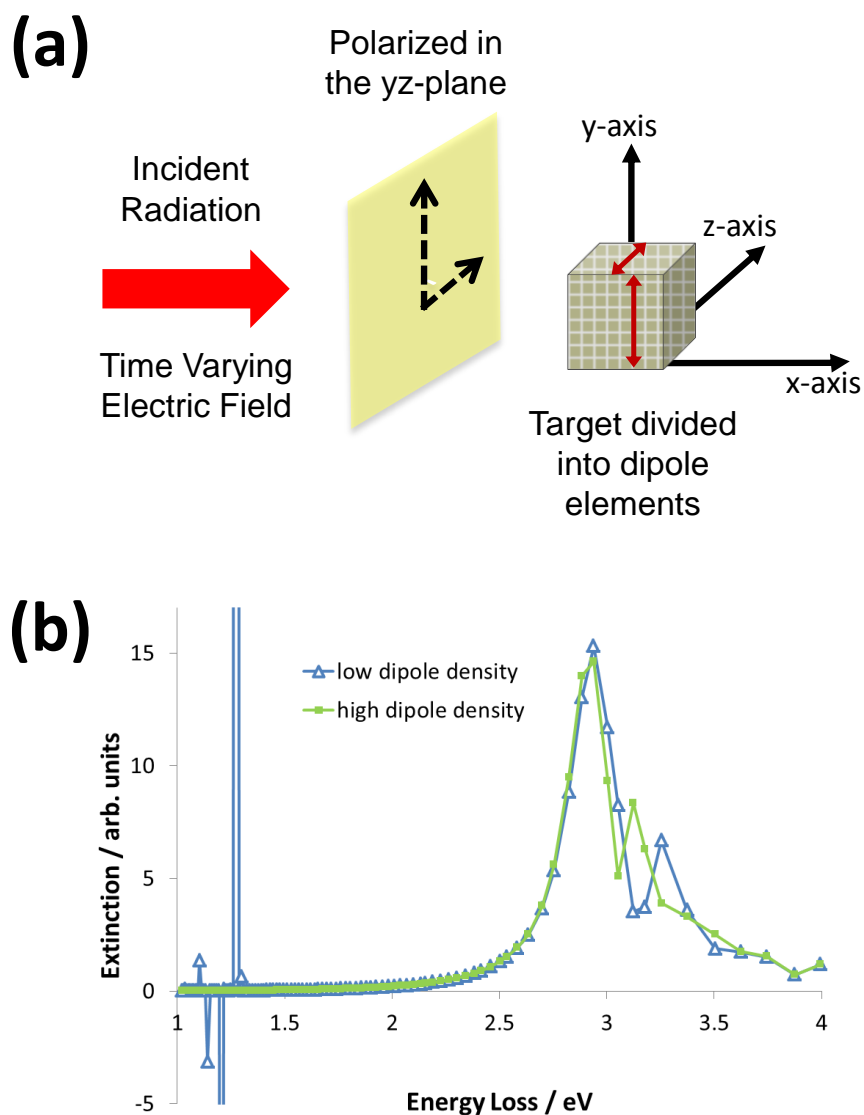
Computer simulation can be an effective technique for linking particle morphology, observed using STEM, to the dielectric response of the constituent metals. The discrete dipole approximation (DDA) has been utilised to this effect in this study, implemented through the DDSCAT and DDfield programs.<sup>13</sup>

DDA is a numerical method that calculates the response of a target under the influence of an external electric field by treating it as an array of dipoles. In the DDSCAT programme a user defined target is divided into cubic volume units, each of which is treated as a dipole. Each dipole has a frequency dependent dielectric function associated with it that is input to the program by the user. The program calculates the response of each dipole under the influence of both the incident electromagnetic radiation of specified wavelength and the fields generated by neighbouring dipoles, working iteratively until a self-consistent solution is reached.

Figure 4.11(a) gives a schematic representation of the DDSCAT simulation set up. In the program the incident radiation is always directed along the x-axis. The polarisation of incident radiation can be specified by the user to be either y-axis polarised, z-axis polarised, or a combination of both. The orientation of incident polarization relative to the simulation target can be altered by tilting the target within the simulation.

The dimensions of the dipole volume segments are defined by the user, and must be of sufficient density to obtain a physically representative simulation. If dipole density is too low then the resulting peak positions can be inaccurate and spurious features can appear in the resulting spectra, as illustrated in Figure 4.11(b), but using a greater number of dipoles increases computation time.



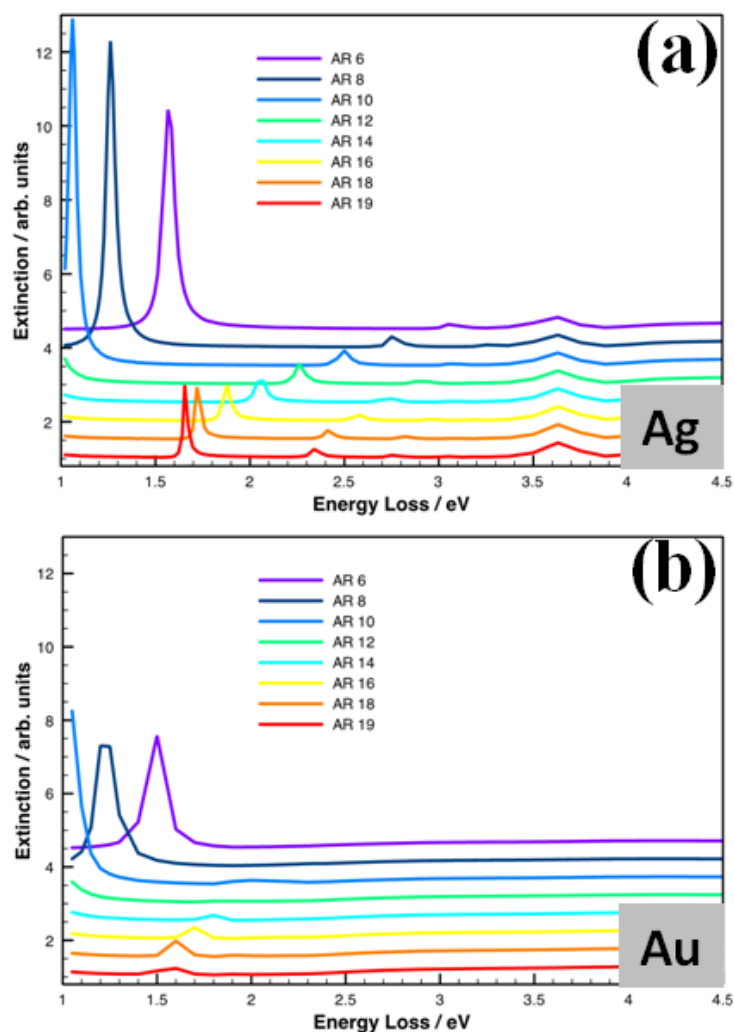


**Figure 4.11: Illustration of DDA simulation in the DDSCAT program and the impact of dipole density.** (a) Schematic representation of DDSCAT simulation, and (b) DDSCAT simulated spectra for an Ag cube showing the impact of varying dipole density.

As DDSCAT simplifies the issue of optical response to the dielectric response of individual dipole elements, its accuracy is reliant on the input dielectric data. For the work presented in this thesis we have used experimentally determined dielectric data that were obtained from bulk metals<sup>14</sup> or thin films,<sup>15,16</sup> using surface based techniques. In segregated targets DDSCAT treats each interface as a clearly defined boundary, as each

volume element must be associated with only one dielectric function. This may not be a physically accurate treatment in all cases, in particular in segregated particles with extremely thin shells, or where there is mixing between metals at their interface.

As DDA optical simulation is relatively easy to run it can provide an efficient means to systematically investigate the impact of structural and compositional variation, which is difficult to achieve experimentally due to the need for extremely well controlled series of samples. An example of systematic DDSCAT simulation is given in Figure 4.12.

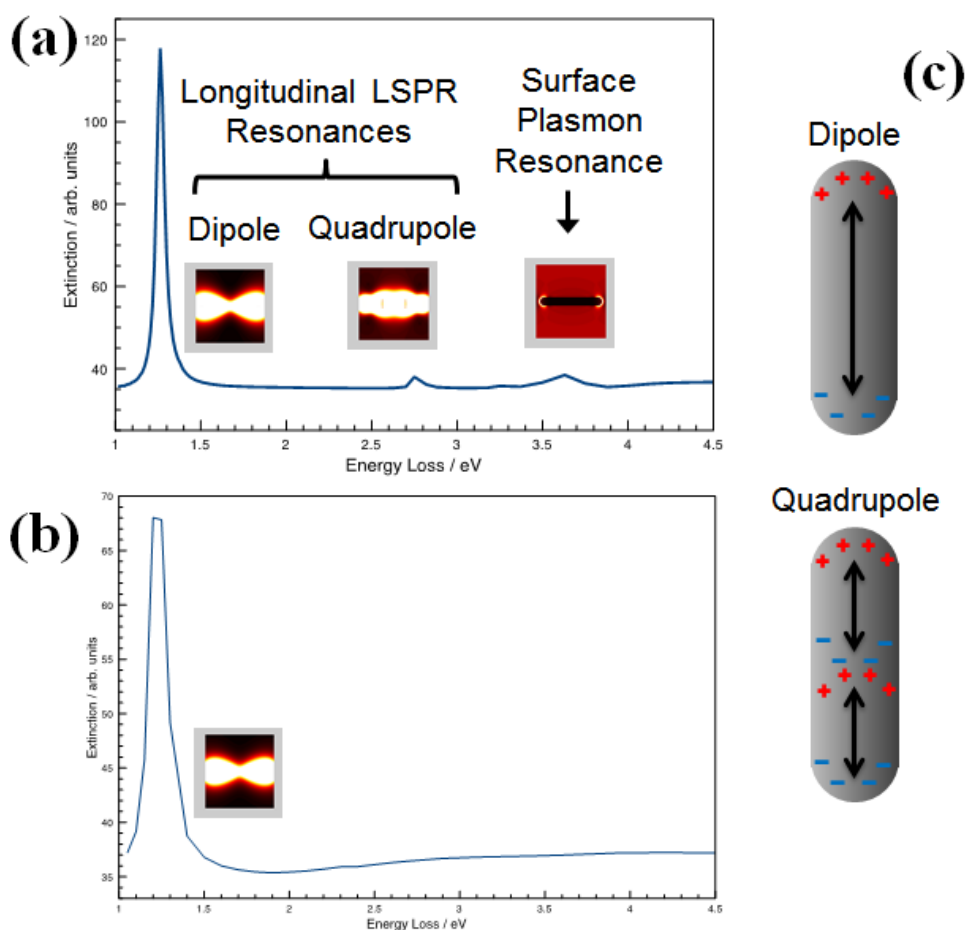


**Figure 4.12:** An example of systematic simulation of optical response. DDSCAT simulated optical extinction spectra showing the impact of systematic variation of target aspect ratio for (a) Ag and (b) Au nanorods.

In the simulated spectra shown in Figure 4.12 the apparent peak shift to lower energy across the series of targets can be associated with increasing aspect ratio, because it occurs for both Au and Ag nanorods, but the rate of peak shift varies between Ag and Au, indicating this can be related to their differing dielectric responses.

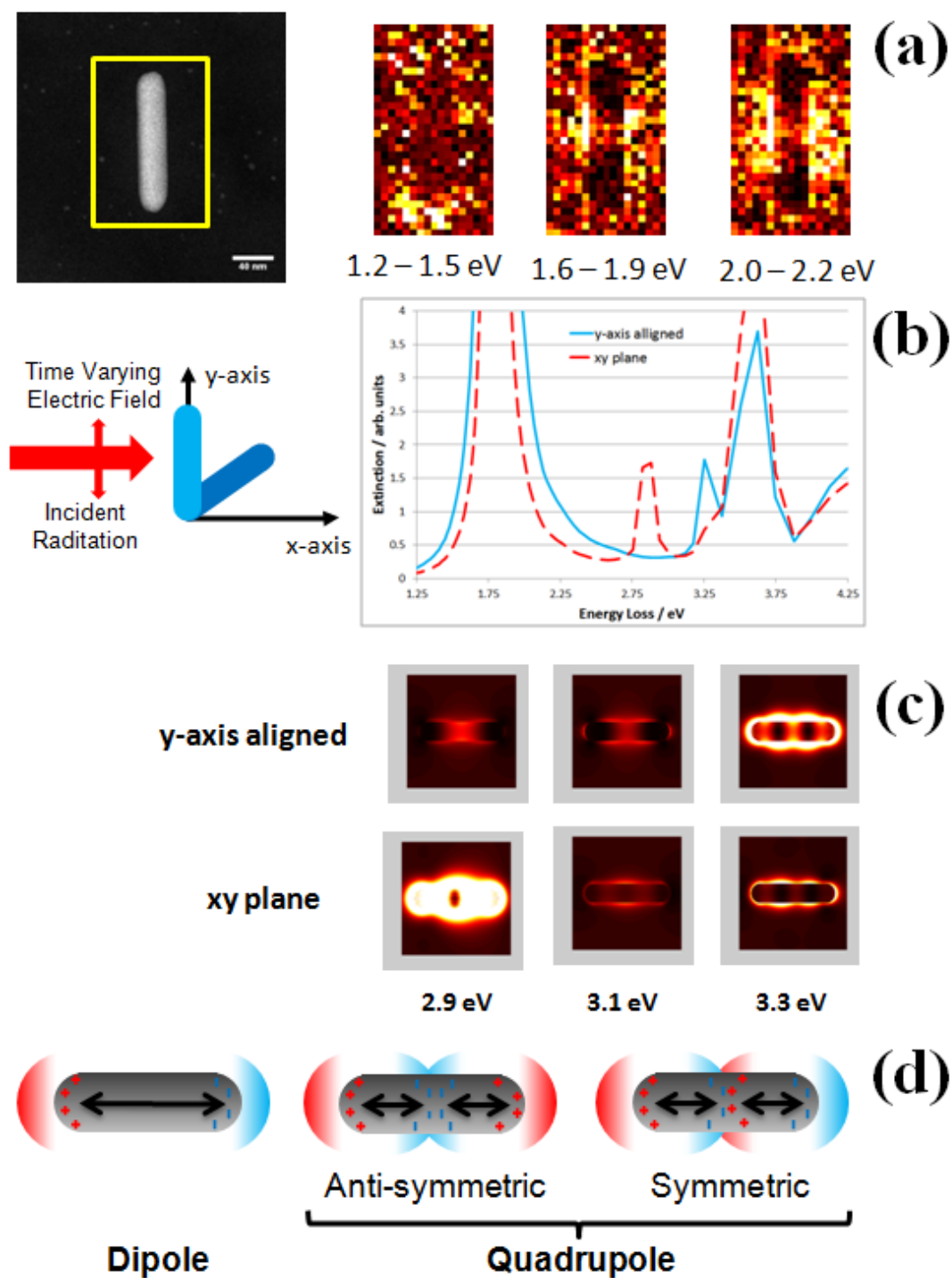
In addition to simulating spectra through the DDSCAT program, the associated program DDfield allows the simulation of the electric fields induced around the target. Output from the main DDSCAT program gives the polarization of the dipoles, from which DDfield calculates field vectors at coordinates defined by the user. The magnitude of the simulated induced fields can be plotted to show their spatial distribution. Figure 4.13 shows an example of how this can be used to identify different LSPR modes.

From just examining the spectra given in Figure 4.13 the nature of their features cannot be determined, however, DDfield simulations show, for example, that the feature in the Ag spectrum (Figure 4.13(a)) at approximately 3.7 eV it is not a longitudinal LSPR mode, because it has only a weak induced field with incident polarisation along its long axis. In comparison the features appearing at approximately 1.3 eV and 2.8 eV in the Ag spectrum both have strong induced fields for this polarisation, indicating they are caused by longitudinal LSPR modes, with the field patterns consistent with two modes of oscillation, dipole and quadrupole. By conducting the same simulation for an identical Au nanorod (Figure 4.13(b)) we can see that the appearance of the higher order quadrupole mode of oscillation is dependent on target composition.



**Figure 4.13:** An example illustrating the use of field simulation to identify spectral features. Simulated spectra for (a) Ag and (b) Au nanorods targets with simulated induced electric fields for each identified spectral feature, and (c) schematic illustrations of dipole and quadrupole longitudinal LSPR modes.

DDfield simulations can be compared STEM-EELS spectrum image maps to assist with interpretation. In Figure 4.14 the STEM-EELS results show variation in the pattern of the measured fields over the energy loss range from 1.2 eV to 2.2 eV. The fields localised to the ends of the nanorod in the 1.2 eV to 1.5 eV range can be readily assigned to dipole oscillation, but in the other energy loss windows shown we see two distinct field patterns central to the nanorod.



*Figure 4.14: An example illustrating the use of DDfield to interpret STEM-EELS plasmon maps.* (a) Ag nanorod with STEM-EELS plasmon maps for the energy ranges noted, (b) DDSCAT simulated spectra with schematic diagram illustrating target orientations ( y-axis (blue) and in the xy plane at  $45^\circ$  to the incident radiation (red)), (c) DDfield electric field simulations at the energies noted, and (d) schematic representations of different modes of oscillation.

DDSCAT simulation conducted to excite only longitudinal modes (described as ‘y-axis aligned’ in Figure 4.14) shows spectral features at around 1.8 eV, 3.3 eV and 3.7 eV (note that small discrepancy in the position of features in the spectrum between simulation and experiment can be caused by the influence of carbon substrate). DDfield simulations identify the 1.8 eV and 3.7 eV features as respectively to the longitudinal dipole mode and the Ag surface plasmon mode (results not shown), and show that the 3.3 eV feature has a double node central field consistent with the mapped field in the 2.0 eV to 2.2 eV energy loss range.

With the simulation target oriented to excite only longitudinal modes no other features are apparent in the spectrum that might correspond to the mapped field in the 1.6 eV to 1.9 eV range, however, when the target is tilted (described as ‘xy plane’ in Figure 4.14) phase retardation is introduced and this causes a further peak to appear. DDfield simulation for this feature shows a single central node, consistent with the mapped field in the 1.6 eV to 1.9 eV energy loss range. The requirement to tilt the target to reveal this mode allows us to identify the two central fields as corresponding to two quadrupole modes of oscillation and illustrates a key difference between optical and fast electron excitation of LSPR response. In optical excitation anti-symmetric modes of oscillation can only be excited by introducing phase retardation, indicating the 2.9 eV feature corresponds to the anti-symmetric quadrupole mode while the 3.3 eV feature corresponds to the symmetric quadrupole mode.

### **4.3. Conclusions**

This chapter has described the capabilities of STEM-EELS in characterising the electronic response of bimetallic nanoparticles. The ability to map the LSPR response of

these systems on a single particle basis makes STEM-EELS a valuable tool in characterising the LSPR behaviour of bimetallic nanoparticles, where small variations in structure and composition can potentially impact the response. The results presented in Chapters 6 and 7 of this thesis explore this further.

In comparison, the greater simplicity and ensemble nature of UV-vis results described in Section 4.2.1 of this chapter, is better suited to initial characterisation and to gaining an overall impression of a sample. This technique is used to link the evolution of optical response to change in particle structure across a series of samples, in Chapter 5 of this thesis.

The use of computer simulation in forming a link between experimentally determined dielectric response and individual particle size, structure and composition, can be invaluable in aiding the interpretation of both STEM-EELS and UV-vis experimental results and forms part of the results presented in Chapters 5 and 6 of this thesis.

## List of References

128. Krivanek, O.L.; Lovejoy, T.C.; Dellby, N.; Carpenter, R.W., Monochromated STEM with a 30 meV, Atom-Sized Electron Probe, *Microscopy*, **2013**, *62*, 3-21
129. Sanchez, S.I.; Small, M.W.; Sivaramakrishnan, S.; Wen, J.G.; Zuo, J.M.; Nuzzo, R.G., Visualizing Materials Chemistry at Atomic Resolution, *Anal. Chem.*, **2010**, *82*, 2599-2607
130. Egerton, R.F., *Electron Energy-Loss Spectroscopy in the Electron Microscope*, Springer: New York, 2011.
131. Garcia de Abajo, F.J.; Kociak, M., Probing the Photonic Local Density of States with Electron Energy Loss Spectroscopy, *Phys. Rev. Lett.*, **2008**, *100*, 106804
132. Williams, D.B.; Carter, C.B., *Transmission Electron Microscopy*, Springer: New York, 2009
133. Hohenester, U.; Ditlbacher, H.; Krenn, J.R., Electron Energy-Loss Spectra of Plasmonic Nanoparticles, *Phys. Rev. Lett.*, **2009**, *103*, 106801
134. Maigne, A., How to Optimize Your EELS Experiments By Adjusting the Collection Angle of Your Spectrometer?, *Gatan KnowHow*, [www.gatan.com/resources/knowhow](http://www.gatan.com/resources/knowhow)
135. Nelayah, J.; Kociak, M.; Stephan, O.; Garcia de Abajo, F.J.; Tence, M.; Henrard, L.; Taverna, D.; Pstoriza-Santos, I.; Liz-Marzan, L.M.; Colliex, C., Mapping Surface Plasmons on a Single Metallic Nanoparticle, *Nature Phys.*, **2007**, *3*, 348-353
136. Digital Micrograph, Version 1.83.842, Gatan Inc. USA
137. Bosman, M.; Keast, V.J.; Garcia-Munoz, J.L.; D'Alfonso, A.J.; Findlay, S.D.; Allen, L.J., Two-Dimensional Mapping of Chemical Information at Atomic Resolution, *Phys. Rev. Lett.*, **2007**, *99*, 086102
138. Chu, M.W.; Myroshnychenko, V.; Chen, C.H.; Den, J.P.; Mou, C.Y.; Garcia de Abajo, F.J., Probing Bright and Dark Surface-Plasmon Modes in Individual and Coupled Noble Metal Nanoparticles Using an Electron Beam, *Nano Lett.*, **2008**, *9*, 399-404
139. Kreibig, U.; Vollmer, M., *Optical properties of metal clusters*, Springer-Verlag: Berlin, 1995
140. Draine, B.T.; Flatau, P.J., Discrete-dipole approximation for scattering calculations, *J. Opt. Soc. Am.*, **1994**, *11*, 1491
141. *Handbook of Optical Constants of Solids*, ed. Palik, E.D., Academic Press, London, 1998



142. Johnson, P.B.; Christy, R.W., Optical Constants of the Noble Metals, *Phys. Rev. B*, **1972**, 6, 4370-4379
143. Johnson, P.B.; Christy, R.W., Optical Constants of Transition Metals: Ti, V, Cr, Mn, Fe, Co, Ni, and Pd, *Phys. Rev. B*, **1974**, 9, 5056-5070

---

## Chapter 5

# Structure of Segregated Bimetallic Nanorods

In this chapter we present results using the imaging and energy dispersive X-ray spectroscopy (EDX) capabilities of aberration corrected scanning transmission electron microscopy (ac-STEM) to characterise the structure of two, similar segregated bimetallic systems, AuRh and AuPd nanorods. As described in the supplementary information for reference 2, extracts from which are reproduced in Appendix I, these systems were both synthesised through colloidal sequential seed mediated methods, which made use of Au nanorods as templates for the deposition of either Rh or Pd. The shell metals have adjacent atomic numbers, 45 and 46 respectively, and many of the key parameters of these systems are similar (see Tables 2.1 and 2.2 Chapter 2), thus they make ideal comparators.

AuRh is a little understood bimetallic system, and to date has not been studied in nanorod form; the work we present in Section 5.1 characterises the growth mode of Rh on Au-seed nanorods at the single particle level, including consideration of the impact of the Rh growth preference on the optical response of the particles. A substantial part of this work has been published in reference 1. In Section 5.2 we then conduct a more detailed

characterisation of the metal-metal interfaces formed in bimetallic nanoparticles through a comparative study of the atomic structures formed in AuRh and AuPd core-shell nanorods. This work has been published in reference 2.

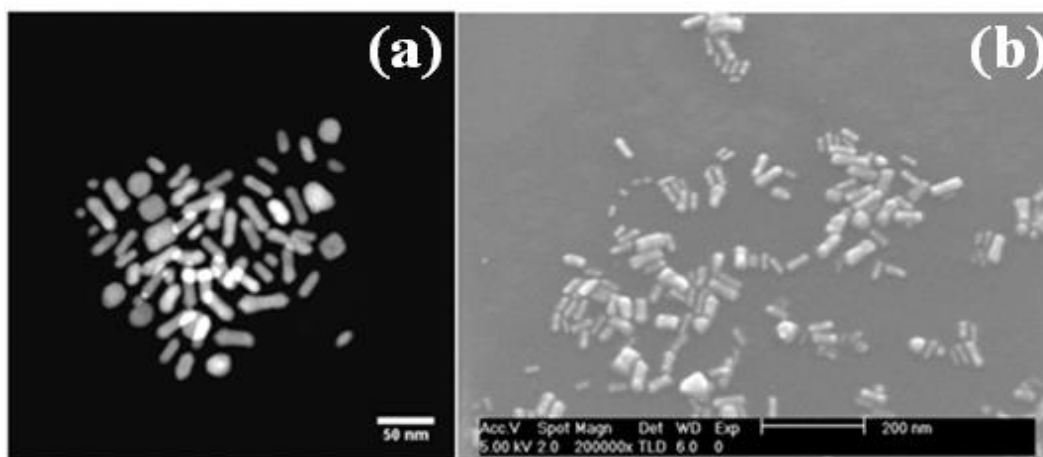
All of the STEM imaging, and spectroscopy, SEM imaging, optical response simulation calculations, and data analysis presented in this chapter were conducted by the author, under the supervision of Dr Ziyou Li. The AuRh and Au nanorod samples were synthesised, and initial UV-visible spectroscopy (UV-vis) data collected by, Wilai Siriwatcharapiboon and Dr Sarah Horswell (Department of Chemistry, University of Birmingham, UK). The AuPd nanorod sample was synthesised by Bishnu Khanal and Eugene Zubarev (Department of Chemistry, Rice University, USA). Custom shape files used for optical response simulation were compiled by Andrew Logsdail and Roy Johnston (Department of Chemistry, University of Birmingham, UK). The molecular dynamics simulations were conducted by Ivailo Atanasov and Roy Johnston (Department of Chemistry, University of Birmingham, UK).

## **5.1 Rh Over-Growth on Au-Seed Nanorods**

The AuRh samples were made using a seed mediated method, whereby Au nanorods are synthesised first, and then used as a template for Rh shell deposition in a separate reduction. The method is described in detail in reference 1 and a summary extracted from the supplementary information of reference 2 is given in Appendix I. During sample synthesis the volume of Au-seed and Rh-salt solutions were varied to produce a range of samples with varying nominal Au:Rh ratios of 10:1, 7:3, 1:1, and 1:2. Our work has been focused on the AuRh samples with the highest and lowest Rh concentrations and on the Au-seed nanorods.

### 5.1.1. Au seed nanorods

In systems formed using a seed mediated approach, the overall particle structure proceeds from interaction between the substrate seed particle and the depositing metal, so understanding the nature of shell metal over-growth requires characterisation of the seed particle substrate. The Au-seed nanorods were synthesised chemically, in solution, by first making small, approximately spherical, Au nanoparticles, and then growing these into nanorods in a second process.<sup>3,4</sup> The growth phase takes place over a longer period than the formation of the initial seed, and uses the surfactant cetyl trimethyl ammonium bromide (CTAB), together with silver nitrate, to promote and control the asymmetric growth needed to form nanorods. Figure 5.1(a) shows a low magnification high angle annular dark field (HAADF) STEM image of Au nanorods that is typical of this sample.

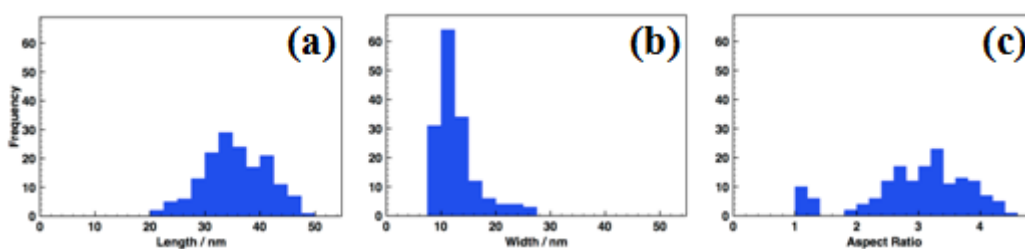


**Figure 5.1:** Typical STEM-HAADF and SEM images of Au nanorods.

Low magnification images of Au-seed nanorods, (a) HAADF-STEM and (b) 45° tilted SEM.

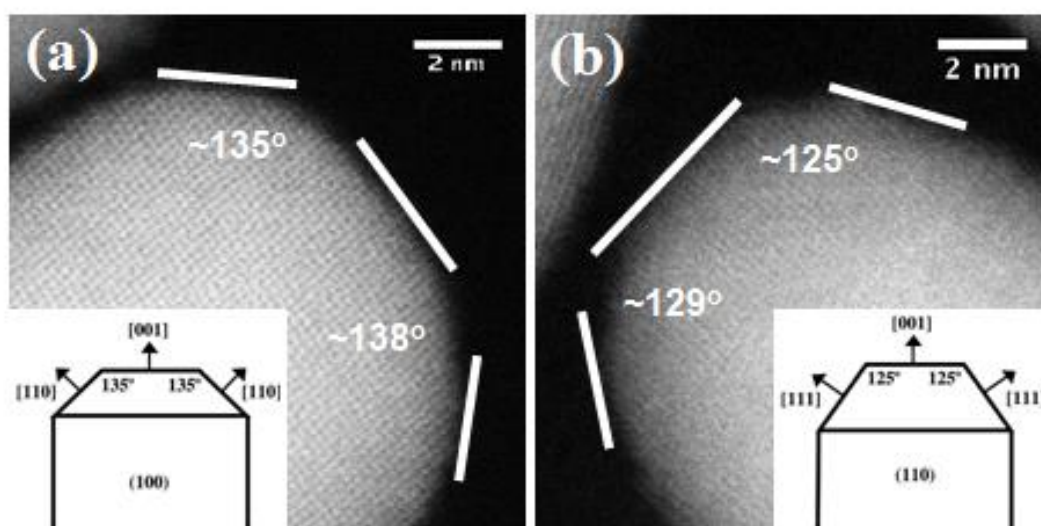
From Figure 5.1(a) it can be seen that the Au nanorod sample was not monodisperse, and in particular that it included a proportion of square shaped particles in addition to nanorods. This is often a problem with nanoparticles formed through chemical methods, as the level of control required to form monodisperse samples is challenging. In the context of structural characterisation this problem can be overcome by using characterisation techniques that can be carried out on a single particle basis, such as STEM characterisation. However, the irregularity of the sample can present problems with techniques that are conducted on an ensemble basis, such as UV-vis; this issue is discussed further below.

We used the surface contour contrast of scanning electron microscopy (SEM) to characterise the 3D morphology of the Au nanorods. Figure 5.1(b) shows a typical SEM image of the Au nanorods, where it can be seen that they have an approximately hemispherical-capped, cylindrical morphology, with a smooth surface. This observation is consistent with the 2D projection that we see in the STEM-HAADF image. SEM images were used to conduct size analysis on a sample of 157 Au nanorods; a summary of these results is given in Figure 5.2. From this analysis the Au nanorods have, respectively, a mean length, width and aspect ratio (length divided by width) of 35.4 nm, 12.8 nm and 3.0, with standard deviations respectively of 9.6 nm, 5.5 nm and 1.0. These standard deviations are consistent with the relatively large variation in particle size apparent in both STEM and SEM images of the sample. The tail that can be seen in the width histogram of Figure 5.2(b), and the second small peak in the aspect ratio histogram of Figure 5.2(c), can be attributed to the presence of the square particles in the sample.



**Figure 5.2: Au nanorod size analysis.** Histograms of the size measurements conducted on 157 Au nanorods, showing (a) length, (b) width, and (c) aspect ratio (length / width). From reference 1.

For a more detailed characterisation of the Au nanorods we conducted high resolution STEM-HAADF imaging, examples of which are shown in Figure 5.3. Although the overall shape of the nanorod ends is rounded when viewed in low magnification, when viewed at higher magnifications faceting becomes apparent. Examination of STEM-HAADF images of a number of Au nanorods reveals two different appearances to the end faceting, one more rounded and one less rounded; examples of each are shown Figure 5.3.



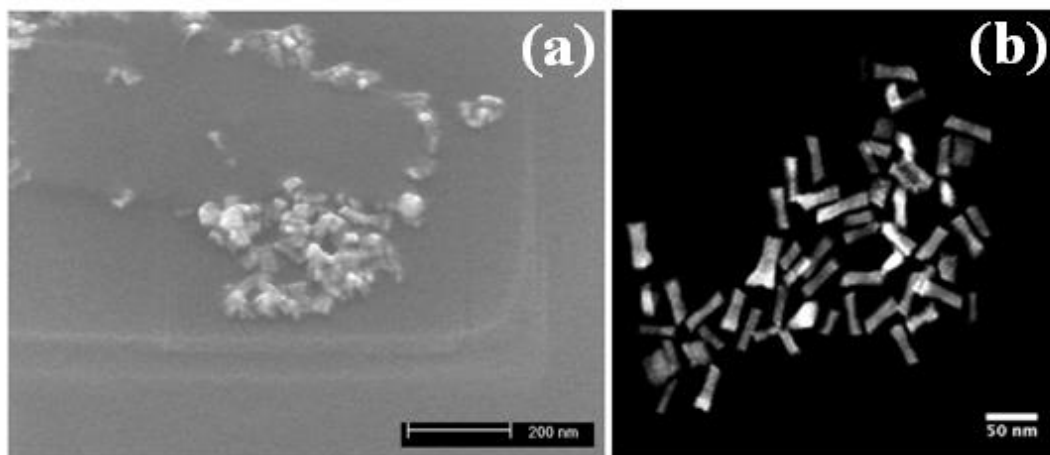
**Figure 5.3: STEM-HAADF images of the ends of Au nanorods.** With nanorod ends of (a) less rounded, and (b) more rounded morphology, together with schematic representations of possible structural models corresponding to these morphologies inset. From reference 1.

In bulk form Au packs into a face centred cubic (fcc) configuration. Using the bulk lattice parameter of Au (0.408 nm from Table 2.1 Chapter 2), and a model for single crystal Au nanorods proposed by Wang *et al.*,<sup>5</sup> we can build a simple schematic model to determine the angles that might be expected between the principal low index facets at the ends of the Au nanorods. Two such models, based on the same faceting structure but with nanorods in different orientations relative to the electron beam, are shown inset to the images in Figure 5.3. The angles between the rod end and end corner facets apparent in STEM-HAADF images of Figure 5.3 are consistent with the angles expected based on the simple schematic diagrams given, with an angle of  $135^\circ$  between [110] and [001] facets in the less rounded morphology and  $125^\circ$  between [111] and [001] facets in the more rounded morphology. These results indicate that these Au nanorods have morphology consistent with the model proposed by Wang *et al.*<sup>5</sup> Other more recent work has proposed an alternative model for Au nanorods based on higher index faceting.<sup>6</sup> In this model the nanorod ends are pyramids formed by {0 1 3} facets, with {0 5 12} side and end linking facets. However, our analysis indicates this model is not consistent with the sample studied here, and that the Au-seed nanorods used for Rh over-growth predominantly comprise low index {100}, {110} and {111} facets.

### 5.1.2. AuRh nanorods

Figure 5.4(a) and (b) show, respectively, typical SEM and low magnification STEM-HAADF images of AuRh nanorods from the most Rh-rich (Au:Rh 1:2) sample. Comparison of these images shown in Figure 5.4 with those of the Au-only nanorods of Figure 5.1 shows a clear change in appearance in the nanorods on Rh deposition. Variations in contrast through the body of the nanorods can be seen in both of the images presented in Figure 5.4, which are consistent with an uneven surface in the case of the

SEM image and variations in sample thickness in the case of the STEM image. Nanorod morphology is difficult to distinguish in the SEM image but can be seen in the STEM-HAADF image in the majority of particles; they appear more irregular and angular appearance than the smooth and rounded appearance of the Au-only nanorods.



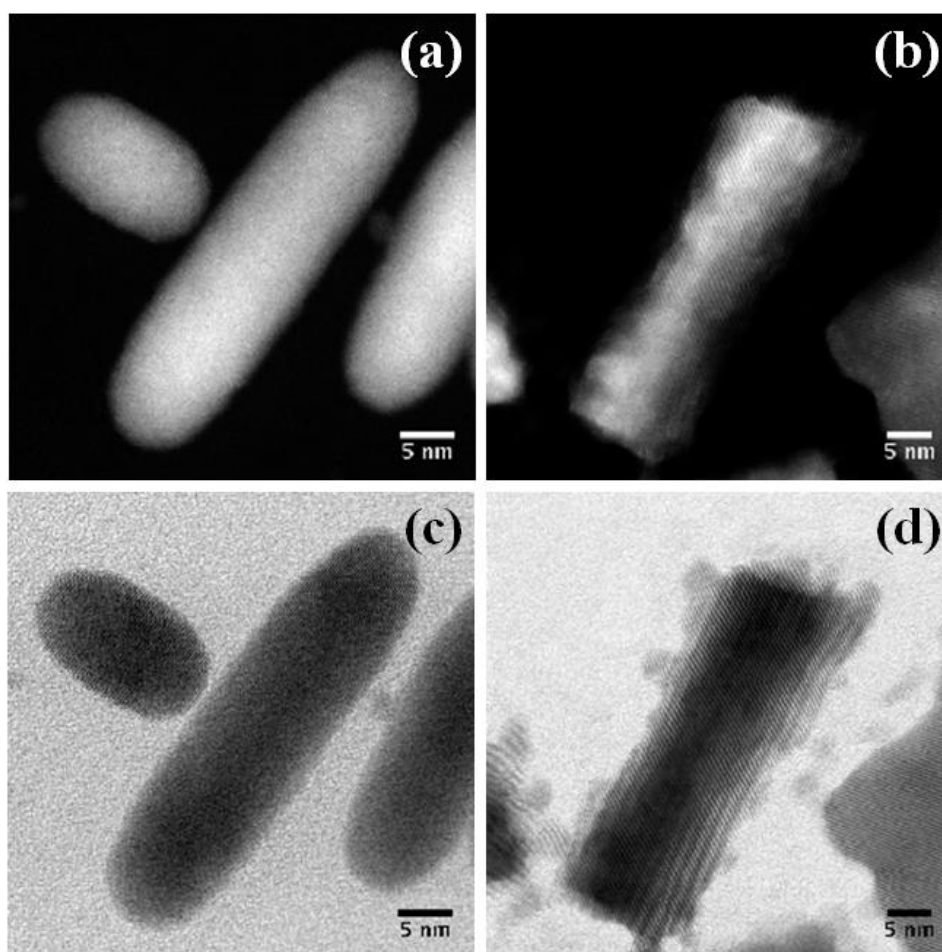
**Figure 5.4: Typical SEM and STEM-HAADF images of AuRh nanorods.**

(a) SEM image taken at  $45^\circ$  tilt, and (b) low magnification HAADF-STEM image, of AuRh nanorods.

Figure 5.5 shows simultaneously acquired HAADF and bright field (BF) images of typical single Au-only and AuRh nanorods for closer inspection of the changes caused on Rh deposition. Comparison of the Au-only and AuRh images in Figure 5.5 shows more clearly the shift from the smooth, rounded morphology of the bare Au nanorod to the uneven and angular shape of the AuRh nanorod. The full extent of Rh over-growth is only apparent in the BF image of Figure 5.5(d), because the difference in the HAADF image intensity between the centre and the outer edge of the nanorod is too great for the outermost layers to be apparent in Figure 5.5(b) without saturating the centre of the image. The atomic numbers of Rh and Au (45 and 79, respectively) are sufficiently different that



we might expect Z-contrast in STEM-HAADF images from elemental variation in this sample. Thus, the significant difference in HAADF image contrast apparent between the centre and the outermost edges of the nanorod in Figure 5.5(b) can be attributed qualitatively to the synthesis method followed for this sample resulting in the formation of core-shell structure.

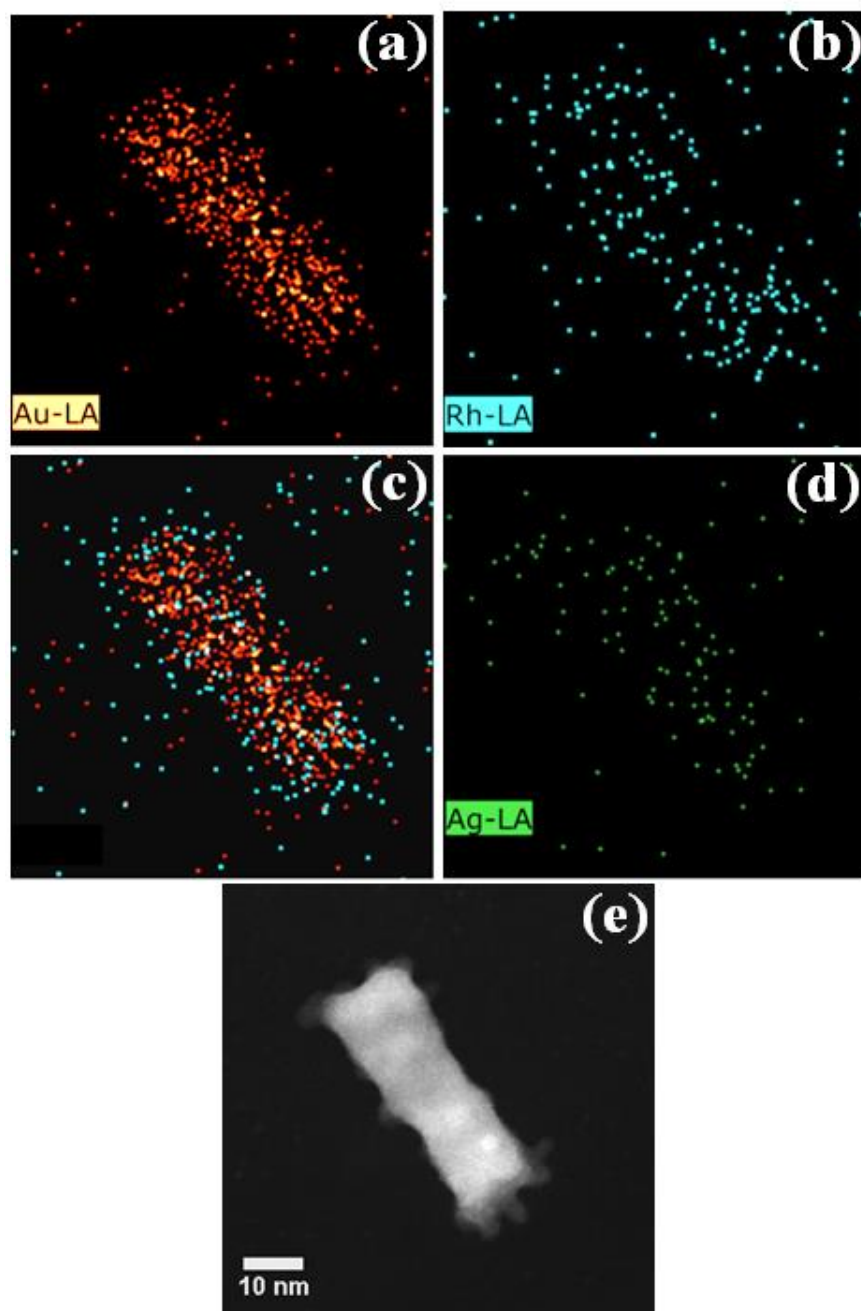


*Figure 5.5: A comparison of typical Au-only and AuRh nanorods. HAADF-STEM images of (a) a Au-only nanorod, and (b) a AuRh nanorod, with corresponding simultaneously acquired BF-STEM images in (c) and (d) respectively. From reference 1.*

In both Figure 5.5(b) and (d) the random variation in contrast through the body of the rod, and uneven delineation at the edge of the rod, indicates a non-uniform growth mode followed by Rh on the Au nanorods. The out-growths that can be seen in the BF image of Figure 5.5(d) may be consistent with an island phase of growth. In addition, the angular appearance of the rod ends after Rh deposition, compared to the round ends of the Au-only nanorod of Figure 5.5(a) and (c), indicates Rh over-growth may have followed a facet preference at the end and end corners of the nanorods, either in initial deposition or subsequent over-growth. These observations are indicative of a complex deposition and growth pattern for Rh on Au-seed nanorods.

We conducted EDX elemental mapping measurements on the AuRh nanorods to verify the spatial distribution of Au and Rh; Figure 5.6 shows typical STEM-EDX results, taken from the AuRh nanorod shown in Figure 5.6(e), with (a) to (d) displaying elemental maps of the EDX signals for, respectively, Au, Rh, Au and Rh overlaid, and Ag.

Comparison of the spatial extent of the Au signal of Figure 5.6(a) with that of the Rh signal of Figure 5.6(b) indicates the formation of a core-shell structure. In addition to revealing a core-shell structure, the distribution of the Rh signal in Figure 5.6(b) also shows a pattern broadly consistent with increased amounts of Rh present at the ends of the nanorods, supporting the change in morphology apparent in the STEM images of Figures 5.4 and 5.5. Previous studies have suggested that the presence of Ag residue, left over from the synthesis of Au nanorods, may have been responsible for a similar rod-end preference found for Pt deposited on Au nanorods;<sup>7</sup> however, the Ag elemental map of Figure 5.6(d) shows no rod-end preference in the signal, so it seems unlikely that the observed end growth of Rh has been caused by the presence of Ag residues in the sample.



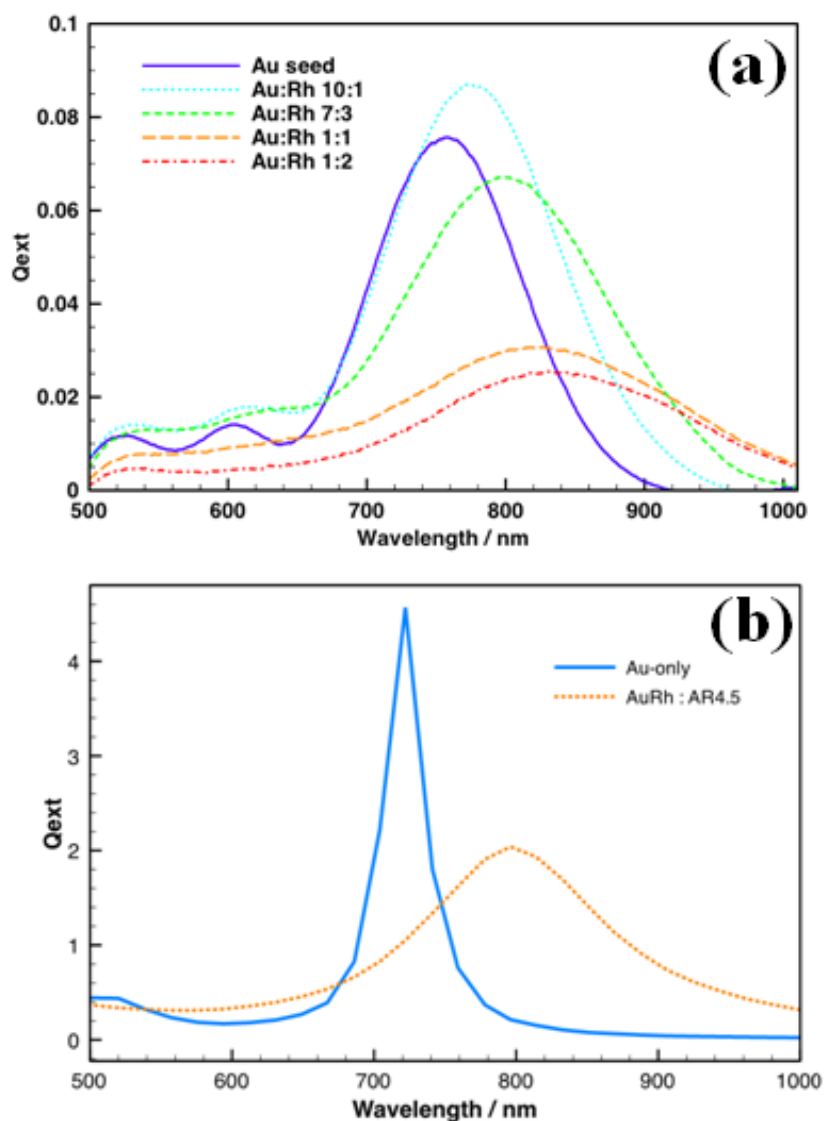
*Figure 5.6: STEM-EDX elemental maps of an AuRh nanorod. (a) The Au signal, (b) the Rh signal, (c) both the Au and Rh signals, and (d) the signal from residual Ag in the sample, with (e) corresponding STEM-HAADF image. From reference 1.*

### 5.1.3. Impact on optical response

UV-vis measurements, taken within 24 hours of sample synthesis, are shown in Figure 5.7(a).<sup>1</sup> An evolution in optical response with increasing proportions of Rh is apparent in these results from the shifting of peak positions, and the increased damping and broadening of the response. To understand this better, and establish a link to our structural characterisation, we conducted simulations of the optical response using DDSCAT software.<sup>8</sup> We have used custom-made target shapes based on dimensions measured from typical STEM images and experimentally determined values for the dielectric constants.<sup>9,10</sup> For the purposes of simulation, the Rh shell was treated as evenly coating the Au seed rod core, which is consistent with the ensemble nature of UV-vis results, where small scale variations in structure average out over the whole sample, but as our STEM imaging shows is not accurate in respect of individual nanorods.

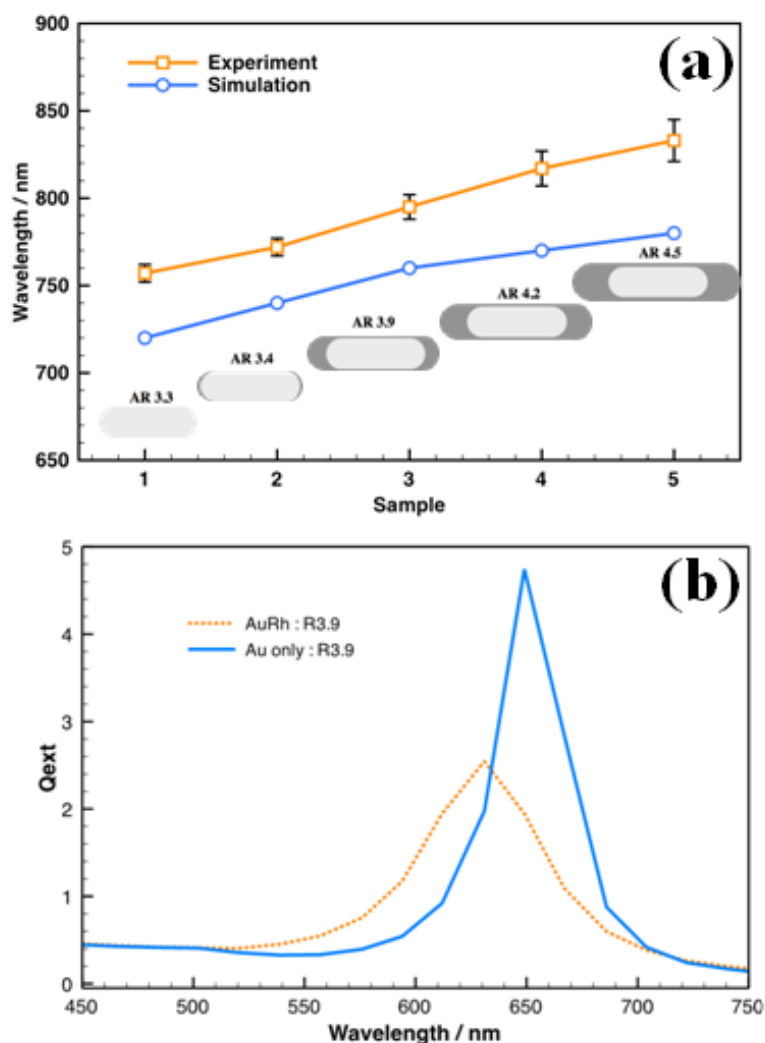
For comparison to the experimental results of Figure 5.7(a), Figure 5.7(b) shows examples of simulated spectra compiled from targets with dimensions that correspond to the Au-only seed and the Au:Rh 1:2 nanorods (described as 'AR4.5' in the plot legend). The experimental spectra in both cases show peaks that are slightly red-shifted and broader than those seen in simulation, which is consistent with the size and shape variation present in the experimental sample. The trend of damping and red-shifting of the response between Au-only and the most Rh-rich of the AuRh samples is consistent between experiment and simulation. By varying the polarisation of incident radiation in the simulation (results not shown here), we can attribute the intense feature apparent at 755 nm in the Au-only experimental spectrum (dark blue line in Figure 5.7(a)) to the longitudinal LSPR, and the weaker feature apparent at approximately 520nm to the transverse LSPR. In addition, through simulation of square shaped particles, we can attribute the feature apparent at 600

nm in the UV-vis spectra for the Au-only and less Rh-rich samples can be attributed to shape variation in the sample demonstrating the difficulties presented in the interpretation of ensemble results when there is a lack of monodispersity in a sample.



**Figure 5.7: UV-vis and optical simulation results for Au-only and AuRh nanorods.** (a) UV-vis results for a series of Au only and Au:Rh 10:1, 7:3, 1:1, and 1:2 core-shell nanorods (Reference 1), and (b) simulated spectra for Au-only nanorod of aspect ratio 3.3 and AuRh with aspect ratio 4.5.

To investigate the trend in response with increasing Rh content we have conducted simulations using a series of targets corresponding to each sample in the series, reflecting the preference for Rh growth at the ends of the nanorods, and made comparison of the frequency of their longitudinal response between experiment and simulation; Figure 5.8(a) shows a summary of these results.



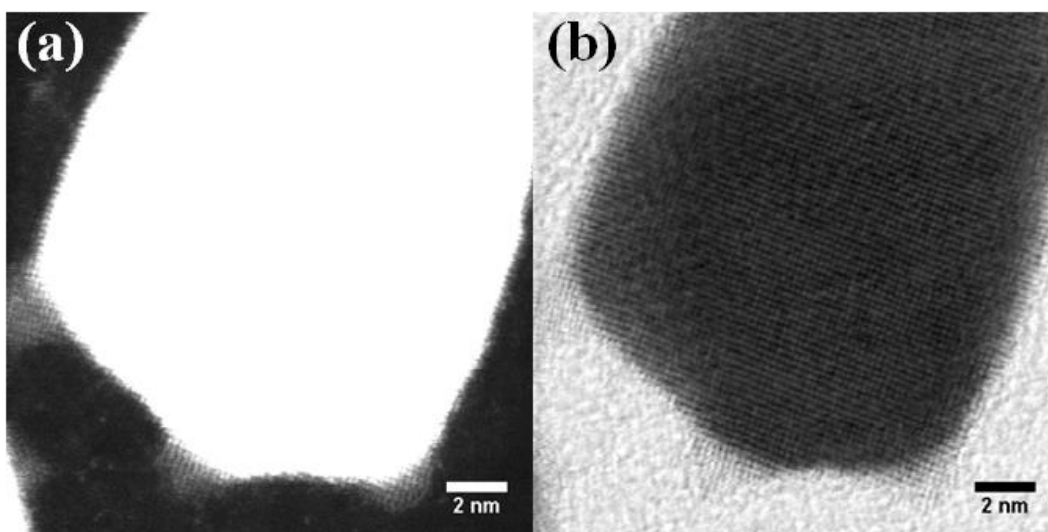
**Figure 5.8: Investigating the impact of Rh end growth on optical response using UV-vis and DDA simulation.** (a) Comparison of the position of the longitudinal LSPR between experimental UV-vis and DDSCAT optical simulation for the target shapes shown (Reference 1), and (b) simulated spectra for Au-only and AuRh core-shell nanorods of equal aspect ratio.

Schematic representations of the custom shape files used in simulation are given in Figure 5.8(a), labelled according to aspect ratio from AR3.3 for the Au-only seed nanorods, to AR4.5 for the Au:Rh 1:2 sample. Although the simulation consistently slightly underestimates the surface plasmon wavelength, the trend of progressive peak red shift with increasing Rh content, in particular at the ends of the nanorods, is well matched between the simulation and experimental results. As longitudinal LSPR response is sensitive to particle morphology and composition these results suggest that the evolution in target morphology across the series of simulation shape files is representative of corresponding structural trends in the average particle across the series of samples caused by increasing Rh content.

To ascertain whether the trend in longitudinal LSPR wavelength is due to the increasing proportion of Rh in the samples or to changes in aspect ratio we have simulated spectra for an Au-only nanorod with dimensions and aspect ratio equal to that of the AR3.9 AuRh nanorod. The results shown in Figure 5.8(b) show a blue shift in longitudinal LSPR response to shorter wavelengths between the Au-only and AuRh nanorods of equal aspect ratio, consistent with the surface plasmon resonance of Rh occurring at UV wavelengths (Table 2.4 Chapter 2). These results are contrary to the red shift trend that we observe experimentally, indicating that compositional variation did not cause a red shift in the longitudinal LSPR, but rather the observed trend can be attributed to the increase in aspect ratio caused by the Rh end growth preference. This demonstrates the importance of gaining a fundamental understanding of both the composition and morphology of bimetallic nanoparticles at the single particle level in order to understand their LSPR response.

#### 5.1.4. Rh growth mode

To understand how the nanorod end preference might have been established we have examined the initial stages of Rh deposition and growth by conducting STEM imaging of the least Rh rich of the AuRh samples, Au:Rh 10:1. Figure 5.9 shows simultaneously acquired, atomically resolved STEM-HAADF and STEM-BF images taken from the end of a low coverage AuRh nanorod. As with Figure 5.5(b) above, the full extent of Rh growth is not apparent in normal HAADF contrast; only by saturating contrast in the HAADF image for Figure 5.9(a) can the full extent of the low contrast Rh outgrowths be seen.



**Figure 5.9:** *STEM-HAADF and BF images of low coverage AuRh nanorod.* Simultaneously acquired atomically resolved (a) STEM-HAADF and (b) BF-STEM images of a low coverage AuRh nanorod, showing the initial stages of Rh deposition on the end and corner facets. From reference 1.



The out-growths apparent in the HAADF image of Figure 5.9(a) match features in the BF image of Figure 5.9(b). The appearance of these out-growths, when compared to the smooth, rounded appearance of the Au-seed nanorods (Figures 5.5(a), 5.3 and 5.1), together with their low HAADF image intensity, is consistent with them being formed by Rh deposition. The more regular appearance of this nanorod indicates it has low Rh coverage, so the location of these out-growths on the end and end-corner facets of the nanorod is consistent with an initial deposition or growth preference, which then persists through thicker Rh over-growth to produce the angular appearance of the more Rh-rich samples (Figures 5.4, 5.5 and 5.6). Their appearance is suggestive of an island growth mode. The surface science findings of Kibler *et al.*<sup>11</sup> and Liu and Bader,<sup>12</sup> discussed in Section 2.1.1 above, both found Rh grown on Au surfaces proceeded to an island growth mode after the initial formation of a bilayer. However, the study of Altman and Colton characterised Rh deposited onto Au(111) surface as following a purely island growth mode.<sup>13</sup> Although the images of Figure 5.9 are to atomic resolution, the level of detail available is still not sufficient to say whether an initial layer of Rh was formed before proceeding to the observed out-growths, or whether the out-growths formed directly on the Au surface.

In this section we have used ac-STEM imaging and EDX spectroscopy, in combination with UV-vis and DDA optical response simulation, to demonstrate the successful deposition of Rh onto Au nanorods via a sequential wet chemical route. We have shown that Rh shows an initial preference for deposition at the end and corner locations on the Au-seed nanorods. We have also shown that the persistence of this preference through thicker Rh deposition, and a tendency for layer-island growth, results in an overall surface morphology that is uneven, and angular in appearance, and which has a

marked influence on the optical response of this system. These results are indicative of complex metal-metal interactions between Au and Rh, which we investigate further in the next section by examining the interfacial structures in this system.

## 5.2 Atomic Structure of the Metal-Metal Interfaces in Bimetallic Nanorods

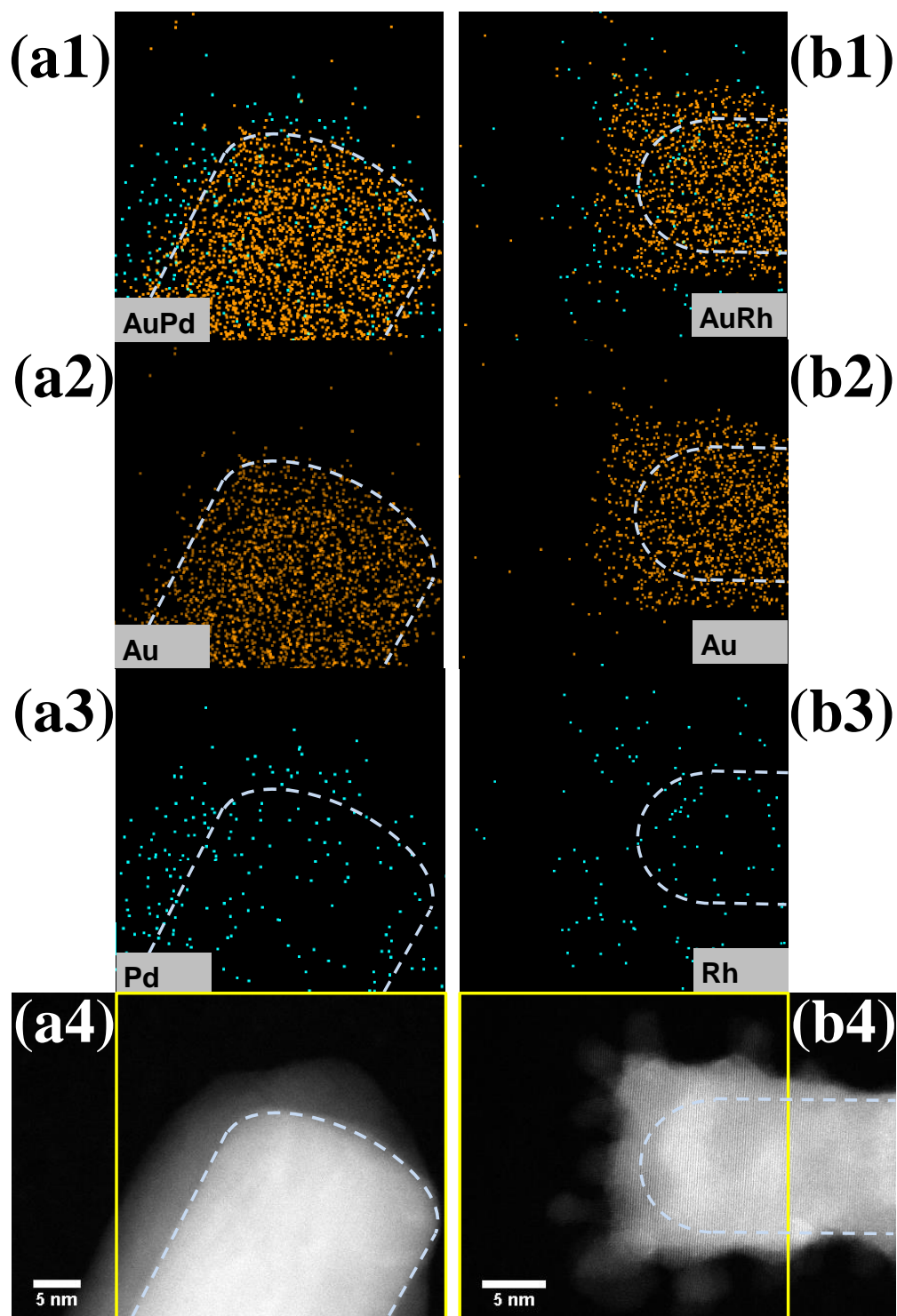
In segregated bimetallic nanoparticles the metal-metal interactions that give rise to their structure, and thus also their tuneable properties, are concentrated at the buried interface between core and shell. The atomically resolved imaging and spectroscopic capabilities of ac-STEM allow the possibility to probe the structure of buried interfaces to the best possible spatial resolution and thus determine their atomic structure. However, even if their atomic structure can be identified, the driving forces that formed it may remain unclear. The work presented in this section seeks to address this problem by using an approach of comparative study, utilising ac-STEM to probe the interfacial structures of two nanorod systems and draw conclusions from comparison between them.

The subjects of this study are the Au<sub>core</sub>Rh<sub>shell</sub> nanorods that were the subject of the previous section, and a comparable Au<sub>core</sub>Pd<sub>shell</sub> nanorod sample (a low magnification image of this sample is given in Figure 3.8). By comparing the atomic structures and key parameters for these two systems we seek to gain a level of understanding as to the driving forces that formed them that cannot be gained from examining either system in isolation. Results from this study have been published in reference 2.

### 5.2.1. STEM-EDX results

Figure 5.10(a) and (b) show typical EDX elemental maps from the ends of the  $\text{Au}_{\text{core}}\text{Pd}_{\text{shell}}$  and  $\text{Au}_{\text{core}}\text{Rh}_{\text{shell}}$  nanorods, together with corresponding STEM-HAADF images.<sup>2</sup> Core-shell structure is apparent from the relative spatial distributions of core and shell metal signals for both samples in Figures 5.10(a1) and (b1).

The elemental information of EDX signal maps can be compared to STEM-HAADF Z-contrast (Figures 5.10(a4) and (b4)). Abrupt STEM-HAADF image contrast variation is seen between core and shell in the AuPd sample (Figure 5.10(a4)), which matches well with the clear delineation of its Au EDX signal (Figure 5.10(a2)). In comparison a more gradual change in STEM-HAADF image contrast is seen in the AuRh nanorod (Figure 5.10(b4)), consistent with its more diffuse Au EDX signal (Figure 5.10(b2)). This latter observation means that, whilst the position of the Au-core is clear in the AuPd nanorod, it is more difficult to locate in the AuRh nanorod. However, its approximate location can be inferred by considering the nature of the Au-seed template, and we have included a schematic approximation to this morphology, shown as a dashed line in the STEM-HAADF of Figure 5.10(b1), the size of which is based on the width at the centre of the nanorod, where Rh coverage is lowest; this is intended to act as a guide for gauging the spatial distribution of the EDX signals, and is not intended to indicate the precise location of the Au-core. Comparison of the EDX Au and Rh signals of Figures 5.10(b2) and (b3) with the associated STEM-HAADF image of Figure 5.10(b4), and the schematic representation of hemispherical cylindrical morphology, highlights the uneven edge of Au signal.



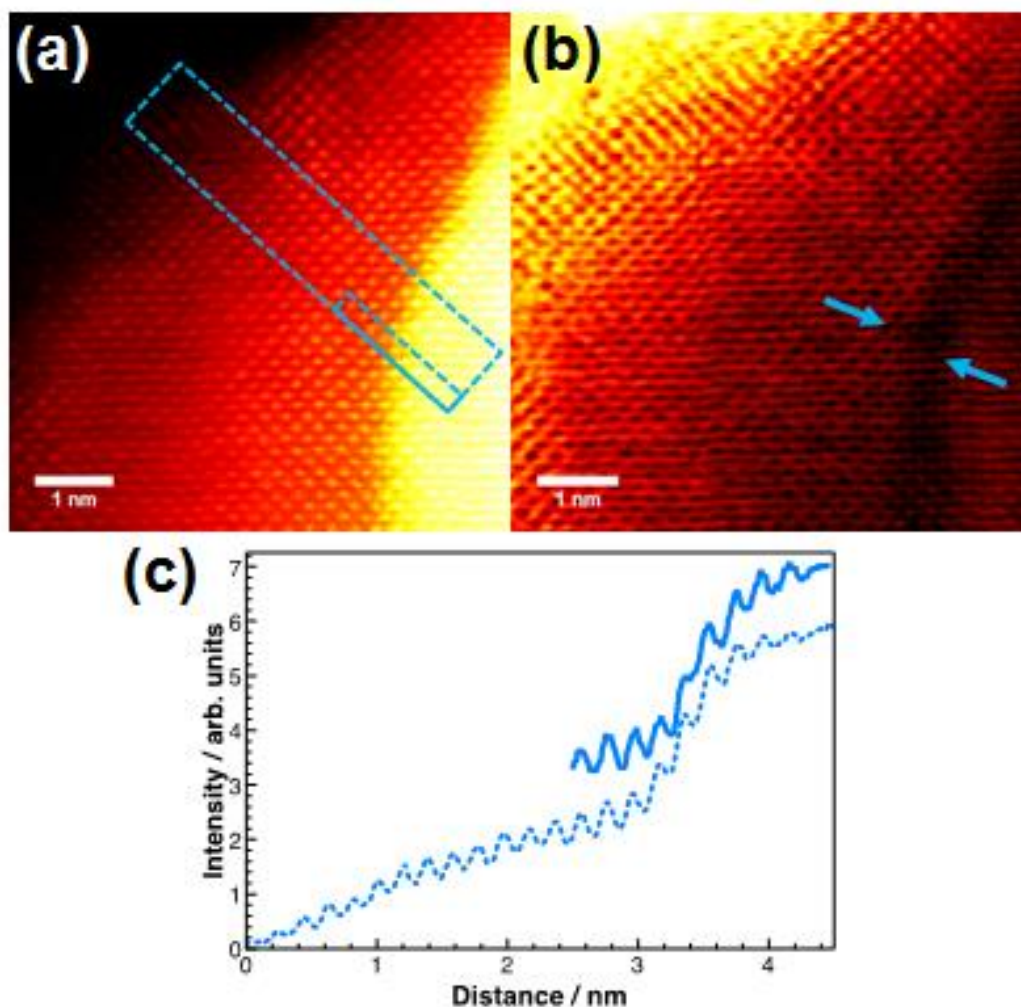
**Figure 5.10: EDX elemental maps from AuRh and AuPd nanorods.** (a)  $\text{Au}_{\text{core}}\text{Pd}_{\text{shell}}$  and (b)  $\text{Au}_{\text{core}}\text{Rh}_{\text{shell}}$  nanorods EDX elemental maps of (1) overlaid core and shell signals, (2) core only, and (3) shell only signals, with (4) corresponding HAADF-STEM images. The dashed lines give schematic indications of the location of the Au-cores and the yellow lines indicate the region of the STEM-HAADF image that corresponds to the EDX map in each case. From reference 2.

Whilst the spatial resolution of EDX is not measured at atomic length scales, in the instrument used in this study it is good enough to reveal details with nanometre proportions. Thus, close examination of the elemental maps of Figure 5.10(b) shows that the Au signal extends out into Rh outgrowths; this is particularly evident in the angular appearance of the Au signal distribution at the end corners of the nanorod in Figure 5.10(b2), which matches the angular appearance of the Rh out-growths apparent in Figure 5.10(b4) and is inconsistent with the morphology of the Au-seed.

### **5.2.2. STEM imaging results**

The observed correlation in the spatial distribution of the respective EDX signals and HAADF image intensity variations of AuPd and AuRh nanorods are suggestive of differing degrees of interfacial mixing between the two systems. To investigate these structures at the atomic scale we require atomically resolved *Z*-contrast imaging to the best possible magnification. Figure 5.11(a) and (b) display simultaneously obtained atomically resolved HAADF and BF images from the interfacial area of an AuPd nanorod.

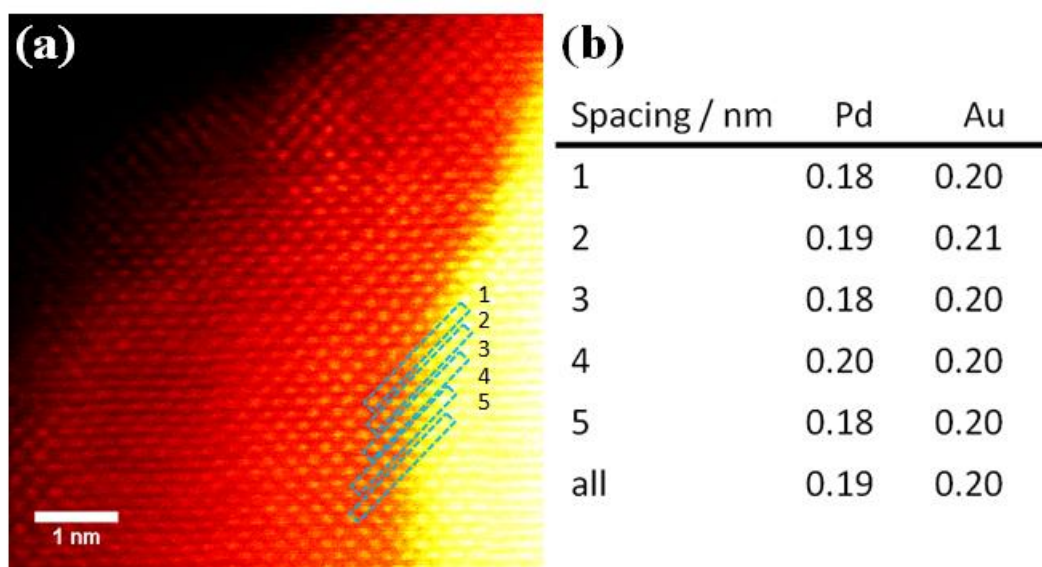
The HAADF image shows an abrupt contrast change comparable to that noted in Figure 5.10(a1) and seen in low magnification in Figure 3.8. Given the typical smooth morphology of the AuPd rods, we can attribute the sharp contrast variation qualitatively to elemental segregation between Au and Pd, caused by their differing atomic numbers. This observation is consistent with findings of other research groups who have also used *Z*-contrast in aberration corrected STEM-HAADF imaging to identify core-shell structure in AuPd nanoparticles prepared via wet chemistry methods.<sup>14-16</sup>



**Figure 5.11: Atomically resolved STEM-HAADF and BF images of the AuPd metal-metal interface.** Simultaneously acquired (a) STEM-HAADF and (b) STEM-BF images of an Au<sub>core</sub>Pd<sub>shell</sub> nanorod, with (c) line intensity profiles taken as indicated in (a). From reference 2.

To quantify how sharp this interfacial region is we plot line intensity profiles in Figure 5.11(c), extracted as indicated from the ‘as taken’ HAADF image using Digital Micrograph software,<sup>17</sup> averaged over four atomic column width (70 pixels), and over on single atomic column width (16 pixels). The image intensity change apparent in Figure 5.11(c) is comparable to the Z-contrast power exponent factor for the instrument used in this study in comparable imaging conditions of 1.5.<sup>18,19</sup> Examination of Figure 5.11(c)

shows the abrupt contrast change occurs over just two atomic layers, and is consistent between both line profiles. As shown in Figure 5.12 this abrupt contrast variation is coincident with a change in lattice spacing from 0.20 nm on the more intense side, consistent with the {200} lattice spacing of Au, and 0.19 nm on the less intense side, consistent with the {200} lattice spacing of Pd (see Figure 5.12).



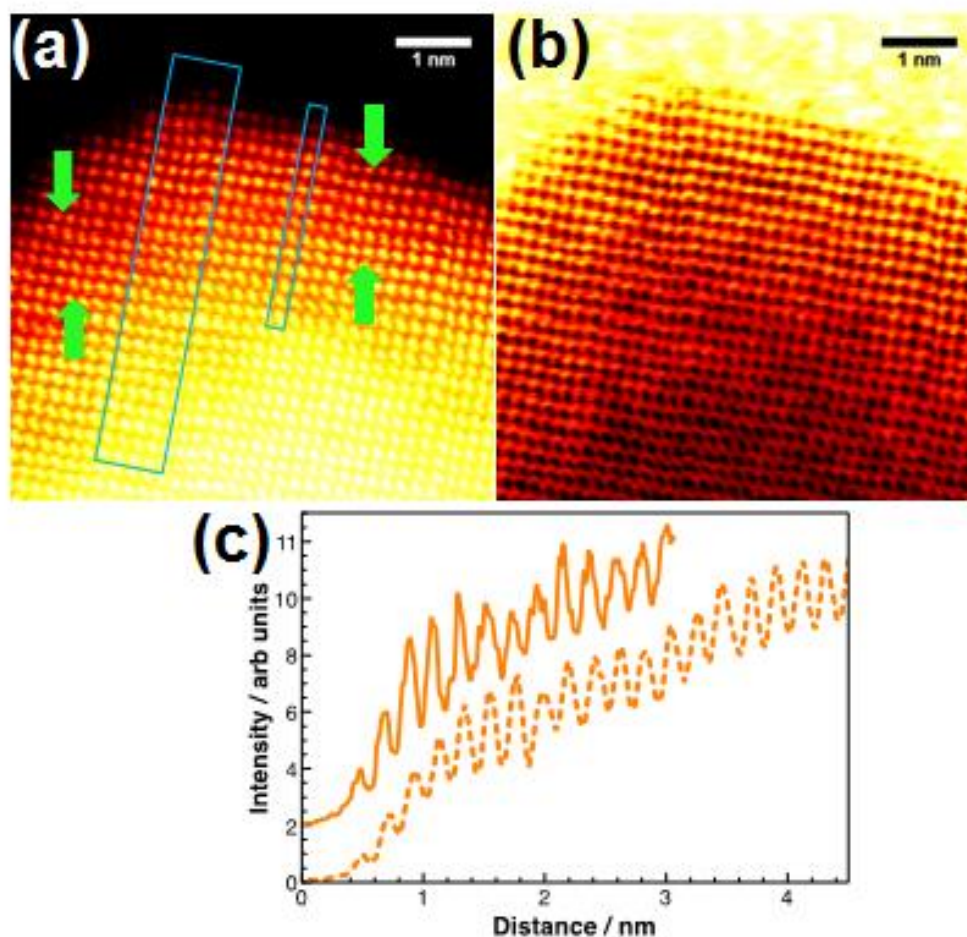
**Figure 5.12: Lattice spacing measurements around the AuPd metal-metal interface.** (a) STEM-HAADF image of AuPd nanorod, and (b) lattice spacing measurements acquired from line intensity profiles taken as indicated in (a).

The measurements shown in Figure 5.12 were taken from single column line intensity profiles (16 pixel width) as indicated. The error in each measurement is estimated to be  $\pm 0.01$  nm, which is comparable to the lattice space difference between Au and Pd; however, by taking a number of measurements we are able to gain confidence in this result through the consistent trend in relative spacing either side of the interface. The 5% lattice mismatch between the bulk lattice constants of Au and Pd (Table 2.2 in Chapter 2), and the measured differences in lattice spacing, can be associated with a strain-induced



phase contrast feature indicated by arrows in the BF image of Figure 5.11(b), which is spatially coincident with the abrupt change in HAADF image intensity at the core-shell interface.

In distinct contrast to AuPd, comparable high magnification HAADF and BF images taken from an AuRh nanorod (Figure 5.13(a) and (b)) show random intensity variation through the interfacial region; indicated by arrows in Figure 5.13(a).



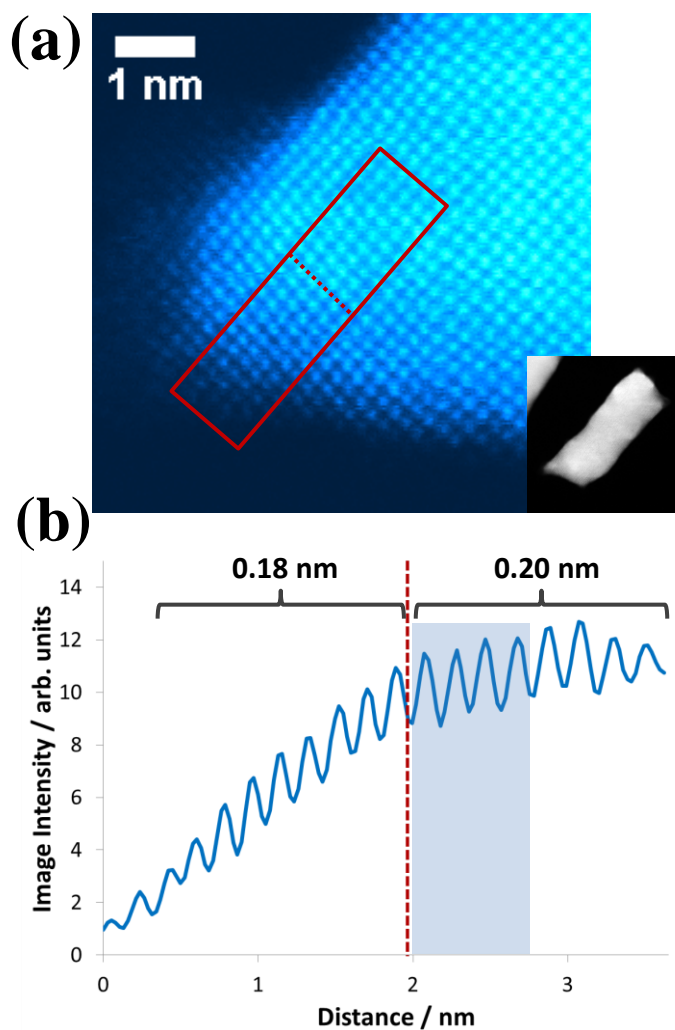
**Figure 5.13: Atomically resolved STEM-HAADF and BF images of the AuRh metal-metal interface** Simultaneously acquired (a) STEM-HAADF and (b) STEM-BF images of an Au<sub>core</sub>Rh<sub>shell</sub> nanorod, with (c) line intensity profiles taken as indicated in (a) over 4 atomic columns (70 pixels) and a single atomic column (16 pixels), taken from reference 2



The random STEM-HAADF image contrast variation can be seen clearly in image intensity profiles, such as the one given in Figure 5.13(c) (averaged over 16 pixels), where no systematic variation in column to column image intensity is apparent. In comparison, the profile taken over four atomic columns (70 pixels) shows a more progressive change in intensity due to the averaging of random column to column variations. Despite the comparable atomic number differences between Au and Pd, and Au and Rh, which might be expected to give comparable image intensity variation in a core-shell system, the line profiles of Figure 5.13(c) and (d) exhibit no clear change in intensity similar to that seen in AuPd.

The randomness in image intensity apparent in Figure 5.13 is typical of this AuRh sample, and has been seen in nanorods with both low and high Rh coverage. It is not altered by varying the focal condition or by tilting the sample relative to the electron beam.<sup>20</sup> In addition, despite the 7% lattice mismatch between Au and Rh (Table 2.1 Chapter 2), the atomic column spacing from the centre to the edge of the nanorod shows no systematic variation, but remains consistent with the Au lattice spacing. However, in AuRh nanorods with thicker Rh coating, such as the example shown in Figure 5.14(a), we do find the smaller lattice spacing corresponding to Rh bulk values appearing in more extensive Rh outgrowths. Figure 5.14(b) shows an image intensity profile, taken as indicated in Figure 5.14(a) averaged over 4 atomic columns (70 pixels), from which the given mean lattice spacings have been measured; these measurements have been conducted to an accuracy of  $\pm 0.01$  nm. The spacing of 0.18 nm is comparable to the {200} spacing of Rh, and 0.20 nm is comparable to the {200} spacing of Au (0.19 nm and 0.20 nm respectively). The change in spacing corresponds to a change the nature of the intensity profile; to right side of the red line in Figure 5.14(b), in the shaded region, random

variations in intensity comparable to those shown in Figure 5.13 are seen, whereas in contrast to the left of the red line a progressive reduction in image contrast is apparent, consistent with reducing sample thickness at the edge of the nanorod.



**Figure 5.14: Lattice spacing measurements around the AuRh metal-metal interface** (a) STEM-HAADF image of the end of a Au<sub>core</sub>Rh<sub>shell</sub> nanorod with thicker Rh out-growth, with lower magnification image of the whole nanorod shown inset. (b) Line intensity profile taken as indicated in (a). The dashed red line indicates where lattice spacing changes and corresponds to the dashed red line in the HAADF-STEM image. The shaded area in (b) highlights a region of randomly varying image contrast.

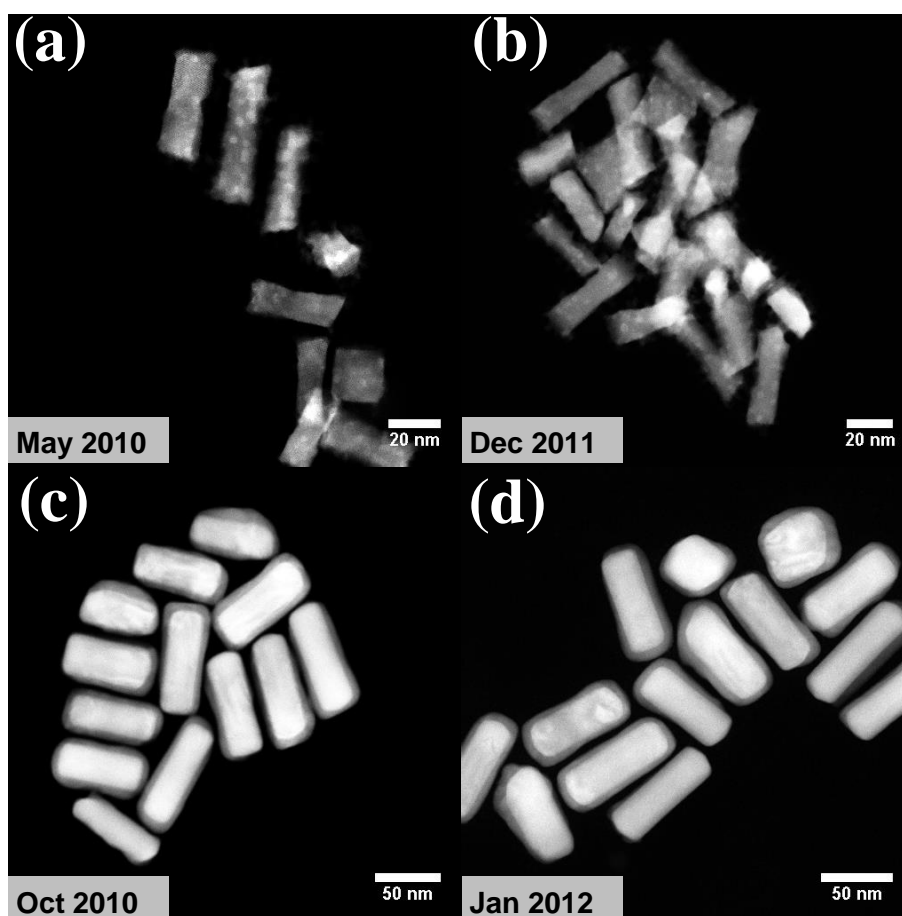
It should also be noted that we see no phase contrast features in AuRh STEM-BF images comparable to that observed in the AuPd system, despite the larger AuRh lattice mismatch. This suggests that lattice mismatch strain may be relieved by alloying at the AuRh interface, where the atomically segregated AuPd interface is strained.

### **5.2.3. Discussion**

Both samples have been monitored for more than one year, whilst stored in solution, with no apparent degradation or alteration in the structure of their interfaces, as illustrated by typical low magnification images of each sample taken more than one year apart given in Figure 5.15. Both samples have also been heated to a temperature of 120°C for several hours while deposited on amorphous carbon TEM supports, again with no apparent alteration in their interfacial structures. Whilst it is not possible for us to directly observe the deposition of shell metals in these systems, and so identify at exactly what stage the interfacial mixing between the metals may have occurred, the sequential method followed, and the long term stability of the observed structures, means that we can infer that the mixing of Au and Rh atoms happened either during or immediately after Rh deposition. This is contrary to their bulk behaviour where they are completely immiscible.<sup>21</sup>

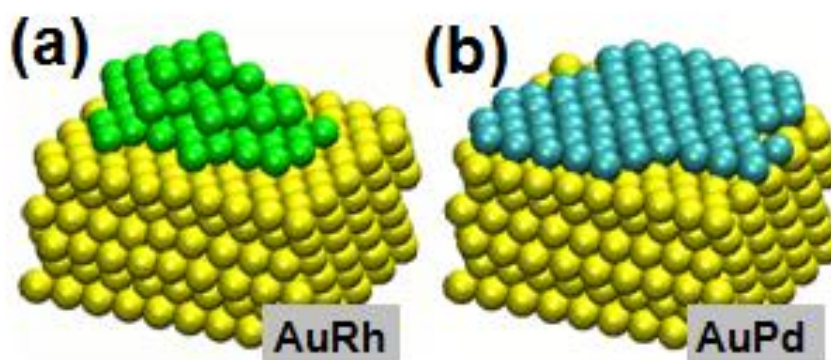
When examined comparatively, the behaviour of these systems cannot be attributed to differences in surface energies or lattice constants, as Au has the lower surface energy and larger lattice constant in both systems, which would indicate a preference for Au coverage of either Rh or Pd; this suggests other factors must be considered. Comparison of cohesive energies shows a significant difference between these systems as the bulk cohesive energy of Rh is higher than that of Au, whereas there is little difference in the

bulk cohesive energies of Au and Pd (from Tables 2.1 and 2.2 in Chapter 2 Au: 3.8 eV/atom, Rh 5.8 eV/atom, and Pd 3.9 eV/atom), and theoretical diatomic binding energies also indicate that AuRh bonds are stronger than AuPd bonds (2.37 eV and 1.44 eV, respectively<sup>22</sup>), which may be relevant to atomic structure in the initial stages of deposition, and thus to the interfacial structures formed.<sup>23</sup>



**Figure 5.15: STEM-HAADF images of AuRh and AuPd nanorods taken more than one year apart** (a) and (b) AuRh nanorods acquired in respectively April 2010 and December 2011. (c) and (d) AuPd nanorods acquired in respectively October 2010 and January 2012.

We have conducted molecular dynamics simulations of the initial stages of Rh and Pd deposition onto Au surfaces to investigate the role played by reaction kinetics in forming the observed interfacial structures. The details of these calculations are described in the supplementary information of reference 2, extracts of which are reproduced in Appendix II. The results indicate that Rh has a tendency to form 3D islands on Au surfaces, where in contrast Pd tends to wet Au surfaces, as shown in Figure 5.16.



**Figure 5.16: Molecular dynamics simulation results for AuRh and AuPd.**

Results from molecular dynamics simulations showing the initial stages of (a) Rh, and (b) Pd deposition on to Au {111} surface at 300K. From reference 2.

For Pd deposited onto Au {100} surface the simulations showed occasional interchange of Pd adatoms with Au surface atoms, which were not observed on Au {111} surface. This difference may be attributed to the greater kinetic stability of the close packed {111} surface, and thus may indicate that the formation of a segregated interface in this system can be linked to the rate of Pd deposition. This suggests that segregation between Au and Pd may be achieved where rapid deposition of a stabilising wetting layer on the Au surface prevents intermixing at the AuPd interface. This observation is

consistent with other theoretical calculations for small AuPd clusters that indicated increasing shell thickness can improve the stability of segregated structures.<sup>24</sup>

Our molecular dynamics results do not show random intermixing between Au and Rh similar to that seen in our experimental observations of this system. However, the clustering behaviour apparent in our AuRh simulations may be instrumental to the observed intermixing if, in the initial stages of Rh overgrowth, mobile Au atoms on still exposed regions of the substrate migrate on to the surface of Rh clusters and become buried by further deposits of Rh. We have seen a tendency for low-coordinated Au atoms to climb on to Rh clusters in simulations conducted at temperatures of up to 500K over nanosecond timescales. In addition, it has recently been reported that clustered growth in a similar Au<sub>core</sub>Pt<sub>shell</sub> nanorod system could be prevented by chemically blocking the route for Au migration.<sup>25</sup>

This work represents the first time that an alloyed interface has been directly visualized to atomic detail for an AuRh system. Surface science studies by Chado *et al.* and by Ovari *et al.* conducted on thermally evaporated Rh on Au reported re-ordering in the metals, such that Au covered the post-deposited Rh, consistent with their relative surface energies.<sup>26,27</sup> They also found the degree of re-ordering was dependent on the relative concentrations of Au and Rh. These findings are broadly consistent with the results presented in this thesis for chemically synthesized AuRh samples; though we note the possible roles played by evaporation temperature, vacuum environment and single crystalline substrates in the growth of thin film systems.

The stability of these structures over long periods of time when stored in solution indicates that, although they may not be in thermodynamic equilibrium, they are kinetically stable, which is a factor that may be highly relevant for their use in practical applications.

In this section, we have shown the capability of ac-STEM in the characterisation of the atomic structures formed through metal-metal interactions in segregated bimetallic nanoparticles, when supported by appropriate molecular dynamics simulations. We have found atomically sharp segregation between miscible Au and Pd, and random intermixing between immiscible Au and Rh, which is the first time that this latter phenomenon has been unambiguously demonstrated. Through comparative study, supported by theoretical simulation, we have shown that the formation of these observed structures can be attributed to kinetic factors.

### **5.3. Conclusions**

In this chapter we have presented work demonstrating the capability of ac-STEM imaging and spectroscopy, supported by appropriate theoretical simulation, in characterising the structure of bimetallic nanoparticles from the single particle level down to the detail of metal-metal atomic structure.

We have shown how Rh deposition proceeds in an uneven, island-like mode, producing core-shell structure with an angular appearance, which proceeds from a facet preference established in the early stages of the synthesis process and with a nanorod end preference that has a significant impact on the optical response of these samples. This work represents the first time that the successful deposition and characterisation of the growth mode of Rh on Au nanorods has been presented.

We have used the full spatial resolution capabilities of ac-STEM imaging and EDX to conduct a comparative study of the metal-metal interfaces of similar AuRh and AuPd segregated nanorods, revealing significant differences in their structure at the atomic scale.

This work has revealed unambiguously the formation of an interfacial alloy layer in an Au<sub>core</sub>Rh<sub>shell</sub> nanorod system; the first time that alloying between these metals has been shown to atomic detail. By taking a comparative approach to the problem of understanding the driving forces behind the formation of structure in these systems, supported by molecular dynamics simulations, we have been able to attribute the observed interfacial structures to reaction kinetics.

The work presented in this chapter has demonstrated the considerable capabilities of ac-STEM imaging and spectroscopy in gaining understanding of both the atomic structure in bimetallic nanoparticles, and the driving forces behind its formation. This work highlights the need for further, more detailed studies of the atomic structures formed in these systems, by making use of ac-STEM alongside controlled sample synthesis to further our understanding of the driving forces behind the formation of structure. Gaining complete knowledge of reaction kinetics, and how they might be manipulated to influence particle structure, would allow the potential for tailored synthesis, and thus the more effective exploitation of the enhanced properties these systems offer.



## List of References

- 144.Chantry, R.L.; Siritwatcharapiboon, W.; Horswell, S.L.; Logsdail, A.J.; Johnston, R.L.; Li, Z.Y., Overgrowth of Rhodium on Gold Nanorods, *J. Phys. Chem. C* **2012**, *116*, 10312-10317
- 145.Chantry, R.L.; Siritwatcharapiboon, W.; Horswell, S.L.; Khanal, B.P.; Zubarev, E.R.; Atanasov, I.; Johnston, R.L.; Li, Z.Y., An Atomistic View of the Interfacial Structures of Au-Core Rh and Pd-Shell Nanorods, *Nanoscale*, **2013**, *5*, 7452-7457
- 146.He, W.; Wu, X.; Liu, J.; Zhang, K.; Chu, W.; Feng, L.; Hu, X.; Zhou, W.; Xie, S., Pt-Guided Formation of Pt-Ag Alloy Nanoislands on Au Nanorods and Improved Methanol Electro-Oxidation, *J. Phys. Chem. C* **2009**, *113*, 10505-10510
- 147.Nikoobakht, B.; El-Sayed, M.A., Preparation and Growth Mechanism of Gold Nanorods Using Seed-Mediated Growth Method, *Chem. Mater.* **2003**, *15*, 1957-1962
- 148.Wang, Z. L.; Mohamed, M. B.; Link, S.; El-Sayed, M. A., Crystallographic Facets and Shapes of Gold Nanorods of Different Aspect Ratios, *Surf. Sci.*, **1999**, *440*, L809-L814.
- 149.Katz-Boon, H.; Rossouw, C. J.; Weyland, M.; Funston, A. M.; Mulvaney, P.; Etheridge, J., Three-Dimensional Morphology and Crystallography of Gold Nanorods, *Nano Lett.*, **2011**, *11*, 273-278.
- 150.Grzelczak M.; Perez-Juste J.; Rodriguez-Gonzalez B.; Liz-Marzan L.M., Influence of Silver Ions on the Growth Mode of Platinum on Gold Nanorods, *J. Mater. Chem.*, **2006**, *16*, 3946-3951
- 151.Draine B.T.; Flatau P.J., Discrete Dipole Approximation for Scattering Calculations, *J. Opt. Soc. Am. A*, **1994**, *11*, 1491-1499
- 152.Johnson, P.B.; Christy, R.W., Optical Constants of the Noble Metals, *Phys. Rev. B*, **1972**, *6*, 4370-4379
- 153.*Handbook of Optical Constants of Solids*, ed. Palik, E.D., Academic Press, London, 1998
- 154.Kibler, L.A.; Kleinert, M.; Kolb, D.M., The Initial Stages of Rhodium Deposition on Au(111), *J. Electroanal. Chem.*, **1999**, *467*, 249-257
- 155.Liu, C.; Bader, S.D., Absence of Ferromagnetism in Epitaxial Films of Ultrathin Pd, Rh, and Rh on Pd grown on Au(100), *Phys. Rev. B*, **1991**, *440*, 12062-12065
- 156.Altman, E.I.; Colton, R.J., Growth of Rh on Au(111): Surface Intermixing of Immiscible Metals, *Surf. Sci. Lett.* **1994**, *304*, L400-L406

157. Akita, T.; Hiroki, T.; Tanaka, S.; Kojima, T.; Kohyama, M.; Iwase, A.; Hori, F., Analytical TEM Observation of Au-Pd Nanoparticles Prepared by Sonochemical Method, *Catal. Today*, **2008**, *131*, 90-97
158. Ding, Y.; Fan, F.; Tian, Z.; Wang, Z.L., Atomic Structure of Au-Pd Bimetallic Alloyed Nanoparticles, *J. Am. Chem. Soc.*, **2010**, *132*, 12480-12486
159. Ferrer, D.; Blom, D.A.; Allard, L.F.; Mejia, S.; Perez-Tijerina, E.; Jose-Yacaman, M., Atomic Structure of Three-Layer Au/Pd Nanoparticles Revealed by Aberration Corrected Scanning Transmission Microscopy, *J. Mater. Chem.*, **2008**, *18*, 2442-2446
160. Digital Micrograph, Version 1.83.842, Gatan Inc. USA
161. Wang, Z.W.; Li, Z.Y.; Park, S.J.; Abdela, A.; Tang, D.; Palmer, R.E., Quantitative Z-Contrast Imaging in the Scanning Transmission Electron Microscope with Size-Selected Clusters, *Phys. Rev. B* **2011**, *84*, 073408
162. Wang, Z.W.; Palmer, R.E., Intensity Calibration and Atomic Imaging of Size-Selected Au and Pd Clusters in Aberration-Corrected HAADF-STEM, *J. Phys. Conf. Ser.*, **2012**, *371*, 012010
163. Langlois, C.; Wang, Z.W.; Pearmain, D.; Ricolleau, C.; Li, Z.Y., HAADF-STEM imaging of CuAg core-shell nanoparticles, *J. Phys. Conf. Ser.*, **2010**, *241*, 012043
164. Curtarolo, S.; Morgan, D.; Ceder, G., Accuracy of *Ab Initio* Methods in Predicting the Crystal Structures of Metals: A Review of 80 Binary Alloys, *Calphad* **2005**, *29*, 163-211
165. Morse, M.D., Clusters of Transition-Metal Atoms, *Chem. Rev.* **1986**, *86*, 1049-1109
166. Mutaftschiev, B., *The Atomistic Nature of Crystal Growth*, Springer: Berlin, 2001.
167. Logsdail, A.J.; Johnston, R.L., Interdependence of Structure and Chemical Order in High Symmetry (PdAu)<sub>N</sub> Nanoclusters, *RSC Adv.*, **2012**, *2*, 5863-5869
168. Fennell, J.; He, D.S.; Tanyi, A.M.; Logsdail, A.J.; Johnston, R.L.; Li, Z.Y.; Horswell, S.L., *J. Am. Chem. Soc.*, **2013**, *135*, 6554-6561
169. Chado, I.; Scheurer, F.; Bucher, J.P., Absence of Ferromagnetic Order in Ultrathin Rh Deposits Grown Under Various Conditions on Gold, *Phys. Rev. B* **2001**, *64*, 094410
170. Ovari, L.; Bugyi, L.; Majzik, Z.; Berko, A.; Kiss, J., Surface Structure and Composition of Au-Rh Bimetallic Nanoclusters on TiO<sub>2</sub>(110): a LEIS and STM Study, *J. Phys. Chem. C* **2008**, *112*, 18011-18016

---

## Chapter 6

# Localised Surface Plasmon Response of Bimetallic Nanorods

Bimetallic nanoparticles offer considerable potential in the developing field of plasmonic enhancements to, and monitoring of, catalytic reactivity.<sup>1-4</sup> They allow the possibility to combine the localised surface plasmon resonance (LSPR) response of one metal with the catalytic reactivity of another. In addition, the sensitivity of bimetallic nanoparticle LSPR to structure and composition gives unrivalled potential to tune the response to the frequency desired for specific applications.<sup>5,6</sup> Recent studies have demonstrated plasmonic enhancements to catalytic reactivity in bimetallic nanorods using laser irradiation,<sup>2,4</sup> and identified the possibility for harvesting solar energy through this approach; however, the mechanisms responsible for enhancement were not identified.

The origin of bimetallic LSPR must lie in the dielectric interactions between the constituent metals. So gaining this necessary level of understanding to allow full control over this property, and thus facilitate its effective exploitation, requires characterisation of LSPR to the best possible spatial resolution, with direct correlation to structural

characterisation. The work presented in this chapter uses the single particle LSPR characterisation capabilities of electron energy loss spectroscopy in a scanning transmission electron microscope (STEM-EELS), alongside elementally sensitive STEM-HAADF imaging, to characterise the LSPR response of catalytically relevant AuPd and AuRh core-shell nanorod systems.

The samples chosen for this work both have shell metals that are active catalysts in bulk form deposited onto Au template nanorods, and thus are systems that are of interest for investigating plasmonic enhancement to reactivity; AuPd nanorods have already been shown to be desirable in this regard.<sup>2,4</sup> They are also of interest in the more general understanding of bimetallic LSPR, as they combine metals with very different surface plasmon responses. The surface plasmon of Au occurs in the visible part of the spectrum, while the responses of the shell metals of the two systems studied in this chapter, Pd and Rh, occur in the UV part of the spectrum.<sup>7-13</sup> This requires characterisation of LSPR response over an extended energy loss range, from 1.5 eV to 9.5 eV, to cover the resonances of both core and shell metals, which is experimentally challenging, but allows a greater possibility to identify the impact of the shell response than might be the case in systems with more comparable plasmonic properties, such as Au and Ag. Also, by characterising two, dielectrically similar but structurally different systems, with AuPd having an even shell and clear interface where AuRh has a much more irregular appearance, we hope to gain further insights in to structural dependence of LSPR response. In Section 6.1 we present results investigating the LSPR response of AuPd nanorods, then in Section 6.2 we examine the LSPR response of dielectrically similar but more structurally complex AuRh nanorods. Finally in Section 6.3 we use discrete dipole

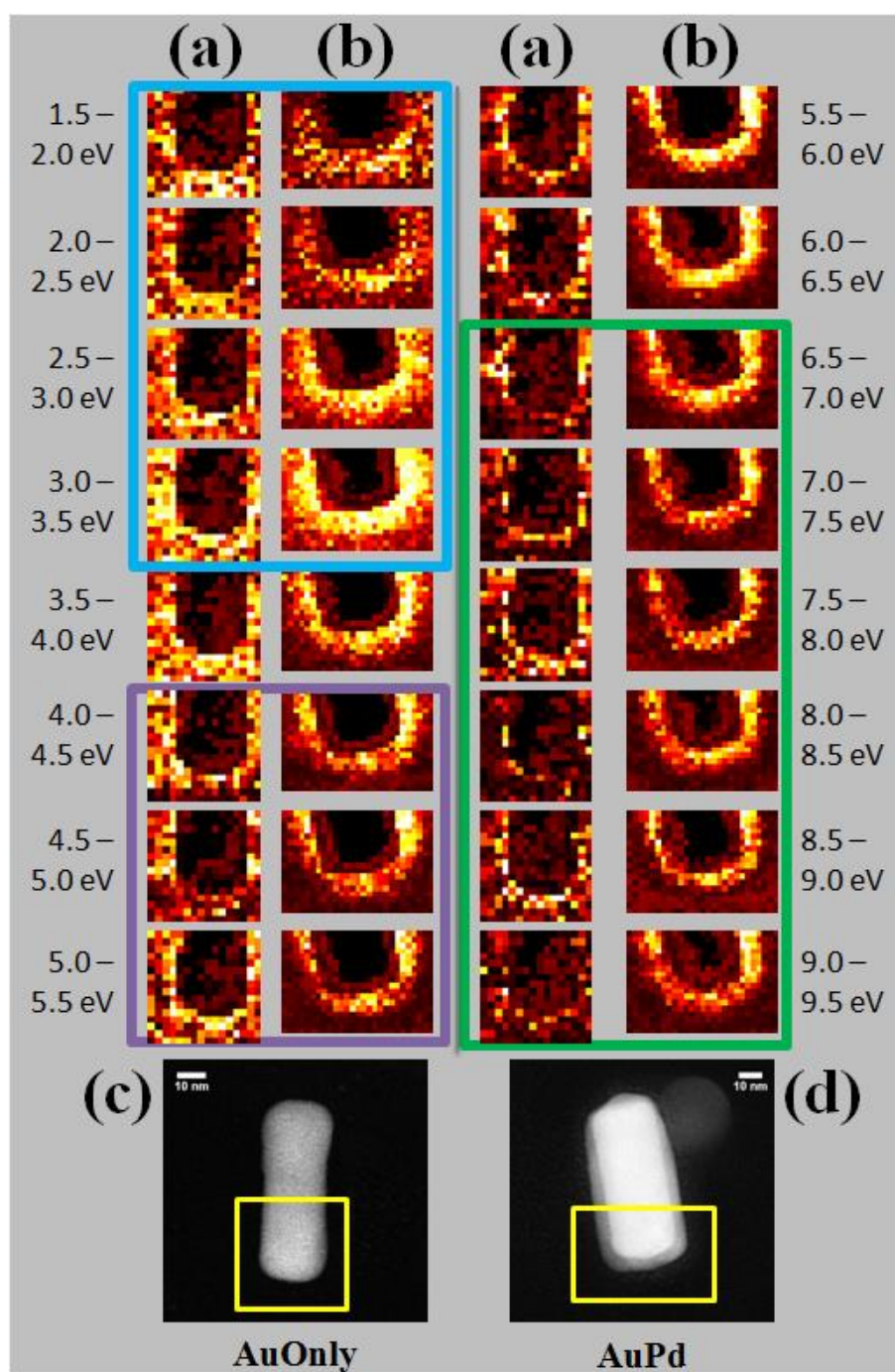
approximate (DDA) simulation to systematically investigate the impact that uneven shell growth has on LSPR response.

All of the STEM-EELS data, associated analysis, and the majority of the DDA simulation work were conducted by the author under the supervision of Dr Ziyou Li. In Section 6.3 DDA simulation work presented in Figures 6.11 and 6.12 was carried out by Nima Zardoshti, a second year undergraduate summer project student, under the supervision of the author. The AuPd sample was synthesised by Bishnu Khanal and Eugene Zubarev (Department of Chemistry, Rice University, United States of America) and the Au-only and AuRh nanorod samples were synthesised by Wilai Siriwatcharapiboon and Sarah Horswell (Department of Chemistry, University of Birmingham).

## **6.1 LSPR Response of AuPd Nanorods**

### ***6.1.1. STEM-EELS spectrum image mapping***

Figure 6.1 shows typical examples of STEM-EELS plasmon maps taken from the ends of Au-only and AuPd nanorods. The maps show the integrated signal intensity extracted from each pixel spectrum over arbitrary 0.5 eV energy loss ranges using Digital Micrograph software.<sup>14</sup> The signals were extracted after subtraction of a background signal based on a power law fitting made over the 0.8 eV to 1.0 eV signal range. Each pixel spectrum was acquired using 3 second dwell time, 0.05 eV/channel dispersion and a 2 mm aperture on the spectrometer, with a microscope emission current lowered to 40  $\mu$ A giving energy resolution of around 0.7 eV. These parameters were applied consistently for all of the results presented in this chapter.



**Figure 6.1:** STEM-EELS plasmon maps from the ends of Au-only and AuPd nanorods. (a) Au-only and (b) Au<sub>core</sub>Pd<sub>shell</sub> nanorods, taken as indicated respectively in the images (c) and (d). Coloured boxes highlight maps showing marked differences between the Au-only and AuPd response.

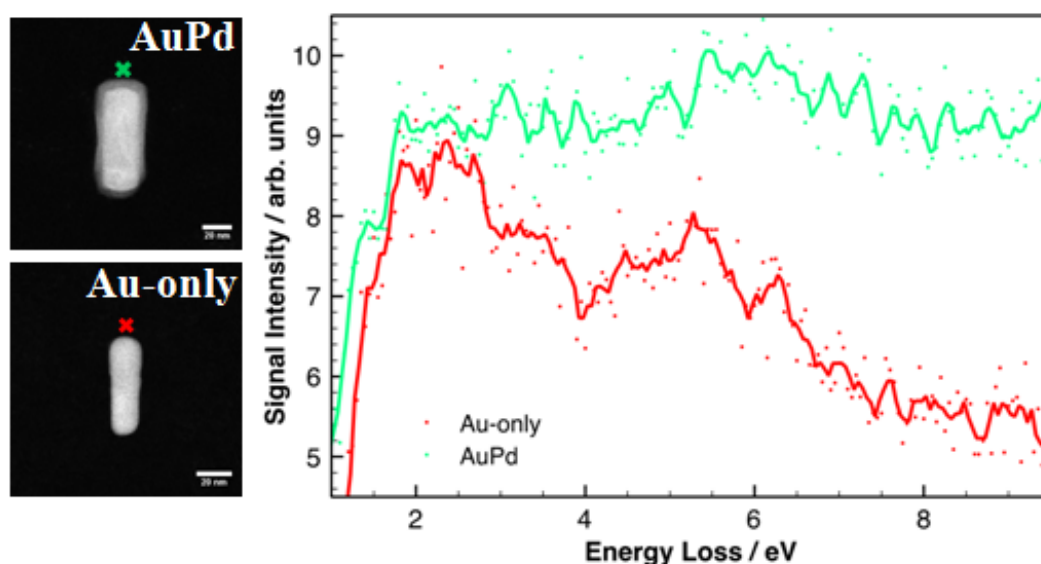
The maps shown in Figure 6.1 cover arbitrary 0.5 eV energy loss windows through the energy loss range from 1.5 eV to 9.5 eV to reveal variations in the induced fields

caused by the LSPR response of each system from visible through to UV wavelengths. Differences in response between the monometallic and bimetallic systems shown in Figure 6.1 can be seen by comparing the trend in mapped signal intensity, both spatially and energetically, between these two series of maps. Maps with particularly distinct differences between the Au response and the AuPd response are highlighted in Figure 6.1 by coloured boxes and are discussed further below.

For energy losses above around 4.0 eV the AuPd nanorod has a generally more uniform response than the Au-only nanorod, with consistent appearance of mapped signal evenly around the end of the nanorod evident in all of the maps from 4.0 eV to 9.5 eV energy loss; over this same range the Au-only signal shows more variation. The difference between Au-only and AuPd response is particularly noticeable from 4.0 eV to 5.5 eV energy loss, highlighted by the purple box in Figure 6.1, and from 6.5 eV to 9.5 eV energy loss, highlighted by the green box. In both of these instances the Au-only signal can be seen to fluctuate from map to map, with dips in signal strength particularly apparent in the 4.5 eV to 5.0 eV, 7.0 eV to 7.5 eV and 8.0 eV to 8.5 eV maps.

For comparison with these observations Figure 6.2 shows typical experimental point spectra taken from the ends of other Au-only and AuPd nanorods approximately as indicated in their STEM-HAADF images. The raw experimental data is shown as dots and lines show least squares fits to each data set. These spectra are the sum of 4 individual spectra that were acquired using the experimental parameters as set out above, and are background subtracted using the same procedure applied in producing the maps of Figure 6.1. The spectra have been offset in the y-axis for clarity of plotting. Comparison of the mapped and spectral results of Figures 6.1 and 6.2 show consistent patterns in the differing trends for these two sets of Au-only and AuPd nanorods. In Figure 6.2 the Au-only signal

shows a greater variation with an overall trend of a generally falling signal across this energy loss range, whereas the AuPd signal has a more general signal strength and weaker individual spectral features.



**Figure 6.2:** Typical examples of Au-only and AuPd STEM-EELS spectra over the energy loss range from 1.5 eV to 9.5 eV. STEM-EELS experimental point spectra for taken approximately as indicated in the associated images from the ends of Au-only (red) and Au<sub>core</sub>Pd<sub>shell</sub> (green) nanorods. Both spectra are background subtracted using a power law fit over the energy loss window 0.8 eV to 1.0 eV. The ‘as taken’ data shown by dots and noise reduced data, using least squares fitting, is shown as solid lines.

Consistent with the Au-only to AuPd variation highlighted by the purple box in Figure 6.1, the Au-only signal in Figure 6.2 shows a number of clear spectral features, within a broader shoulder feature, between 4 eV and 6.5 eV; these features can be associated with interband responses of Au.<sup>9</sup> In addition, a weak, broad feature can be seen in the AuPd spectrum from around 5.0 eV to 8.0 eV, which is consistent with the generally stronger response apparent in the AuPd maps of Figure 6.1 for all energy losses above 5

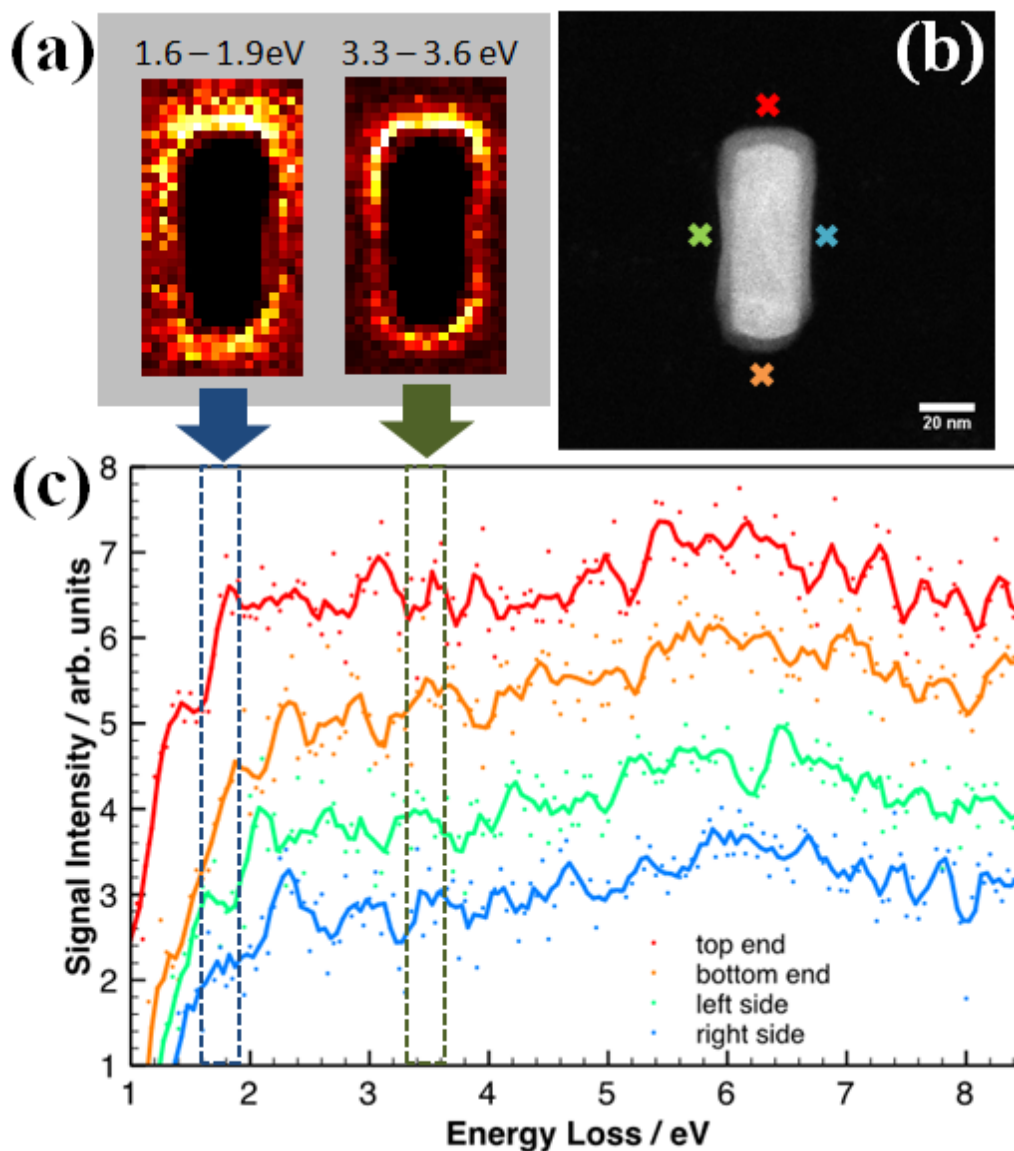


eV, highlighted by the green box in Figure 6.1. This latter observation coincides with the location of the Pd surface plasmon resonance that has been measured experimentally at 7 eV to 9 eV in thin film systems (Table 2.4, Chapter 2).<sup>9,12,13</sup>

The variations in response between monometallic and bimetallic experimental maps in the energy loss region highlighted by the blue box in Figure 6.1, between 2.5 eV and 3.5 eV, have field patterns that are localised to the ends of the nanorods, which suggests these are induced by longitudinal LSPR modes. For the Au-only nanorod the longitudinal field pattern is only clearly distinguishable in the 1.5 eV and 2.0 eV map, whereas for AuPd the longitudinal field pattern persists over a wider energy loss range covering several maps from 1.5 eV to 3.5 eV. The strength of the AuPd mapped longitudinal response appears to vary over this range with a dip around 2.0 eV to 2.5 eV, and a more intense response in the 3.0 eV to 3.5 eV map. These results suggest there may be a significant modification to the longitudinal LSPR behaviour caused by the addition of the Pd shell; however, it is difficult to unambiguously identify individual spectral features in single spectra such as those shown in Figure 6.2 that are consistent with these observations, so to investigate this further we have conducted mapping over whole AuPd nanorods.

Maps covering whole nanorods have reduced spatial resolution compared to the maps of the nanorod ends shown Figure 6.1, and so are less sensitive to more localised variations in signal such as are apparent in the bottom left corner of the AuPd maps of Figure 6.1(b) where we see a corresponding variation in image contrast within the Pd shell. However, whole nanorod maps have the advantage of sampling spectra over a greater spatial area, including from both ends of the nanorod, and thus can more clearly identify the localised field patterns that are typical of longitudinal LSPR modes. Figure 6.3(a) shows two spectrum image maps taken from the AuPd nanorod shown in the STEM-

HAADF image of Figure 6.3(b) that demonstrate signals localised to the ends of the nanorods that are indicative of longitudinal modes of oscillation.



**Figure 6.3:** STEM-EELS spectrum image maps and point spectra taken around an AuPd nanorod. (a) Longitudinal resonances identified from STEM-EELS spectrum image maps. (b) STEM-HAADF image of the AuPd nanorod showing the approximate positions at which the point spectra shown in (c) were acquired. (c) Point spectra with dashed boxes indicating the energy loss ranges covered by the spectrum image maps of (a).

The maps shown in Figure 6.3(a) correspond to two peaks that can be identified in the mapped longitudinal field intensity, appearing in the energy loss ranges from 1.6 eV to 1.9 eV and from 3.3 eV to 3.6 eV. These were found by manually scanning the mapped 0.3 eV wide energy loss window across the spectrum in 0.05 eV increments. The map energy loss range of 0.3 eV wide was found to produce the most clearly defined field patterns. Given that the observed fields are induced by electron oscillations, it seems likely that resonant modes can be associated with these peaks in mapped field intensity, and thus lie within each of these identified energy loss ranges, indicating this system has two longitudinal LSPR modes.

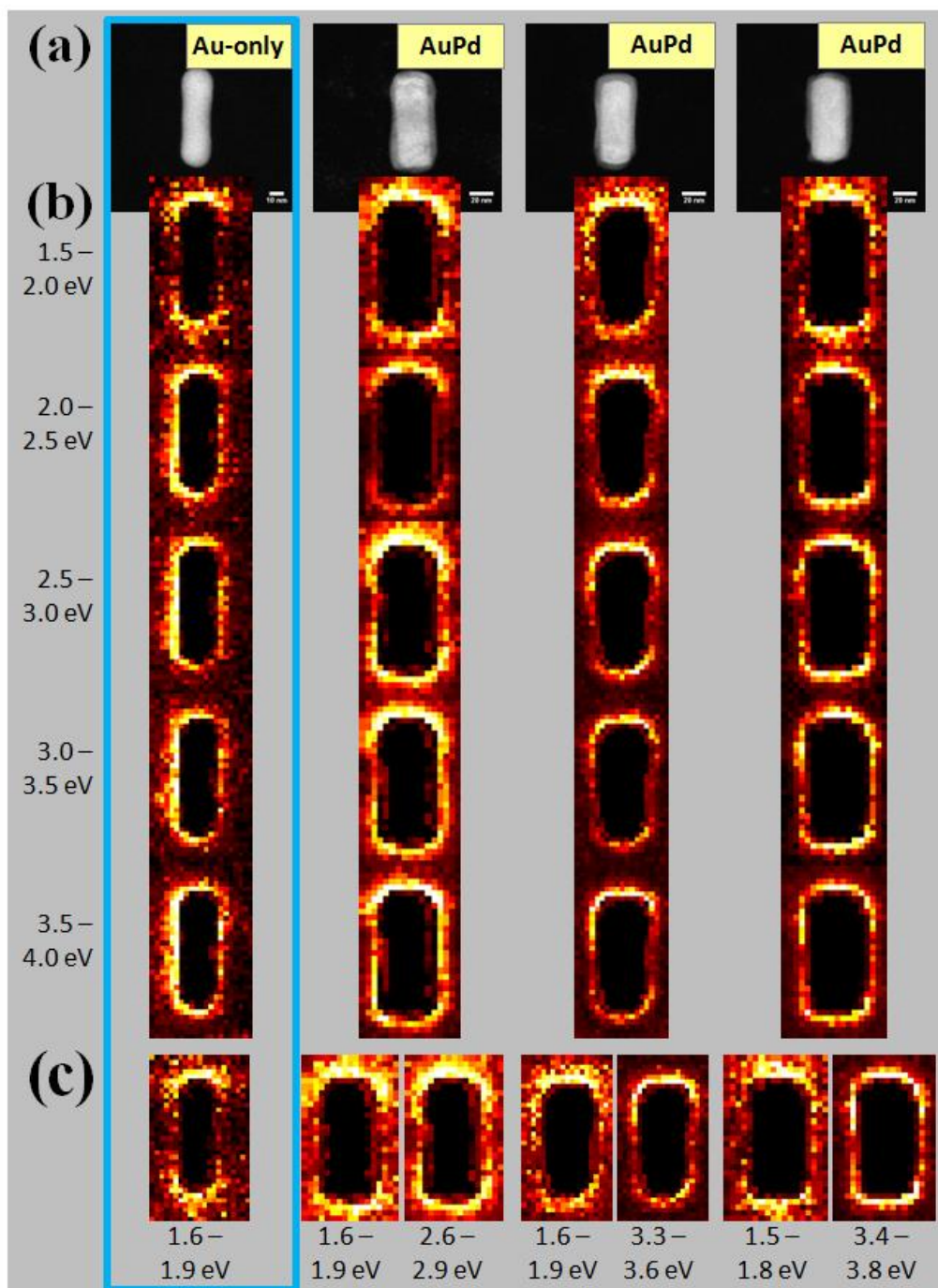
In addition to acquiring the spectrum image maps shown in Figure 6.3(a) we also acquired a series of point spectra from around the same nanorod for comparison. These were taken approximately at the locations around the AuPd nanorod as indicated in Figure 6.3(b), using the same acquisition parameters described above. The spectra are shown in Figure 6.3(c), with the red and orange plots taken from positions at the ends of the nanorod and the green and blue plots from positions at the sides of the nanorod. The raw experimental data are given as dots and least square fitting to the data as lines. The energy loss ranges that correspond to the maps of Figure 6.3(a) are outlined by dashed boxes in Figure 6.3(c) for comparison. Close examination of the region of the spectra corresponding to the lower energy map, from 1.6 eV to 1.9 eV, shows shoulder features appearing in the end spectra (red and orange in Figure 6.3(c)), with no corresponding features apparent in the side spectra (green and blue in Figure 6.3(c)). The difference between the side and end spectra over the 3.3 eV to 3.6 eV energy loss range is less well defined, but can be seen in the sharper peaks appearing in features in this energy range in the end spectra compared to the side spectra suggesting this longitudinal mode overlaps

with another, less well defined feature in the AuPd spectrum. We find longitudinal response over extended energy loss range, with two peaks in mapped field intensity, in all AuPd nanorods of this type. Figure 6.4 shows maps over arbitrary 0.5 eV energy loss windows from 1.5 eV to 4.0 eV for the nanorod of Figure 6.3 and two further examples.

For all three of the AuPd nanorods shown in Figure 6.4 field patterns localised to the ends of the nanorods can be seen in all of the given maps, with a consistent pattern of extended longitudinal response. In addition, Figure 6.4(c) also shows maps taken over 0.3 eV energy loss ranges where we have identified peaks in mapped longitudinal field intensity for each nanorod; in all three cases two peaks in intensity were identified, one between 1.5 eV and 2.0 eV and a second at higher energy loss. Corresponding maps for a whole Au-only nanorod, shown in Figure 6.4 for comparison, only show a longitudinal mode field pattern in the 1.5 eV to 2.0 eV map, and we find only one peak in mapped intensity of its longitudinal LSPR response.

Spectrum image maps sample the integrated signal intensity for the selected energy loss ranges over large numbers of acquired spectra. For example, the maps of Figure 6.3 were acquired over a region 19 pixels wide by 35 pixels deep and thus sample integrated signal intensity for the selected energy loss ranges over a total of 665 acquired spectra. Being able to sample large numbers of spectra in this way, across a number of AuPd nanorods, is a distinct advantage in characterising the weak signals with low signal to noise ratio that are inherent to this system. Through the use of this technique we can unambiguously identify the appearance of longitudinal LSPR modes, covering an extended energy loss range and with multiple peaks in the intensity in these AuPd nanorods. Although the response we see is a combined response of core and shell, as we see nothing

similar in Au-only nanorods, we can attribute the origin of this behaviour to the addition of the Pd shell.



**Figure 6.4:** STEM-EELS spectrum image maps from whole Au and AuPd nanorods. (a) STEM-HAADF images of the nanorods with (b) spectrum image maps for arbitrary 0.5 eV energy loss ranges from 1.5 eV to 4.0 eV, and (c) 0.3 eV wide energy loss ranges where peaks in longitudinal field intensity are found.

Comparison of the energy loss ranges for the identified peaks in AuPd longitudinal LSPR induced field intensity shows that the lower energy loss peak in the mapped longitudinal response appears at markedly similar energy loss ranges across all three nanorods, whereas the peak in mapped longitudinal response occurring in the 3.0 eV to 4.0 eV range shows variation from nanorod to nanorod. Examination of the STEM-HAADF images of Figure 6.4(a) shows all three have comparable Au-cores, are of a similar size and have relatively uniform and even shells with only small variations in their Pd coverage. Given the similarity in the energy loss at which the lower peak in intensity occurs with the longitudinal LSPR response of Au-only nanorods, it seems likely that the consistency in the energy loss at which this mode occurs can be associated with the uniformity of the Au-cores. This observation, together with the consistency of the frequency of this response with the longitudinal LSPR of the Au-only nanorod, allows us to attribute the origin of this mode to the response of the Au-core. It is interesting to note that this response is not noticeably modified by small variations in the Pd-shell. In comparison, variations in frequency of the longitudinal mode appearing at higher energy losses indicate this mode may be more sensitive to shell morphology. This observation is consistent with it originating from the longitudinal response of the Pd shell. However, it may also reflect sensitivity in LSPR caused by coupling between interband responses and the longitudinal LSPR response of the Pd shell. This latter observation is consistent with the appearance of broader, weaker features in the side spectra compared to the end spectra of Figure 6.3 in the energy loss ranges where the higher energy loss longitudinal peak in field intensity was identified.

These results demonstrate a more complex longitudinal LSPR response in AuPd core-shell nanorod systems, with two peaks in longitudinal field intensity that can be

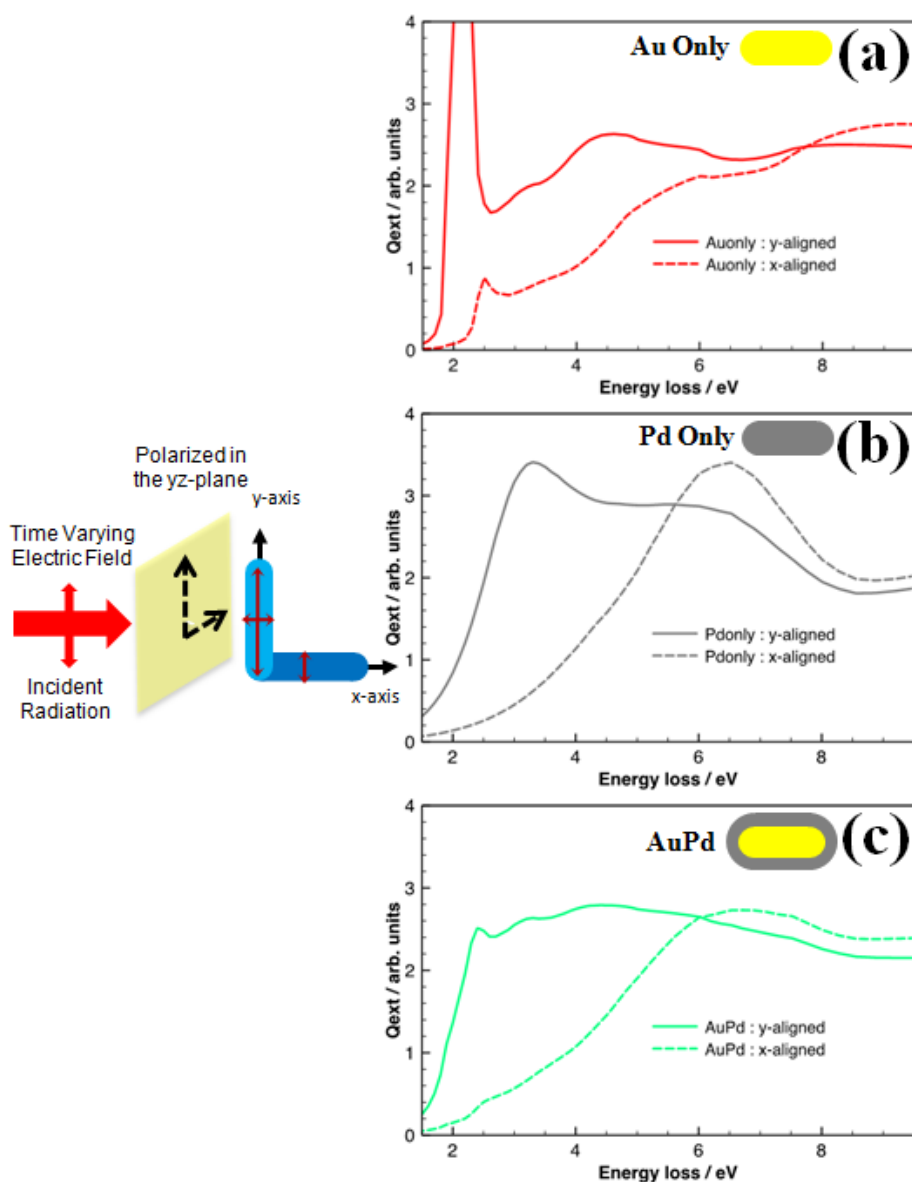
associated with two longitudinal modes originating respectively from the responses of the Au-core and the Pd-shell. To investigate this further we have conducted DDA simulations, which are presented in the next section.

### **6.1.2. Comparison to DDA simulation**

Figure 6.5 shows DDA simulation results prepared using DDSCAT software,<sup>15</sup> for Au-only, Pd-only and AuPd nanorod targets. Conducting the simulation with the targets in two different orientations relative to the incident radiation (shown schematically) allows us to identify the impact that longitudinal LSPR modes on the spectra. With the target nanorods oriented along the y-axis (described as ‘y-aligned’) and incident radiation polarised along y and z axes, the simulation excites both transverse and longitudinal LSPR modes; this is the orientation that is most comparable to STEM-EELS excitation, where the radial polarisation of the beam electric field also has the potential to excite transverse and longitudinal modes simultaneously. With the target oriented along the x-axis (described as ‘x-aligned’ in the plots) only transverse modes are excited.

The Pd-only spectra of Figure 6.5(b) shows a broad transverse LSPR mode occurring at between 6 eV and 7 eV, consistent with the Pd surface plasmon resonance,<sup>9,12,13</sup> with the response falling continuously at energy losses below 6 eV. In comparison the transverse LSPR of the Au-only target shows a relatively weaker, but more clearly defined response at around 2.5 eV. Comparison of these spectra with the x-aligned AuPd spectrum shows the transverse response of the AuPd nanorod target is more consistent with the Pd-only target, with only a weak feature appearing at around 2.5 eV associated with the Au-core response. Comparison of the y-aligned and x-aligned simulated spectra shows the emergence of a longitudinal response at around 2.0 eV for the

Au-only target and between 3.0 eV and 3.5 eV for the Pd-only target. In contrast, the simulated AuPd spectra of Figure 6.5(c) show the emergence of a much broader and weaker longitudinal response than either of the monometallic targets. This is consistent with the damping that is generally caused by the introduction of the metal-metal interface in segregated particles.<sup>16</sup>



**Figure 6.5:** Simulated spectra for Au-only, Pd-only and AuPd nanorods.

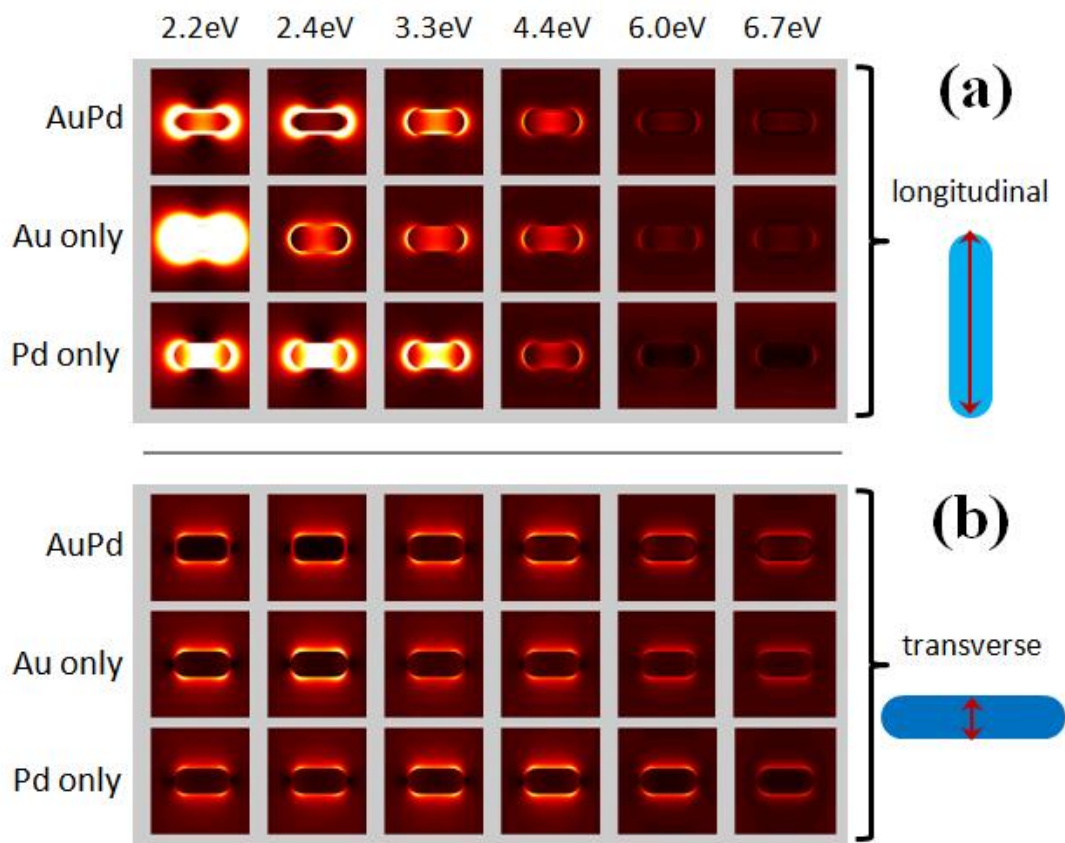
(a) Au-only, (b) Pd-only, and (c) Au<sub>core</sub>Pd<sub>shell</sub>, with incident radiation polarised along the y and z axes, and the target aligned along the x (dashed line) and y (solid line) axes, showing the emergence of the longitudinal excitation.



The y-aligned AuPd spectrum shows only one feature apparent at around 2.0 eV to 2.5 eV that can unambiguously be associated with a longitudinal LSPR mode. Given that the Pd-only target has no features occurring at this energy loss, this feature can be attributed to the longitudinal LSPR response of the Au-core. We do not see a clear second longitudinal peak between 3.0 eV and 4.0 eV in these simulated results. However, field simulations conducted where we see weak features in the spectrum (given in Figure 6.6) do show longitudinal field patterns for the AuPd target persisting over an extended energy loss range, and not just at energy loss associated with the peak feature at between 2.0 eV and 2.5 eV in the spectrum of Figure 6.5(c). This observation is consistent with the extended longitudinal responses found in the experimental results of Figures 6.1 and 6.4.

It is notable that comparison of the field simulations with the simulated spectra of Figure 6.5 shows that for all three targets the strongest fields induced by longitudinal LSPR modes do not occur at the energy loss where the signal strength in the spectrum is greatest, but in general occur at energy loss below the peak. For example, the Pd-only longitudinal feature in the simulated spectrum of Figure 6.5(b) occurs at approximately 3.3 eV, whereas the strongest simulated field shown in Figure 6.6(a) is at 2.4 eV, and both this and the simulated field at 2.2 eV are stronger than the field at 3.3 eV. However, this is not a pattern that we have observed experimentally, suggesting it may be due to differences between optical and fast electron LSPR excitation, in particular in respect of interactions between LSPR and surface plasmon resonance responses.

Our simulation results support the extended longitudinal response we observe experimentally, but do not indicate the presence of two longitudinal modes in this system. It is interesting to compare our AuPd results with the AuAg work conducted by Rodriguez-Gonzalez *et al.* who demonstrated the presence of a clearly identifiable longitudinal and



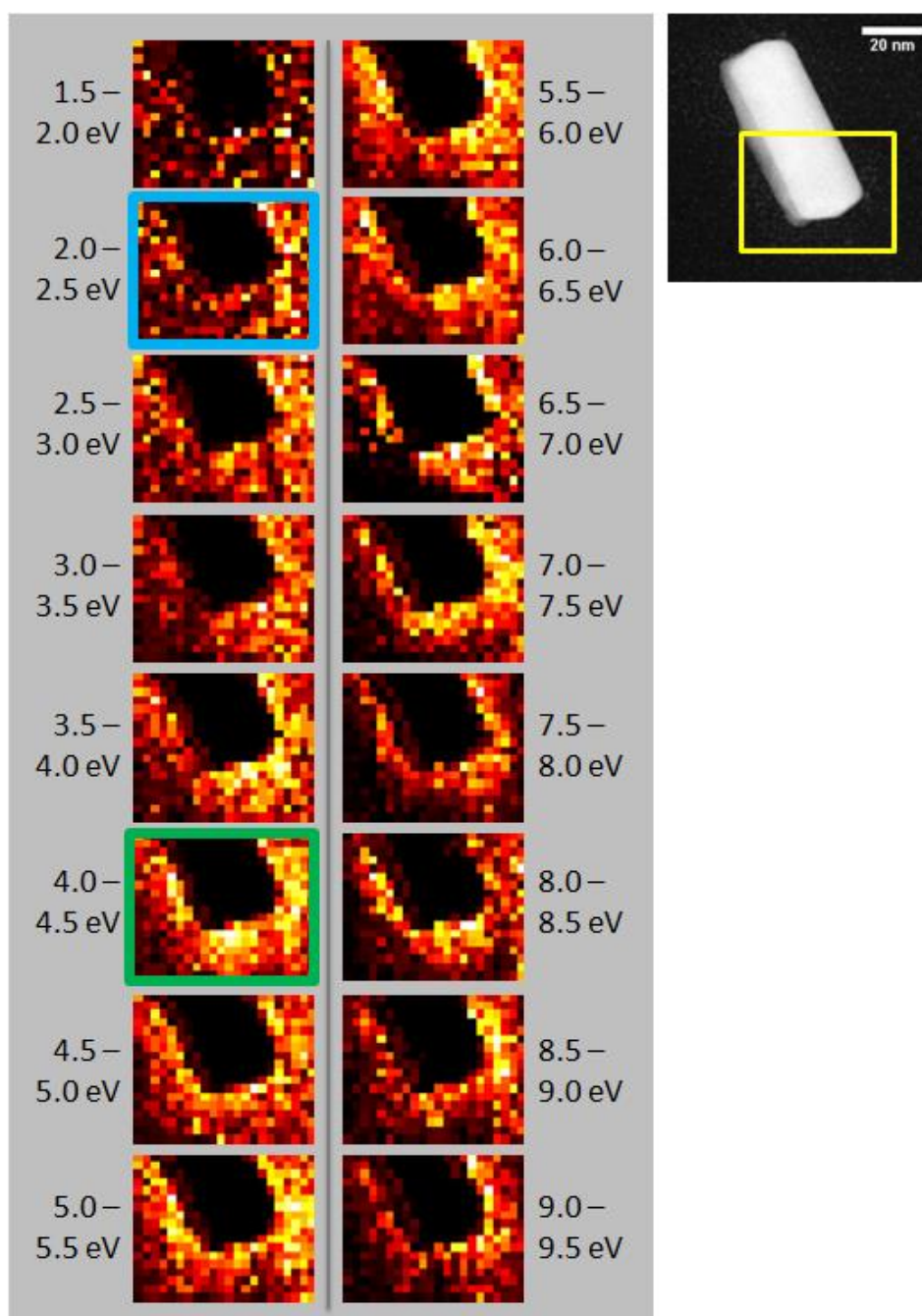
**Figure 6.6:** *DDfield* simulations for AuPd, Au-only and Pd-only nanorods. Simulated induced electric fields shown with incident radiation polarised to excite (a) longitudinal and (b) transverse LSPR resonances.

transverse modes, but did not find an extended longitudinal response or identify multiple longitudinal modes in their AuAg core-shell dumbbell nanorod sample.<sup>17</sup> This may be due to the relatively closer proximity in the surface plasmon resonances of Au and Ag in the visible region of the spectrum causing a strongly coupled longitudinal response between the core and shell metals, which we do not see between Au and Pd. A similar explanation may also apply to the blue shifts observed by Rodriguez-Gonzalez *et al.* in the longitudinal response of the Au-core on the addition of the Ag shell, which we do not see in the results presented here for AuPd nanorods. This point may merit more detailed investigation using samples with varying Pd shell thickness.

### **6.1.3. Asymmetric shell growth**

Our experiments have identified significant variations in response caused by uneven or asymmetric shell coverage in AuPd nanorods. Figure 6.7 shows a series of STEM-EELS spectrum image maps, and associated STEM-HAADF image, from an Au nanorod where Z-contrast shows asymmetric Pd shell coverage. Consistent with the results presented above two longitudinal modes can be seen in these maps, presenting with an asymmetry that matches well with the asymmetry in Pd shell coverage. We see fields localised to the corner of the nanorod with little Pd coverage in the 2.0 eV to 2.5 eV map (highlighted by a blue box in Figure 6.7) and localised to the corner with more Pd coverage in the 4.0 eV to 4.5 eV map (highlighted by a green box in Figure 6.7). The appearance of the second longitudinal mode in this nanorod indicates this phenomenon is not dependent on the existence of a complete Pd shell.

A further point of note in relation to Figure 6.7 is that the mapped signal intensity at higher energy losses, from around 4.0 eV to 8.0 eV, is notably less uniform, both from map to map and in spatial distribution, in this nanorod than was the case for the nanorod of Figure 6.1 above. In this series the signal can be seen to be localised to the Pd-shell in some maps and not others, where in the maps of Figure 6.1(b) the signal appears relatively uniformly across the whole energy range. This suggests that the greater uniformity of signal in the AuPd maps of Figure 6.1(b) can be associated with even Pd shell coverage, either through stronger Pd response or because of more effective coupling between core and shell responses. These results demonstrate the importance of correlating observed LSPR response to bimetallic morphology on a single particle basis and the need for well controlled samples for tailored LSPR response.



*Figure 6.7: spectrum image maps from an Au nanorod with asymmetric coverage.* STEM-EELS spectrum image plasmon maps over arbitrary energy ranges 0.5 eV wide for an Au nanorod, with a partial Pd-shell coverage, with corresponding STEM-HAADF image.

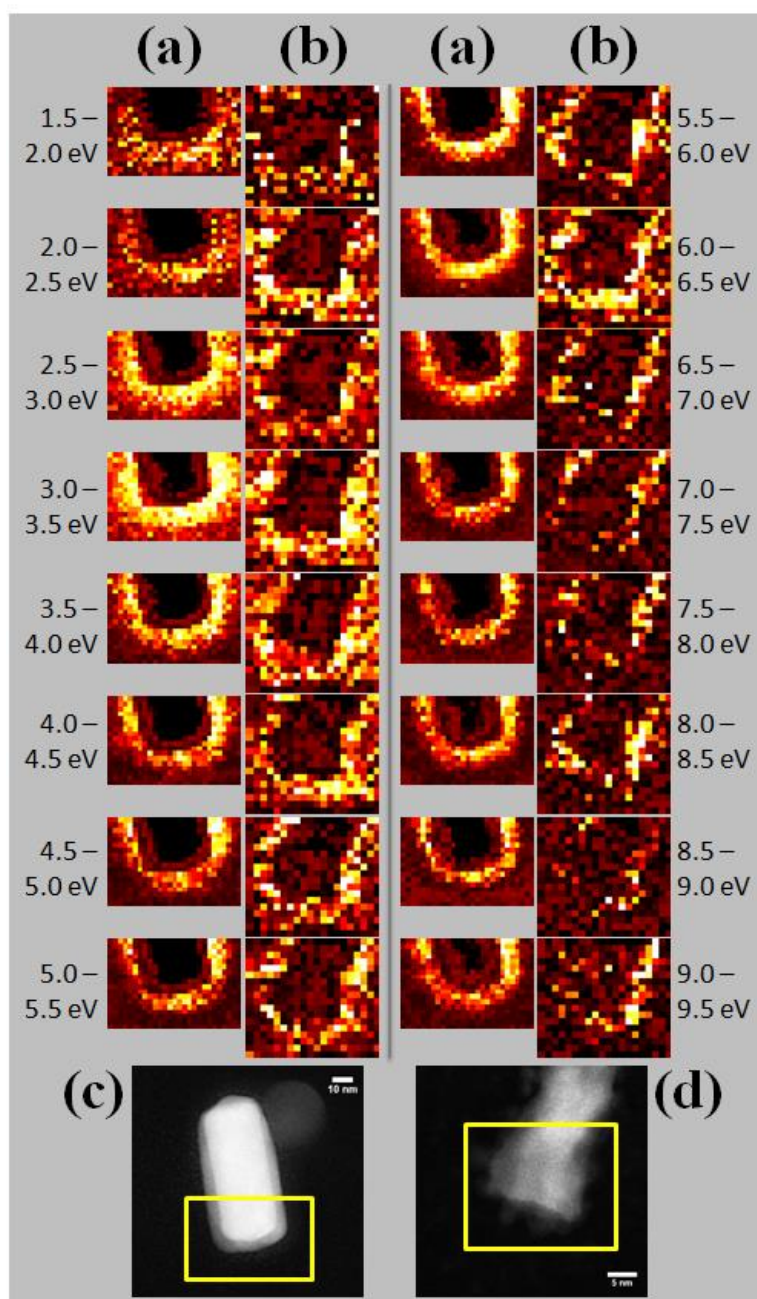
#### 6.1.4. Summary

The above experimental and simulated results show that the addition of a Pd shell causes a marked change in response at energy losses between around 5 eV and 8 eV, consistent with the surface plasmon resonance of Pd, but also cause significant alteration in the longitudinal LSPR response of the nanorod, giving longitudinal response over extended energy loss range from 1.5 eV through to around 4.5 eV, with an additional peak in field intensity appearing in the energy loss range between 2.5 eV and 4.0 eV. We have also shown that the energy loss at which the second longitudinal mode appears shows greater variation from nanorod to nanorod than the lower energy longitudinal mode, and thus may be sensitive to the particular morphology of individual Pd shells. This observation is supported by the observed variation in response seen where there is an incomplete Pd shell coverage. These results have implications for better understanding and exploitation of catalytic enhancements to reactivity, in particular as reactivity gradients along nanorods have recently been discovered that may be suggestive of localised ‘hot spots’ in reactivity.<sup>18</sup> This suggests that localised fields induced by LSPR response may have a significant role to play in catalytic enhancements where there is also localisation in reactivity.

## 6.2 LSPR Response of AuRh Nanorods

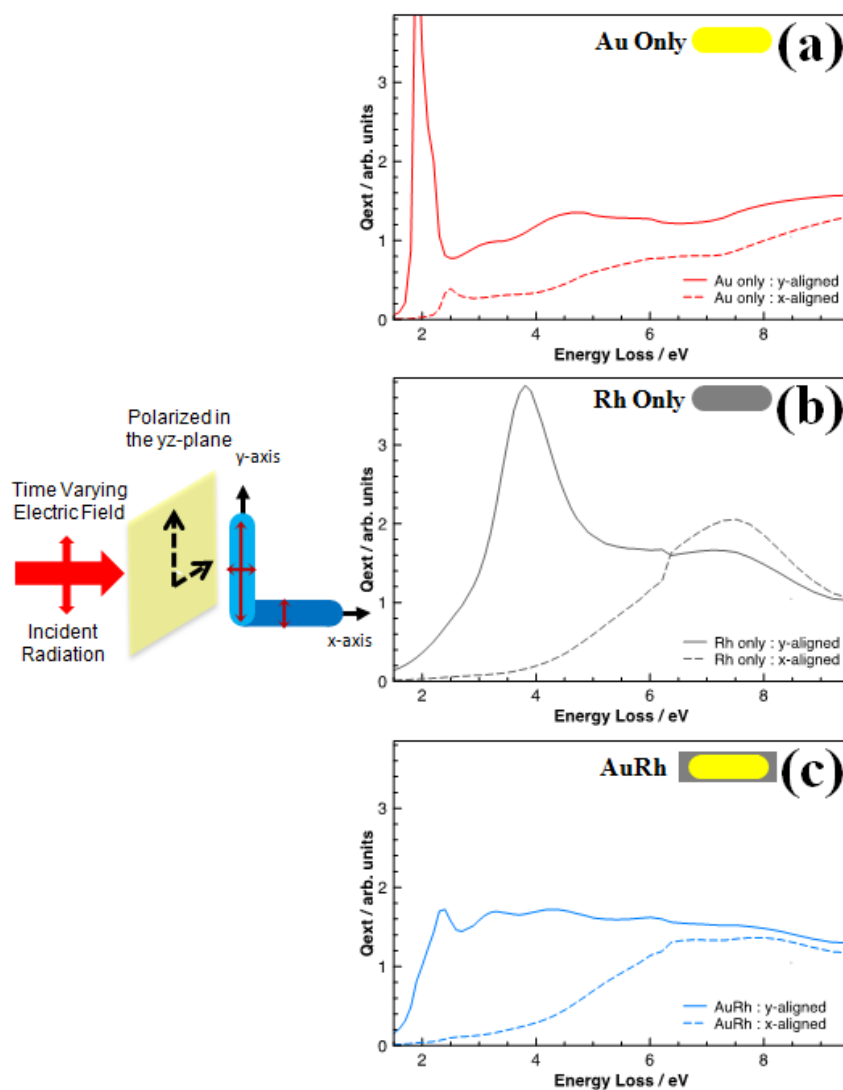
In this section we characterise the LSPR response of the Au<sub>core</sub>Rh<sub>shell</sub> nanorod system that was the focus of the structural characterisation presented in Chapter 5. Figure 6.8 shows experimental STEM-EELS spectrum image maps taken over arbitrary 0.5 eV energy loss ranges from 1.5 eV to 9.5 eV from an AuRh nanorod, with the similar maps from an AuPd nanorod (reproduced from Figure 6.1). Comparison of these maps shows

there is, in general, a much greater variation in the measured response of the AuRh nanorod, both spatially and energetically, in particular at higher energy losses, from around 6.0 eV to 9.5 eV, over which range the AuPd response is notably uniform.



**Figure 6.8:** *Spectrum image maps from the ends of AuPd and AuRh nanorods.* STEM-EELS spectrum image maps over arbitrary 0.5 eV energy loss ranges from the ends of (a) AuPd and (b) AuRh nanorods, with (c) and (d) corresponding images. The AuPd maps are as given in Figure 6.1.

Difference in response between AuPd and AuRh systems is contrary to the apparent similarity in the dielectric responses of their constituent metals (optical constants shown in Figure 2.11 in Chapter 2). The uniform response observed in AuPd nanorods is consistent with the slowly changing real part of its optical constants<sup>19-21</sup> and with its surface plasmon resonance at around 7 eV to 9 eV.<sup>9,12,13</sup> The optical constants of Rh bear marked similarity to those of Pd, and DDA simulations based on these optical constants (Figure 6.9) suggest we might expect a broadly similar LSPR response.



**Figure 6.9:** Simulated spectra for Au-only, Rh-only and AuRh nanorods.

(a) Au-only, (b) Rh-only, and (c) AuRh nanorods with targets aligned along x and y axes to show the emergence of longitudinal LSPR modes.

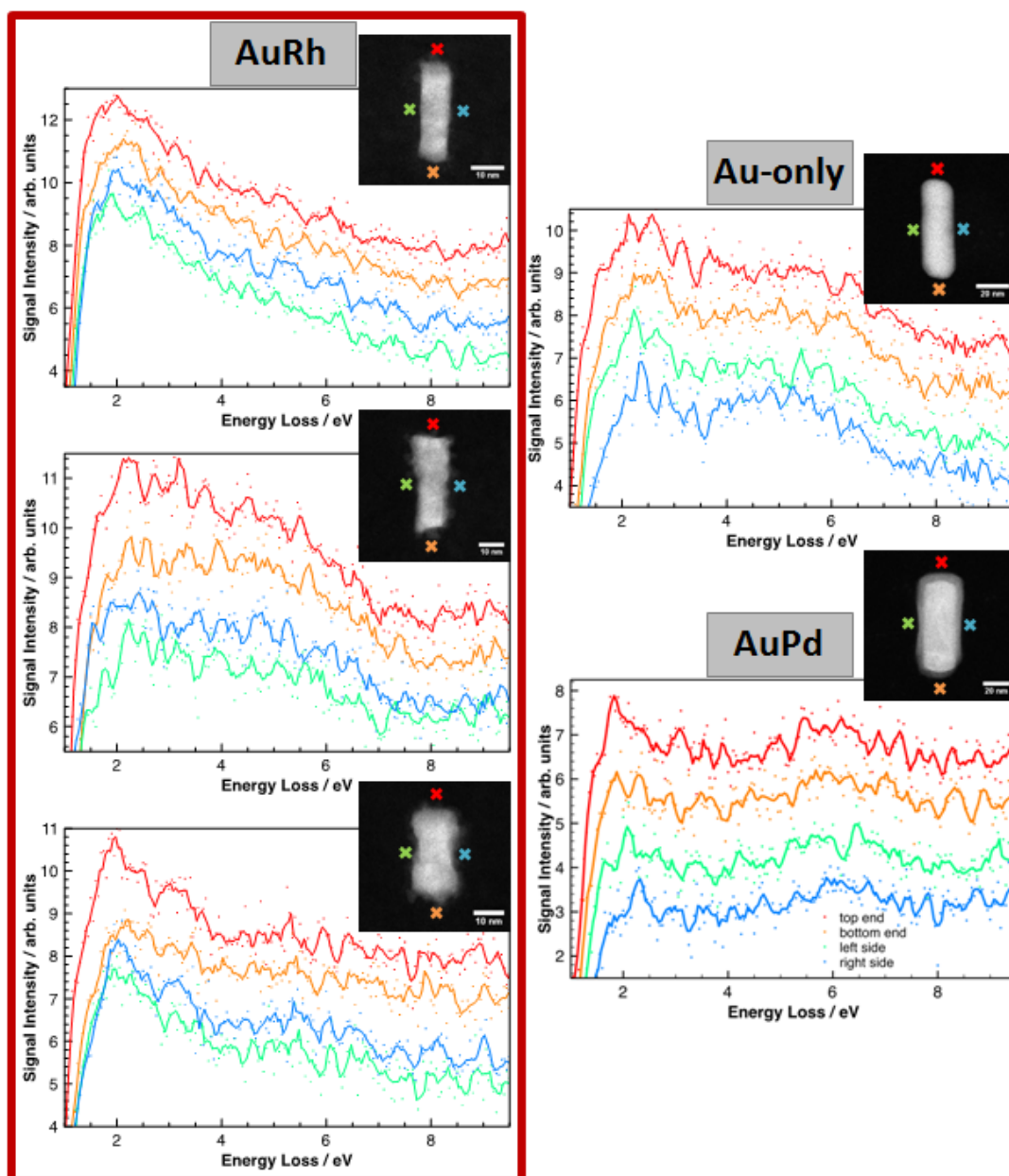


That we do not see similar trends in mapped response between AuRh and AuPd nanorods may be due to the extremely irregular morphology of the AuRh particles. The response may be impacted by the wider variation in composition, more uneven shell coverage, and potentially varying amounts of alloying between Au and Rh, where the AuPd nanorods had more uniform morphology and a clear interface.

To better understand how morphology variation affects the response of AuRh nanorods we have acquired STEM-EELS data from a series of nanorods exhibiting widely varying appearance; these results are shown in Figure 6.10. The spectra shown in Figure 6.10 were taken at points around the nanorods to demonstrate the observed trends are not caused by local affects, but are representative of the whole particle. Comparison of the three AuRh spectra shows considerable variation in the general trends of response, in particular in the energy loss range from around 4 eV to 8 eV. Over this energy loss range the top AuRh nanorod shows a uniformly falling signal with only weak spectral features, the middle AuRh nanorod shows a number of spectral features within a broader shoulder feature with a similarly falling background, and the bottom AuRh nanorod shows a similar broad feature incorporating other narrower features but overlaying a much less steeply falling background.

Similar to the variations in response, the STEM-HAADF images of Figure 6.10 show considerable variation in the size and morphology of these nanorods that, given the general uniformity of the Au-seed nanorods for this sample (shown in Chapter 5 of this thesis) can be attributed to variations in Rh over-growth. Variations in both the overall morphology and the thickness of Rh coverage are apparent. The bottom and middle AuRh nanorods appear to have more extensive Rh over-growth, and numerous out-growths, whilst the top nanorod has a more even appearance; this observation suggests the broad





**Figure 6.10:** Point spectra taken from around AuRh, Au-only and AuPd nanorods. Spectra acquired from the top (red), bottom (orange), left (green) and right (blue) of AuRh, Au-only and AuPd nanorods.

feature apparent in their spectra may be associated with greater Rh content, similar to the broad feature seen in AuPd spectra. However, comparison of these AuRh spectra to typical Au-only and AuPd spectra, shown in Figure 6.10 for comparison, indicates that the general shape of the AuRh response over this part of the spectra more closely resembles

that of Au nanorods than AuPd nanorods. This similarity is most noticeable in the generally falling background seen in all three sets of AuRh spectra and in the presence of a broad feature between 4 eV and 7 eV in the spectra of the middle and bottom AuRh nanorods. In comparison, the broad feature associated with Pd content in the AuPd spectra occurs at higher energy loss.

One factor that might contribute to the lack of consistency between the general trends in AuRh and AuPd response is the relative proportions of the core and shell metals; however, the AuRh nanorod that appears from its more even morphology apparent in its STEM-HAADF image to have the least Rh content, the top nanorod of the three shown in Figure 6.10, in fact has spectra that show the least similarity to the Au-only spectra suggesting that the determining factors for the observed trends are more complex than simply Rh content. Other factors that will also impact on the observed variations in LSPR response between AuRh and AuPd nanorods are the unevenness of the Rh shell compared to the Pd shell, and the degree of interfacial inter-mixing between Au and Rh compared to the clearly segregated interface of the AuPd system. The varied and irregular morphology of the AuRh system, makes determining the exact cause of the differing trends we see in the LSPR response extremely challenging.

Despite the irregular morphology of the AuRh nanorods we can still identify one interesting trend from mapping the response of this system. In common with our results for AuPd nanorods we see measured field patterns consistent with the appearance of longitudinal LSPR response over an extended energy loss range in the AuRh system. The series of nanorod end AuRh maps shown in Figure 6.8 have patterns suggestive of longitudinal LSPR modes in the 2.0 eV to 2.5 eV and 3.0 eV to 3.5 eV maps. A further interesting observation is that the measured field patterns shown in Figure 6.8 show a

notably more complex pattern than the longitudinal modes seen for either Au-only or AuPd nanorods. For example, the Rh out-growth at the bottom right hand corner of the nanorod coincides with localised field enhancements in the 3.5 eV to 4.0 eV map that are consistent with its angular appearance, yet no equivalent enhancement is seen at the opposite corner, either in this energy loss range or any other, despite its similarly angular appearance. One possible explanation for this observation is that variation in response in these two parts of the nanorod may be caused by differing degrees of AuRh mixing in each of these outgrowths.

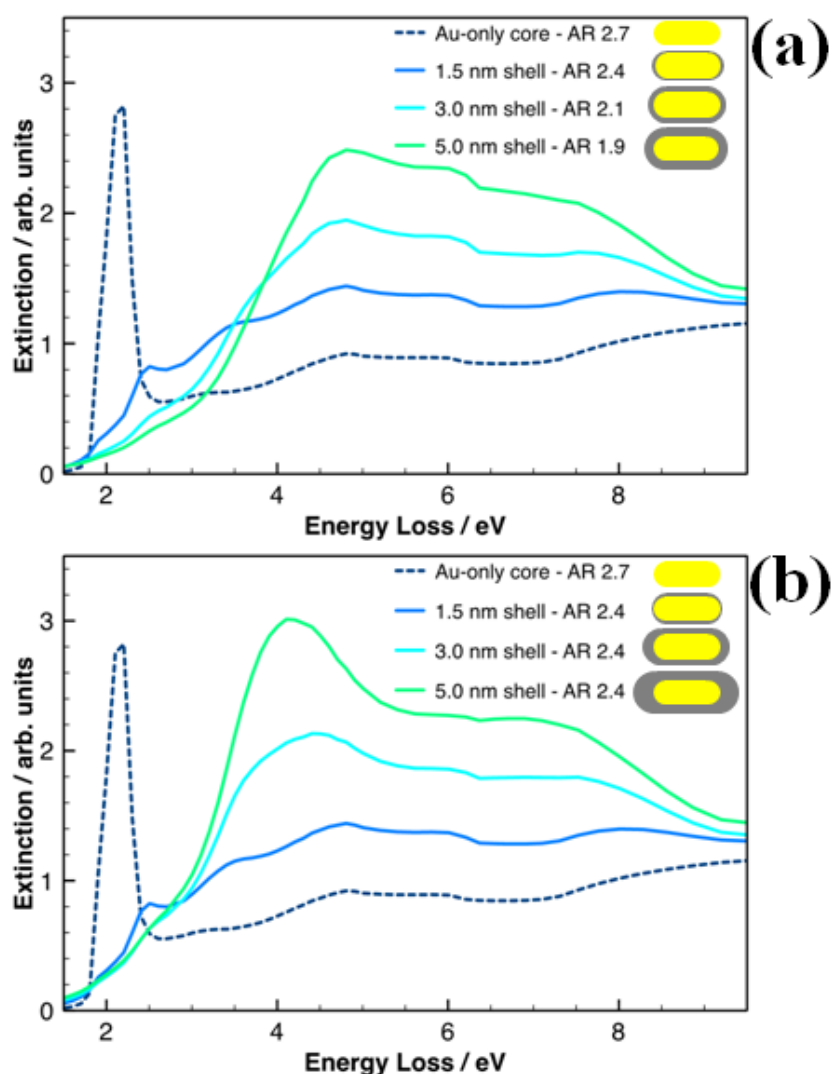
The results presented in this section illustrate the scale of the challenge posed in characterising LSPR response in systems with varying structure and morphology. Detailed characterisation of a series of AuRh samples with more controlled variations in morphology, for example through controlling the degree of interfacial mixing or the uniformity of Rh shell coverage, and by making comparison to Rh-only particles as well as Au-only particles, would be required to gain further understanding of the driving forces responsible for the variation in response that we see in the results presented here. Given the desirability of Rh for use in industrial catalysis and the detection of plasmonic enhancement to reactivity in the similar AuPd nanorod system,<sup>2,4</sup> we believe that conducting a more detailed investigation of the LSPR response of AuRh systems, in conjunction with associated catalysis testing, is merited.

### 6.3 Investigating the Impact of Uneven Shell Growth Using Optical Response Simulation

The experimental results presented in the previous two sections highlighted the variation in response caused by irregular or asymmetric particle morphology; in this section we investigate this further using systematic DDA simulation. We use a model AuRh core-shell system, simulating the response with varying shell thickness and shell arrangement, to identify general trends in response. All of the simulated spectra presented in this section have the target nanorods oriented relative to the incident radiation with polarisation along two axes, to excite both the longitudinal and transverse LSPR.

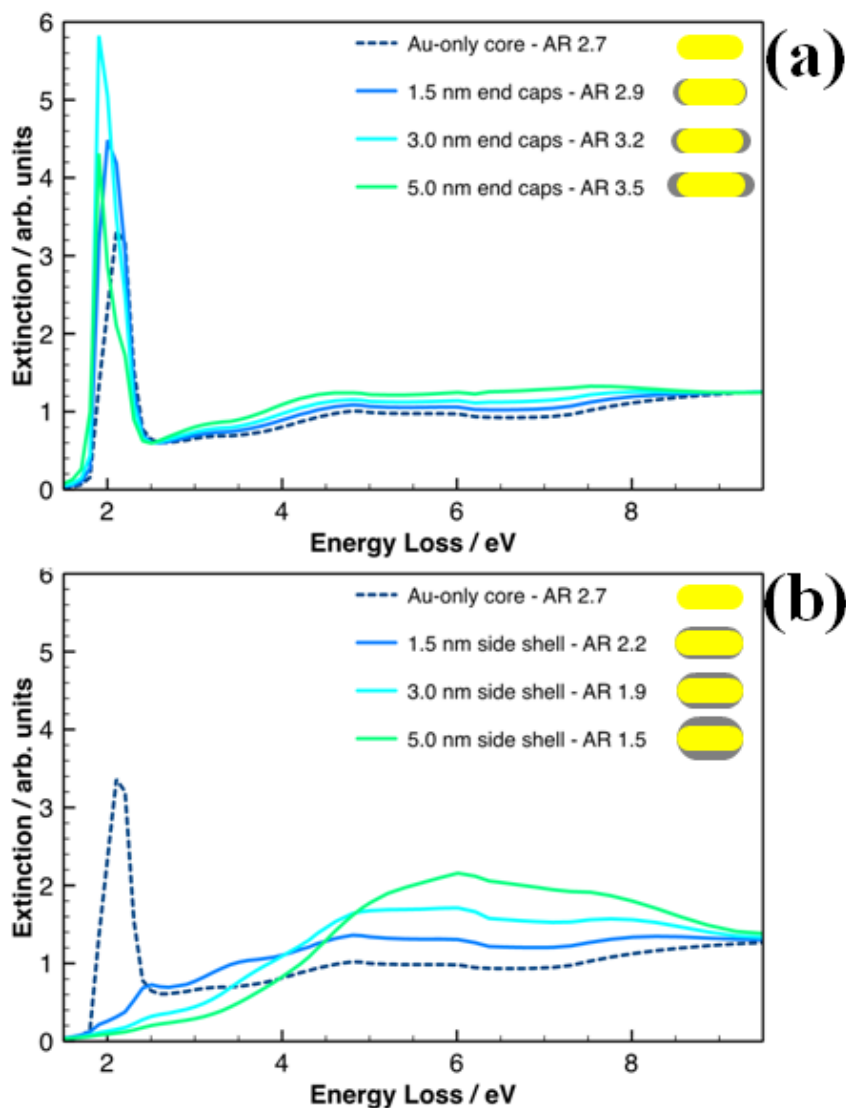
Figure 6.11 shows simulated spectra for bimetallic Au<sub>core</sub>Rh<sub>shell</sub> nanorods with shells of increasing thickness on an Au-core (shown schematically), together with the simulated spectrum for the Au-core. In Figure 6.11(a) the target shell thickness increases evenly across the series of targets from a nominal 1.5 nm shell to a 5.0 nm shell; this causes a reduction in the aspect ratio of the targets from 2.7 for the Au-core to 1.9 for the thickest shell covering (given labelled 'AR' in the chart legend). In contrast, Figure 6.11(b) shows a similar series of simulations where the shell thickness is increased more at the ends than the sides of the nanorods, so as to maintain constant aspect ratio between the targets. Comparison of these two sets of plots highlights the impact that altering both aspect ratio and composition has on the appearance of the spectra. In the constant aspect ratio plots we see a much stronger response appearing at around 4.0 eV to 5.0 eV, which can be associated with the longitudinal LSPR of the shell metal dominating the Au-core longitudinal response in the two thickest shell targets. In contrast, in the even shell plots of Figure 6.11(a) this feature is not apparent as a separate feature in the spectra. This is in

part because the lower aspect ratio of the even shell plots is not sufficient to fully separate the longitudinal mode of the shell metal; however, the altered composition of the targets, with the greater proportion of shell metal required to maintain aspect ratio in the plots of Figure 6.11(b), also contributes to the observed variations by making the Rh response relatively stronger.<sup>22-24</sup>



**Figure 6.11:** Simulated spectra for AuRh nanorods with full shells. (a) With even thickness shells of 1.5 nm, 3.0 nm and 5.0 nm, and (b) with same side shell thickness as (a) but with increased end shell thickness so as to maintain aspect ratio. The Au-only core spectrum is included on both plots for comparison.

In order to understand how adding shell at the ends of the nanorod may differ from adding shell at the sides of the nanorod, Figure 6.12(a) and (b) shows a series of plots with increasing thicknesses of shell on respectively the ends and the sides of the Au-core target; the resulting aspect ratios are as shown in the chart legends.

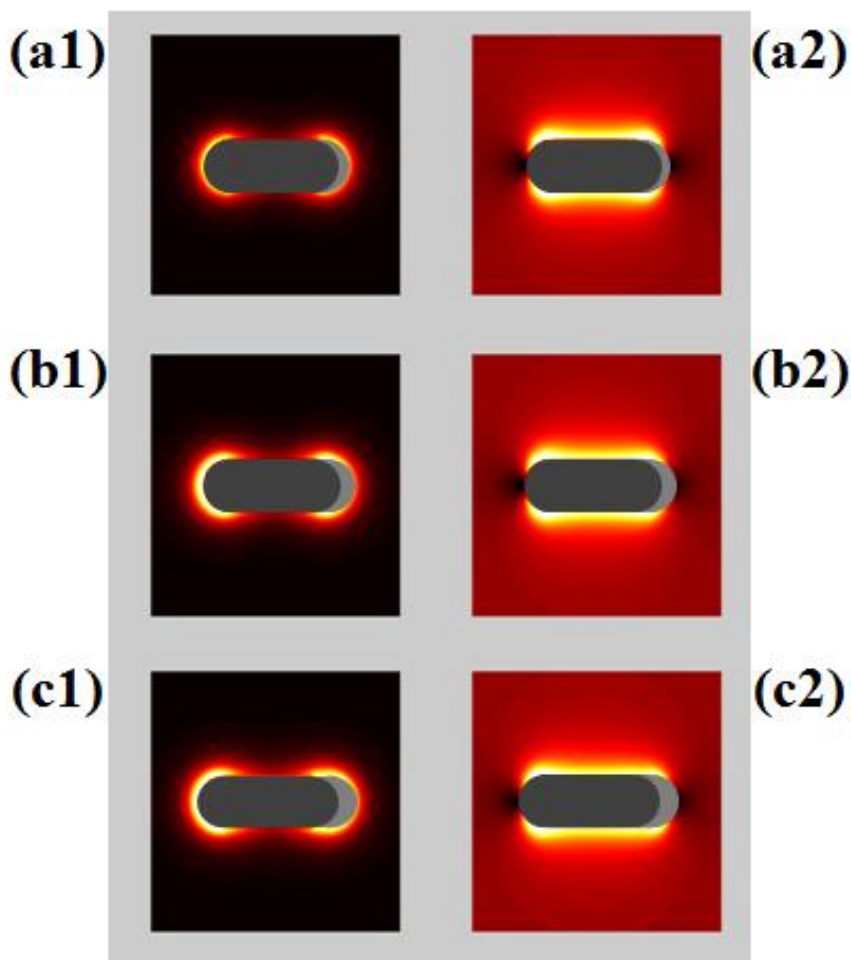


**Figure 6.12: Simulated spectra for AuRh nanorods with end and side shells only.** Simulated spectra for Au<sub>core</sub>Rh<sub>shell</sub> nanorods (a) with Rh end shells of 1.5 nm, 3.0 nm and 5.0 nm, and (b) Rh side shells of 1.5 nm, 3.0 nm and 5.0 nm. The Au-only spectrum is included on both plots for comparison.

Examination of the feature appearing at around 2 eV in Figure 6.12(a), which can be associated with the longitudinal response of the Au-core, indicates that adding shell metal only to the end of the nanorod red-shifts the peak to lower energy, consistent with the associated increase in aspect ratio. However, what is also of note is that adding shell metal to the ends of the nanorod does not quench the response, but in fact increases the amplitude of the signal relative to the Au-core. In comparison adding shell thickness only to the sides of the nanorods, shown in Figure 6.12(b), results in significant reduction in the amplitude of the signal at around 2.0 eV, even for the thinnest of shells. These results indicate that LSPR response is extremely sensitive to the balance of shell arrangement between the sides and the ends of the core nanorod, which is a factor that is extremely relevant in systems such as the AuRh nanorods characterised in Chapter 5 of this thesis where the shell metal has a greater tendency to deposit on the ends of the nanorods rather than the sides.

To investigate the impact that the shell metals have on the induced electric fields for these systems, and in particular to assess whether the increased signal amplitude from the longitudinal response of the Au-core caused by the addition of shell metal to the ends of the nanorod corresponds to more intense induced electric fields, we have simulated responses for Au-core nanorods with shell metal added only to one end; Figure 6.13 shows field plots from these simulations. Asymmetry in the simulated induced fields is increasingly apparent with increasing shell metal thickness added to the right end of the target as shown. This is most evident in the fields with incident radiation polarised along the long axis of the nanorod, showing fields induced by the longitudinal LSPR response, but can be seen in both sets of field plots. This indicates that although the addition of end

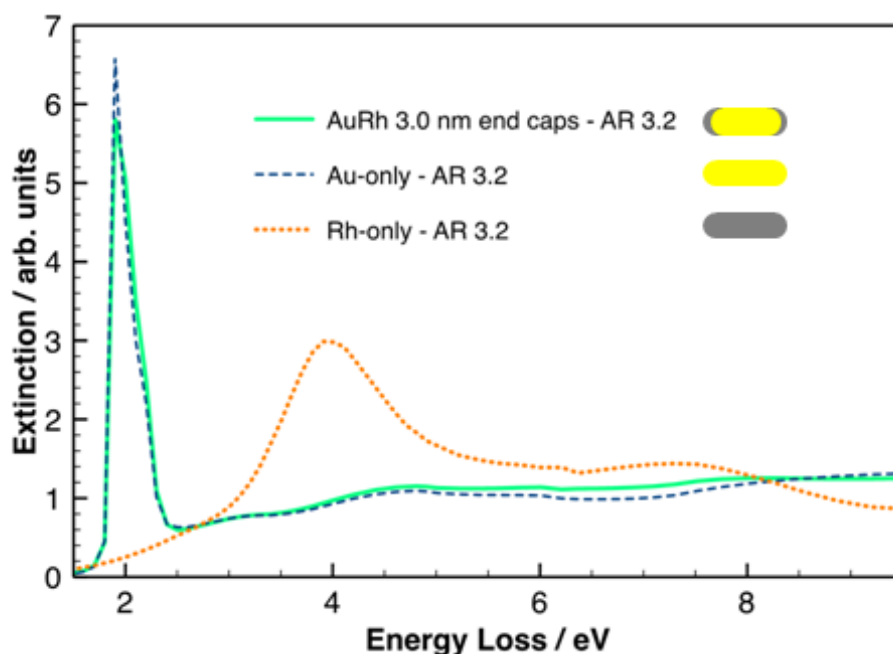
shell increases the amplitude of the response, it does not increase the amplitude of the induced field.



**Figure 6.13:** *DDfield simulations for AuRh nanorods with shell only at one end.* Simulated electric fields for AuRh nanorods, with end cap shells at the right end of (a) 1.5 nm, (b) 3.0 nm, and (c) 5.0 nm thick. For each 1 is taken with incident radiation polarized along the rod axis, to excite the longitudinal localised surface plasmon only, and 2 was taken with incident radiation polarized across the rod axis, to excite the transverse localised surface plasmon only. Schematic representations of the target shape files are shown overlaid to the plots.



The addition of a shell metal has three relevant effects that impact LSPR response; it alters composition, aspect ratio, and overall volume of the particle. Figure 6.14 shows a comparison between an end-capped nanorod, with 3.0 nm of shell metal added to both ends of the Au-core and Au-only and Rh-only nanorods of equivalent total volume and dimensions.



**Figure 6.14:** Simulated spectra for end-capped AuRh, Au-only and Rh-only nanorods of equal volume. Simulated spectra for AuRh nanorod with 3.0 nm Rh end caps and Au-only and Rh-only nanorods of equivalent dimensions.

The end-capped target response is notably similar to the Au-only response, consistent with its Au content, and the Rh-only plot shows no significant signal around 2 eV, indicating that the shell metal does not contribute noticeably to the overall signal of the bimetallic system at this energy level. In addition, comparison of the strength of signal deriving from the longitudinal response of the Au-core, appearing as a sharp feature at

around 2.0 eV in both the end-capped and Au-only simulated spectra, shows that is marginally less intense for the bimetallic target than it is for the monometallic target. So, whilst adding a shell end cap of Rh increases the amplitude of response compared to the core only, it does not when compared to an Au nanorod of identical volume, indicating the increase in signal strength can be attributed to the increased volume of the nanorod rather than an alteration to its dielectric response.

These results illustrate a key issue associated with the nature of the fields induced by LSPR response in bimetallic core-shell systems. The collective oscillation of free electrons in a target is initiated by the external applied field, but perpetuates through the combined effects of both the external field and the induced fields caused by electron oscillation. For nanorod targets the induced electric fields are much stronger at the nanorod ends than at the sides, due to the much greater curvature of the particle surface at the ends. Our DDA simulation results suggest that the strong induced fields at the end of the nanorod caused by the longitudinal LSPR response of the Au-core are sufficient to drive a response in the shell metal even though the shell metal has no resonant response of its own at these energy levels. In comparison, the relatively weaker induced fields at the sides of the nanorod are insufficient to cause a similar response in the shell metal. The greater damping effect caused by adding shell to the sides of the nanorod compared to the ends of the nanorod can also be associated with the relatively weaker induced field strength at the sides, as these weaker fields are more easily quenched than the stronger fields at the ends of the nanorod, causing the overall response to be damped. Experimental confirmation of these results is required, as they suggest considerable potential to manipulate the fields induced by LSPR response by controlled shell growth.

## **6.4 Conclusions**

In this chapter we have demonstrated that STEM-EELS spectrum imaging is an extremely effective technique for the characterisation of the LSPR response of bimetallic nanoparticles, due to its ability to correlate response to structure on an individual particle basis, and to sample LSPR response spatially over large numbers of acquired spectra allowing the unambiguous identification of longitudinal LSPR modes even where the signal to noise ratio is relatively poor. Through using this technique we have shown a marked change in the mapped response between monometallic Au-only nanorods and bimetallic AuPd nanorods. This is apparent in a longitudinal response that extends over a much greater energy loss range in the bimetallic sample, with the appearance of two peaks in mapped field intensity corresponding to the longitudinal LSPR responses originating respectively from the core and shell metals. No similar trend in response has been demonstrated in bimetallic nanorods before. We have also shown the impact of the Pd surface plasmon response in the more uniform and stronger signal apparent at energy losses above 6.0 eV in AuPd nanorods compared to Au-only nanorods. These results may have important implications in gaining understanding of and control over LSPR enhancements to catalytic reactivity that have already been identified in this system and indicate a need for a correlated study of reactivity and LSPR response.

Through mapping AuRh nanorods, and making comparison to the response of AuPd nanorods, we have demonstrated that STEM-EELS spectrum image mapping is capable of discriminating between the responses of two apparently similar weakly plasmonic but catalytically relevant systems. We have shown that AuRh nanorods in general have a much more varied response than AuPd nanorods, however, we have not

been able to determine the cause of this variation due to the irregular morphology of the AuRh sample. Similar to the results for AuPd we have demonstrated that the AuRh system also exhibits longitudinal LSPR response over a more extended energy range. These results represent the first time that the LSPR response of the AuRh system has been studied on a single particle basis and highlight the need for a more detailed investigation of the AuRh system. In addition, the significant variation we see with changes in particle morphology, together with the results of our DDA simulation of irregular shell growth, suggest the need for a systematic investigation of the impact of different arrangements of shell through a combination of controlled sample synthesis and single particle STEM-EELS LSPR characterisation.

The work presented in this chapter demonstrates the role that STEM-EELS can play in characterising the varied and complex LSPR response of bimetallic nanoparticles systems and highlights the need for detailed single particle characterisation if we are to fully understand the driving forces behind the observed behaviour. Our single particle plasmon mapping results demonstrate the considerable potential that bimetallic nanoparticles offer to manipulate electric field enhancements both in single particles and at the sub-particle level, through gaining control over particle structure and composition, which may be of particular interest to localised enhancements to catalytic reactivity in these systems.

## List of References

171. Christopher, P.; Xin, H.; Linic, S., Visible-light-enhanced catalytic oxidation reactions on plasmonic silver nanostructures. *Nature Chem.*, **2011**, *3*, 467-472.
172. Huang, J.; Zhu, Y.; Lin, M.; Wang, Q.; Zhao, L.; Yang, Y.; Yao, K.X.; Han, Y, Site-Specific Growth of Au-Pd Alloy Horns on Au Nanorods: A Platform for Highly Sensitive Monitoring of Catalytic Reactions by Surface Enhanced Raman Spectroscopy, *J. Am. Chem. Soc.*, **2013**, *135*, 8552-8561
173. Shan, X.; Díez-Pérez, I.; Wang, L.; Wiktor, P.; Gu, Y.; Zhang, L.; Wang, W.; Lu, J.; Wang, S.; Gong, Q.; Li, J.; Tao, N., Imaging the electrocatalytic activity of single nanoparticles, *Nature Nanotech.*, **2012**, *7*, 668–672.
174. Wang, F.; Li, C.; Chen, H.; Jiang, R.; Sun, L.D.; Li, Q.; Wang, J.; Yu, J.C.; Yan, C.H., Plasmonic Harvesting of Light Energy for Suzuki Coupling Reactions, *J. Am. Chem. Soc.* **20103**, *135*, 5588-5601
175. Blaber, M.G.; Arnold, M.D.; Ford, M.J., A Review of the Optical Properties of Alloys and Intermetallics for Plasmonics, *J. Phys.: Condens. Matter.*, **2010**, *22*, 143201
176. Cortie, M.B.; McDonagh, A.M., Synthesis and Optical Properties of Hybrid and Alloy Plasmonic Nanoparticles, *Chem. Rev.* **2011**, *111*, 3713-3735
177. Ingram, J.C.; Nebesny, K.W.; Pemberton, J.E., Optical Constants of the Noble Metals Determined by Reflection Electron Energy Loss Spectroscopy, *Appl. Surf. Sci.*, **1990**, *44*, 293-300
178. Leiro, J.; Minni, E.; Suoninen, E., Study of Plasmon Structure in XPS Spectra of Silver and Gold, *J. Phys. F: Met. Phys.*, **1983**, *13*, 215-221
179. Lynch, M.J.; Swan, J.B., The Characteristic Loss Spectra of the Second and Third Series Transition Metals, *Aust. J. Phys.*, **1968**, *21*, 811-816
180. Pierce, D.T.; Spicer, W.E., Optical Properties of Rhodium, *Phys. Stat. Sol. (b)*, **1973**, *60*, 689-694
181. Thiam, M.M.; Nehasil, V.; Matolin, V.; Gruzza, B., The AES and EELS Study of Small Rhodium Clusters Deposited onto Alumina Substrates, *Surf. Sci.* **2001**, *487*, 231-242
182. Vankar, V.D.; Vook, R.W., EELS and AES Study of Epitaxially Grown Pd(111) Thin Films, *Surf. Sci.*, **1983**, *131*, 463-474
183. Vehse, R.C.; Arakawa, E.T., Optical and Photoemissive Properties of Palladium in the Vacuum Ultraviolet Spectral Region, *Phys. Rev. B*, **1970**, *1*, 517-522
184. Digital Micrograph, Version 1.83.842, Gatan Inc. USA

185. Draine, B.T.; Flatau, P.J., Discrete-dipole approximation for scattering calculations, *J. Opt. Soc. Am.*, **1994**, *11*, 1491
186. Kreibig, U.; Vollmer, M., *Optical properties of metal clusters*, Springer-Verlag: Berlin, 1995
187. Rodriguez-Gonzalez, B.; Attouchi, F.; Cardinal, F.F.; Myroshnychenko, V.; Stephan, O.; Garcia de Abajo, F.J.; Liz-Marzan, L.M.; Kociak, M., Surface Plasmon Mapping of Dumbbell-Shaped Gold Nanorods: The Effect of Silver Coating, *Langmuir*, **2012**, *28*, 9063-9070.
188. Zhou, X.; Andoy, N.M.; Liu, G.; Choudhary, E.; Han, K.-S.; Shen, H.; Chen, P., Quantitative super-resolution imaging uncovers reactivity patterns on single nanocatalysts, *Nature Nanotech.* **2012**, *7*, 237–241
189. Johnson, P.B.; Christy, R.W., Optical Constants of the Noble Metals, *Phys. Rev. B*, **1972**, *6*, 4370-4379
190. Johnson, P.B.; Christy, R.W., Optical Constants of Transition Metals: Ti, V, Cr, Mn, Fe, Co, Ni, and Pd, *Phys. Rev. B*, **1974**, *9*, 5056-5070
191. *Handbook of Optical Constants of Solids*, ed. Palik, E.D., Academic Press, London, 1998
192. Duan, J.; Park, K.; MacCuspie, R.I.; Vaia, R.A.; Pachter, R., Optical Properties of Rodlike Metallic Nanostructures: Insight from Theory and Experiment, *J. Phys. Chem. C*. **2009**, *113*, 15524-15532.
193. Hu, J.W.; Li, J.F.; Ren, B.; Wu, D.Y.; Sun, S.G.; Tian, Z.Q., Palladium-Coated Gold Nanoparticles with a Controlled Shell Thickness Used as Surface Enhanced Raman Scattering Substrate, *J. Phys. Chem. C*. **2007**, *111*, 1105-1112
194. Jana, D.; Dandapat. A.; De, G., Au@Pd Core-Shell Nanoparticle Incorporated Alumina Sols and Coatings: Transformation of Au@Pd to Au-Pd Alloy Nanoparticles, *J. Phys. Chem. C*. **2009**, *113*, 9101-9107

---

## Chapter 7

# AuAg Nanoparticle Oxidation

The long term stability of nanoparticles is a matter that is important to their commercial exploitation. In bimetallic nanoparticles the additional complexity introduced by their heterogeneous metal-metal interactions extends to their long term evolution. For example, oxidation may affect only one metal in a system, or affect both metals either separately or in combination. It will induce varying degrees of structural and compositional change in different systems, and may proceed differently at different stages of evolution. As oxidation has the potential to affect not just the surface of the particles but also the overall particle structure<sup>1</sup> it can potentially have a profound impact on both catalytic and plasmonic properties of bimetallic nanoparticles. However, despite the importance of these issues to the practical use of these systems, to date we have found little work exploring their long term stability when stored in air.

The sample chosen for this study is a system of AuAg nanoparticles. In bulk form Ag oxidises readily, whereas Au does not oxidise. The prolonged oxidation of Ag thin films has been shown to result in significant structural change beyond just the surface

layers,<sup>2</sup> so Ag oxidation might be expected to have a significant impact on the structure and resulting properties of nanoparticles with Ag content, although the degree to which the presence of a second metal may influence this could potentially vary between systems. Gaining a full understanding of these processes requires elemental and structural characterisation conducted to atomic resolution, so in this chapter we explore the combined imaging and spectroscopic capabilities of aberration corrected scanning transmission electron microscopy (ac-STEM) in investigating the impact that prolonged storage in air has on AuAg nanoparticles. We use a similarly synthesised and aged Ag-only sample as a benchmark comparator to allow us to identify the impact that the Au content of the bimetallic sample has on the long term structural evolution of this system.

In Section 7.1 we summarise the initial stages of this work, which were conducted at the single particle level; this work has been published in reference 1. In Section 7.2 we use STEM high angle annular dark field (HAADF) imaging to characterise the atomic structures formed in Ag nanoparticles through prolonged exposure to air to provide a monometallic comparator for the atomic scale characterisation of our AuAg system. Then in Section 7.3 we use STEM imaging and energy dispersive X-ray spectroscopy (EDX) to identify the location and influence of the Au content on the structure of the aged AuAg sample at the atomic scale. Finally in Section 7.4 we use STEM electron energy loss spectroscopy (EELS) spectrum image mapping to characterise the impact that sample evolution has on the localised surface plasmon resonance (LSPR) response of AuAg nanoparticles.

All of the ac-STEM work and associated analysis presented in this chapter was conducted by the author, under the supervision of Dr Ziyou Li. The AuAg and Ag-only samples were prepared, and initial high resolution transmission electron microscopy

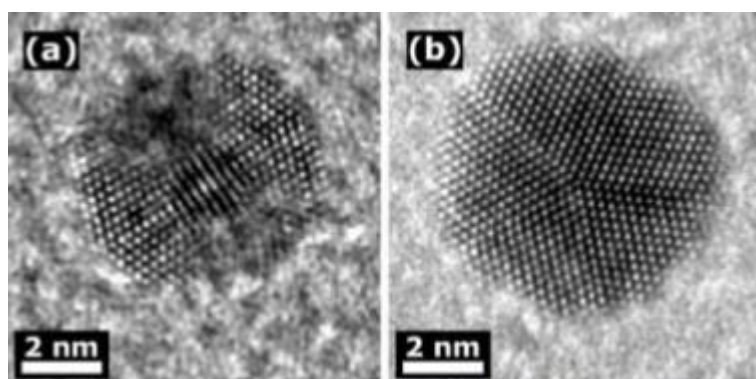


(HRTEM) imaging and image analysis of the AuAg sample conducted, by our collaborator Domagoj Belic, under the supervision of Professor Simon Brown (University of Canterbury, New Zealand).

## **7.1 Initial Studies**

The AuAg and Ag-only nanoparticle samples were prepared in gas phase, through inert gas aggregation in a magnetron sputtering cluster source.<sup>1</sup> They were prepared at the same time and using the same synthesis conditions from Ag-only and mixed 15% Au 85% Ag targets of 99.99% purity. EDX results obtained immediately following synthesis confirmed the Au content of the AuAg samples at  $14 \pm 1\%$ .<sup>1</sup> Both sets of samples were deposited directly onto holey amorphous carbon coated copper TEM supports and were stored in proprietary grid storage boxes in air, under ambient conditions, throughout the period of this study. The initial phase of this study was concentrated on characterising the structural change in the AuAg system at the single particle level; this work has been published in reference 1 and is summarised in this section.

HRTEM characterisation of an AuAg sample with less than 3% substrate coverage, conducted within less than one hour of sample synthesis, showed that the particles had predominantly icosahedral and decahedral structures (Figure 7.1).<sup>1</sup> The uniform appearance of the AuAg nanoparticles in HRTEM images, such as those shown in Figure 7.1, with no features apparent that might be attributed to a segregated structure, indicates the formation of randomly mixed alloyed particles.

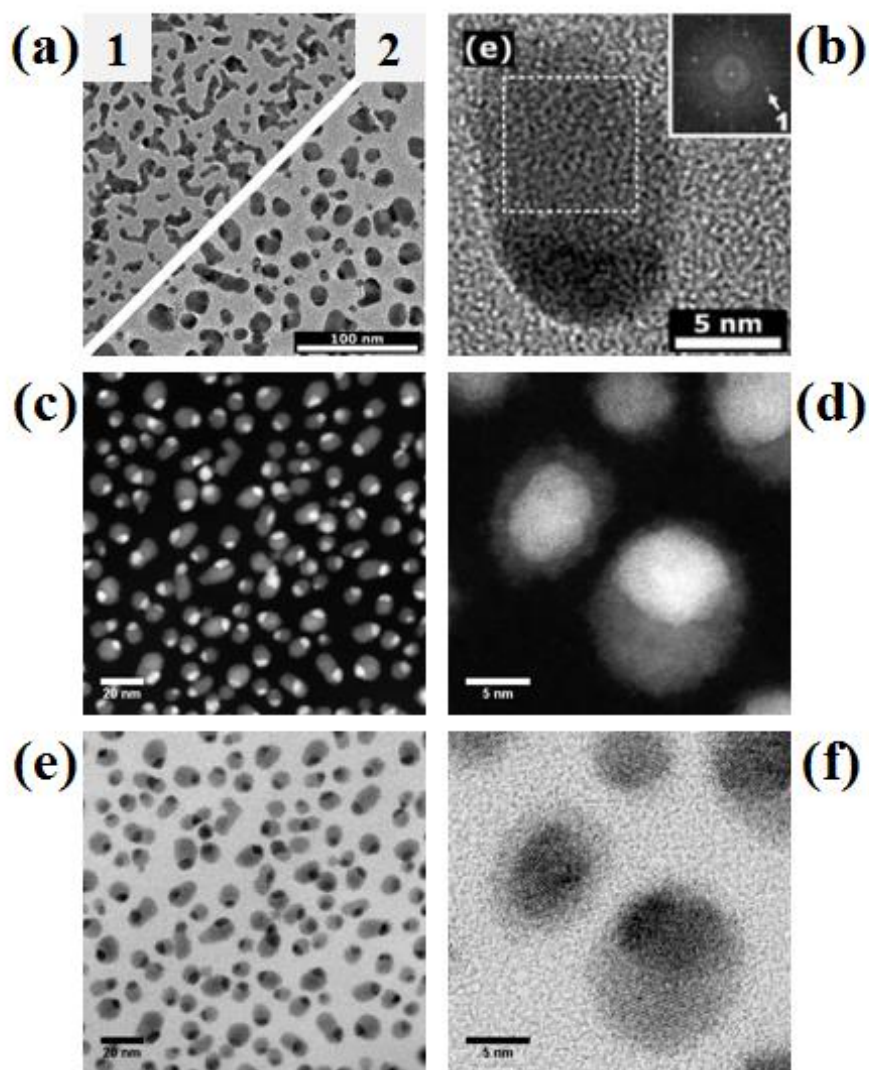


**Figure 7.1:** *HRTEM images of AuAg nanoparticles.* The images were acquired within one hour of synthesis and were considered typical of the sample at that time, showing (a) icosahedral and (b) decahedral structures. From reference 1.

Figure 7.2 shows extracts taken from reference 1 that summarise results from the initial phase of this study. Figure 7.2(a) shows low magnification TEM images of an AuAg sample prepared with higher substrate coverage that were taken immediately following synthesis (Figure 7.2(a1)) and after the samples had been stored in air for more than one year (Figure 7.2(a2)). Comparison of these two images shows the particles aggregated, and became more uniform in size and structure over this period. Figure 7.2(b) shows an HRTEM image of a single particle taken from the aged sample of Figure 7.1(a2) illustrating the development of an asymmetric segregated structure that was typical of the sample at this stage.

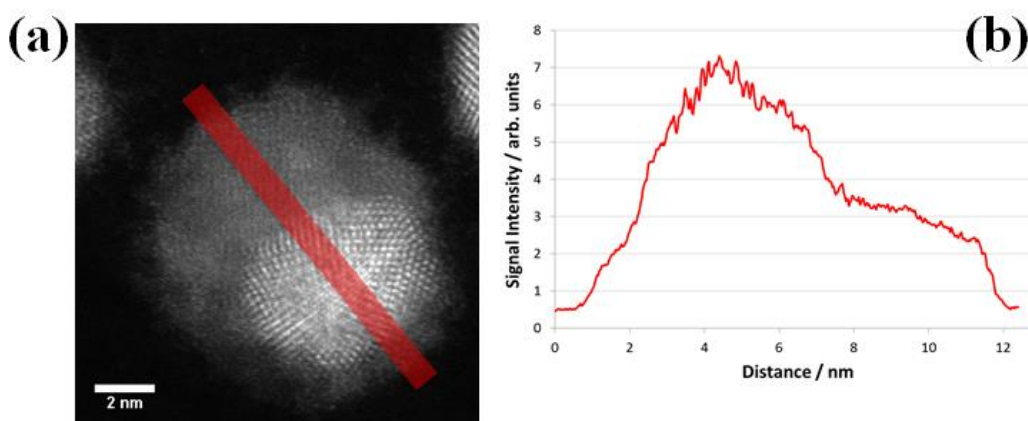
Analysis of lattice spacing data extracted from fast fourier transforms (fft) taken from the lower contrast parts of HRTEM images, such as the example shown in Figure 7.2(b) where the inset fft was taken as indicated by the dashed box, showed the presence of atomic structure consistent with the formation of cubic  $\text{Ag}_2\text{O}$ . For example, the spot marked '1' in the fft inset to Figure 7.2(b) derives from atomic spacing of  $0.27 \pm 0.01$  nm, which is consistent with  $\{111\}$  inter-planar distance for cubic  $\text{Ag}_2\text{O}$ . These results indicate

that the observed structural change in these particles, resulting in asymmetric segregation where previously they were fully alloyed, can be attributed to Ag oxidation.



**Figure 7.2: HRTEM and STEM-HAADF images of aged AuAg nanoparticles.** Low magnification TEM images comparing AuAg sample appearance (a1) within one hour of synthesis and, (a2) after aging for more than one year in air, (b) a typical HRTEM image of an AuAg particle after 15 months of ageing, with fft inset taken as indicated by the dashed box. (c) and (d) STEM-HAADF, and (e) and (f) simultaneously acquired bright field (BF) images, after more than two years of ageing. (a) and (b) are reproduced from reference 1.

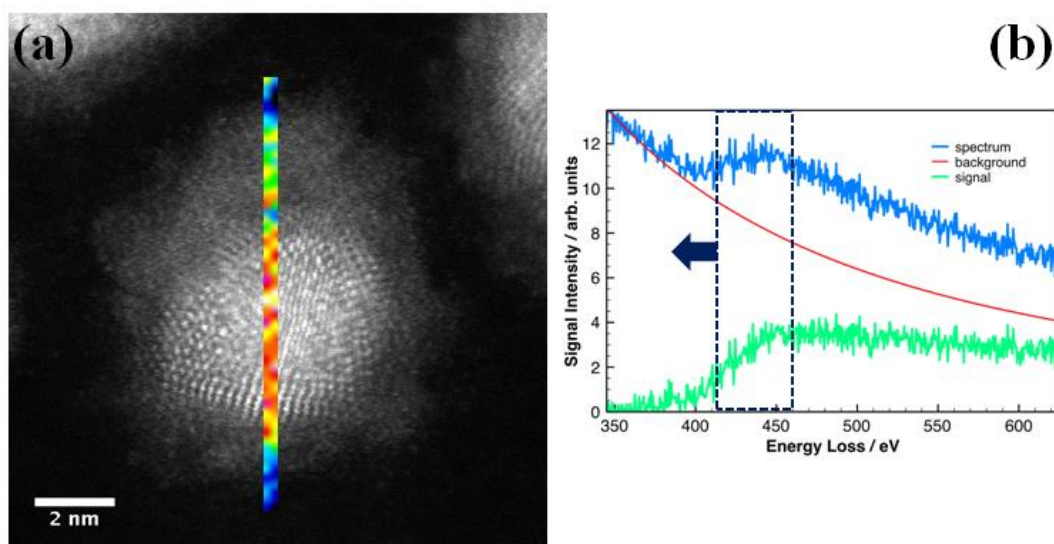
Simultaneously acquired STEM-HAADF and bright field (BF) images of this same sample, taken more than two years after synthesis (Figure 7.2(c) to (f)), show similar contrast variation to the HRTEM images, and reveal the presence of a thin shell surrounding the core of the particle, indicative of the formation of core-shell structure. Figure 7.3 gives a line intensity profile taken from the STEM-HAADF image of a typical AuAg particle from the same sample. This line intensity profile shows the change in image intensity associated with the segregated structure takes place over a length scale of less than one nanometre. Given the generally rounded appearance of these particles, the elemental dependence of STEM-HAADF image contrast allows us to attribute the appearance of these particles to elemental segregation.<sup>1</sup>



**Figure 7.3: Image intensity analysis from an aged AuAg nanoparticle.** (a) STEM-HAADF image, and (b) line intensity profile taken as indicated.

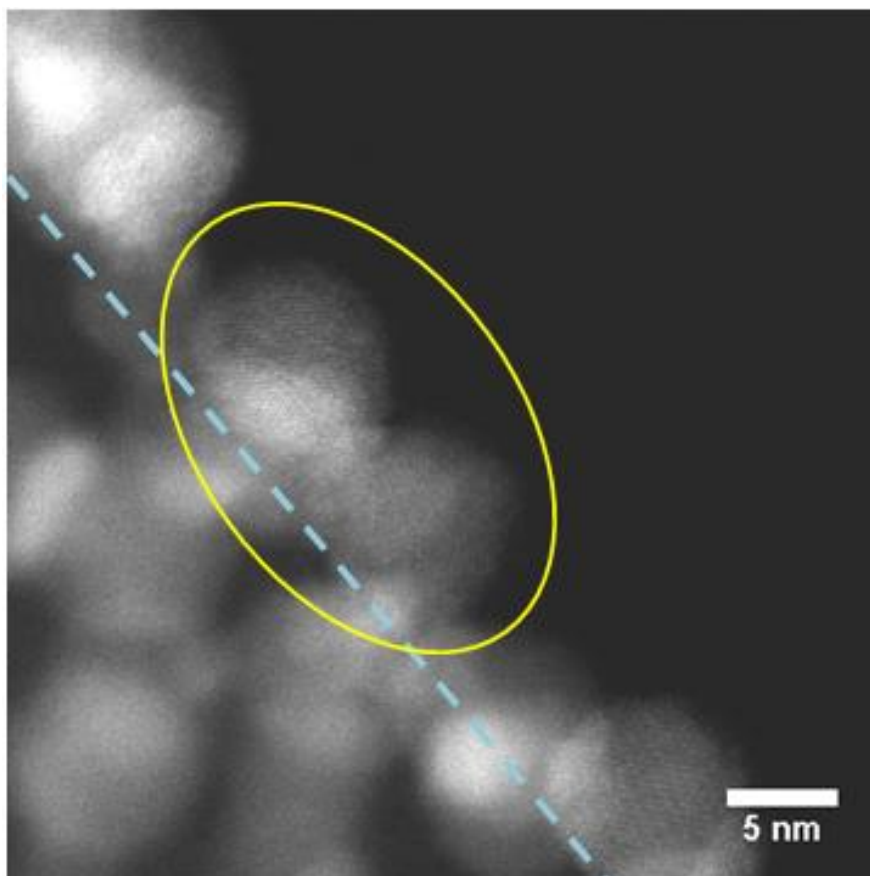
To investigate the elemental content of the bright core of the particles we conducted core loss EELS. Figure 7.4 shows typical results in which red and blue represent respectively greater or lesser integrated signal intensity for the Ag core loss edge. The mapped signal strength is greatest in the core of the particle and exhibits an abrupt change

that corresponds spatially with a similarly abrupt change in STEM-HAADF image intensity at the interface between core and shell.



**Figure 7.4:** *STEM-EELS core loss mapping from an aged AuAg nanoparticle.* (a) STEM-HAADF image with STEM-EELS spectrum image map of the Ag core loss signal, where red represents strong integrated signal intensity and blue weaker integrated signal intensity, with (b) an example spectrum taken from the spectrum image map given in (a) showing the Ag core loss edge.

The particles exhibit a generally uniform, rounded appearance viewed in profile, with the bright core fully enclosed by the shell (shown in Figure 7.5), allowing us to associate the variation in integrated signal intensity shown in Figure 7.4 with concentration of Ag along the path of the electron beam. Thus these results show that the bright core of the particles retains a significant Ag content. Taken in combination with the HRTEM and STEM-HAADF imaging, these results indicate that Ag oxidation through prolonged exposure of these particles to air has led to the formation of a segregated structure comprising an AuAg core and an Ag<sub>2</sub>O shell.<sup>1</sup>

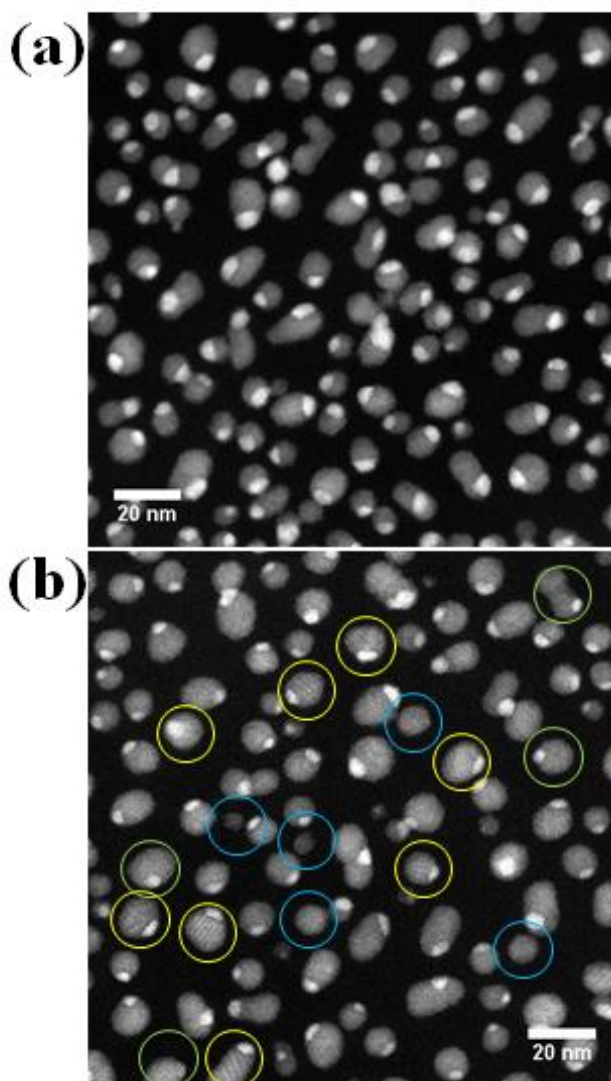


**Figure 7.5:** *STEM-EELS of aged AuAg nanoparticles in profile.* A STEM-HAADF image showing typically rounded outlines of AuAg nanoparticles when viewed in profile. The image was acquired at the edge of a hole in the amorphous carbon substrate (approximate position indicated by a dash line). Examples of particles where the oxide shell can be seen to enclose the brighter core are circled yellow.

The observed asymmetry that occurs in the majority of these particles, with only a very thin oxide shell apparent on one side of the core, suggests that, although Ag oxidation is initiated from the core of the particle, the  $\text{Ag}_2\text{O}$  formed prefers not to remain bound to the core. This may result from a preference for  $\text{Ag}_2\text{O}$  to wet the carbon substrate, but may also be influenced by differences in cohesive or surface energy between the AuAg core and  $\text{Ag}_2\text{O}$ . We consider this issue further in the context of the Ag-only sample in Section 7.2 below.



To examine whether the observed asymmetric segregated structure is a stable state for this system we re-imaged the sample after a further 18 months aging in air. Figure 7.6 shows typical low magnification images taken during the initial study in January 2011 and after a further period of aging in July 2012.



**Figure 7.6:** *STEM-HAADF images of AuAg particles taken more than 12 months apart.* (a) January 2011, and (b) July 2012, with examples ringed exhibiting no core (blue), small core (green), and bright patterns in the oxide regions (yellow).

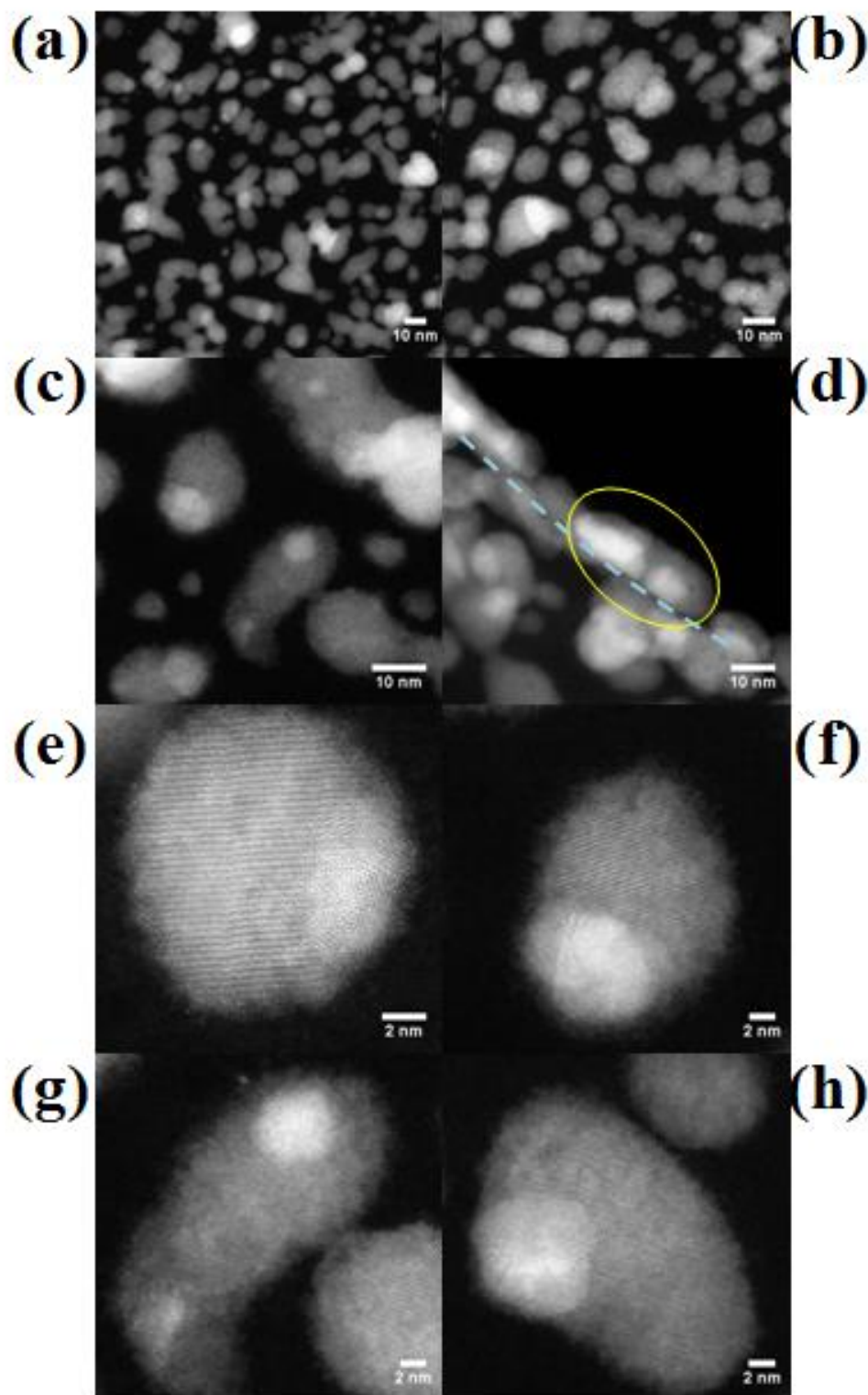
The sample was stored in air, under ambient conditions, throughout the period between these two images. Initial inspection of these images shows a broad similarity in the appearance of the particles, in particular in the appearance of off-centred core-shell structures in the majority of particles in both images. However, the overall impression from comparison of these images, and others like them, suggests further aging has resulted in continued evolution in the structure of the particles. From comparison of these images we can see a qualitative trend of smaller cores and more extensive shells (examples ringed green in Figure 7.6(b)) with further aging. We also see indications that there may be a greater proportion of fully oxidised particles with no cores in the later images (ringed blue in Figure 7.6(b)) and can identify the appearance of bright lattice patterns within the oxide regions of some particles (examples ringed yellow in Figure 7.6(b)) where no equivalent patterns are seen in the earlier images.

A trend of reducing core and increasing shell with further exposure to air is consistent with continued progressive oxidation of Ag in the core and migration of the resulting Ag oxide to the asymmetric shell of the particles. This observation is broadly consistent with the findings of Petterson and Snyder that Ag oxidation in thin films progressed until there was no non-oxidised Ag left, with a corresponding increase in film thickness.<sup>2</sup> However, this does not explain the appearance of bright lattice patterns in the later images of the sample, and also raises the question as to the location of the Au content of the particles, in particular where very small, or no, bright cores are seen in the later images, suggesting the need for more detailed examination alongside the comparator monometallic Ag-only sample.



## 7.2 Oxidation of Ag-only nanoparticles

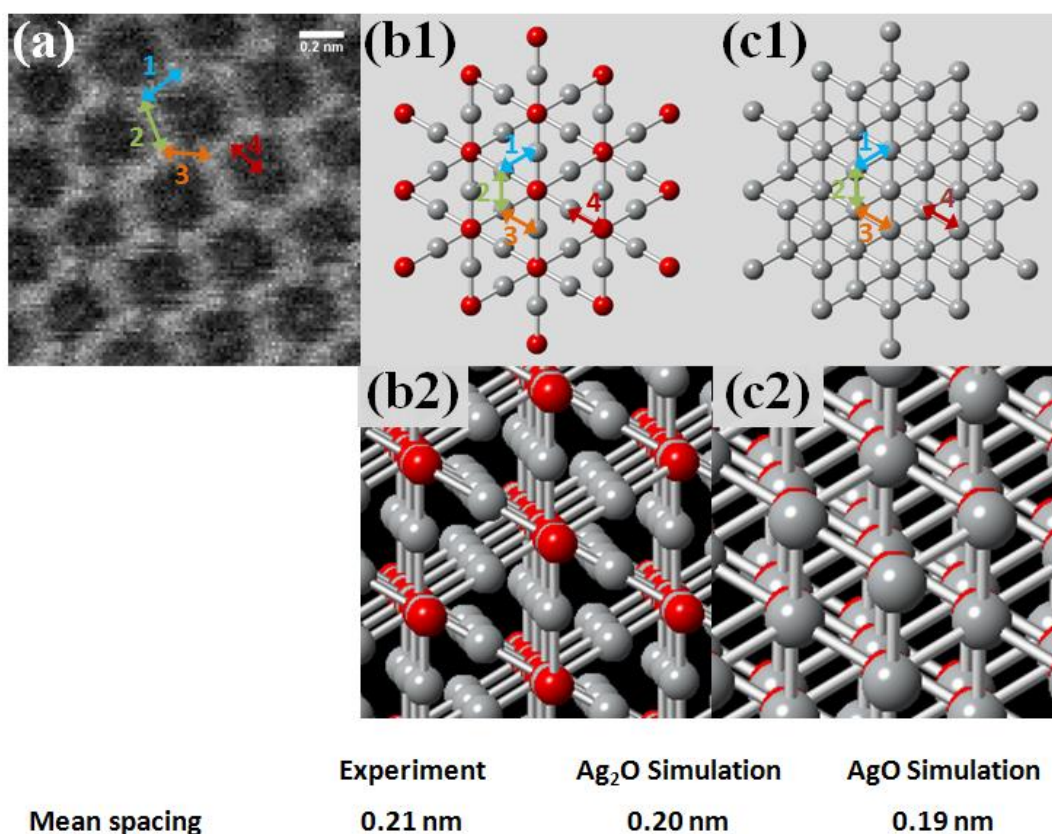
Figure 7.7 shows a selection of typical STEM-HAADF images of Ag-only sample that was synthesised at the same time and using the same method as the AuAg sample discussed in the previous section. As with the AuAg sample, the Ag-only sample has been stored in air throughout the period since synthesis. Comparison of the low magnification images of Ag-only sample in Figure 7.7 with the similarly aged AuAg sample in Figure 7.6 shows greater variation in particle shape and larger particle size in the Ag-only sample. These observations are consistent with a greater tendency for the aged Ag-only nanoparticles to wet the carbon substrate. The image of Figure 7.7(d), taken at the edge of a hole in the carbon substrate (indicated by dashed line) allowing examination of the particles in profile, shows a flattened appearance to the particles (a typical example particle is ringed yellow). The images of Figure 7.7 (e) to (h) show examples of asymmetric core-shell particles from the Ag-only sample. As can be seen from the lower magnification images of Figure 7.7(a) and (b), this type of particle appears less frequently in the Ag-only sample than the AuAg sample, however, where core-shell structures are seen, as with the AuAg sample, the core is most often off-centre to the particle structure. Thus, whilst the greater proportion of core-shell particles in the AuAg sample can be attributed to their Au content, the common asymmetry in the structural evolution of the two samples suggests that this is a feature of Ag nanoparticle oxidation and may be linked to the observed tendency for oxidised Ag nanoparticles to wet the carbon substrate.



**Figure 7.7:** *STEM-HAADF images of aged Ag-only particles.* (a) to (c) in a range of lower magnifications, (d) taken at the edge of a hole in the carbon (indicated by a dashed line), showing the particles in profile (example ringed yellow), and (e) to (f) higher magnification images of single particles. All images were taken after the sample had been stored in air for more than two years.

### 7.2.1 Atomic structure of aged Ag nanoparticles

To identify the type of Ag oxide that may have formed through the aging of Ag nanoparticles in air we have examined one of the simpler structures we have observed in more detail, making comparison to theoretical models for cubic forms of Ag oxide. Figure 7.8(a) gives an extract from a high resolution STEM-HAADF image taken from an aged Ag-only particle alongside theoretical models of cubic forms of  $\text{Ag}_2\text{O}^4$  and  $\text{AgO}^5$  in  $\{111\}$  orientation (Figures 7.8(b) and (c)).

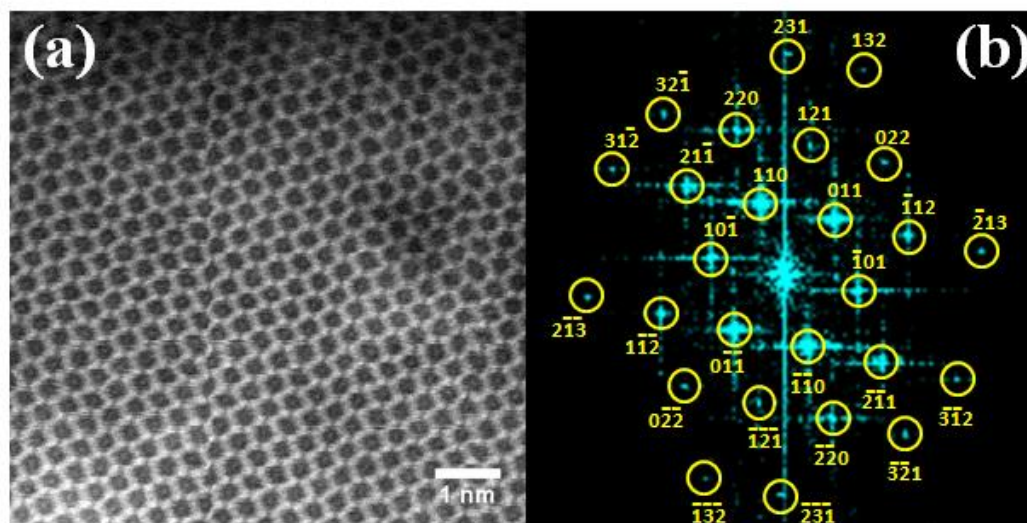


**Figure 7.8: Comparison between experimental and theoretical Ag oxide structures in  $\{111\}$  orientation.** (a) HAADF-STEM image of aged Ag-only sample, (b) and (c) respectively simulated cubic  $\text{Ag}_2\text{O}$  and  $\text{AgO}$  structures in  $\{111\}$  orientation, prepared using CrystalMaker software<sup>3</sup> using coordinate files from respectively references 4 and 5. In (b2) and (c2) the models are slightly offset to show atomic column compositions (Ag grey, O red).

The STEM-HAADF image extract of Figure 7.8(a) shows atomic structure comprising six atomic columns in hexagonal arrangement with a seventh atomic column central to them; this atomic structure is consistent with {111} oriented cubic structure, as is evident from comparison to the simulated structures. The atomic column spacings measured from the STEM-HAADF image as indicated, across a number of different hexagonal structures in the image from which this extract was taken, give a mean atomic column spacing of  $0.21 \pm 0.01$  nm, which is most consistent with the theoretical cubic Ag<sub>2</sub>O structure.

The elemental dependence of STEM-HAADF image contrast allows us to make a qualitative comparison between column to column variations in image intensity and the atomic column compositions of the simulation models. The short length scale of the contrast variation compared to the smooth, rounded appearance of the particles indicates that thickness effects do not cause the dimmer image contrast of the central atomic columns seen in the STEM-HAADF image of Figure 7.8(a). Figure 7.8(b2) and (c2) show images taken from the theoretical simulation models for cubic Ag<sub>2</sub>O and AgO with the structures slightly offset from {111} orientation to show the atomic column composition. These images show that in AgO all the atomic columns have a uniform atomic composition of alternating Ag and O atoms, whereas in Ag<sub>2</sub>O the column compositions vary with the outer columns containing only Ag atoms and the central column containing both Ag and O atoms. Thus, the dimmer image contrast for the central atomic column compared to the surrounding hexagonal ring of columns revealed by atomically resolved elementally sensitive STEM-HAADF imaging, together with the lattice spacing measurements describe above, allows us to identify this structure as most consistent with Ag<sub>2</sub>O. An fft of the

whole image from which Figure 7.8(a) was extracted can be fully indexed to cubic  $\text{Ag}_2\text{O}$  in  $\{111\}$  orientation, as shown in Figure 7.9.



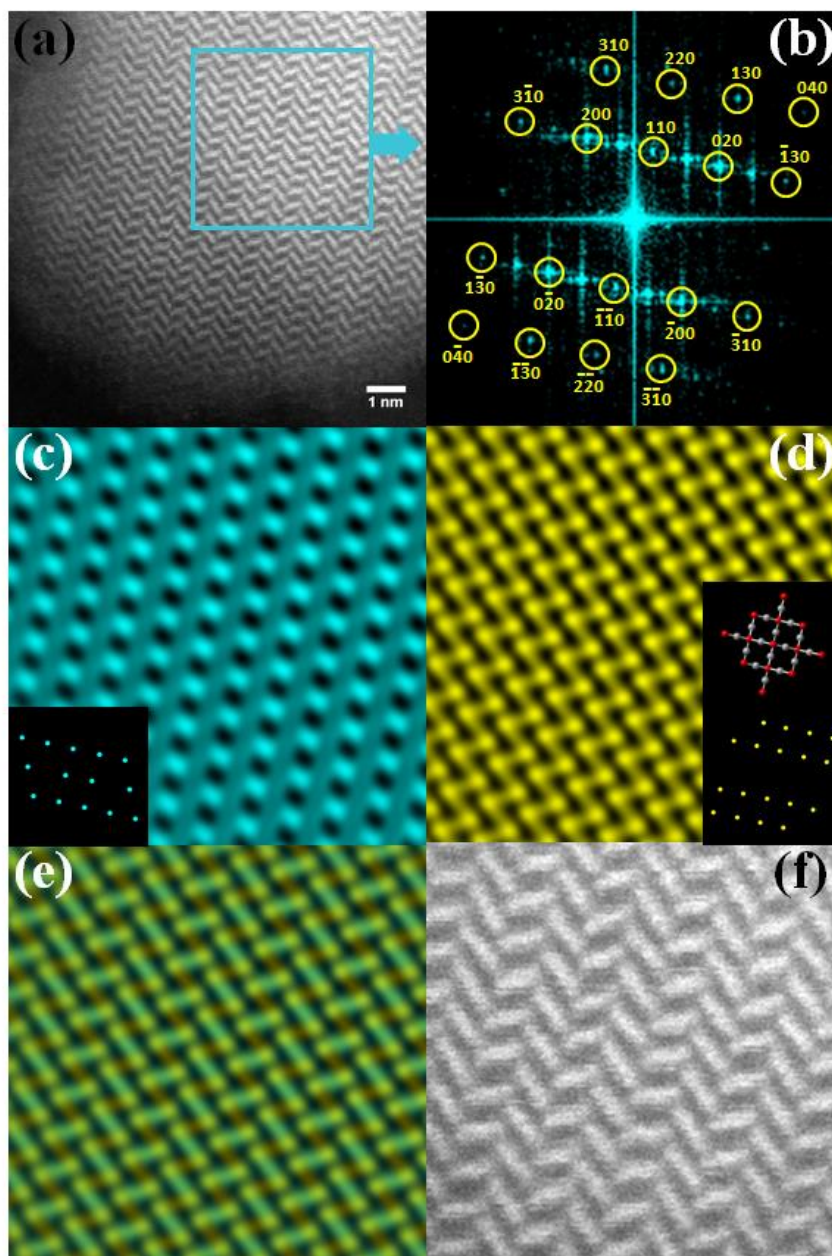
**Figure 7.9: STEM-HAADF image and fft of  $\text{Ag}_2\text{O}$  in  $\{111\}$  orientation.** (a) STEM-HAADF image of an aged Ag-only particle, with (b) whole image fft indexed to cubic  $\text{Ag}_2\text{O}$  reflections in  $\{111\}$  orientation.

### 7.2.2 More complex structures

Figures 7.10(a) shows an example of one of the more complex structures we find in aged Ag-only nanoparticles. As shown in Figures 7.10(b) a proportion of the fft spots in the diffraction pattern associated with this structure can be indexed to cubic  $\text{Ag}_2\text{O}$  atomic structure in  $\{001\}$  orientation, however, there are also a number of spots that cannot be related to regular cubic  $\text{Ag}_2\text{O}$  atomic structure. To identify the parts of the images that can be associated with the cubic  $\text{Ag}_2\text{O}$  and non-cubic  $\text{Ag}_2\text{O}$  reflections, Figure 7.10(c) and (d) show filtered images produced using fft masks that select the appropriate parts of the diffraction pattern; an overlay of the two filtered images given in Figures 7.10(e) allows



comparison between them and to a corresponding extract from the STEM-HAADF image shown in Figure 7.10(f).



**Figure 7.10:** *Ag<sub>2</sub>O with more complex structure in {100} orientation.* (a) STEM-HAADF image of an aged Ag-only particle, with (b) fft taken as indicated , indexed for {100}orientation (unlabelled spots are not found in {100} orientation). (c) and (d) filtered images formed from respectively non-{100} and {100} masks shown inset, with simulation of {100} oriented Ag<sub>2</sub>O also inset to (d). (e) Overlay of (c) and (d), and (f) a corresponding extract from (a).

The overlay image of Figure 7.10(e) indicates that the non-cubic Ag<sub>2</sub>O diffraction spots originate from atoms occupying positions between Ag atomic columns in regular cubic Ag<sub>2</sub>O atomic structure, resulting in the formation of the zigzag pattern seen in the STEM-HAADF image. One possible explanation for this observation is through the formation of surface layers with atomic structures differing from the underlying cubic Ag<sub>2</sub>O substrate. We have found references in the literature to the formation of surface oxide structures deviating from the underlying cubic Ag substrates in {100} and {111} orientation identified using surface science techniques.<sup>6-13</sup>

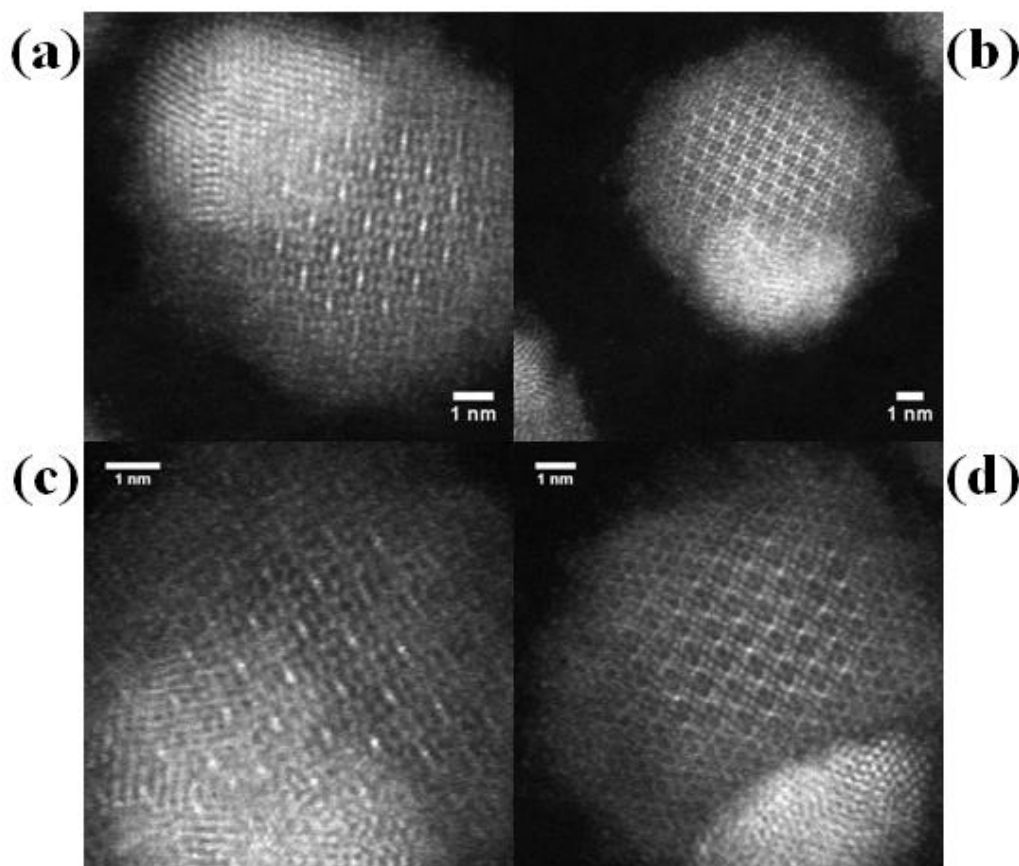
The results presented in this section confirm the formation of cubic Ag<sub>2</sub>O through the prolonged ageing of Ag nanoparticles when stored in air under ambient conditions, consistent with the identification made in our initial studies.<sup>1</sup> Analysis suggests the possibility that more complex surface layer structures may also have formed in this sample.

### **7.3. Oxidation of AuAg nanoparticles**

#### ***7.3.1 Comparison of aged AuAg and Ag-only nanoparticles***

Figure 7.11 shows typical atomically resolved STEM-HAADF images of aged AuAg nanoparticles, taken from the sample shown in lower magnification in Figure 7.6 above. Comparison of the images given in Figure 7.11 with similar images taken from the aged Ag-only sample given in Figure 7.7, show that both samples exhibit contrast variations that can be attributed to elemental segregation, but that we see regular bright contrast patterns within the oxidised regions of the aged AuAg particles that are not seen in the Ag-only images. This observation suggests there may be marked differences in the

atomic structures formed through the aging of these samples, and in particular in the elemental composition of their oxidised shells.



**Figure 7.11:** *Atomically resolved STEM-HAADF images of aged AuAg nanoparticles.* (a) and (b) taken with 10 cm camera length, with an inner collection angle of 62 mrad. (c) and (d) taken with HAADF3 camera length, with an inner collection angle of 92 mrad.

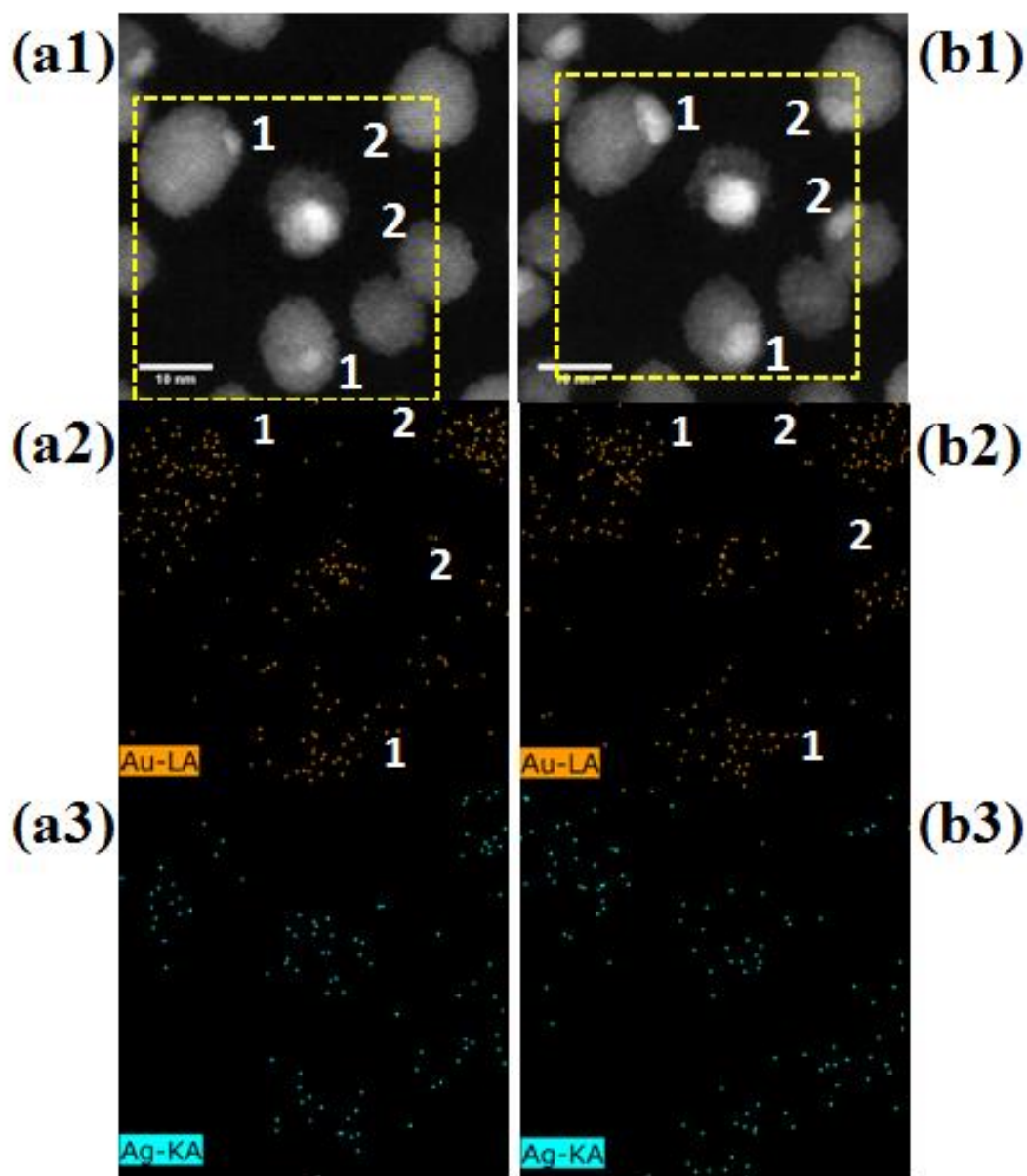
To rule out channelling, effects as the cause of the observed bright patterns we have imaged this sample using two different camera lengths. The images shown in Figures 7.11(a) and (b) were taken using the 10 cm camera length, which has an inner collection angle of 62 mrad. Figures 7.11(c) and (d) show similar particles, with the same bright patterns, taken with the HAADF3 camera length, which has a significantly larger inner



collection angle of 92 mrad. The consistent appearance of the bright patterns in images taken using these two camera lengths indicates that they are not caused by channelling effects. The greater elemental sensitivity of the larger HAADF3 inner collection angle shows the bright pattern in Figure 7.11(c) extending over the core of the particle. This observation suggests this pattern may be caused by a surface layer structure.

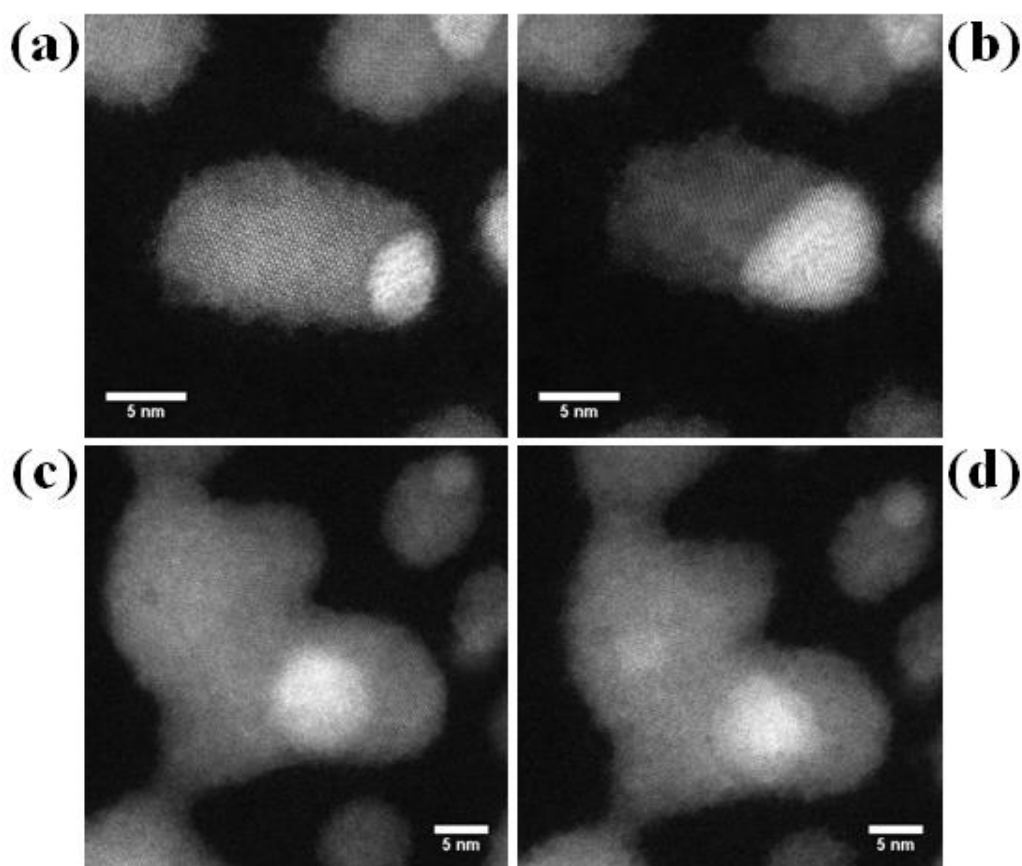
We have conducted high resolution STEM-EDX elemental mapping to identify the location of Au in these particle; Figure 7.12(a1-3) shows typical results. The number of counts acquired in our EDX results is low, but is sufficient for qualitative identification of the elements present. Examination of Figure 7.12(a2) shows Au signal clearly deriving from the oxide regions of all the particles within the field of view. It is notable that this includes from particles that have very small cores (examples marked '1' in Figure 7.12(a1-2)) and also from particles with no cores (examples marked '2' in Figure 7.12(a1-2)).

The STEM-HAADF image of Figure 7.12(b1) was taken after acquisition of the STEM-EDX maps of Figure 7.12(a). Comparison of the two STEM-HAADF images shows interaction with the electron beam during acquisition of the EDX map causes structural changes in the particles. In particular, there is an increase in the size of the cores in the particles marked '1' and the appearance of cores where there none previously in the particles marked '2'. The STEM-EDX map of Figure 7.12(b2), taken immediately after the STEM-HAADF image, shows a corresponding change in the spatial distribution of the Au signal, with greater localisation to the core regions of these particles when compared to the earlier EDX maps of Figure 7.12(a). It is notable that no similar pattern of increased localisation is seen in the Ag signal. These results indicate that Au atoms are present in the oxidised regions formed during the long term evolution of these particles, and that this phenomenon is sensitive to interaction with the electron beam.



**Figure 7.12: STEM-EDX elemental maps of aged AuAg nanoparticles.** STEM-HAADF images (top row) taken immediately before the STEM-EDX Au (middle) and Ag (bottom) elemental maps. The particles were scanned continuously by the electron beam for more than 20 minutes between the images of (a) and (b).

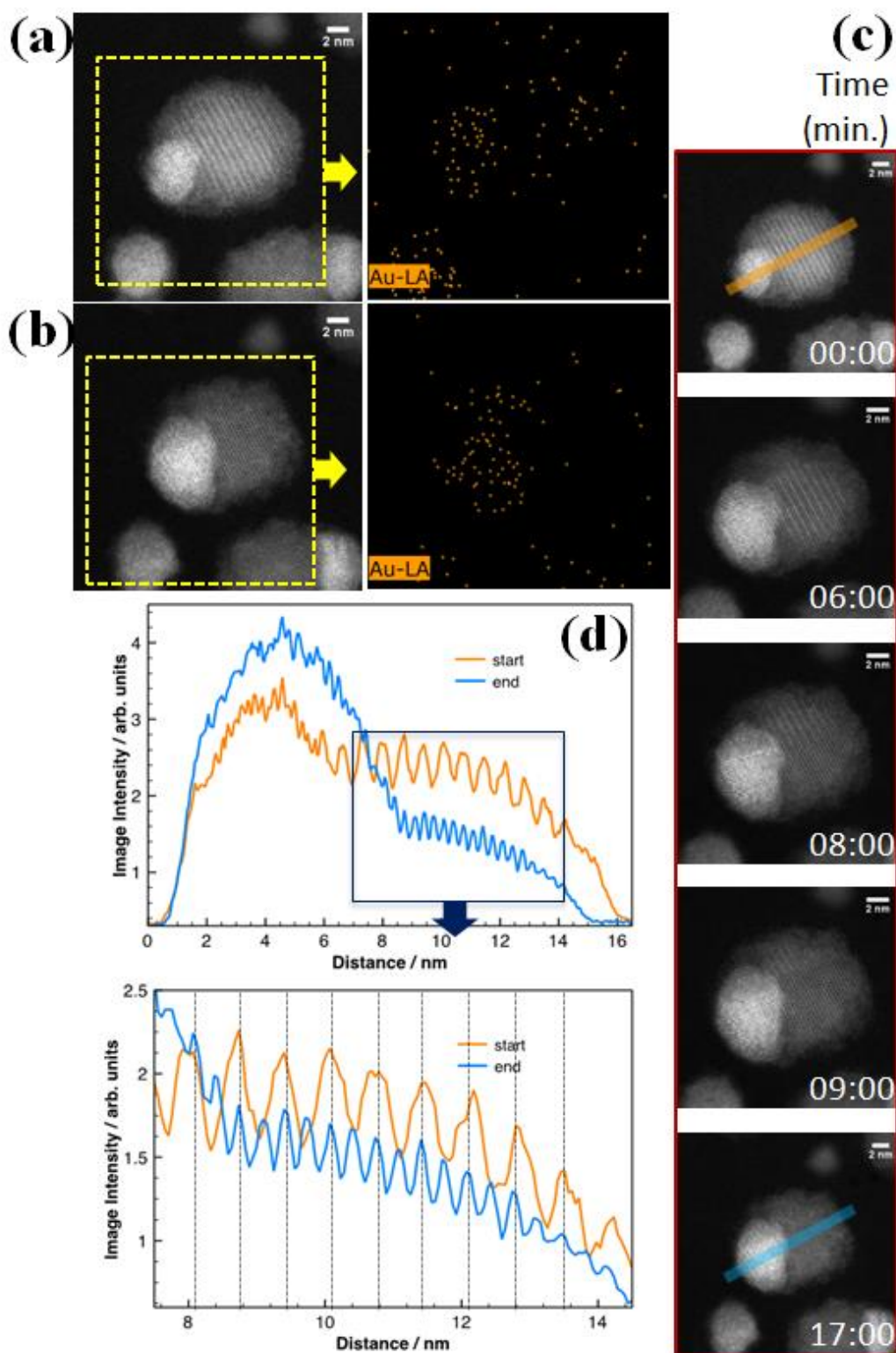
Figure 7.13 shows results comparing the sensitivity of the AuAg sample to the electron beam with that of the Ag-only sample. It is clear from these images that the aged Ag-only nanoparticles are much more stable under the electron beam than the aged AuAg nanoparticles, and thus that the instability apparent in Figure 7.12 is not inherent to  $\text{Ag}_2\text{O}$  structures but is related to the presence of Au in the AuAg sample. If the particles are left sufficiently long under the electron beam their segregated structure can be fully reversed, returning them to AuAg alloyed particles.



**Figure 7.13: AuAg and Ag-only nanoparticles before and after interaction with the electron beam.** STEM-HAADF images acquired before and after continuously scanning of the sample by the electron beam for approximately 20 minutes. (a) and (b) AuAg, and (c) and (d) Ag-only

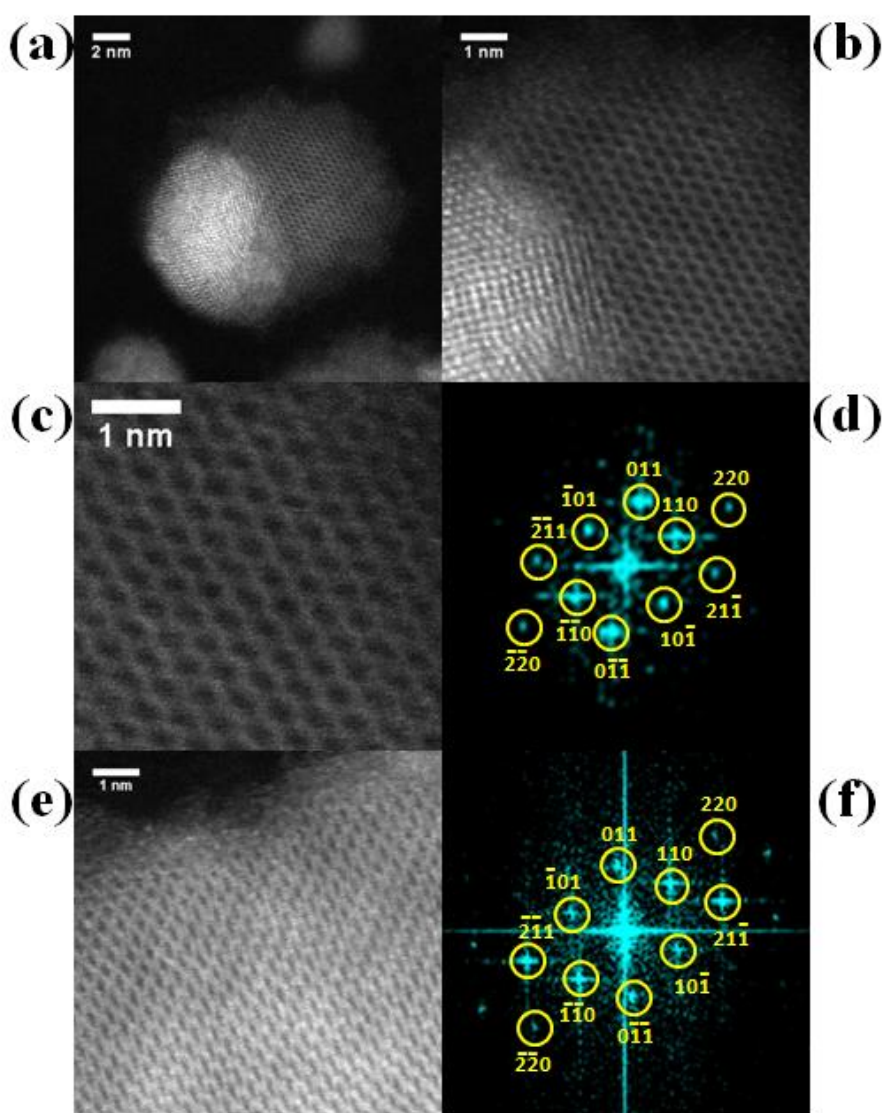
Figure 7.14 shows results monitoring the change that occurs in an AuAg nanoparticle due to interaction with the electron beam in more detail. The STEM-HAADF image of Figure 7.14(a) was taken when the particle had undergone only minimal interaction. The associated STEM-EDX map, taken immediately after the STEM-HAADF image, shows the Au signal is greatest in the bright core, but is also seen throughout the oxidised region of the particle. In comparison, Figure 7.14(b) shows a similar STEM-EDX map taken after the particle had been scanned by the electron beam for approximately 17 minutes. The series of STEM-HAADF images given in Figure 7.14(c) show how the atomic structure of the particle evolved under the electron beam during the period between the images of Figure 7.14(a) and (b), and in particular how the brighter lattice fringes in the oxidised part of the particle first narrow and then recede towards the top of the particle as the core increases in size.

The line intensity profiles given in Figure 7.14(d), taken at the start and end of the process, from the STEM-HAADF images as indicated in Figure 7.14(c), illustrate the scale of change in the particle and match well to the corresponding change in the spatial extent of the Au EDX signal. The line intensity profiles also show a clear correlation in lattice spacing apparent in the oxide parts of these profiles (shown separately with the plots offset for comparison in Figure 7.14(e)) before and after interaction with the electron beam. There are two peaks in intensity in the ‘end’ profile for every one peak in intensity in the ‘start’ profile. These results confirm the presence of Au atoms in the oxidised regions of these aged AuAg nanoparticles, and also indicate that the Au atoms are incorporated into the oxide atomic structure in an ordered manner.



**Figure 7.14:** Monitoring the evolution of an aged AuAg nanoparticle under the electron beam. (a) and (b) STEM-HAADF images and EDX maps of the Au signal of an aged AuAg particle taken before and after interaction with the electron beam. (c) Images taken at intervals over the period of interaction, and (d) line intensity profiles taken as indicated in (c) over 60 pixel width.

Through atomically resolved imaging we can examine the resulting structure after the Au atoms have returned to the core and make comparison to atomic structures identified in the Ag-only sample. Figure 7.15 shows higher magnification images taken after the bright lattice fringes have fully receded and immediately prior to acquiring the final EDX elemental map.



**Figure 7.15:** Atomic structure of an oxidised AuAg nanoparticle after interaction with the electron beam. (a) and (b) STEM-HAADF images of the particle from Figure 7.14 showing the atomic structure after the bright lattice fringes have fully receded. (c) Enlarged extract from (b), with (d) fft. (e) STEM-HAADF image of an Ag-only particle, with (f) fft index for {111} orientation.

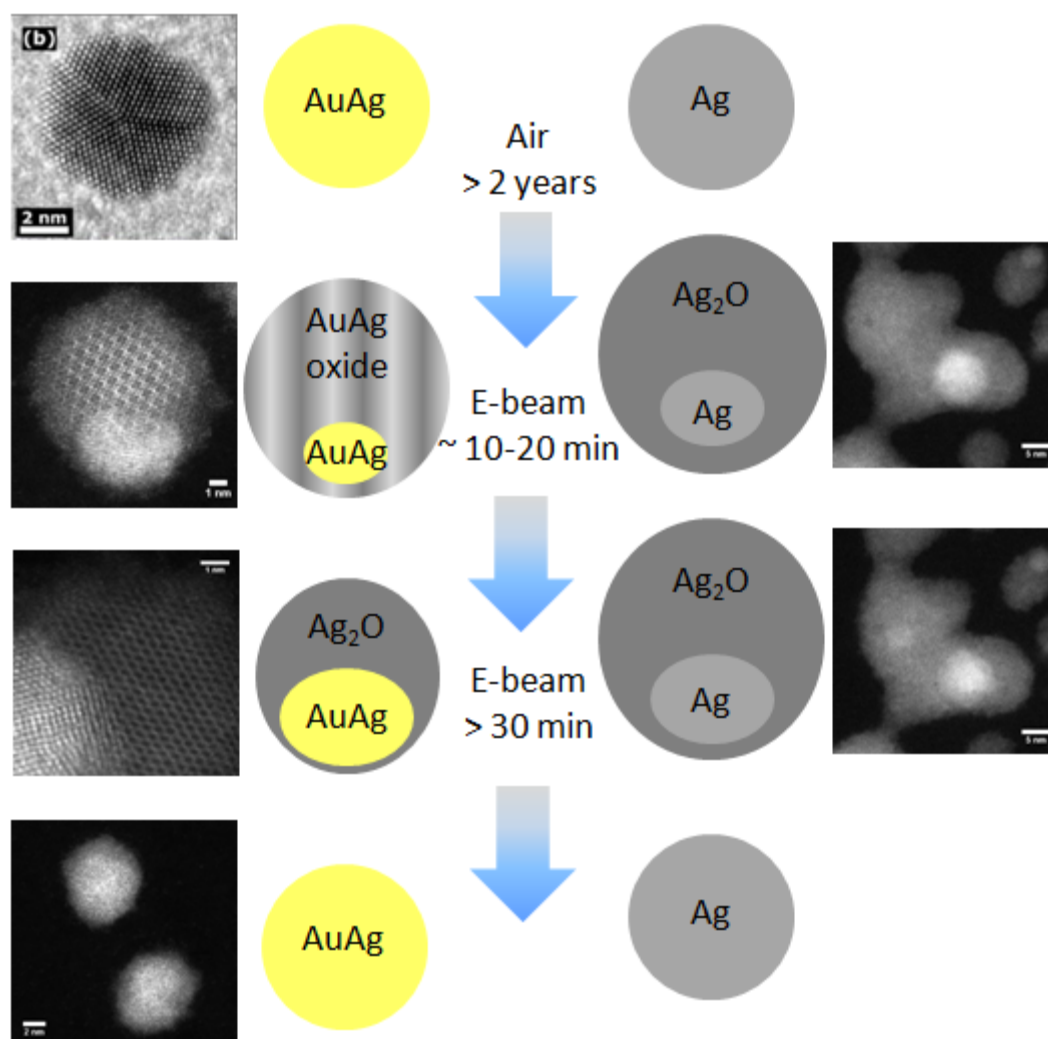
An fft taken from the enlarged extract of the oxidised part of the particle (Figure 7.15(c)) can be indexed to {111} oriented  $\text{Ag}_2\text{O}$ , as shown in Figure 7.15(d). Figure 7.15(e) shows a STEM-HAADF image of an Ag-only particle with an fft (Figure 7.15(f)) that bears a marked similarity to the fft of the AuAg nanoparticle, indicating that they both have atomic structures that are consistent with cubic  $\text{Ag}_2\text{O}$  atomic structure. These results indicate that the underlying crystal structure of the oxidised part of the AuAg particle after the Au atoms have migrated to the core through interaction with the electron beam is consistent with the cubic  $\text{Ag}_2\text{O}$  atomic structure.

The structural evolution of aged AuAg nanoparticles compared to aged Ag-only nanoparticles is summarised schematically in Figure 7.16. Our comparison of these systems suggests a marked similarity in their oxidised atomic structures, consistent with their formation being driven in both systems by the oxidation of Ag. However, in the AuAg system we find Au atoms present in the oxide structure in an ordered manner, and these structures exhibit a greater sensitivity to external influencing factors, such as the electron beam.

### ***7.3.2 Au atoms in AuAg oxide surface structures***

By exploiting the atomic resolution and elemental sensitivity of STEM-HAADF imaging, we can associate the bright lattice patterns we observed in the oxidised parts of the aged AuAg nanoparticles with the location of Au atoms within the AuAg oxide atomic structure. Figures 7.17 and 7.18 show examples analysing typical bright lattice patterns found in aged AuAg particles that are associated with particles in respectively {111} and {001} orientations.

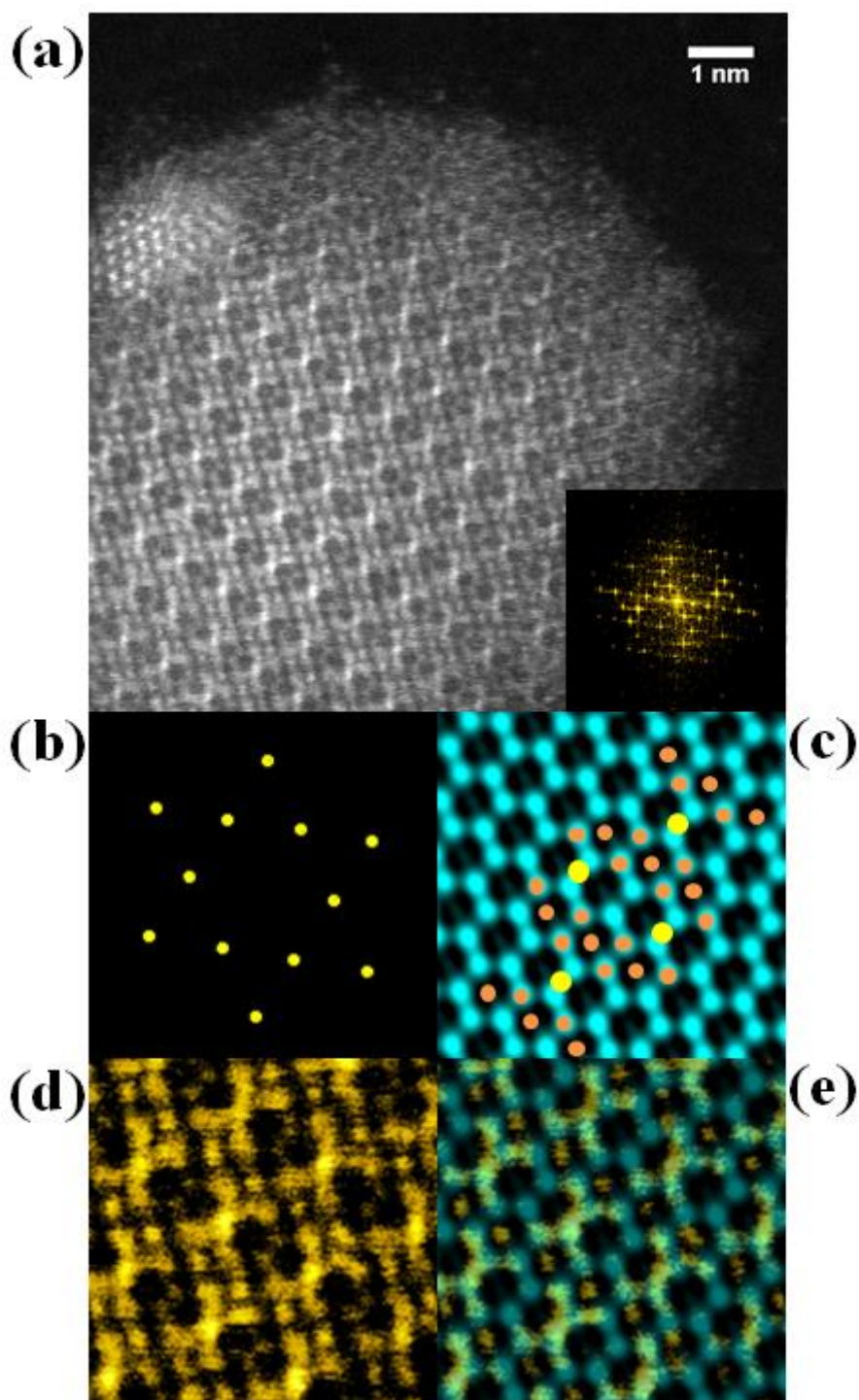




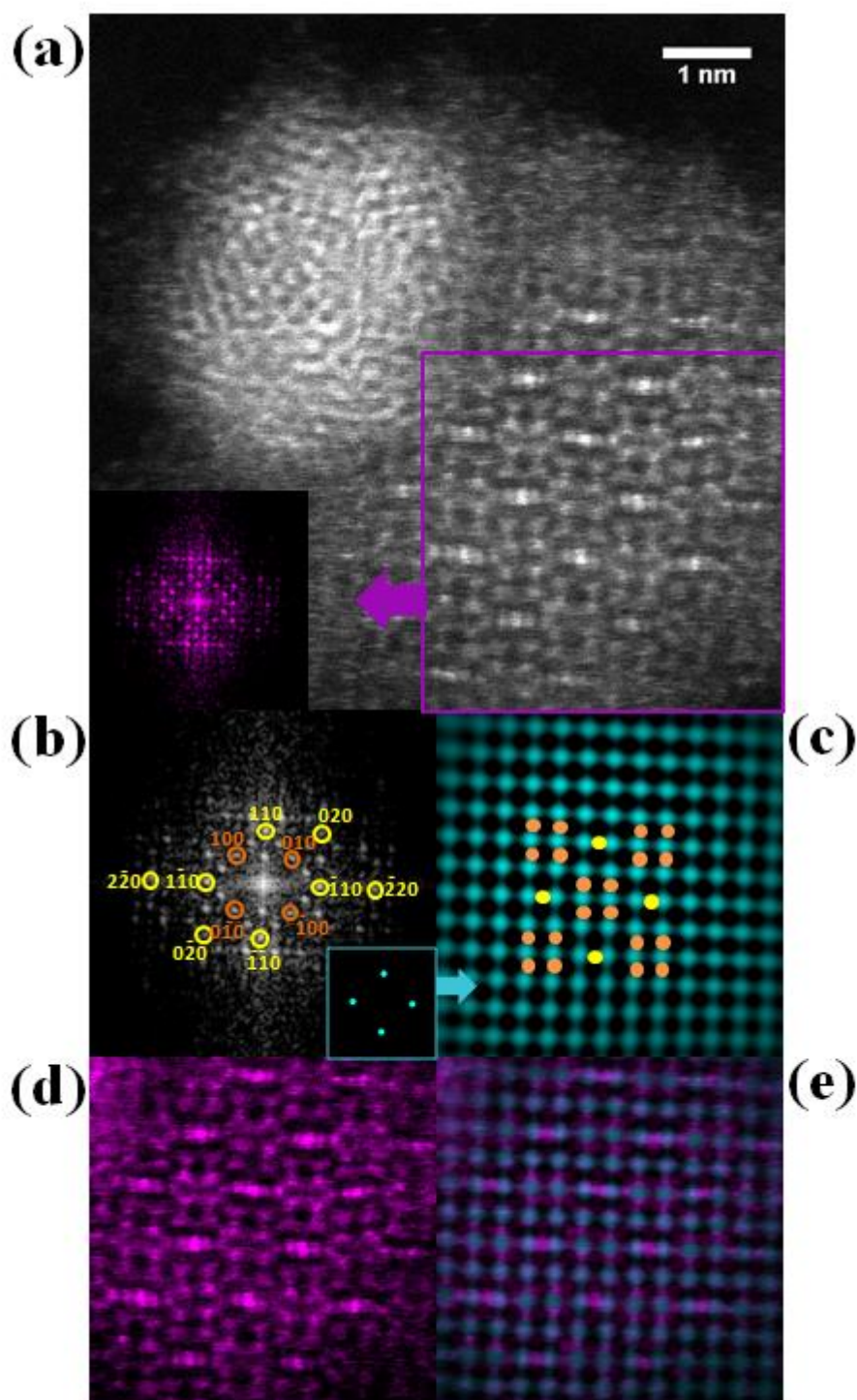
**Figure 7.16: Schematic comparison of the structural evolution of AuAg and Ag-only nanoparticles.** Showing schematically the impact prolonged aging in air and interaction with the electron beam on AuAg and Ag-only nanoparticles.

The fft inset to the STEM-HAADF image of Figure 7.17(a) is consistent with a cubic structure and can be partially indexed to cubic Ag<sub>2</sub>O {111} reflections. The {111} diffraction spots can be used to make an fft mask (shown in Figure 7.17(b)), the inverse of which produces a filtered image that reveals the parts of the original image that correspond to the cubic Ag<sub>2</sub>O atomic structure in {111} orientation; Figure 7.17(c) shows the filtered image formed from the mask shown in Figure 7.17(b).





**Figure 7.17:** *An aged AuAg nanoparticle exhibiting complex lattice structure in {111} orientation.* (a) STEM-HAADF image with whole image fft inset. (b) fft mask of the [111] diffraction spots and (c) filtered image produced using the mask (b), with schematic overlay showing the location of the brightest features. (d) Enlarged extract the STEM-HAADF image of (a) shown in false colour. (e) Overlay of (c) and (d).



**Figure 7.18:** An aged AuAg nanoparticle exhibiting complex lattice structure in  $\{100\}$  orientation (a) STEM-HAADF image of an aged AuAg particle, with fft inset take as indicated. (b) Indexed fft from (a). (c) Inverse fft using the mask inset to (b), with schematic overlay. (d) Extract from (a) in false colour. (e) Overlay of the images (c) and (d).

Figure 7.17(d) shows a false colour enlarged extract from the region of the STEM-HAADF image of Figure 7.17(a) that corresponds to the filtered image of Figure 7.17(c) and Figure 7.17(e) shows an overlay of Figure 7.17(c) and (d) for comparison. The overlaid image allows us to identify where the brightest features in the HAADF image are located relative to the cubic Ag<sub>2</sub>O atomic structure revealed by the filtered image; these features are marked by schematic dots on the filtered image of Figure 7.17(c), with yellow corresponding to the most intense features and orange to secondary features in the bright lattice pattern.

Comparison of the schematic dots with the filtered image of Figure 7.17(c) shows that the yellow dots occupy positions in between two Ag columns in the hexagonal ring of {111} oriented cubic Ag<sub>2</sub>O structure, whereas the orange dots are positioned over the top of atomic columns, both in the hexagonal ring and central to it. It is notable that orange dots located over the central atomic columns in the hexagonal structures appear in every other row of the pattern, which is consistent with observations made in relation to the ‘start’ and ‘end’ lattice structures shown in Figure 7.14 above, where the bright lattice fringe spacing in the oxide region of the particle at the start was twice the lattice spacing in the same region at the end.

In Figure 7.18 the fft associated with this bright lattice pattern can be partially indexed to cubic Ag<sub>2</sub>O reflections in {001} orientation, including some forbidden reflections. Identification of the location of lattice features relative to this orientation of cubic Ag<sub>2</sub>O atomic structure shows a common trend in the location of the brightest lattice features, identified by yellow dots, as they similarly occupy locations between what would be purely Ag columns in {001} oriented cubic Ag<sub>2</sub>O atomic structure. Thus the incorporation of Au atoms in locations between what would be Ag columns in Ag<sub>2</sub>O

atomic structure appears to be a common feature of the structures formed through AuAg oxidation that is not dependent on particle orientation.

In comparison, there is no consistency between the two patterns in the location of the orange dots, which represent secondary features. In Figure 7.17 the orange dots of the secondary features are positioned over columns in the hexagonal structure that in cubic  $\text{Ag}_2\text{O}$  that comprise both Ag only (hexagon columns) and a mix of Ag and O atoms (central column). In contrast, in Figure 7.18(c) the secondary features marked by orange dots are position in locations between what would be purely Ag columns in  $\{001\}$  oriented cubic  $\text{Ag}_2\text{O}$ . These secondary features can be associated with the location of Au atoms in the oxide structure, because no similar patterns are seen in  $\text{Ag}_2\text{O}$  formed in our aged Ag-only sample, but the variation in their location between the two patterns shown in Figures 7.17 and 7.18 suggests they may have different origins.

Our characterisation of the similarly aged Ag-only sample revealed the formation of complex  $\text{Ag}_2\text{O}$  atomic structures in surface layers with structures differing from the underlying cubic structure. The sensitivity of the AuAg oxide bright lattice patterns to interaction with the electron beam and the appearance of bright patterns over the core when imaged using HAADF3 camera length (shown in Figure 7.11) indicates these patterns can be associated with Au atoms located in ordered surface with atomic structure that differs from the underlying cubic structure.

### ***7.3.3 Au atoms in AuAg oxide underlying structures***

In addition to the above results, we have also found indications that Au atoms are incorporated in underlying structures in locations that are consistent with substitution of Au atoms into regular cubic  $\text{Ag}_2\text{O}$  atomic structure; one example is shown in Figure 7.19.





The STEM-HAADF image of Figure 7.19(a) shows an aged AuAg nanoparticle with a bright lattice pattern present in the centre of the oxidised part of the particle. This pattern is the same as the example shown in Figure 7.17 and is in  $\{111\}$  orientation (fft shown in Figure 7.19(b)). Examination of the region around the bright patterns shows a simpler atomic structure. An enlarged example of this structure is shown in Figure 7.19(c)) reveals an atomic structure that is consistent with the cubic  $\{111\}$  pattern of a central atomic column surrounded by a hexagon of atomic columns. These observations are consistent with the bright pattern in the centre of the particle being caused by surface over layers, whilst the surrounding simpler pattern reveals a simpler underlying atomic structure.

Comparison of an enlarged section of the particle shown in Figure 7.19(c) with the STEM-HAADF image extract of  $\text{Ag}_2\text{O}$  in  $\{111\}$  orientation shown in Figure 7.17(d) (taken from the Ag-only sample that was examined in detail in Section 7.2 above) shows a marked similarity in the pattern of atomic columns and single column wide line intensity profiles, taken as indicated in Figure 7.19(e) shows an almost exact match in atomic column spacing. However, despite this obvious similarity, the pattern of variation in column to column image intensity differs between the two structures, indicating they have differing elemental compositions. The AuAg line profile follows a trend of three columns of similar intensity followed by a fourth of lower intensity (against a background trend in intensity that can be attributed to thickness effects at the edge of the particle). In comparison, the Ag-only line profile shows an alternating pattern of brighter image intensity from the hexagonal ring columns and dimmer image intensity from the central column that is consistent with atomic column composition in  $\{111\}$  oriented cubic  $\text{Ag}_2\text{O}$  structure. The observed variation between AuAg and Ag-only column to column intensity

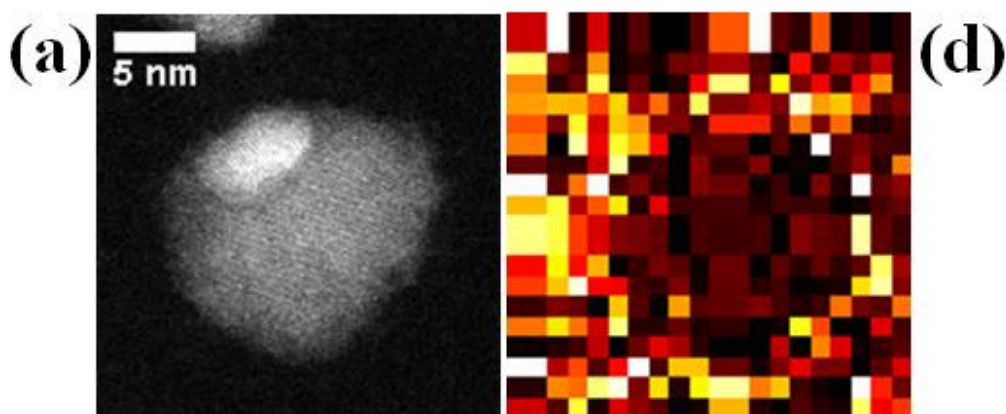
patterns in {111} orientation is indicative of compositional variation and specifically can be attributed to the presence of Au atoms in alternating central atomic columns in the atomic structure (indicated by arrows in Figure 7.19(e)). As the atomic column spacing is consistent between the AuAg and Ag-only structures, this indicates the substitution of Au atoms into locations within the central atomic column of {111} oriented cubic Ag<sub>2</sub>O structure in the AuAg sample.

The results presented in this section demonstrate the formation of ordered AuAg oxide structures with Au atoms substituted into cubic Ag<sub>2</sub>O atomic through the long term aging in air of AuAg nanoparticles. Given the clear differences we see in the overall particle morphology between aged AuAg and aged Ag-only nanoparticles, it seems likely that the Au atoms play an active role in the structural evolution of the bimetallic system.

## 7.4 Impact on Localised Surface Plasmon Response

In this section we use STEM-EELS to investigate the impact on LSPR of the structural evolution caused by aging in air of AuAg nanoparticles. Figure 7.20(a) shows a STEM-HAADF image of an aged AuAg particle, exhibiting a typical bright, off-centred core, and dimmer, more extensive oxidised region. Ag has its surface plasmon response at around 3.7 eV (Table 2.4 Chapter 2). Figure 7.20(b) shows STEM-EELS spectrum image map of the particle over the energy loss range 3.7 eV to 4.0 eV; asymmetry is apparent in this map that corresponds well with the position of the particle core in the STEM-HAADF image, indicating that the dielectric response of the oxide region of the particle damps the metallic Ag response from the core. This observation is consistent with the findings of Qiu *et al.* who reported a shift from metallic to dielectric behaviour with the progressive

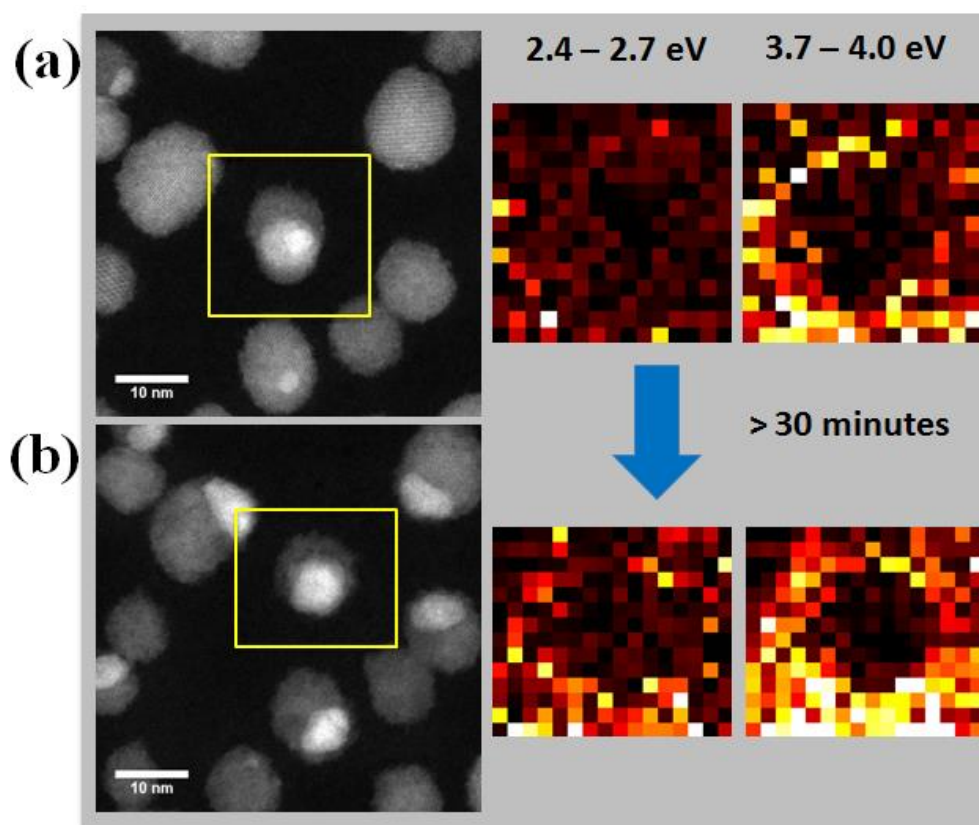
oxidation of thin film Ag systems, as the free electrons became bound in the oxidised atomic structure.<sup>14</sup>



**Figure 7.20:** *STEM-EELS map of an aged AuAg nanoparticle.* (a) STEM-HAADF image of an aged AuAg particle. (b) corresponding STEM-EELS spectrum image map for the energy loss range 3.7 eV to 4.0 eV.

Figure 7.21 shows results demonstrating the impact of sample evolution on the LSPR response with STEM-EELS spectrum image maps taken at different stages of structural change under the electron beam. The maps in Figure 7.21 are presented using fixed contrast limits, allowing direct comparison of signal strength between the maps. Examination of the spectrum image maps in Figures 7.21(a) and (b) over the 3.7 eV to 4.0 eV energy loss window shows a clear alteration in the LSPR response with the change in particle structure, with the signal becoming noticeably stronger. This is consistent with the destruction of the oxide structure under the electron beam freeing the Ag atoms to behave as a metal. It is notable that the signal retains its asymmetry in the later map, indicating that even a thin oxide shell can have a marked impact on Ag LSPR response.





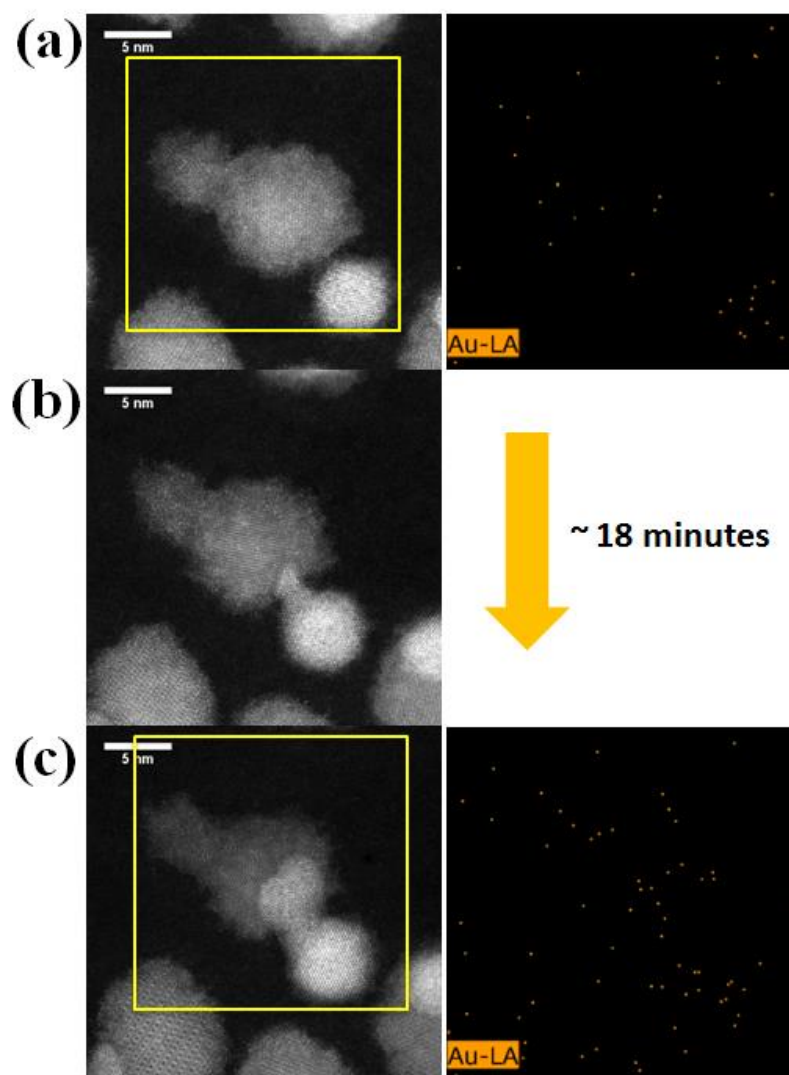
**Figure 7.21: Evolution of STEM-EELS mapping of an aged AuAg nanoparticle through interaction with the electron beam.** (a) and (b) STEM-HAADF images and corresponding STEM-EELS spectrum image maps for the energy loss ranges noted, taken as indicated by yellow boxes. Between (a) and (b) the particle had been exposed to the electron beam for more than 30 minutes.

Figure 7.21 also gives spectrum image maps for the 2.4 eV to 2.7 eV energy loss range, corresponding to the surface plasmon resonance of Au (Table 2.4 Chapter 2). In Figure 7.21(a) there is almost no response in this energy loss range, however, in Figure 7.21(b) a clearly asymmetric response can be seen, with a spatial distribution that correlates with the side of the particle where we see the core. These results demonstrate the marked impact that oxidation has on the LSPR response of this system, and show that distinct LSPR signals can be detected for both Au and Ag in these particles after reversal

of oxidation. This is despite the low Au content of these particles and the mixed state of the core.

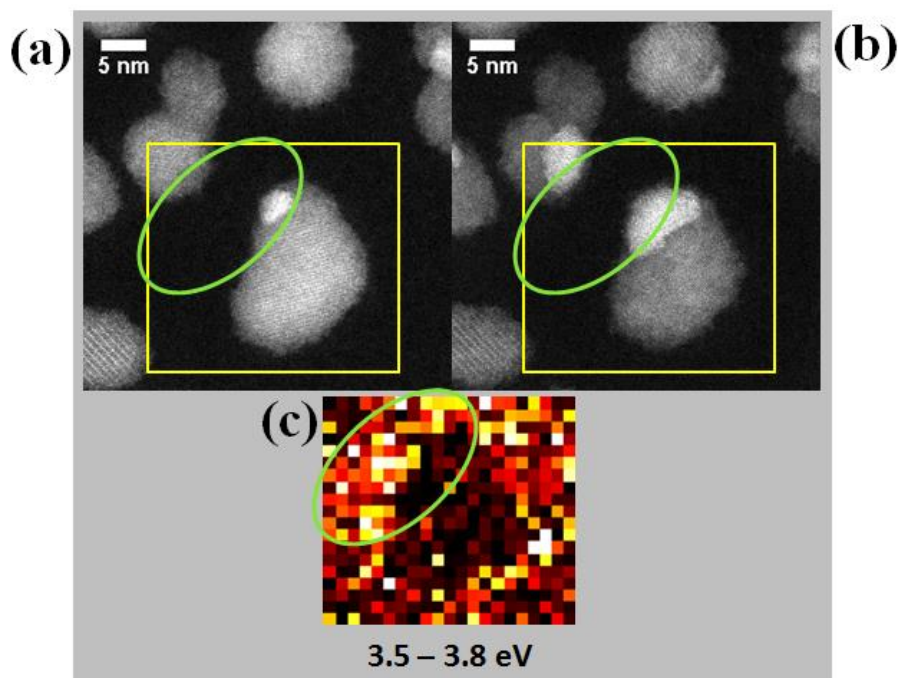
During observations made on this aged AuAg sample we have also identified indications that their LSPR response may influence their structural evolution under the electron beam. Figure 7.22 shows a series of STEM-HAADF images of two initially separated particles, the larger of which has the appearance of a fully oxidised particle with low Au content, and where the smaller is a metal-rich particle. After approximately 18 minutes scanning by the electron beam the larger particle can be seen to have formed a bright core.

Figure 7.22(b) shows the initial stages of the process, where the gap between the particles has been bridged and a small core has started to form, whilst in Figure 7.22(c) the particles are fully joined with a large core now apparent in the oxidised particle. This behaviour is not typical of this sample as the particles usually remain separated under the electron beam. The Au EDX signal associated with this latter image shows a shift in the pattern of the Au signal to greater localisation in the location of the newly formed core. Once a core has formed our results of Figures 7.20 and 7.21 indicate that it will have an LSPR response under the electron beam. The proximity of the newly formed core to the adjacent metal-rich particle will result in LSPR coupling, and associated induced electric field enhancements between the two.<sup>15,16</sup> As aggregation under the electron beam is not typical behaviour for this sample it seems possible that field enhancement in the gap between the particles played a role in the joining of these particles. LSPR induced movement has been reported between adjacent Au nanoparticles.<sup>17</sup>



**Figure 7.22:** *The evolution of two aged AuAg nanoparticles under the electron beam.* (a) to (c) STEM-HAADF images and corresponding Au EDX maps taken as indicated by yellow boxes. The maps were acquired over approximately (a) 5 minutes, and (b) 10 minutes.

We have seen similar indications in other particles in this sample where cores form in locations that may be related to LSPR coupling, but where the particles do not aggregate; such as the example shown in Figure 7.23. Figure 7.23(a) and (b) show STEM-HAADF images before and after the acquisition of the spectrum image map shown in Figure 7.23(c).



**Figure 7.23:** Example of core formation between adjacent AuAg nanoparticles. (a) and (b) STEM-HAADF images taken before and after the spectrum image map of (c) (acquired over a period of approximately 23 minutes).

In Figure 7.23 core is formed between the two images in the fully oxidised particle in the top left corner of the area through interaction with the electron beam during the period over which the spectrum image map was acquired. The spectrum image map shows an asymmetric response consistent with the location of the core in the central particle and localised to the gap between it and the oxidised particle (ringed in green). As in Figure 7.22, the new core forms in a location that has a marked correlation to the LSPR response of the adjacent particle. These results, together with those shown in Figure 7.22, suggest the possibility that LSPR response of adjacent metallic particles, or metallic particle cores, may influence the location of core formation in fully oxidised particles. The possibility to manipulate particle structure using LSPR induced electric fields is a phenomenon that has potential in the field of the self-assembly of nanoscale devices, and we believe may merit further investigation.

## **7.5 Conclusions**

In this chapter we have used ac-STEM to investigate the structures formed through the long term evolution of AuAg and Ag-only nanoparticles when stored in air under ambient conditions. We have used a combination of atomic resolution imaging and sub-nanometre resolution spectroscopy to identify the formation of AuAg oxides with atomic structure based on  $\text{Ag}_2\text{O}$  in both non-cubic surface layer structures and in underlying regular cubic structures. We have demonstrated the sensitivity of these structures to interaction with the electron beam. We have also used STEM-EELS spectrum image mapping to show the impact that off-centred segregation that forms in this system has on the LSPR response and have found indications that this response may in itself influence structural alteration in these particles.

## List of References

195. Belic, D.; Chantry, R.L.; Li, Z.Y.; Brown, S.A., Ag-Au nanoclusters: structure and phase segregation, *Appl. Phys. Lett.*, **2011**, *99*, 117914
196. Petterson, L.A.A.; Snyder, P.G., Preparation and Characterisation of Oxidised Silver Thin Films, *Thin Solid Films*, **1995**, *270*, 69-72
197. Crystallmaker version 2.6.3, Crystallmaker Software Limited, Oxford, England.
198. Wyckoff, R.W.G., The Crystal Structure of Silver Oxide ( $\text{Ag}_2\text{O}$ ), *Am. J. Sci.*, **1922**, *3*, 184-188
199. Stehlik, B.; Weidenthaler, P., Kristallstruktur von Silber(II)-Oxyd, *Collect. Czech. Chem. C.*, **1959**, *24*, 1416-1419
200. Carlisle, C.I.; Fujimoto, T.; Sim, W.S.; King, D.A., Atomic Imaging of the Transition Between Oxygen Chemisorptions and Oxide Film Growth on  $\text{Ag}\{111\}$ , *Surf. Sci.* **2000**, *470*, 15-31
201. Carlisle, C.I.; King, D.A., Imaging the Surface and Interface Atoms of an Oxide Film on  $\text{Ag}\{111\}$  by Scanning Tunneling Microscope: Experiment and Theory, *Phys. Rev. Lett.* **2000**, *84*, 3899-3902
202. Costina, I.; Schmid, M.; Schiechl, H.; Gajdos, M.; Stierle, A.; Kumaragurubaran, S.; Hafner, J.; Dosch, H.; Varga, P., Combined STM, LEED, DFT Study of  $\text{Ag}(100)$  Exposed to Oxygen Near Atmospheric Pressures, *Surf. Sci.* **2006**, *600*, 617-624
203. Michaelides, A.; Bocquet, M.L.; Sautet, P.; Alavi, A.; King, D.A., Structures and Thermodynamic Phase Transitions for Oxygen and Silver Oxide Phases on  $\text{Ag}\{111\}$ , *Chem. Phys. Lett.* **2003**, *367*, 344-350
204. Roviada, G.; Pratesi, F.; Maglietta, M.; Ferroni, E., Chemisorption of Oxygen on the Silver (111) Surface, *Surf. Sci.* **1974**, *43*, 230-256 Wang, Z.W.; Palmer, R.E., Intensity Calibration and Atomic Imaging of Size-Selected Au and Pd Clusters in Aberration-Corrected HAADF-STEM, *J. Phys. Conf. Ser.* **2012**, *371*, 012010
205. Schmid, M.; Reicho, A.; Stierle, A.; Costina, I.; Klikovits, J.; Kostelnik, P.; Dubay, O.; Kresse, G.; Gustafson, J.; Lundgren, E.; Andersen, J.N.; Dosch, H.; Varga, P., Structure of  $\text{Ag}(111)\text{-p}(4 \times 4)\text{-O}$ : No Silver Oxide, *Phys. Rev. Lett.* **2006**, *96*, 146102
206. Schnadt, J.; Michaelides, A.; Knudsen, J.; Vang, R.T.; Reuter, K.; Laegsgaard, E.; Scheffler, M.; Besenbacher, F., Revisiting the Structure of the  $\text{p}(4 \times 4)$  Surface Oxide on  $\text{Ag}(111)$ , *Phys. Rev. Lett.*, **2006**, *96*, 146101
207. Schnadt, J.; Knudsen, J.; Hu, X.L.; Michaelides, A.; Vang, R.T.; Reuter, K.; Li, Z.; Laegsgaard, E.; Scheffler, M.; Besenbacher, F., Experimental and Theoretical Study of Oxygen Adsorption Structures on  $\text{Ag}(111)$ , *Phys. Rev. B*, **2009**, *80*, 075424

208. Qiu, J.H.; Zhou, P.; Gao, X.Y.; Yu, J.N.; Wang, S.Y.; Li, J.; Zheng, Y.X.; Yang, Y.M.; Song, Q.H.; Chen, L.Y., Ellipsometric Study of the Optical Properties of Silver Oxide Prepared by Reactive Magnetron Sputtering, *J. Korean Phys. Soc.*, **2005**, *46*, S269-S275
209. Grzelczak, M.; Mezzasalma, S.A.; Ni, W.; Herasimenka, Y.; Feruglio, L.; Montini, T.; Perez-Juste, J.; Fornasiero, P.; Prato, M.; Liz-Marzan, I.M., Antibonding Plasmon Modes in Colloidal Gold Nanorod Clusters, *Langmuir*, **2011**, *28*, 8826-8833
210. Halas, N.J.; Lal, S.; Chang, W.S.; Link, S.; Nordlander, P., Plasmons in Strongly Coupled Metallic Nanostructures, *Chem. Rev.* **2011**, *111*, 3913-3961
211. Batson, P.E.; Reyes-Coronado, A.; Barrera, R.G.; Rivacoba, A.; Echenique, P.M.; Aizpurua, J., Plasmonic Nanobilliards: Controlling Nanoparticle Movement Using Forces Induced by Swift Electrons, *Nano Lett.*, **2011**, *11*, 3388-3393

---

## Chapter 8

### Conclusions & Future Work

In this thesis we have presented work exploring the capabilities of aberration corrected scanning transmission electron microscopy (ac-STEM) in characterising the structure and localised surface plasmon resonance (LSPR) properties of bimetallic nanoparticles. In this chapter we summarise the principle conclusions from this work, and consider what opportunities this study has revealed for future work in this field.

#### 8.1 Conclusions

##### *8.1.1 Structural Characterisation*

The first stage of the work presented in Chapter 5 revealed the complex growth mode followed by Rh deposited on Au seed nanorods. We showed that Rh over-growth follows an island growth mode, with a marked preference for initial deposition at the ends and end corners of the nanorods that persisted through subsequent over-growth to form core-shell nanorods with irregular and angular appearance when compared to the Au-seed



nanorods. This growth pattern was linked to the trend in optical properties of the nanorods across the series of samples with varying the proportions of Au and Rh. This was the first time that the complex growth mode of Rh on Au seed nanorods had been demonstrated.

In the second stage of this work we applied the atomically resolved elemental sensitivity of ac-STEM imaging to characterising the atomic structure of the metal-metal interfaces of AuRh and AuPd nanorods. We showed the existence of a clearly segregated interface between bulk miscible Au and Pd and a randomly mixed alloy layer at the interface between bulk immiscible Au and Rh. By making a direct comparison between these two similar nanorod systems, we also revealed the key role played by reaction kinetics in forming the interfacial structures in these systems. This is the first time that alloying between bulk immiscible Au and Rh metals has been unambiguously demonstrated.

### ***8.1.2 LSPR response***

In Chapter 6 of this thesis we presented results using the spectrum image mapping facility of electron energy loss spectroscopy (EELS) in STEM to improve our understanding of the origins of localised surface plasmon resonance (LSPR) response in bimetallic core-shell nanoparticles. We demonstrated the existence of longitudinal LSPR response of an extended range in both AuPd and AuRh nanorods, which is the first time that such a phenomenon has been revealed. We showed that AuPd nanorods have to longitudinal LSPR modes that can be attributed respectively to the responses of the core and shell metals. We also showed the marked impact that the Pd surface plasmon resonance has on the LSPR response of AuPd nanorods at energy losses above 4 eV.

Through examining the response AuRh nanorods, and through systematic optical response simulation the work, we also showed the sensitivity of bimetallic LSPR response to irregular particle morphology. This work demonstrated the importance of correlating LSPR response to composition and morphology on a single particle basis to gain full understanding of the LSPR response of systems with complex and variable structure, which is the case in many bimetallic systems.

### ***8.1.3 Long term stability***

In Chapter 7 we presented results revealing the marked structural change that takes place in alloyed AuAg nanoparticles through long term aging in air, forming asymmetric core shell structures through the impact of oxidation. By making comparison to similar aged Ag-only nanoparticles we identified the formation of ordered AuAg oxide structures both in non-cubic surface layers and in underlying cubic structures that are based on Ag<sub>2</sub>O atomic structure. Using the atomically resolved elemental sensitivity of STEM-HAADF imaging to demonstrate that location Au atoms in the AuAg oxide atomic structure. We showed that that the bimetallic oxide structures are both more complex and more sensitive to external influences than their monometallic equivalent.

Using STEM-EELS spectrum image mapping, imaging and EDX spectroscopy we have also shown the profound impact that AuAg oxidation has on the LSPR response of this system. We have shown asymmetry in the response caused by the damping effect of the asymmetric oxide shell and have found indications that LSPR response may influence the structural evolution of the oxidised particles under the electron beam.

### 8.1.4 Summary

Taken in combination the work presented in this thesis demonstrates that ac-STEM is an extremely effective tool in characterising of the structure and LSPR properties of bimetallic nanoparticles. We have shown how the range of elementally sensitive imaging and spectroscopy techniques it provides to unrivalled spatial resolution within one instrument can be used to gain fundamental understanding of the metal-metal interactions taking place in these systems, and to form direct connections between them and the enhanced properties that make these systems desirable. This work highlights the opportunity offered by ac-STEM to establish direct links between the atomic scale structure of bimetallic nanoparticle systems and their resulting properties. We described a number of such opportunities in the next section.

## 8.2 Future Work

Our characterisation of the growth mode of AuRh nanorods and the interfacial structures of both AuRh and AuPd nanorods demonstrated the role played by reaction kinetics in forming structure in these systems, and thus the potential to gain control over structure formation at the atomic scale. A project systematically investigating the impact of reaction kinetics in both AuRh and AuPd systems would offer the possibility to investigate this further. By using a combination of controlled particle synthesis and atomically resolved ac-STEM imaging, it would be possible to correlate atomic structure with the reaction conditions, and thus better understand the mechanisms driving structure formation. Correlation of these results to catalytic reactivity testing and LSPR response measurements would offer the potential to unambiguously establish a link between atomic structure and resulting particle properties.

We have shown in this thesis that single particle LSPR characterisation of bimetallic samples using STEM-EELS offers considerable potential to further our understanding of bimetallic LSPR response. A project correlating particle structure to LSPR response, for example by measuring variations in response in different bimetallic systems, and with systematically controlled variations in interfacial structure or shell arrangement, allows the possibility to unambiguously establish the origin of bimetallic LSPR response in the dielectric coupling of the LSPR responses of the two metals. In addition, the possibility to correlate such results to variations in catalytic reactivity offers the potential to identify the mechanisms responsible for plasmonic enhancements to reactivity. Finally, through combining the sub-particle spatial resolution of single particle LSPR characterisation with similar single particle catalytic reactivity measurements, it may also be possible to establish a link between LSPR hot spots and localised catalytic reactivity.

Our identification of the formation of AuAg oxide structures through the long term aging in air of AuAg nanoparticles suggests the potential for further investigation of oxidation mechanisms in bimetallic nanoparticles. It would be interesting to compare the evolutionary pattern we have revealed in this system to other bimetallic systems containing either Au or Ag, to better understand the role each metal plays in this process. For example, the role of Ag might be clarified if we see similarly ordered bimetallic oxides form in other Ag containing bimetallic systems, and the role played by Au identified if we see Au atoms become incorporated in the oxide structures of metals other than Ag. It would also be interesting to investigate the impact that AuAg oxidation has on the catalytic reactivity of these particles.

Our work examining the structural changes induced in aged AuAg nanoparticles under the electron beam have suggested the possibility that LSPR response may influence the resulting particle structure, and in particular that the electric fields induced by the LSPR response of metallic particles may influence the migration of Au atoms in these particles. The ability to influence particle structure through manipulating LSPR response may offer a potential route to structural self-assembly, which could be investigated further using STEM-EELS plasmon mapping on similar systems.

In summary, the work we have presented in this thesis signals the considerable potential of ac-STEM, when used in combination with appropriate supporting techniques, in gaining a fundamental understanding of the origin of the enhanced properties of bimetallic nanoparticles, which is essential to their effective exploitation. Its unrivalled capability to correlate structure at the atomic scale with particle properties opens up a number of interesting lines of research within the field of bimetallic nanoparticle characterisation.

---

## **Appendix I**

### **Summary of AuRh and AuPd nanorod synthesis methodology**

The following is a summary the colloidal sequential synthesis processes followed for the AuRh and AuPd core-shell nanorods studied in Chapters 5 and 6 of this thesis. This has been reproduced from the supplementary information of reference 1. The detailed methodology for AuRh synthesis is described in reference 2.

#### **AuRh**

The Au seed NRs were synthesized using the method of Nikoobakht and El Sayed,<sup>3</sup> as modified by He et al.<sup>4</sup> 10.0 mL 0.1 M cetyl trimethyl ammonium bromide (CTAB) aqueous solution was mixed with 100  $\mu$ L 0.025 M HAuCl<sub>4</sub>, with the addition 0.6 mL of ice-cold 0.01 M of NaBH<sub>4</sub>. The seed solution was stirred vigorously for 3 minutes, kept at room temperature and used within 2-5 hours of preparation. The Au NR growth solution

---

was made with 100 mL 0.1 M CTAB, 2.0 mL 0.025 M HAuCl<sub>4</sub>, 1 mL 0.01 M of AgNO<sub>3</sub> and 1 mL 0.1 M ascorbic acid, also prepared at room temperature. 240 μL of seed solution was added to the growth solution with no further stirring or agitation.

Rh was deposited onto the Au NRs by reducing a 0.002 M aqueous solution of sodium hexachlororhodate (III) on to the Au NRs. 6 mL Au NR solution was centrifuged at 6000 rpm for 1 hour, to remove excess CTAB and nanospheres. The supernatant was removed using a pipette and the NRs were re-dispersed in 0.5 mL ultrapure water. The molar ratio of Au:Rh was varied by mixing 0.5 mL of Au NR solution with different volumes of 0.002 M Na<sub>3</sub>RhCl<sub>6</sub>·12H<sub>2</sub>O reagent (0.15, 0.643, 1.5, and 3.0 mL), giving samples with molar ratios Au:Rh of 10:1, 7:3, 1:1 and 1:2. 1 mL 0.2 M ascorbic acid was added and the total volume of each sample was adjusted to 4.5 mL. The mixture was stirred for 2 h at 40 °C. Water purified with a MilliQ Gradient A10 system was used throughout.

## **AuPd**

Gold nanorods were prepared on 500 mL scale using a modified seed-mediated method. 364 mg CTAB was dissolved in 5 mL of water at 30 °C. In a separate vial, 1 mg HAuCl<sub>4</sub>·3H<sub>2</sub>O was dissolved in 5 mL water. These two solutions were mixed together before 0.6 mL 0.01M ice-cold aqueous solution of NaBH<sub>4</sub> was introduced in one step with vigorous stirring (1200 rpm). The colour changed from greenish-yellow to dark brown as the mixture was stirred for 2 minutes. Growth solution was prepared by dissolving 18.22 g CTAB (slight heating is necessary) and 8.5 mg AgNO<sub>3</sub> in 250 mL of water. After 10 minutes, 250 mL of aqueous solution of HAuCl<sub>4</sub>·3H<sub>2</sub>O (prepared separately by dissolving 98.5 mg HAuCl<sub>4</sub>·3H<sub>2</sub>O in 250 mL H<sub>2</sub>O) was added to the mixture of CTAB and AgNO<sub>3</sub>.

---

After an additional 3 minutes, 3.6 mL of 0.08 M solution of ascorbic acid was added to the above mixture. The flask was hand-stirred until the mixture became colourless (typically 3-5 seconds). Next, 0.8 mL of seed solution was added all at once to the growth solution and the mixture was stirred for 15 seconds. The flask containing the growth solution was then placed into an oil bath at 27 oC and kept without stirring. A reddish-brown colour slowly developed within the first 10-15 minutes. In order to convert the remaining Au(I) ions to metallic gold 5 mL 0.1 M solution of ascorbic acid was added to 500 mL solution of Au NRs. The colour changed from brown to dark brown/red within 10 min and the reaction mixture was kept undisturbed for 2 h.

In a separate flask, a stock solution of  $1.974 \times 10^{-3}$  M Pd(II) was prepared by dissolving 35 mg of PdCl<sub>2</sub> in 10 mL 0.2M HCl and stirring for 2-3 hour. After the complete dissolution of PdCl<sub>2</sub>, the solution was further diluted with DI water up to 100 mL. Then 17 mL of  $1.974 \times 10^{-3}$  M solution of PdCl<sub>2</sub> was added to the Au NRs solution and the reaction mixture was left undisturbed for 12 h at 30o C. Addition of another 34 mL of  $1.974 \times 10^{-3}$  M solution of Pd (II), followed by 10 ml of 0.0788 M ascorbic solution was then carried out, which results in the formation of a 10-12 nm Pd shell on the AuNRs.

## List of References

1. Chantry, R.L.; Siritwatcharapiboon, W.; Horswell, S.L.; Khanal, B.P.; Zubarev, E.R.; Atanasov, I.; Johnston, R.L.; Li, Z.Y., An Atomistic View of the Interfacial Structures of Au-Core Rh and Pd-Shell Nanorods, *Nanoscale*, **2013**, *5*, 7452-7457
2. Chantry, R.L.; Siritwatcharapiboon, W.; Horswell, S.L.; Logsdail, A.J.; Johnston, R.L.; Li, Z.Y., Overgrowth of Rhodium on Gold Nanorods, *J. Phys. Chem. C* **2012**, *116*, 10312-10317
3. Nikoobakht, B.; El-Sayed, M.A., *Chem. Mater.*, **2003**, *15*, 1957-1962
4. He, W.; Wu, X.; Liu, J.; Zhang, K.; Chu, W.; Feng, L.; Hu, X.; Zhou, W.; Xie, S.; *J. Phys. Chem. C* **2009**, *113*, 10505-10510



---

## Appendix II

# Summary of the molecular dynamics simulation methodology

The following is a summary the molecular dynamics simulation methodology followed by Ivailo Atanasov and Roy Johnston (Department of Chemistry, University of Birmingham) for the results presented in Chapters 5 of this thesis. This has been adapted from the supplementary information of reference 1.

The molecular dynamics simulations were conducted of the vapour deposition of Au and Pd on planar {100} and {111} Au surfaces, at temperatures between 300 K and 500 K. We have used interatomic potentials based on the second-moment tight-binding approximation.<sup>2</sup> The parameters used are listed in Table S1. The parameter set for the Au-Pd interactions is fitted to bulk elastic constants and experimental mixing enthalpies.<sup>3-5</sup> Those for the Au-Rh system include the Rh-Rh potential from reference 2 and an Au-Au potential separately fitted to surface energies and the hcp-fcc energy difference.<sup>6</sup> The Au-Rh part has been fitted to the miscibility properties of Rh and Au in the bulk. The

predicted Au-Rh heats of solutions of impurities are 0.487 eV and 0.668 eV for Rh in Au and Au in Rh, respectively, in accordance with reference 7.

**Table S1: Parameter sets used for modelling Pd-Au and Rh-Au. Parameter notations correspond to references 2 to 5.**

Parameter	Pd-Au <sup>3-5</sup>			Rh-Au <sup>2</sup>		
	Pd-Pd	Pd-Au	Au-Au	Rh-Rh	Rh-Au	Au-Au
A (eV)	0.1715	0.2764	0.2096	0.062891	0.120341	0.129097
$\xi$ (eV)	1.7019	2.0820	1.8153	1.660162	1.516005	1.522199
p	11.000	10.569	10.139	18.450	9.529	12.500
q	3.7940	3.9130	4.0330	1.8670	1.7893	3.5500
$r_0$ (Å)	2.7485	2.8160	2.8840	2.6891	2.7867	2.8843

In all cases the Au substrates consist of 6 crystallographic planes. The atomic positions of the lowest plane were fixed to the bulk lattice constant at the given temperature, thus taking into account the thermal expansion of Au predicted by the atomic potentials. Periodic boundary conditions in the (x, y) directions were applied. The Au substrate was first equilibrated to the given temperature and then deposited Pd or Rh atoms at random (x, y) positions at a rate of 1 atom/ns. The Nosé-Hoover thermostat with  $Q = 0.55 \times 10^{-25}$  eV s<sup>2</sup> was applied<sup>8</sup> in order to keep the sample temperature constant during the deposition process.

Simulations were also conducted which added several Au atoms to the substrate after 0.5 monolayer coverage of Rh deposited on Au{111}. The system was then annealed for another 20 ns at 300 K, 400K and 500K.

---

## List of References

5. Chantry, R.L.; Siritwatcharapiboon, W.; Horswell, S.L.; Khanal, B.P.; Zubarev, E.R.; Atanasov, I.; Johnston, R.L.; Li, Z.Y., An Atomistic View of the Interfacial Structures of Au-Core Rh and Pd-Shell Nanorods, *Nanoscale*, **2013**, *5*, 7452-7457
6. Cleri, F.; Rosato, V.; *Phys. Rev. B* **1993**, *48*, 22–33
7. Baletto, F.; Ferrando, R.; Fortunelli, A.; Montalenti, F.; Mottet, C., *J. Chem. Phys.* **2002**, *116*, 3856–3863
8. Pittaway, F.; Paz-Borbón, L.O.; Johnston, R.L.; Arslan, H.; Ferrando, R.; Mottet, C.; Barcaro, G.; Fortunelli, A.; *J. Phys. Chem. C* **2009**, *113*, 9141–9152
9. Ismail, R.; Johnston R.L., *Phys. Chem. Chem. Phys.* **2010**, *12*, 8607–8619
10. Ismail, R.; Ferrando, R.; Johnston, R.L., *J. Phys. Chem. C* **2013**, *117*, 293–307
11. Okamoto, H.; Massalski, T.B., *Journal of Metals* **1984**, *36*, 57–57
12. Hünenberger, P.H., *Advanced Computer Simulation*, eds. C. Holm and K. Kremer, Springer: Berlin, 2005, vol. 173, pp. 105–149.